New Techniques for Space Science Missions

Joint program between Sapienza University of Rome and University of Rome Tor Vergata

PhD Program in Astronomy, Astrophysics and Space Science – XXXII Ciclo

Candidate
Stefano Carletta
ID number 1646436

Thesis Advisor
Prof. Paolo Teofilatto

January 2020

Thesis defended on 16 January 2020
in front of a Board of Examiners composed by:

Prof. Carlo Baccigaluppi (chairman)
Prof. Massimo Gervasi
Prof. Pasquale Palumbo

Dedicated to travelers

Abstract

In the last decades, the growing interest in investigating natural science in the space environment sets new targets, constraints and challenges in space mission design, defining what is nowadays known as space science. The goal of this PhD research is the development of new techniques of mission analysis, which can lead to further development of space science missions using CubeSat technology. Two main objectives have been pursued, related to both solar system exploration and low Earth orbit missions.

Due to the low power and thrust available on a CubeSat, low energy trajectories are necessary to allow solar system exploration. These are designed here considering a further constraint on the transfer time, which should be minimized to limit the effects of the hostile space environment on the on-board systems, typically based on components off-the-shelf. According to these issues, the topological properties of the linear dynamics in the circular restricted 3-body problem were investigated to develop a method allowing the design of internal transit and captures, including the possibility to select the osculating orbital elements at capture.

Three guidance strategies are proposed, allowing modification on the ultimate behavior of trajectories to match the desired mission requirements, also in the presence of the gravitational perturbations due to a fourth body. These strategies are effective with modest velocity variations (delta-V) and are tailored to be implemented with compact continuous thrusters, compatible with CubeSats. The method was originally developed in the dynamical framework of the spatial circular restricted 3-body problem and later extended to the elliptic restricted 4-body problem.

The final chapters are related to low Earth orbit missions, presenting the development of a purely magnetic attitude determination and control systems, suitable for implementation as a backup solution on CubeSats. Attitude control allows detumbling and pointing towards the magnetic field. At the same time, attitude determination is obtained from the only measurements of a three-axis magnetometer and a model of the geomagnetic field, without implementing any sophisticate filtering solution. To enhance the computational efficiency of the system, complex matrix operations are arranged into a form of the Faddeev algorithm, which can be conveniently implemented on the field programmable gate array core of a CubeSat on-board computer using systolic array architecture. The performance and the robustness of the algorithm are evaluated by means of both numerical analyses in Matlab Simulink and hardware-in-the-loop simulations in a Helmholtz cage facility.

Contents

List of Acronyms

ADCS Attitude Determination and Control System

COTS Components Off-The-Shelf

CR3BP Circular Restricted 3-Body Problem

EKF Extended Kalman Filter

ER4BP Elliptic Restricted 4-Body Problem

ESA European Space Agency

FPGA Field Programmable Gate Array

ISRO Indian Space Research Organisation

LEO Low Earth OOrbit

LMO Low Moon Orbit

MEMS Micro Electro-Mechanical Systems

NASA National Aeronautics and Space Administration

OBC On-Board Computer

UKF Unscented Kalman Filter

WSB Weak Stability Boundary

Chapter 1

Introduction

Space exploration experienced dramatic changes during the last decades, driven by continuously evolving technology. Several branches of natural science, studying natural phenomena and physiology in different regions of the solar system, are increasingly involved in space flight, defining new targets, constraints and challenges in space mission design. These disciplines are commonly referred to as space science.

An effect of space science on space mission design is that of stressing two requirements: accessibility and affordability. In fact, progress in the field is typically led by institutions whose budgets are considerably lower than those of space and military agencies or commercial companies. In this scenario, small and low-cost satellites, such as CubeSats, could represent a disruptive technology, once adequate tools of mission analysis are developed.

New techniques are therefore necessary, to solve the old problem of space flight complying the modern mission requirements. This thesis collects the results of my PhD research project, pursuing two goals of current interest in CubeSat missions: the design of low-energy trajectories, allowing solar system exploration and testing of purely magnetic attitude determination and control systems, which can improve the capability and reliability of space science missions in low Earth orbits.

1.1 Space science missions: trends, targets and challenges

A variety of factors contribute to define the boundary of space exploration and influence the target of current and future space missions, including the evolving capability of spacecraft, the advantages of space-based activities over the comparable ground-based ones, the direct and indirect economic and social impact, political and financial constraints. In fact, space activities need long term planning to reach the desired goals within limited budget and development time, and these goals should be selected in those areas where major progress can be expected in the following decades.

As stated in their periodic reports, the space agencies ESA [43, 48], ISRO [80], NASA [121, 122] and Roscosmos [152] share the common purpose of developing technology to improve solar system exploration. The majority of missions envisioned are aimed at space science research, including astronomy, astrophysics, planetology

and physiology in the microgravity environment or in different atmospheres. Research in these disciplines could greatly benefit from performing experiments in-situ, to enter domains that are not accessible from ground-based facilities. These innovative and challenging missions can be conveniently classified based on their destination

- low Earth orbits

- Sun-Earth libration (or equilibrium) points[1]

- other celestial bodies (i.e. the Moon, Mars, Venus, Jupiter and its Galilean moons)
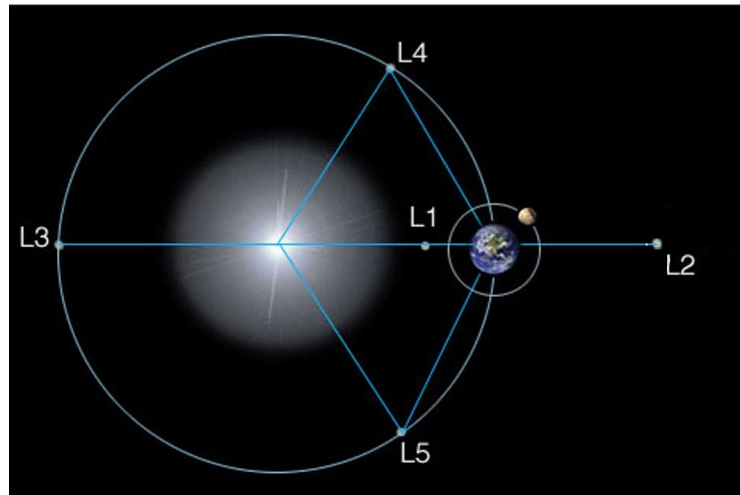
Figure 1.1. The Sun-Earth libration points [128]

The regions surrounding Sun-Earth libration points, sketched in Figure 1.1, are characterized by low environmental disturbances and high observing efficiency, and are thus suitable for investigating stellar and galactic physics [57]. In particular, orbits around the Sun-Earth L_1 offer an unobstructed view of the Sun and successful missions have already been designed taking advantage of it, with the first one being the International Sun-Earth Explorer 3 (ISEE-3), launched in 1978 to take measurements of the solar wind upstream from Earth [54]. Recent missions include LISA Pathfinder, an ESA proof-of-concept launched in 2015 to test technologies necessary for the follow-up mission, the evolved Laser Interferometer Space Antenna (eLISA), a gravitational wave observatory [100, 112]. Lisa Pathfinder demonstrated not only the feasibility of eLISA, which is planned to be launched within the next two decades, but also the flexibility of missions based on low-energy transfers, characterized by extended launch windows although requiring enhanced design techniques [50, 105].

Next-generation space observatories will be placed at Sun-Earth L_2, a region of space characterized by thermal stability, where the spacecraft can easily radiate the heat away and cool down, minimizing the thermal disturbance. Moreover, because of the relative position of the Earth and the Sun, a spacecraft at L_2 would never be

---

[1]Libration points are discussed in detail in sections 1.3 and 2.2.

eclipsed, having a constantly clear view of the universe, for observations, and of the Earth, for communication.

An eminent example is represented by the James Webb Space Telescope (JWST) [121], aimed at producing support for astrophysical studies about the origin of galaxies. Reviewing the Hubble Space Telescope mission, scientists agreed that, in order to achieve this target, the JWST must provide a higher angular resolution and coverage of the mid-IR, thus allowing the observation of the same features in objects at different redshift [50]. From a technical perspective, it means that the telescope must be kept at considerably low temperature and, consequently, NASA mission analysts designed an orbit for it around the Sun-Earth L_2 [10, 167, 183]. The European Space Agency is currently involved in developing several space telescopes to orbit near L_2. The Planetary Transit and Oscillations of stars (PLATO) is planned to be launched in 2025 and it is expected to help enhance our understanding of the formation and the evolution of planetary systems [47]. Dark energy will be the primary source of investigation for the Euclid mission, planned to be launched in 2022 [44, 149], while the Advanced Telescope for High-ENergy Astrophysics (ATHENA) will be equipped with a cryogenic X-ray spectrometer (X-IFU) and the Wide Field Imager (WFI) to study ordinary matter in the universe [111, 150]. Dark energy and matter will be investigated by the X-ray observatory Spektr-RG, launched on July 13th 2019 by Roscosmos, representing the first Russian spacecraft heading to a libration point, the Sun-Earth L_2 [154]. Research on dark energy, dark matter and exoplanets is again the goal of an ambitious NASA mission, the Wide-Field InfraRed Survey Telescope (WFIRST), slated to launch in 2020 [125].

Libration point missions outline a captivating scenario in which space telescopes and probes move along non-Keplerian orbits [58], whose design requires new analytical and computational methods, increasing the complexity of mission design and analysis. Nevertheless, as outlined in section 1.3, the same tools developed for libration point missions can be conveniently used to design low-energy lunar and interplanetary trajectories. In the era of small and low-power satellites (see section 1.2), these innovative pathways can represent the access gate to a whole new class of space missions. Low-energy trajectories show the following benefits [55, 137]

- fuel saving, because of the low ΔV required

- high flexibility, allowing both injection into different orbits from the same launch, and into a targeted orbit from different launch windows

- relaxed operational timeline, because the low ΔV implies slower transfers

This renewed flexibility is one of the reasons why payload mass trends of space exploration satellites are changing and the launcher capability is somehow a less strict limitation than it was until the early 1990's [151].

All the major space agencies are actively involved in missions to the Moon, and some of them are also envisioning human exploration [75, 153]. The expertise gained in lunar missions is pivotal to design the next generation of spacecraft, aimed at exploring the farthest regions of the solar system. ESA's first Small Mission for Advanced Research in Technology (SMART-1), launched in 2003, tested mandatory technologies and design methods for further scientific exploration of the Moon

[56, 148, 159]. NASA Acceleration, Reconnection, Turbulence and Electrodynamics of the Moon Interaction with the Sun (ARTEMIS) is the first mission ever to orbit the Earth-Moon libration points L_1 and L_2 [124]. The mission is made up of two probes, ARTEMIS P1 and P2, designed to transfer from L_1 to L_2 and keep a stable orbit around each point [2, 59, 170]. A proof of low-energy trajectory flexibility was given by Chang'e-2, the second Chinese lunar probe. The satellite, after orbiting the Moon for several months to complete the primary tasks of the mission, was redirected to Sun-Earth L_2, reaching the destination on August 25th 2011, after a 77-day journey [76, 106]. The probe finally performed a flyby of Asteroid Toutatis, completing a successful deep-space phase of the mission.

The future of space science cannot be limited to the exploration of the cislunar and translunar space. To better understand the nature of the universe, we must move farther from the Earth, heading to the other celestial bodies of our solar system and beyond. Interplanetary space science missions are currently being developed, including NASA's Europa Clipper mission, aimed at understanding if the conditions for life could exist on the icy Galilean moon [97] . Similarly, ESA's JUpiter ICy moons Explorer (JUICE), scheduled for launch in 2022 aims at studying the conditions for the emergence of habitable worlds around gas giants in the solar system, in particular the Galilean moons Ganymede, Callisto and Europa [45]. ESA is also developing the Solar Orbiter mission, which will be the first spacecraft to perform close-up studies of the Sun's inner heliosphere [166]. These missions are typically designed on the basis of traditional Keplerian trajectories [19, 20, 96, 98, 99], nevertheless low-energy trajectories represent an interesting alternative or complementary solution to extend the capability of the mission, eventually integrating low-cost secondary spacecraft. Missions to Mars and between the Jovian moons based on low-energy trajectories have been proposed, but not developed yet [52, 67, 107].

Space science is not limited to deep space. The lower cost and complexity of low Earth orbit (LEO) satellites represent an attractive alternative. LEO missions are often dedicated to Earth observation for atmospheric [39, 42, 83], ground [41, 92] and ocean monitoring [6], but can also provide support to answer cosmic questions. Some relevant examples are given by NASA's Spectro-Photometer for the History of the universe, Epoch of Reionization and ices Explorer (SPHEREx), collecting data in both optical and near-infrared light on more than 300 million galaxies and 100 million stars in the Milky Way [40], or the Gravity Recovery And Climate Experiment Follow-On (GRACE-FO), tracking variations in gravity over Earth's surface [123]. Europe is always involved in similar missions, such as the LAser RElativity Satellite (LARES) by the Italian Space Agency (ASI), aiming at measuring the Lense-Thirring effect predicted by general relativity [135] and ESA's CHaracterising ExOPlanet Satellite (CHEOPS), targeting nearby stars which are known to host exoplanets, in the super-Earth to Neptune size range, to characterize them [13, 46].

In the last decade, the development of CubeSat technology set the basis for LEO space science missions accessible to small entities, such as research centers and universities, with limited budgets. In 2014, NASA Next Space Technologies for Exploration Partnerships (NestSTEP) identified low-energy trajectories as the pivotal technology for opening deep space exploration to CubeSats [126], defining one of the most challenging targets in space science and exploration. This thesis proposes suitable solutions to this challenge.

1.2 Space science using CubeSats

CubeSat is a class of nanosatellites characterized by a modular structure and on-board systems mainly realized from commercial off-the-shelf (COTS) components. The elementary unit is represented by a cubic satellite with standardized edge length and mass, respectively equal to 10 cm and 1.33 kg. If compared to bigger spacecraft, these miniaturized satellites can be developed at low-cost and in short time, with projects typically evolving from concept design to deployment in orbit within 24 months. These features determined their rapid diffusion and progress, becoming in almost 10 years fundamental tools for institutions and companies involved in space science research, technology demonstration and space exploration missions. As a matter of fact, CubeSats are nowadays the majority of spacecraft either launched or in development [119]. The popularity of CubeSat missions can be addressed to their flexibility, which allows easily adapting several design parameters (i.e. size, weight, power, cost) to the targeted missions [84]. Moreover, the rapid progress in both miniaturized computers and micro electro-mechanical systems (MEMS) is improving the capabilities of compact electronics, leading CubeSats to represent a suitable alternative platform to explore the cislunar space and the solar system [126, 162].

As of 2016, no CubeSat had ever flown beyond LEO. NASA's Mars Cube One (MarCO) satellites A and B were the first CubeSats to fly to another planet. MarCO 6-unit (6U) CubeSats were launched on May 5th 2018 and completed their journey to Mars on November 26th 2018, proving that CubeSats can survive the trip to deep space [88]. A first generation of space science CubeSats heading to the cislunar space will be launched with the maiden flight of the Space Launch System (SLS) [85, 116]. Some of these missions are designed to follow special low-energy trajectories which will conclude into a ballistc capture by the Moon. Ballistic capture [2]f occurs when a spacecraft is spontaneously trapped by the gravitational field of a celestial body, which the spacecraft will orbit for a relatively long time. In the mentioned missions, the phenomenon is used to design transit trajectories from the Earth to the Moon with significant savings in ΔV, reducing it to values compatible with the performance of compact thrusters suitable for CubeSats [17, 61, 71, 127].

Interest in studying the Moon also led to the design of CubeSat missions to the Earth-Moon libration point L_2. These include the EQUilibriUm Lunar-Earth point 6U Spacecraft (EQUULEUS), aiming at studying the Earth's radiation environment, characterizing the flux of impacting meteors at the dark side of the Moon and demonstrating the validity of CubeSats control systems under the effect of the luni-solar perturbation [23, 134], and the Lunar Meteroid Impact Observer (LUMIO), aiming at qualitative and quantitative characterization of the meteoroid impacts on the lunar far side [175].

The Moon is not meant to be a limit for CubeSat deep space exploration missions. Probes heading to asteroids are currently under development, including ESA's Miniaturised Asteroid Remote Geophysical Observer (M-ARGO) and NASA's Near Earth Asteroid Scout (NEA Scout), which will map asteroids and demonstrate several technologies aimed at improing CubeSat capabilities [113, 178]. The joint

---

[2]An overview of ballistic capture mission is presented in section 1.3 and a rigorous mathematical definition is discussed in section 2.4.

NASA and JPL Interplanetary NanoSpacecraft Pathfinder In a Relevant Environment (INSPIRE) mission is designed to dispatch two CubeSats beyond Earth orbit as demonstrators for functionality, communications, navigation, and payload-hosting technologies which are considered as fundamental for heliophysics and planetary science [87].

CubeSats have proved to be excellent technology demonstrators to test solutions which can be later implemented on bigger spacecraft, improving their reliability. Even though this feature is still appealing for space science missions, the new challenging scenarios described in the previous paragraphs require an increase in the reliability of CubeSat platforms themselves, impacting the development process from concept design to test. In fact, an advantage in using the CubeSat standard is that the relative simplicity of the electronic on-board systems allows extensive Hardware-in-the-Loop (HiL) simulations, furthermore the compact size and low weight of the platform open to innovative methods of experimental testing, based on the use of facilities specifically developed for small satellites. A case of particular interest is that of air-bearing testbeds, facilities aimed at reproducing the microgravity condition experienced in space, which allow simulating spacecraft motion in the terrestrial environment [156, 160].

The development of successful CubeSat space science missions require both novel theoretical methods and experimental techniques. In this manuscript, the theoretical aspects examined include ballistic capture for deep space missions and magnetic attitude determination and control of LEO CubeSats. Experimental techniques and facilities to verify the performance and suitability of the solutions proposed are investigated as well and performed for some test cases.

1.3   Solar system exploration

Space mission design techniques change because of the evolving technology and of the new formulation of problems related to space flight. The main features of space science missions envisioned for the near future were outlined in sections 1.1 and 1.2. From this review, low-energy trajectories emerged as the cornerstone of future space science missions beyond Earth, either based on classic big spacecraft or on innovative small CubeSats. New design concepts introduce new complexities which must be overcome to achieve the expected advances in space exploration. In this section, the state of the art in low-energy trajectory design is discussed, including comparisons with classic techniques. The purpose is to introduce a clear overview of the issue, before to provide a rigorous mathematical formulation of the problem, provided in Chapter 2. For the sake of clearness, the examples given hereafter refer to Earth-Moon missions.

1.3.1   From Keplerian to multi-body dynamics

Traditional orbital transfers are determined based on Keplerian 2-body dynamics, resulting in trajectories that can be represented as conic arcs or patched sequences of them. Considering an Earth-Moon mission, the transfer typically begins in LEO, where the spacecraft was previously injected by the launcher or placed after some maneuvers. When the spacecraft is at the pericenter, a sudden increase of velocity

(ΔV) is provided by the thrusters, raising the apocenter of the orbit to be inside the lunar sphere of influence, where the gravitational attraction of the Moon dominates[3]. When at the apocenter, the spacecraft is inserted into a low lunar orbit, by a further change in the spacecraft velocity. A similar transfer, sketched in Figure 1.2, was followed by the Apollo missions and can take from 3 to 5 days depending on the total ΔV provided, namely the total variation of the spacecraft velocity produced by the engines [128].
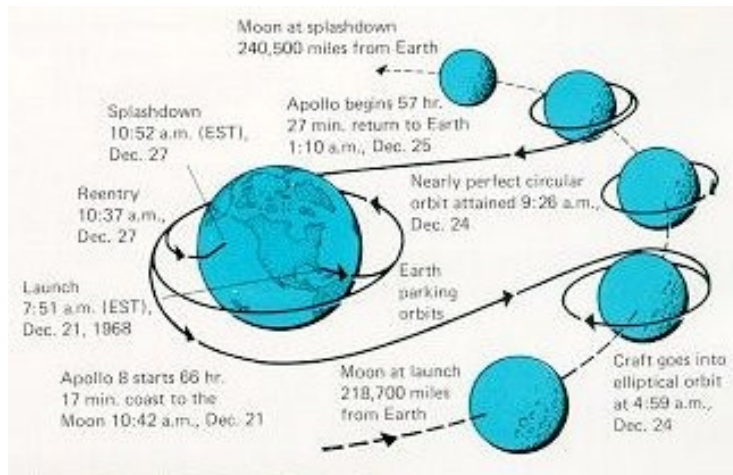
Figure 1.2. Sketch of NASA Apollo 8 Earth-Moon transfer [129]

In 1990 the Japanese Institute of Space and Astronautical Science (ISAS) launched the twin satellites MUSES-A and MUSES-B, aimed at testing the necessary technology for future lunar and interplanetary missions. The plan was to send MUSES-B into lunar orbit, with its twin MUSES-A orbiting in LEO to support telecommunication. Nevertheless, due to some issues occurred after the deployment, MUSES-B suffered a failure and got lost. It was at that point that the ISAS mission control, with the support of Belbruno, who had recently discovered a new class of fuel saving Earth-Moon trajectories, redesigned the mission and changed the flight plan for MUSES-A which reached the Moon in October 1991. The satellite, later renamed Hiten, was not equipped to leave LEO and carried an insufficient amount of fuel to move to the Moon through a traditional transfer [11]. In fact, this successful mission was achieved by modelling the lunar transfer in a multi-body environment, considering the combined gravitational actions on the spacecraft from the three most influential bodies: the Sun, the Earth and the Moon. Hiten trajectory, designed by Belbruno and Miller [12] is shown in Figure 1.3. It can be noted that the trajectory departs from LEO and extends far beyond the translunar space, reaching the proximity of Sun-Earth L_1, before folding back to the Moon. For this reason, Belbruno-Miller trajectories are also called external transfers.

---

[3]The sphere of influence, or Hill sphere, is the region of space in which the gravitational attraction of a celestial body is preeminent over the others [171]
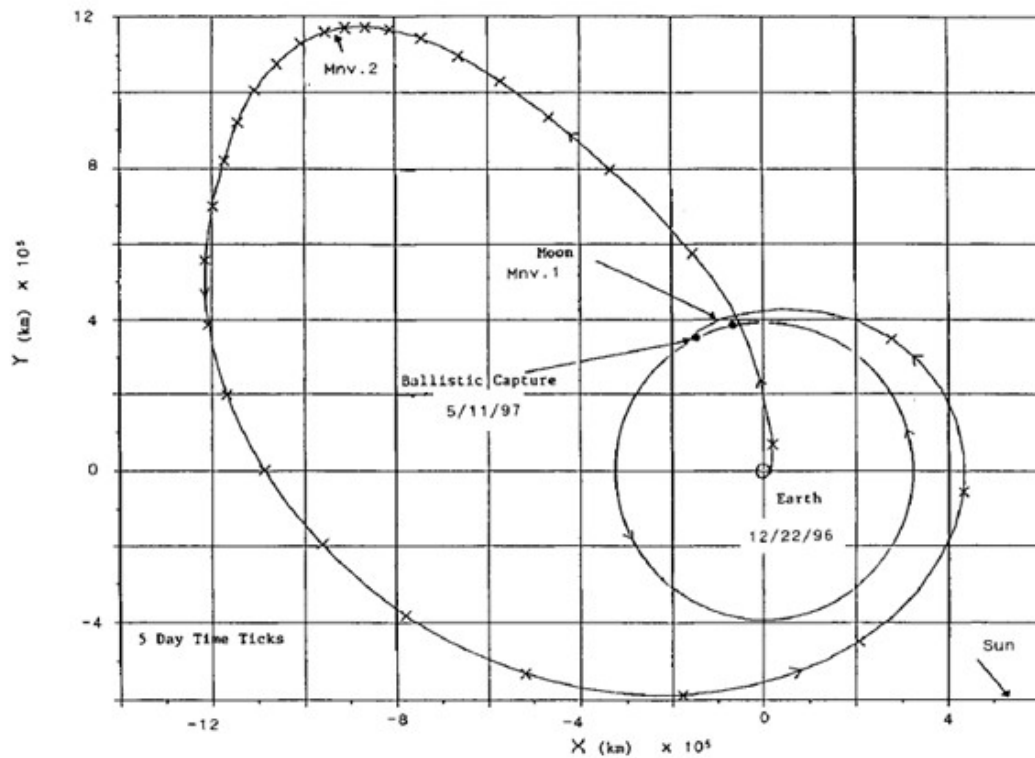
Figure 1.3. The Hiten trajectory [12]

External transfers in such a 4-body system, including the three celestial bodies and the spacecraft, can be computed taking advantage of some simplifying hypotheses

- if compared to that of the three celestial bodies, the mass of the spacecraft, as well as its gravitational field, are negligible

- the eccentricity of the Earth's orbit around the Sun and of the Moon's orbit around the Earth are negligible (as a first approximation)

- close to the Earth (i.e. in LEO) the gravitational pull of the Moon is negligible with respect to that of the Sun and the Earth

- similarly, on a Low Moon Orbit (LMO) the gravitational pull of the Sun is negligible with respect to that of the Earth and the Moon

According to the above mentioned hypotheses, the original 4-body problem can be approximated by a combination of two circular restricted 3-body problems (CR3BP): the Sun-Earth-spacecraft and the Earth-Moon-spacecraft [171]. A segment of the trajectory is then designed from each CR3BP and the final path in the complete 4-body system is obtained by patching these segments [35]. This technique was successfully used to design orbits with prescribed itineraries within the cis- and trans-lunar space [136, 138, 184], to Mars [114, 174] and between the Jovian moons [16, 68]. More accurate trajectories can be obtained by propagating the solutions from the patched CR3BP on more refined models. These propagators typically include the real eccentricity for celestial bodies orbital motion [78], take into account the N-body

environment of the solar system, using the ephemerides model [53, 108, 170], and can integrate the compensating effect on the perturbations produced by thrust corrections [18].

If the spheres of influence of the departure and arrival celestial body are nested (i.e. Earth-Moon, Sun-planet, planet-moon) then low-energy transfers between the two bodies, named the primaries, can be obtained as solutions of one single CR3BP [28]. The resulting trajectories directly connect the two primaries and evolve inside the bigger sphere of influence, therefore they are called internal transfers.
Internal transfers are considerably faster than external ones, which can require up to 3 months from LEO to LMO [136], limiting the exposure of electronic on-board systems to the hostile space environment beyond Earth. This feature can have a dramatic impact on the reliability of the mission, especially when COTS components are extensively used, such as in CubeSats. Based on these trajectories, missions from the Earth to the Moon [69, 140, 143] and between Jupiter and the Galilean moons have been designed [52] . The problem is typically solved for the two-dimensional case, thus assuming the spacecraft trajectory evolves on the same plane of the primaries, therefore only co-planar departure and arrival orbits can be connected. New techniques should be implemented to solve the three-dimensional problem, including the constraints set by the on-board sensors and actuators [90].

1.3.2   The space superhighways

The CR3BP has been extensively studied since the late 19th century and its solutions are known to have a complex and chaotic behavior [139]. One algebraic integral of motion exists for the problem, it is named the Jacobi constant (C) and is proportional to the total (constant) energy of the system, in particular it decreases as the energy increases. The libration points introduced in section 1.1 correspond to the five equilibrium points of the CR3BP. As detailed in Chapter 2, the motion in the proximity of the libration point L_i is only possible if the energy is higher than a specific threshold level or, equivalently, if the Jacobi constant is lower than a threshold value C_i. Using the same subscripts in Figure 1.1, the following relation holds: $C_1 > C_2 > C_3 > C_4 = C_5$.

The libration points L_1, L_2 and L_3 are referred to as the collinear libration points, because they lay on the straight line passing through the centers of the primaries. The linearization of the CR3BP in the proximity of a collinear libration point shows that unstable periodc and quasi-periodic orbits exist. Assuming a fixed value of C, these libration point orbits can be conveniently represented on a Poincaré map [60, 89]. The boundary of the Poincaré map shown in Figure 1.4 corresponds to *Lyapunov* orbits, which lie entirely in the plane of the primaries. The point at the center of the map is associated to a 8-shaped out of plane, or *vertical*, periodic orbit. The surrounding region includes non-planar quasi-periodic *Lissajous* orbits. Close to the top and the bottom of the map, two points can be identified, corresponding to the non-planar periodic *halo* orbits. In the neighborhood of these points, the invariant curves describe again a quasi-periodic motion and related orbits are called *quasi-halo*. The determination of libration point orbits is a crucial step in the definition of low energy transfers because they are located at the intersection of stable and unstable manifolds, forming the *space superhighways* described hereafter.
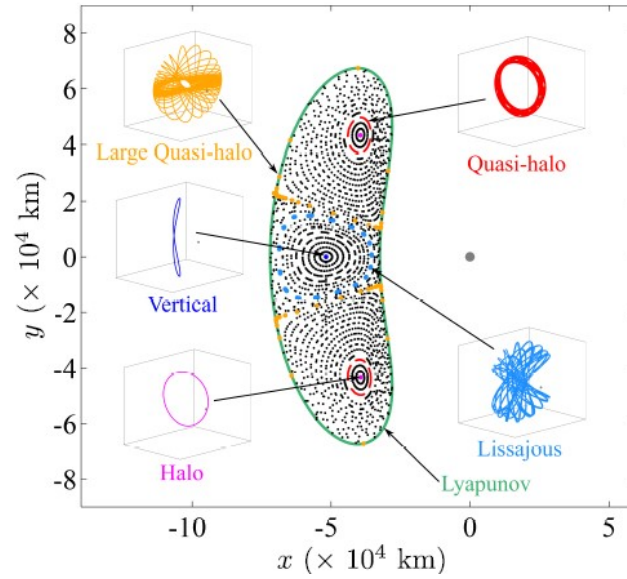
Figure 1.4. Poincaré map of periodic and quasi-periodic libration point orbits in the
vicinity of the Earth-Moon L_1 [60]
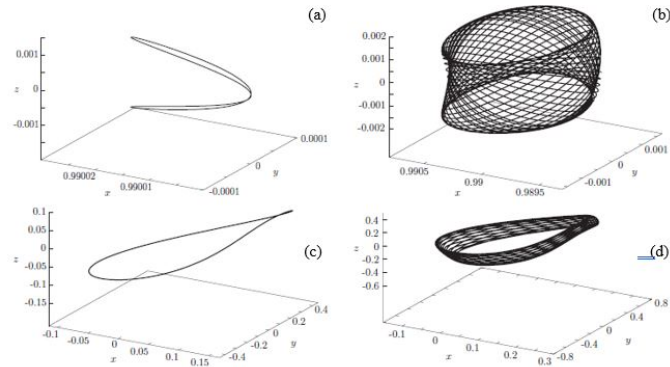
Figure 1.5. Representation of some three-dimensional libration point orbits: (a) vertical
periodic, (b) Lissajous, (c) halo and (d) quasi-halo [67]

The unstable motion along a collinear libration point orbit can be represented in
the six-dimensional phase space, whose coordinates are the three position components
and the corresponding velocity components. As proved by Poincaré in the late
nineteenth century [139], this representation produces a six-dimensional surface,
named the invariant manifold, such that all those trajectories which belong to
the manifold remain on it through their dynamical evolution (69), leading to the
following results

- a spacecraft on a collinear libration point orbit slowly drifts out of it, driven by
  its unstable dynamics, migrating on an isoenergetic ustable invariant manifold

- a spacecraft moving on a stable manifold will converge, within indefinite time,
  to a collinear libration point orbit along an isoenergetic path.

In fact, manifolds are conveniently classified into two groups: *stable* manifolds, containing all the trajectories converging to a collinear libration point orbit, and *unstable* manifolds, which collect all the paths departing from the mentioned orbit. The intersection between the stable and the unstable manifold is the collinear libration point orbit (i.e. Lyapunov, halo, etc.).

Considering a collinear libration point L_i, if the value of the Jacobi constant is slightly lower than the threshold C_i, then the invariant manifolds act as separatrices between *transit* trajectories, orbiting alternately around both the primaries, and *bouncing* trajectories, strictly confined to the neighborhood of just one primary. In the phase space, transit trajectories are included within the hypersurface represented by the invariant manifold, while bouncing trajectories are confined outside the manifold. A clear visualization of this property can be provided considering the simpler case of the planar CR3BP, characterized by four state variables (the in-plane position and velocity components) and the integral of motion C, thus by three-dimensional invariant manifolds. Using Birkhoff's equations [15] and cylindrical isomorphic mapping [64, 65], the phase space can be reduced to dimension three and the invariant manifolds can be represented by cylindrical channels, or tubes, allowing clear graphic representation of the separatrix, with transit and bouncing trajectories running, respectively, inside and outside the tubes. A stable and an unstable manifold, related to a halo orbit about Earth-Moon L_1, are represented in the form of tubes in Figure 1.6. The results discussed for the planar CR3BP can be extended to the spatial problem [141]. In this case, the phase space reduces to dimension five and the advantage of cylindrical representation defaults.
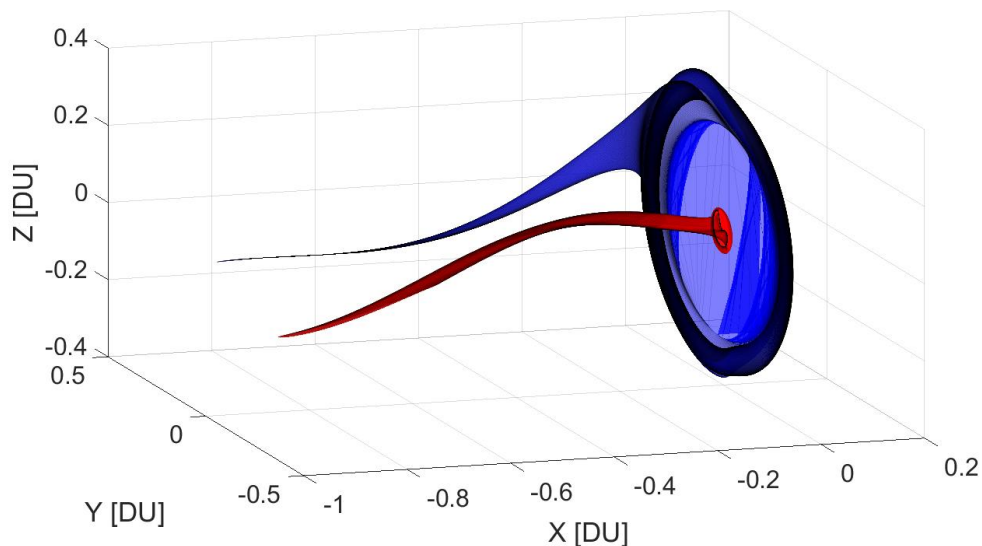

Figure 1.6. The stable (blue) and unstable (red) manifold related to a halo orbit about L_1 represented as tubes [24]

Manifolds are global structures that extend far beyond the neighborhood of the libration points. Whenever two (or more) manifolds intersect in the phase space, motion from one to the other can be performed at theoretically null energy expense, in a so called ballistic flight. The network of invariant manifolds belonging to different 3-body systems represents a pathway in which the spacecraft can move with minimum energy expense, mainly related to orbital corrections. This network is commonly referred to as the space superhighways and several missions have been designed to take advantage of it for moving from the Earth to the Moon and beyond [33, 102, 118, 140, 142].

1.3.3   Ballistic capture and weak stability boundary

Deep space missions can take advantage of low-energy transits trajectories, belonging to the phase subspace delimited by the invariant manifolds. Assuming that the perturbations can be neglected, the energy needed to perform such mission is that required to transfer from the departure orbit to the manifold and from here to the arrival orbit. If some conditions are matched, a spacecraft on a low-energy transit can be trapped by the gravitational field of the closest primary, thus it will start orbiting the celestial body for some relatively long time. Such a trajectory is called a ballistic capture and can be temporary (weak capture) or long-term. Spacecraft are generally temporary captured. CubeSats missions can benefit from ballistic captures, because of the limited ΔV required to perform the orbtal transfer. A typical mission profile for an Earth-Moon ballistic capture would include

1. Propelled transfer from an Earth orbit to the stable manifold heading to L_1 (internal transfer) or L_2 (external transfer)

2. Isoenergetic motion inside the stable manifold towards a collinear libration point orbit

3. Injection into the unstable manifold towards the Moon

4. Ballistic capture from the Moon

5. Propelled stabilization or injection into the final lunar orbit, leaving the unstable manifold.

The concept of weak ballistic capture was introduced by Belbruno in 1987, who also applied it to recover the MUSES mission [12]. The combination of all the possible cases producing weak ballistic capture forms a set called a weak stability boundary (WSB). The WSB can be viewed as the region in which the gravitational forces of the primaries approximately balance the centrifugal force of the moving spacecraft [4]. A WSB exists in the proximity of the primaries and of the collinear libration points and Belbruno used them to design low energy transfers based on two patched CR3BP [91, 95, 144, 174]. In 1969, Conley proved that internal ballistic captures exist as well for the planar CR3BP [29], providing their topological location in the phase space surrounding libration points L_1 and L_2. A number of missions

---

[4]The description of WSB is similar to that of equilibrium point and differs from it because the velocity is not zero.

based on this model have been proposed, aimed at exploring the cislunar space and the Moon [18, 69, 140] and the Jovian moons, with particular interest into Ganymede and Europa [53, 66].

Internal ballistic capture offer the same advantages of internal transfers with respect to external transfers and are particularly attractive when short time to capture is desired. Nevertheless, previous investigations indicate two critical aspects, related to the osculating orbital elements at capture: the inclination with respect to the plane of the primaries is almost negligible and the radius at pericenter is relatively high; these issues limit their use on an extensive number of missions. Recent results suggest that this constraint might be removed [82, 115], opening to solutions which represent an area of investigation for my research project, as detailed in section 1.5.

1.4   From low Earth orbit to deep space

Low-energy trajectories and CubeSat technlogy are tracing a new way for accessing deep space, with significant savings in cost and development time. To fully benefit from this advanced solutions in mission design, a marked improvement of CubeSat platforms is required, involving the development of new on-board systems in terms of both performance and reliability. For these goals to be achieved, the implementation of new facilities and techniques for experimental testing is highly desirable.

Nowadays, most of the techniques used on CubeSats are simple adaptation of those developed for big spacecraft. If this paradigm seemed appropriate in the early days of small satellites, the ten years experience revealed that CubeSats should be considered as a new and independent technology, more than a mere scaled-down version of traditional big satellites. New design techniques specifically tailored for CubeSats are therefore necessary, not only to achieve new goals, such as deep space exploration (section 1.3), but to extend the capability of these platforms for LEO missions also. It is worth noting that increasing the capabilities of small satellites would have a direct impact on improving access to space and could reasonably be a major driver in the growth of space science.

A fundamental system which is worth extensive investigation is the attitude determination and control system (ADCS), aimed at determining and modifying the satellite orientation in space. The accuracy of the ADCS depends on that of the attitude hardware, sensors and actuators, and of the determination and control algorithms, converting the information from the sensors into inputs to the actuators. Both the hardware and the algorithms should be selected to match the requirements set by mission operations. Strict constraints on the selection and complexity of attitude hardware and algorithms result from the limited power and computational efficiency characterizing CubeSats, a major drawback arising from the use of standard low-cost components.

A promising class of ADCS is that based on the use of a three-axis magnetometer, as the only attitude sensor, and three actuators typically represented by magnetic coils, named magnetorquers, producing three mutually orthogonal torques. The interest in such an ADCS is driven by the reliability, compactness, low weight and cost of magnetometers, and by the simplicity and low power-to-torque ratio

characterizing the magnetorquers[5].

Attitude determination using only a three-axis magnetometer is not a trivial task, because this sensor can only resolve two axes of the spacecraft attitude, and a challenging filtering process is required to produce complete estimation on all of the three axes. The first solution to this problem was proposed by Natanson et al. who developed the deterministic attitude determination from magnetometer-only data (DADMOD) algorithm and used it to initialize a real-time sequential filter (RTSF) [131, 132]. Almost the totality of the magnetometer-only attitude determination methods proposed are based on the use of the extended Kalman filter (EKF) and can have accuracy below 5 deg on attitude and 0.01 deg/sec on the angular rates [72, 145, 168]. Better accuracy can be achieved using the more complex unscented Kalman filter (UKF) [109], or the two-step EKF algorithm proposed by Searcy and Pernicka [161], which can estimate attitude with less than 1 deg error, but is effective only for angular rates higher than 0.1 deg/sec.

The design of a Kalman Filter for attitude determination requires processing all of the 6 (or 7, if using quaternions) attitude dynamics variables, as detailed in section 6.1 [181]. Implementing such a Kalman Filter on a CubeSat on-board computer (OBC) can be a real issue, because it requires resources which can exceed the capability of the main core of the OBC, often a field programmable gate array (FPGA).

A goal of my research project is that of developing a purely magnetic ADCS which is specifically addressed for the implementation on the FPGA of a CubeSat OBC. The solution proposed does not depend on the Kalman filter, emphasizes the computational efficiency and can provide an accuracy of the order of few degrees, adequate for most of the CubeSat missions in LEO, which are the target for the solution proposed. Deep space CubeSats could also benefit from it, during the stabilization process after the deployment in LEO from the launcher (detumbling), or as an effective backup solution.

---

[5]For the readers who are new to these systems, the low power-to-torque ratio is a direct consequence of the magnetorquer operating principle, described by Lorentz's force. As detailed in section 6.1, the torque produced by a magnetorquer arises from the interaction between the geomagnetic field and the magnetic dipole moment generated by the actuator, when an electric current is induced in the coil. It follows that the only power required to drive the system is that necessary to induce the electric current, while the contribute of the geomagnetic field is "offered for free" by the Earth.

1.5   Goal of the research project

This research project is aimed at developing new techniques of mission analysis, which can lead to further development of space science missions using CubeSat technology. Two main objectives have been pursued, related to both deep space exploration and LEO missions, and are outlined in the following paragraphs.

Ballistic capture   The exploration of the solar system using CubeSats requires adequate techniques to design low-energy trajectories. The effectiveness of these techniques, thus their suitability to drive actual mission analysis, should be evaluated depending on their capability to predict ballistic captures and their behavior in time.

Part of my research activity was dedicated to the development of a method for systematic design of internal ballistic captures. Internal trajectories were selected because of their relatively short time to capture, as outlined in section 1.3.3.

The method aims at providing a topological description of transit and capture trajectories, including information on the total time and osculating orbital elements at capture. Based on this classification, two guidance strategies were developed, allowing modification to the ultimate behavior of trajectories to match the desired mission requirements. These strategies are effective with modest velocity variations (ΔV) and are tailored to be implemented on compact continuous thrusters, compatible with CubeSats.

The method was originally developed in the dynamical framework of the three-dimensional, or spatial, circular restricted 3-body problem (CR3BP) and was later extended to the more general elliptic restricted 4-body problem (ER4BP), which is adequately accurate for application on several scenarios of interest, such as the Sun-Earth-Moon system or Jupiter and its Galilean moons.

Magnetic Attitude Determination and Control   The development of a simple, reliable and effective purely magnetic ADCS is a goal of my research project. The target is to achieve a low mass, low power and low cost ADCS, tailored for nanosatellites performing space science missions around the Earth. Attitude determination is obtained from the only measurements of a three-axis magnetometer and a model of the geomagnetic field, without the use of any Kalman filter. The determination process starts from the estimation of the angular rates, which are used as an input, along with geomagnetic field data, to estimate the attitude matrix. To enhance the computational efficiency of the system, complex matrix operations are arranged into a form of the Faddeev algorithm, which can be conveniently implemented on the FPGA core of a CubeSat OBC using systolic array architecture. The performance and the robustness of the algorithm are evaluated by means of both numerical analyses in Matlab Simulink and hardware-in-the-loop simulations.

1.6   Structure of the thesis

The thesis is organized into 8 chapters, covering the two topics studied in my PhD research project: the development of internal ballistic capture design techniques and the implementation of a magnetic attitude determination and control system for CubeSats.

In Chapter 1 the goals and challenges of current space science missions using CubeSats are introduced. An overview of the state of the art for both ballistic capture and ADCS is provided, with the aim of indicating the crucial aspects before to contextualize them into a rigorous and complex mathematical framework. Based on this analysis, the goal of the research project is stated. The CR3BP and the Hamiltonian formalism represent the theoretical background to develop novel design techniques for internal ballistic captures. This background is discussed in Chapter 2, including an in-depth analysis of previous works in the field.

In chapters 3 and 4 a method for systematic design of internal ballistic captures, with desired capture time and osculating orbital elements at capture, is presented. The method is verified by means of numerical simulations on the Earth-Moon and the Jupiter-Ganymede systems, investigating the effects of solar gravitational perturbation as well. Two low-thrust guidance strategies, producing powered permanent capture and desired modifications of the orbital elements at capture, are presented and verified for the mentioned cases.

In Chapter 5 the results developed for the CR3BP are extended to the ER4BP, taking advantage of canonical transformations. This new technique allows designing Earth-Moon internal ballistic captures including the gravitational pull of the Sun from the design phase, instead of considering it as a perturbation to be compensated. Further extension of the model can help identifying capture orbits which are stable with respect to orbital resonance, as proved for the Jupiter-Europa-Io system.

In Chapter 6 the theoretical background of magnetic ADCS is introduced, before to implement a magnetometer-only angular rate determination and detumbling method and a magnetometer-only attitude determination strategy. The previous results are then arranged in the form of the Faddeev algorithm, to allow efficient hardware implementation. The implemented algorithm are verified by means of hardware-in-the-loop simulations discussed in Chapter 7, in which the design and development of a ground-based facility for ADCS experimental testing is introduced.

Closing remarks are discussed in Chapter 8, including a critical evaluation of the results obtained in terms of the PhD project objectives, possible implementations and recommendations.

Chapter 2

Hamiltonian dynamics for the circular restricted 3-body problem

The characterization of low-energy trajectories, resulting from the gravitational interactions in a restricted 3-body model, is the final aim of this chapter. Such an environment can be conveniently modeled as a dynamical system, whose solutions are the desired trajectories. For the sake of characterization, a qualitative approach is preferred to investigate the 3-body dynamical system, providing an elegant, global and compact representation of the solutions and of their properties. Based on these properties, the ultimate behavior of low-energy trajectories is evaluated and techniques for space mission design are developed. These techniques can be finally used to determine specific solutions of the problem, through a quantitative approach, as detailed in chapters 3-5.

Low-energy trajectories are studied under the hypotheses of the circular restricted 3-body problem, which can provide effective solutions for a relevant number of space missions. Qualitative dynamics provides powerful tools for this analysis, which were developed since the 18th century, by Euler [49] and Lagrange [94]. In the 19th century, the great effort by mathematicians of the caliber of Jacobi [81], Hill [73, 74], Poincaré [139] and Birkhoff [15], set the bases for more recent developments by Moser [117, 165] and Conley [28, 29] among the others.

2.1 The circular restricted 3-body problem

The circular restricted 3-body problem represents the reference mathematical framework in which the majority of low-energy trajectories are designed. The 3-body system includes two celestial bodies, named the primaries, of mass m_1 and m_2 [1] and a body of negligible mass m, such that $m_1 \geq m_2 >> m$.

---

[1] the subscripts 1 and 2 always refer to the primaries throughout the manuscript

The primaries move around their common center of mass (O) along circular orbits at the constant rate

$$\omega = \sqrt{\frac{G\left(m_1 + m_2\right)}{\left(a_1 + a_2\right)^3}}$$

where $G = 6.67408e - 11 \frac{m^3}{kgs^2}$ is the gravitational constant and a_i indicates the distance of the i-th primary from O [171]. The motion of m, resulting from the only gravitational effects of the two primaries, can be described in an inertial, or sidereal, reference frame $\left[\hat{\Xi}, \hat{H}, \hat{Z}\right]$ centered in O. As sketched in Figure 2.1, the problem is studied considering the position of the primaries at the initial time (t_0) such that $\mathbf{P_1}(t_0) = (-a_1, 0, 0)$ and $\mathbf{P_2}(t_0) = (a_2, 0, 0)$, with $\hat{\Xi}$ pointing towards m_2, $\hat{Z}$ orthogonal to the orbital plane of the primaries and $\hat{H}$ completing the rectangular frame.
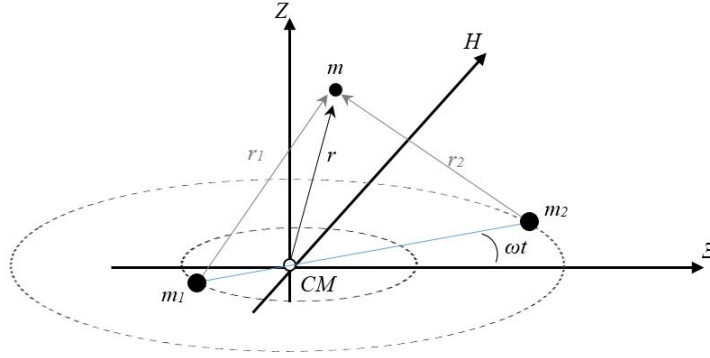
Figure 2.1. The sidereal reference frame for the CR3BP

The dynamic equations of motion for m in the sidereal frame are given below

$$\begin{cases} \ddot{\Xi} = -G\left(m_1 \frac{\Xi - \Xi_1}{R_1^3} + m_2 \frac{\Xi - \Xi_2}{R_2^3}\right) \\ \ddot{H} = -G\left(m_1 \frac{H - H_1}{R_1^3} + m_2 \frac{H - H_2}{R_2^3}\right) \\ \ddot{Z} = -G\left(m_1 \frac{Z - Z_1}{R_1^3} + m_2 \frac{Z - Z_2}{R_2^3}\right) \end{cases} \qquad (2.1)$$

where the *dot* indicates the time derivative and $R_i = \sqrt{\left(\Xi - \Xi_i\right)^2 + \left(H - H_i\right)^2 + \left(Z - Z_i\right)^2}$ are the distances of m from the primaries m_1 and m_2. It can be noticed that, in the hypothesis of the CR3BP, the segment $\overline{P_1 P_2}$ rotates with constant angular velocity ω around O. Therefore the CR3BP can be conveniently reformulated referring to the rotating, or synodic, reference frame $\left[\hat{\xi}, \hat{\eta}, \hat{\zeta}\right]$, with $\hat{\xi}$ connecting the two primaries and pointing towards m_2, $\hat{\zeta}$ parallel to $\hat{Z}$, thus orthogonal to the orbital plane of the primaries, and $\hat{\eta}$ completing the rectangular reference frame. A sketch of the synodic reference frame is shown in Figure 2.2.

Replacing the sidereal coordinates by the synodic ones, system 2.1 can be expressed as follows

$$
\begin{cases}
\ddot{\xi} - 2\omega\dot{\eta} - \omega^2\xi = -G\left(m_1\frac{\xi-\xi_1}{R_1^3} + m_2\frac{\xi-\xi_2}{R_2^3}\right) \\
\ddot{\eta} + 2\omega\dot{\xi} - \omega^2\eta = -G\left(m_1\frac{\eta-\eta_1}{R_1^3} + m_2\frac{\eta-\eta_2}{R_2^3}\right) \\
\ddot{\zeta} = -G\left(m_1\frac{\zeta-\zeta_1}{R_1^3} + m_2\frac{\zeta-\zeta_2}{R_2^3}\right)
\end{cases}
\tag{2.2}
$$

Typically, the dimensionless form of system 2.2 is preferred and this is obtained after introducing the units of mass (MU), distance (DU) and time (TU)

$$
\begin{cases}
MU = m_1 + m_2 \\
DU = a_1 + a_2 \\
TU = 1/\omega = \sqrt{\frac{DU^3}{G \cdot MU}}
\end{cases}
$$

From the definition of MU, the dimensionless masses of the primaries can be expressed in terms of the only mass parameter $\mu \leq \frac{1}{2}$

$$
\begin{cases}
m_1/MU = 1 - \mu \\
m_2/MU = \mu
\end{cases}
$$

Also the dimensionless positions of the primaries, $x_1 = a_1/DU$ and $x_2 = a_2/DU$, can be expressed in terms of μ, based on the definition of the center of mass.

$$
\begin{cases}
a_1 + a_2 = DU \\
-a_1 m_1 + a_2 m_2 = 0
\end{cases}
\rightarrow
\begin{cases}
x_1 = 1 - x_2 \\
\frac{x_1}{x_2} = \frac{\mu}{1-\mu}
\end{cases}
\rightarrow
\begin{cases}
x_1 = -\mu \\
x_2 = 1 - \mu
\end{cases}
$$
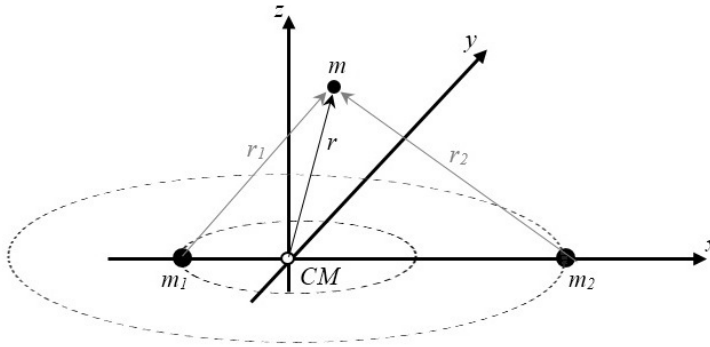
Figure 2.2. The synodic reference frame for the CR3BP

The CR3BP dynamics in the synodic frame, using dimensionless coordinates $[\hat{x}, \hat{y}, \hat{z}]$, is expressed by the following set of equations

$$
\begin{cases}
\ddot{x} - 2\dot{y} - x = -\frac{(1-\mu)(x+\mu)}{r_1^3} - \frac{\mu(x-1+\mu)}{r_2^3} \\
\ddot{y} + 2\dot{x} - y = -\frac{1-\mu}{r_1^3}y - \frac{\mu}{r_2^3}y \\
\ddot{z} = -\frac{1-\mu}{r_1^3}z - \frac{\mu}{r_2^3}z
\end{cases}
\tag{2.3}
$$

where $r_1 = \sqrt{(x + \mu)^2 + y^2 + z^2}$ and $r_2 = \sqrt{(x - 1 + \mu)^2 + y^2 + z^2}$. System 2.3 can be set in the compact form

$$\begin{cases} \ddot{x} - 2\dot{y} = \frac{\partial U}{\partial x} \\ \ddot{y} + 2\dot{x} = \frac{\partial U}{\partial y} \\ \ddot{z} = \frac{\partial U}{\partial z} \end{cases} \tag{2.4}$$

In equations 2.4 the scalar potential function U was introduced

$$U = \frac{x^2 + y^2}{2} + \frac{1 - \mu}{r_1} + \frac{\mu}{r_2} \tag{2.5}$$

It is known from Poincaré that the CR3BP has only one integral of motion [139] and this can be determined operating as follows on the pontential function

$$\dot{\mathbf{r}} \cdot \nabla U = \dot{x}\ddot{x} + \dot{y}\ddot{y} + \dot{z}\ddot{z} = \dot{x}\frac{\partial U}{\partial x} + \dot{y}\frac{\partial U}{\partial y} + \dot{z}\frac{\partial U}{\partial z} \tag{2.6}$$

where $\mathbf{r} = (x, y, z)$. Because U is a function of the spatial coordinates (x, y, z) only, then $\frac{dU}{dt} = \dot{x}\frac{\partial U}{\partial x} + \dot{y}\frac{\partial U}{\partial y} + \dot{z}\frac{\partial U}{\partial z}$ and equation 2.6 can be rewritten as follows

$$\dot{x}\ddot{x} + \dot{y}\ddot{y} + \dot{z}\ddot{z} = \frac{dU}{dt} \tag{2.7}$$

Calculating the integral over time of equation 2.7 produces the above mentioned integral of motion, indicated as C and named the Jacobi constant

$$2U - \dot{x}^2 + \dot{y}^2 + \dot{z}^2 = C \tag{2.8}$$

The Jacobi constant provides useful information regarding the regions of motion of m. It is worth recalling that the totality of solutions for a dynamical system with three degrees of freedom, such as the three-dimensional CR3BP, is included within the a six-dimensional manifold $F(x, y, z, \dot{x}, \dot{y}, \dot{z})$, named the *phase space*. The existence of C reduces the phase space to a five-dimensional subspace $F(x, y, z, \dot{x}, \dot{y}, \dot{z}) = C$, in which each and every point represents a particular solution of the CR3BP for a fixed value of C.

The manifold can be further reduced after isolating points in the phase space characterized by a magnitude of the velocity equal to zero, producing the zero velocity surface (ZVS) $F(x, y, z, 0, 0, 0) = C$, also named Hill surfaces. The explicit expression for the ZVS, obtained introducing equation 2.5 into equation 2.8, is reported below

$$x^2 + y^2 + 2\left(\frac{1 - \mu}{r_1} + \frac{\mu}{r_2}\right) = C \tag{2.9}$$

An analysis of equation 2.9 shows that the ZVS are always symmetric with respect to the $[\hat{x}, \hat{y}]$ and $[\hat{x}, \hat{z}]$ planes and, for the limiting case $\mu = 1/2$, also with respect to the $[\hat{y}, \hat{z}]$ plane. The ZVS are the locus of points where the velocity of m is equal to zero, therefore they define the boundary for the regions of motion, a subspace expressed by the following equation

$$x^2 + y^2 + 2\left(\frac{1 - \mu}{r_1} + \frac{\mu}{r_2}\right) < C$$

The shape of the ZVS changes with C and so do the regions of motion, as shown in Figure 2.3 where the ZVS are sketched as level surfaces with the parameter C.
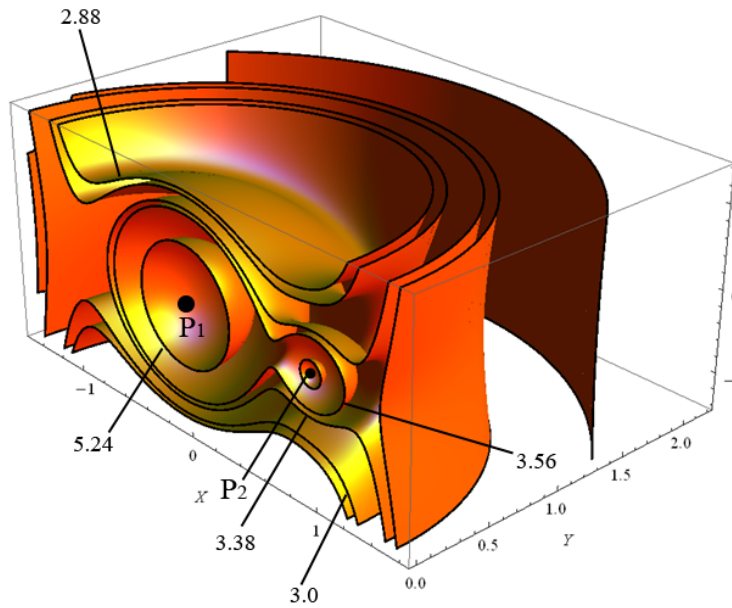
Figure 2.3. Sketch of the zero velocity surfaces as a function of C, the position of the primaries is indicated by P_i [185]

For a clear description of the change in the regions of motion with C, it is better to refer to the zero velocity curves (ZVC), produced by the intersection of the ZVS with the plane $z = 0$. The ZVC for six values of C are shown in Figure 2.4, where the white areas represent the regions of motion and C decreases from case (a) to (f).
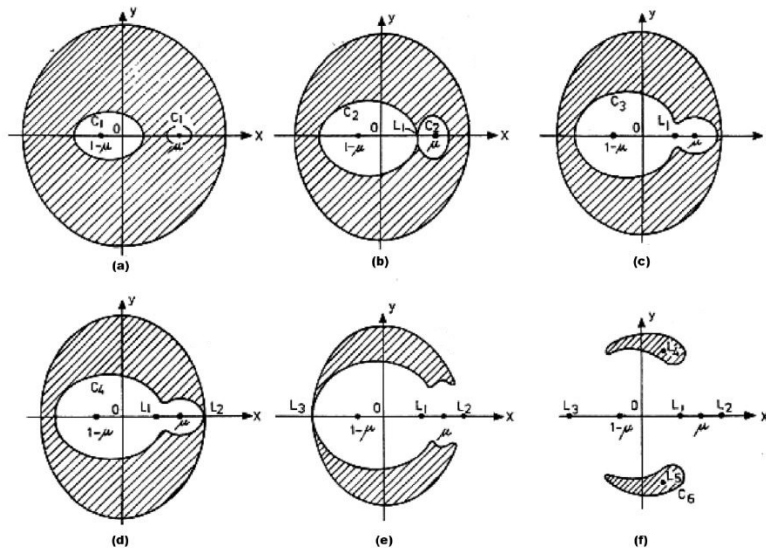
Figure 2.4. Sketch of the zero velocity curves with C decreasing from (a) to (f)

Considering the case (a) in Figure 2.4, m can move only in the proximity of the primaries or at very long distance from both of them, outside the outer circle bounding the dashed area where the motion is not allowed. As C decreases, the regions of motion surrounding the primaries collide (b) and this occurs for a value of the Jacobi constant indicated as C_1, in correspondence of the libration point L_1, discussed in detail in section 2.3. For $C < C_1$, the primaries are included in the same region of motion (c-f), therefore transit from one to the other is allowed. In (c) and (d), an inner and an outer region of motion exist, the former surrounding the primaries and the latter far away from them. As C decreases, it can reach the value C_2, where these two regions merge into a single one (d), with the collision occurring at the libration point L_2. Therefore, for $C > C_2$ only one region of motion exists (e-f), thus the motion of m can evolve indefinitely in the proximity of the primaries or away from them.

It can be noticed from cases (b-d) that, as C decreases from C_1 to C_2, the "neck" surrounding L_1 widens. If the Jacobi constant is slightly smaller than C_1, a linear formulation of equations 2.3 represents an accurate approximation of the real dynamics inside the mentioned neck. The same consideration applies in the surrounding of L_2 when the Jacobi constant is smaller but close to C_2. setting the bases for the characterization of low-energy trajectories.

2.2 Collinear equilibrium points and linear dynamics in the equilibrium region

A total of five equilibrium (or libration) points exist for the CR3BP, all belonging to the $[\hat{x}, \hat{y}]$ plane. Three out of five equilibrium points, indicated as L_1, L_2 and L_3 are named collinear, because they belong to $\hat{x}$. Their location can be determined from system 2.3, by setting the time derivatives equal to zero

$$\begin{cases} x - \frac{(1-\mu)(x+\mu)}{r_1^3} - \frac{\mu(x-1+\mu)}{r_2^3} = 0 \\ y - \frac{1-\mu}{r_1^3}y - \frac{\mu}{r_2^3}y = 0 \\ \frac{1-\mu}{r_1^3}z + \frac{\mu}{r_2^3}z = 0 \end{cases} \tag{2.10}$$

Producing $L_{i,y} = L_{i,z} = 0$ for $i = 1, 2, 3$, $r_1 = \sqrt{(x+\mu)^2}$, $r_2 = \sqrt{(x-1+\mu)^2}$ and

$$x - \frac{(1-\mu)(x+\mu)}{|x+\mu|^2} - \frac{\mu(x-1+\mu)}{|x-1+\mu|^2} = 0 \tag{2.11}$$

A close analytical solution of the fifth grade equation 2.11 does not exist, but the location of the three real solutions can be inferred by studying the sign of the absolute values at the denominator, leading to

$$\begin{cases} L_{1,x} : -\mu < x < 1 - \mu \\ L_{2,x} : x > 1 - \mu \\ L_{3,x} : x < -\mu \end{cases} \tag{2.12}$$

The stability of the collinear equilibrium points can be studied using the small deviation equations, obtained from the linear equations of motion calculated at L_i. From the linear expansion of equation 2.5 it follows

$$\nabla U = \nabla U^* + (\mathbf{r} - \mathbf{r}^*) \nabla^2 U + ... + o \approx \tilde{\mathbf{r}} \nabla^2 U \tag{2.13}$$

where the symbol $*$ indicates a value calculated at L_i, $\mathbf{r}$ is the position vector, $\tilde{\mathbf{r}} = \mathbf{r} - \mathbf{r}^*$ and $\mathbf{r}^* = (x - L_{i,x}, y, z)$. It can be proved that $\frac{\partial^2 U}{\partial x \partial y} = \frac{\partial^2 U}{\partial x \partial z} = \frac{\partial^2 U}{\partial y \partial z} = 0$, then the linear equations of motion are given by the following system

$$\begin{cases} \ddot{x} - 2\dot{y} - \tilde{x}\frac{\partial^2 U}{\partial \tilde{x} \partial \tilde{x}} = 0 \\ \ddot{y} + 2\dot{x} - y\frac{\partial^2 U}{\partial y \partial y} = 0 \\ \ddot{z} - z\frac{\partial^2 U}{\partial z \partial z} = 0 \end{cases} \tag{2.14}$$

System 2.14 can be conveniently rearranged in the matrix state space form, introducing the velocities $u = \dot{x}$, $v = \dot{y}$ and $w = \dot{z}$.

$$\begin{bmatrix} \dot{x} \\ \dot{y} \\ \dot{z} \\ \dot{u} \\ \dot{v} \\ \dot{w} \end{bmatrix} = \begin{bmatrix} 0 & 0 & 0 & 1 & 0 & 0 \\ 0 & 0 & 0 & 0 & 1 & 0 \\ 0 & 0 & 0 & 0 & 0 & 1 \\ 1 + 2\gamma^2 & 0 & 0 & 0 & 2 & 0 \\ 0 & 1 - \gamma^2 & 0 & -2 & 0 & 0 \\ 0 & 0 & -\gamma^2 & 0 & 0 & 0 \end{bmatrix} \begin{bmatrix} \tilde{x} \\ y \\ z \\ u \\ v \\ w \end{bmatrix} \tag{2.15}$$

where $\tilde{x} = x - L_{i,x}$ and, for the sake of compactness, the parameter $\gamma^2 = -\frac{\partial^2 U}{\partial z \partial z}$ is introduced, which verifies the following equalities $1 + 2\gamma^2 = \frac{\partial^2 U}{\partial x \partial x}$ and $1 - \gamma^2 = \frac{\partial^2 U}{\partial y \partial y}$. The dynamic matrix in 2.15 is hereafter indicated as $\mathbf{A}$.

The characteristic equation for the system 2.15 can be calculated from $|\lambda \mathbf{I} - \mathbf{A}|$, where $\mathbf{I}$ is the identity matrix

$$\lambda^4 + \left(2 - \gamma^2\right) \lambda^2 + \left(1 - \gamma^2\right) \left(1 + 2\gamma^2\right) = 0 \tag{2.16}$$

The solutions of equation 2.16 are the six eigenvalues $\pm\alpha$, $\pm j\beta$ and $\pm j\gamma$, where j indicates the imaginary unit. As indicated by Routh-Hurwitz criterion [77, 155], for a stable equilibrium equation 2.16 should have two real negative roots, leading to the condition $\left(1 - \gamma^2\right) > 0$, which is not verified for the collinear libration points, as can be inferred from the solutions 2.12 or determined numerically.

It follows that, because $\left(1 - \gamma^2\right) < 0$ then the equilibrium at he collinear libration points is unstable, thus any perturbation acting on m will lead it to depart from the equilibrium point.

The phase space surrounding the collinear equilibrium points L_i, in which the linear system 2.15 provides an adequately accurate description of the actual dynamics of the CR3BP, is named the *equilibrium region*. It can be noticed that, inside the equilibrium region, the in-plane motion, evolving onto the $[\hat{x}, \hat{y}]$ plane, is uncoupled from the out of plane motion, along $\hat{z}$. The out of plane motion is stable and periodic, as described by

$$\begin{cases} z = 2\gamma_1 \cos \gamma t - 2\gamma_2 \sin \gamma t \\ w = -\gamma \left(2\gamma_1 \sin \gamma t - 2\gamma_2 \cos \gamma t\right) \end{cases} \tag{2.17}$$

where the coefficients γ_1 and γ_2, reported in system 2.19, are obtained from the initial condition.

The in-plane motion is more complex and includes both unstable aperiodic terms and stable periodic ones

$$\begin{cases} \tilde{x} = \alpha_1 e^{\alpha t} + \alpha_2 e^{-\alpha t} + 2\beta_1 \cos \beta t - 2\beta_2 \sin \beta t \\ y = \alpha_1 \sigma e^{\alpha t} - \alpha_2 \sigma e^{-\alpha t} - 2\tau \left(\beta_1 \sin \beta t + \beta_2 \cos \beta t \right) \\ u = \alpha_1 \alpha e^{\alpha t} - \alpha_2 \alpha e^{-\alpha t} - 2\beta \left(\beta_1 \sin \beta t + \beta_2 \cos \beta t \right) \\ v = \alpha_1 \alpha \sigma e^{\alpha t} - \alpha_2 \alpha \sigma e^{-\alpha t} - 2\beta\tau \left(\beta_1 \cos \beta t - \beta_2 \sin \beta t \right) \end{cases} \quad (2.18)$$

where $\sigma = -2\alpha / \left(\alpha^2 + \gamma^2 - 1 \right)$, $\tau = -2\beta / \left(-\beta^2 + \gamma^2 - 1 \right)$ and the coefficients α_1, α_2, β_1 and β_2 are calculated from the initial condition and reported the set below

$$\begin{cases} \alpha_1 = \frac{\left(1+2\gamma^2\right)\tilde{x}_0 + \left(1-\gamma^2\right)y_0 + \alpha u_0 - \alpha\sigma v_0}{2\left[(1-\gamma^2)\sigma^2 + \alpha^2\right]} \\ \alpha_2 = \frac{\left(1+2\gamma^2\right)\tilde{x}_0 - \left(1-\gamma^2\right)\sigma y_0 - \alpha u_0 - \alpha\sigma v_0}{2\left[(1-\gamma^2)\sigma^2 + \alpha^2\right]} \\ \beta_1 = -\frac{\left(1+2\gamma^2\right)\tilde{x}_0 + \beta\tau v_0}{2\left[(1-\gamma^2)\tau^2 + \beta^2\right]} \\ \beta_2 = -\frac{\left(1-\gamma^2\right)\tau y_0 + \beta u_0}{2\left[(1-\gamma^2)\tau^2 + \beta^2\right]} \\ \gamma_1 = \frac{z_0}{2} \\ \gamma_2 = \frac{w_0}{2\gamma} \end{cases} \quad (2.19)$$

where the subscript 0 indicates the value calculated at $t_0 = 0$. Referring to systems 2.17 and 2.18, libration point orbits can be classified depending on the value of the parameters $\alpha_{1,2}$, $\beta_{1,2}$ and $\gamma_{1,2}$, obtaining

- $\alpha_1 = \alpha_2 = \beta_1 = \beta_2 = 0 \rightarrow$ vertical harmonic motion

- $\alpha_1 = \alpha_2 = \gamma_1 = \gamma_2 = 0 \rightarrow$ planar periodic, or Lyapunov, orbit

- $\alpha_1 = \alpha_2 = 0 \rightarrow$ quasi-periodic three-dimensional orbit

- $\alpha_1 = 0 \rightarrow$ trajectory asymptotic to a quasi-periodic orbit

- $\alpha_2 = 0 \rightarrow$ trajectory departing from a quasi-periodic orbit

Regarding the quasi-periodic orbit, it can be noticed that the amplitude of the in-plane and out of plane oscillations depends, respectively, on $\beta_{1,2}$ and $\gamma_{1,2}$. As will be clarified in section 2.3, the value of the mentioned parameters depends on the energy of the system, or equivalently on C. For C just below C_i, the in-plane amplitude is greater than the out of plane, therefore the corresponding quasi-periodic orbit about L_i is a Lissajous orbit. As C decreases, the amplitude for the two oscillations becomes comparable and the Lissajous is replaced by a quasi-halo orbit. If the in-plane and the out of plane motion are perfectly coupled, then the dynamics evolves onto a plane tilted with respect to $[\hat{x}, \hat{y}]$ and the resulting trajectory is called a halo orbit. The results discussed in this manuscript refer to values of the Jacobi constant slightly smaller than C_1 or C_2, therefore quasi-periodic Lissajous orbits are going to be considered. A representation of libration point orbits is shown in Figure 1.5.

2.3 Hamiltonian formalism and Siegel-Moser canonical transformation

A deeper insight on the dynamical behavior in the equilibrium region, surrounding the collinear libration points L_1 and L_2, was provided by Conley, for the limiting case of the planar CR3BP. Conley's work leads to a clear and compact topological classification of transit, bouncing and capture orbits, including a characterization on the capture time, and the representation of all of these results on a simple two-dimensional plot of the phase space [29]. This result can be extended to the spatial CR3BP, after rearranging the CR3BP using the Hamiltonian formalism.

In the Hamiltonian model, the dimensionless position and velocity coordinates are replaced by the conjugate positions $[q_1, q_2, q_3] = [x, y, z]$ and momenta $[p_1, p_2, p_3] = [u - y, v + x, w]$. The dynamic equations of motion, equivalent to system 2.3, can be expressed as follows

$$\begin{cases} \dot{\mathbf{q}} = \frac{\partial H}{\partial \mathbf{p}} \\ \dot{\mathbf{p}} = -\frac{\partial H}{\partial \mathbf{q}} \end{cases} \tag{2.20}$$

where H is the Hamiltonian function for the CR3BP [2], reported below [171]

$$H = \frac{1}{2}(p_1^2 + p_2^2 + p_3^2) + (p_1 q_2 - p_2 q_1) - \left(\frac{1-\mu}{r_1} + \frac{\mu}{r_2}\right) \tag{2.21}$$

Introducing equation 2.21 into system 2.20, the following set representing the CR3BP dynamics is obtained

$$\begin{cases} \dot{q_1} = p_1 + q_2 \\ \dot{q_2} = p_2 - q_1 \\ \dot{q_3} = p_3 \\ \dot{p_1} = p_2 - \frac{(1-\mu)(q_1+\mu)}{r_1^3} - \frac{\mu(q_1-1+\mu)}{r_2^3} \\ \dot{p_2} = -p_1 - \frac{(1-\mu)q_2}{r_1^3} - \frac{\mu q_2}{r_2^3} \\ \dot{p_3} = -\frac{(1-\mu)q_3}{r_1^3} - \frac{\mu q_3}{r_2^3} \end{cases} \tag{2.22}$$

with $r_1 = \sqrt{(q_1 + \mu)^2 + q_2^2 + q_3^2}$ and $r_2 = \sqrt{(q_1 - 1 + \mu)^2 + q_2^2 + q_3^2}$.
The linear form of system 2.22 about L_i, equivalent to system 2.15, can be obtained after deriving the linear Hamiltonian function. This is done by applying the translations

$$\begin{cases} \tilde{q_1} = q_1 - L_{i,x} \\ \tilde{p_2} = p_2 - L_{i,x} \end{cases}$$

and expanding in power series the non polynomial terms of equation 2.21, reported in the Appenix A, producing the following result

$$H_2 = \frac{1}{2}\left(p_1^2 + \tilde{p_2}^2 + p_3^2\right) + (p_1 q_2 - \tilde{p_2}\tilde{q_1}) - K\left(\tilde{q_1}^2 - \frac{1}{2}q_2^2 - \frac{1}{2}q_3\right) \tag{2.23}$$

---

[2]By replacing conjugate coordinates with dimensionless position and velocity components it results $H = -2C$

with $K = \frac{1-\mu}{|L_{i,x}+\mu|^3} + \frac{\mu}{|L_{i,x}-1+\mu|^3}$. The linear system associated to H_2 can be expressed in matrix form as follows (for the sake of compactness the tilde sign was removed)

$$
\begin{bmatrix} \dot{q}_1 \\ \dot{q}_2 \\ \dot{q}_3 \\ \dot{p}_1 \\ \dot{p}_2 \\ \dot{p}_3 \end{bmatrix} = \begin{bmatrix} 0 & 1 & 0 & 1 & 0 & 0 \\ -1 & 0 & 0 & 0 & 1 & 0 \\ 0 & 0 & 0 & 0 & 0 & 1 \\ 2K & 0 & 0 & 0 & 1 & 0 \\ 0 & -K & 0 & -1 & 0 & 0 \\ 0 & 0 & -K & 0 & 0 & 0 \end{bmatrix} \begin{bmatrix} q_1 \\ q_2 \\ q_3 \\ p_1 \\ p_2 \\ p_3 \end{bmatrix}
\tag{2.24}
$$

A crucial step in the development of Conley's Hamiltonian representation is the definition of a coordinate transformation $(\mathbf{x}, \mathbf{y}) = \mathbf{T_N}(\mathbf{q}, \mathbf{p})$ that

- diagonalizes $\mathbf{A}$

- is canonical

- verifies the reality condition, thus transforms complex variables $(\mathbf{x}, \mathbf{y})$ into the real ones $(\mathbf{q}, \mathbf{p})$

Such a transformation was proposed by Siegel and Moser and can be obtained as follows [165]. First the eigenvalues of $\mathbf{A}$, indicated as $\pm\rho$, $\pm j\lambda_1$ and $\pm j\lambda_2$, are collected in the diagonal matrix $\mathbf{\Lambda}$

$$
\mathbf{\Lambda} = \begin{bmatrix} \rho & 0 & 0 & 0 & 0 & 0 \\ 0 & -\rho & 0 & 0 & 0 & 0 \\ 0 & 0 & j\lambda_1 & 0 & 0 & 0 \\ 0 & 0 & 0 & -j\lambda_1 & 0 & 0 \\ 0 & 0 & 0 & 0 & j\lambda_2 & 0 \\ 0 & 0 & 0 & 0 & 0 & -j\lambda_2 \end{bmatrix}
\tag{2.25}
$$

The permutation $\mathbf{P}$ is then applied to $\mathbf{\Lambda}$

$$
\mathbf{P} = \begin{pmatrix} 1 & 2 & 3 & 4 & 5 & 6 \\ 1 & 4 & 2 & 5 & 3 & 6 \end{pmatrix}
\tag{2.26}
$$

obtaining the Siegel-Moser form

$$
\mathbf{T} = \begin{bmatrix} \rho & 0 & 0 & 0 & 0 & 0 \\ 0 & j\lambda_1 & 0 & 0 & 0 & 0 \\ 0 & 0 & j\lambda_2 & 0 & 0 & 0 \\ 0 & 0 & 0 & -\rho & 0 & 0 \\ 0 & 0 & 0 & 0 & -j\lambda_1 & 0 \\ 0 & 0 & 0 & 0 & 0 & -j\lambda_2 \end{bmatrix}
\tag{2.27}
$$

For the canonical condition to be verified, $\mathbf{T}$ must be transformed into a symplectic form. Setting $\mathbf{B} = \left(\mathbf{J}^{-1}\mathbf{T}^T\mathbf{J}\right)^{-1}$, with

$$
\mathbf{J} = \begin{bmatrix} \mathbf{0} & \mathbf{I} \\ -\mathbf{I} & \mathbf{0} \end{bmatrix}
$$

and isolating from $\mathbf{B}$ the (3×3) block

$$\mathbf{B_1} = \mathbf{B_{i \times j}} \qquad i, j = 1, 2, 3$$

then matrix $\mathbf{Q}$ can be defined as follows

$$\mathbf{Q} = \begin{bmatrix} \mathbf{B_1} & \mathbf{0} \\ \mathbf{0} & \mathbf{I} \end{bmatrix} \tag{2.28}$$

Post-multiplying the inverse of $\mathbf{Q}$ to $\mathbf{T}$ results into the symplectic matrix

$$\mathbf{S} = \mathbf{T}\mathbf{Q}^{-1} \tag{2.29}$$

Indicating $\mathbf{s_i}$ the i-th column of $\mathbf{S}$ and considering equations (2.27) and (2.29), it can be noticed that $\mathbf{s_1}$ and $\mathbf{s_4}$ are real vectors, while $\mathbf{s_2}$, $\mathbf{s_3}$, $\mathbf{s_5}$ and $\mathbf{s_6}$ are complex ones. For the reality condition to be satisfied a final step is required. Setting $k_1 = 1/\sqrt{\mathbf{s_2}\mathbf{s_5^T}}$ and $k_2 = 1/\sqrt{\mathbf{s_3}\mathbf{s_6^T}}$ and arranging these parameters into the following matrix

$$\mathbf{R} = \begin{bmatrix} 1 & 0 & 0 & 0 & 0 & 0 \\ 0 & k_1 & 0 & 0 & 0 & 0 \\ 0 & 0 & k_2 & 0 & 0 & 0 \\ 0 & 0 & 0 & 1 & 0 & 0 \\ 0 & 0 & 0 & 0 & \frac{1}{k_1} & 0 \\ 0 & 0 & 0 & 0 & 0 & \frac{1}{k_2} \end{bmatrix}$$

The desired transformation matrix $\mathbf{T_N}$ can be finally obtained from the following multiplication

$$\mathbf{T_N} = \mathbf{S}\mathbf{R} \tag{2.30}$$

Applying equation 2.30 produces the transformation

$$\begin{bmatrix} x_1 & x_2 & x_3 & y_1 & y_2 & y_3 \end{bmatrix}^T = \mathbf{T_N} \begin{bmatrix} q_1 & q_2 & q_3 & p_1 & p_2 & p_3 \end{bmatrix}^T \tag{2.31}$$

where $x_1, y_1 \in \mathbb{R}$, $x_2, y_2, x_3, y_3 \in \mathbb{C}$, $y_2 = \Im(x_2) + j\Re(x_2)$, $y_3 = \Im(x_3) + j\Re(x_3)$, $j = \sqrt{-1}$, $\Re$ and $\Im$ indicating, respectively, the real and imaginary part [165].

The Hamiltonian function in the transformed coordinates can be expressed as follows

$$H = \rho x_1 y_1 + \frac{\lambda_1}{2}\left(x_2^2 + y_2^2\right) + \frac{\lambda_2}{2}\left(x_3^2 + y_3^2\right) + O_3\left(x_i, y_i\right) \tag{2.32}$$

Therefore the linear Hamiltonian can be obtained from equation (2.31) by neglecting the higher order terms O_3 [104]

$$H_2 = \rho x_1 y_1 + \frac{\lambda_1}{2}\left(x_2^2 + y_2^2\right) + \frac{\lambda_2}{2}\left(x_3^2 + y_3^2\right) = h \tag{2.33}$$

It is worth recalling that the Hamiltonian function for the CR3BP is constant and equal to $-2C$ and the canonical transformation 2.30 preserve this condition. In fact, as reported in equation 2.32, H_2 is equal to the constant h, named the *energy level*

and corresponding to the energy of the linear system.

The solution of the linear system corresponding to equation 2.33 are given below

$$
\begin{cases}
x_1 = \alpha_1 e^{\rho t} \\
y_1 = \alpha_2 e^{-\rho t} \\
x_2 = \beta_1 \cos\left(\lambda_1 t\right) + j\beta_2 \sin\left(\lambda_1 t\right) \\
y_2 = -\beta_1 \sin\left(\lambda_1 t\right) + j\beta_2 \cos\left(\lambda_1 t\right) \\
x_3 = \gamma_1 \cos\left(\lambda_2 t\right) + j\gamma_2 \sin\left(\lambda_2 t\right) \\
y_3 = -\gamma_1 \sin\left(\lambda_2 t\right) + j\gamma_2 \cos\left(\lambda_2 t\right)
\end{cases}
\tag{2.34}
$$

where $\alpha_{1,2}$, $\beta_{1,2}$ and $\gamma_{1,2}$ are constants related to the initial conditions, equivalent to those given in system 2.19.

Inside the equilibrium region, the three functions $\rho x_1 y_1$, $\frac{\lambda_1}{2}\left(x_2^2 + y_2^2\right)$ and $\frac{\lambda_2}{2}\left(x_3^2 + y_3^2\right)$ are local integrals of the system and represent a fraction of h [117]. Each term depends on a distinct couple of variables, thus they can be represented in distinct spaces. Particular interest will be devoted to the level surface $\rho x_1 y_1$, correlated to the parameters α_1 and α_2, on which the set of initial conditions corresponding to ballistic captures can be represented.

2.4 The flow in the equilibrium region and Conley's theorem

A topological analysis of the flow corresponding to H_2 leads to a rigorous description of the equilibrium region and allows predicting the behavior of trajectories crossing it. According to equation 2.33, the linear dynamics evolves inside a five-dimensional phase space, hereafter represented by the 5-ball $\mathcal{B}$ centered in L_i. Once fixed the energy level $h > 0$, the flow inside $\mathcal{B}$ is characterized by the composition of the three local integrals of motion defined by Moser [117]. These correspond to the flow of an unstable critical point, evolving onto the $[\hat{x}_1, \hat{y}_1]$ plane and described by the hyperbolas

$$
\begin{cases}
0 < x_1 y_1 \leq \frac{h}{\rho} = k \\
k = -\frac{h}{\rho} \leq x_1 y_1 < 0
\end{cases}
\tag{2.35}
$$

and the flow of two centers, corresponding to two uncoupled harmonic oscillators respectively onto the $[\hat{x}_2, \hat{y}_2]$ and the $[\hat{x}_3, \hat{y}_3]$ plane

$$
\mathcal{Z}_1 = \frac{\lambda_1}{2}\left(x_2^2 + y_2^2\right) = h_1
\tag{2.36}
$$

$$
\mathcal{Z}_2 = \frac{\lambda_2}{2}\left(x_3^2 + y_3^2\right) = h_2
\tag{2.37}
$$

Based on the previous considerations, the following statement can be formulated: any point in $\mathcal{B}$ characterized by $x_1 = y_1 = 0$ is associated to a trajectory always evolving inside $\mathcal{B}$. Equivalently, any point of a trajectory crossing $\mathcal{B}$ is characterized by $x_1 \neq 0$ and $y_1 \neq 0$. The flow onto the $[\hat{x}_1, \hat{y}_1]$ plane is therefore sufficient to identify trajectories which cross $\mathcal{B}$, but does not provide complete information regarding the

behavior of these trajectories outside the equilibrium region. To achieve this result the parameter ε is introduced, such that, if ε is small enough, it is possible to define a subspace $\mathcal{L}$ of $\mathcal{B}$ satisfying the following conditions

$$\mathcal{L} : \begin{cases} \rho x_1 y_1 + \frac{\lambda_1}{2} \left(x_2^2 + y_2^2 \right) + \frac{\lambda_2}{2} \left(x_3^2 + y_3^2 \right) = h \\ |x_1 + y_1| \leq \varepsilon \end{cases} \tag{2.38}$$

In fact, $\mathcal{L}$ represents the equilibrium region, as originally defined by Conley [28]. The straight lines $|x_1 - y_1| \leq \varepsilon$ represent a boundary of $\mathcal{L}$. As sketched in Figure 2.5, each (green) straight line separates one of the primaries from L_i, which is the origin of the reference system. It follows that, to transfer between the two primaries the spacecraft m should cross both the straight lines, thus the equilibrium region, and this is in fact coherent with the definition of transit trajectories provided before. Another boundary of $\mathcal{L}$ onto the $[\hat{x}_1, \hat{y}_1]$ plane is represented by the (green) limit hyperbolas. These correspond to solutions of equation 2.35 when the whole energy of the system is associated to the unstable flow $(k = h/\rho)$; in such a case, the flow occurs only onto the $[\hat{x}_1, \hat{y}_1]$ plane

$$x_1 y_1 = \pm \frac{h}{\rho}$$

For $k \leq h/\rho$, the flow is described by the hyperbolas $x_1 y_1 = \pm k$, onto the $[\hat{x}_1, \hat{y}_1]$ plane, and by the periodic terms onto the $[\hat{x}_2, \hat{y}_2]$ and $[\hat{x}_3, \hat{y}_3]$ planes. Hyperbolas characterized by $x_1 y_1 < 0$, represented in Figure 2.5 by black solid lines, cross both of the green straight lines $|x_1 - y_1| \leq \varepsilon$, separating the primaries, and are in fact representative of *transit* trajectories. Differently, solution $x_1 y_1 > 0$, named *bouncing* trajectories and represented by black dashed lines in Figure 2.5, only cross one of the green straight lines, thus are not suitable to perform transfers between the primaries.

Having characterized the flow inside the equilibrium region, it is of interest to investigate the ultimate behavior of orbits crossing the equilibrium region. A rigorous description is given by Conley [29], based on the topological description of $\mathcal{L}$ which, as defined by equation 2.35, is equivalent to the product of a 4-sphere $\mathcal{S}^4$ with an interval $|x_1 - y_1| \leq \varepsilon$. Considering the projection of $\mathcal{S}^4$ onto the $[\hat{x}_1, \hat{y}_1]$ plane, the intersection of the axes with a straight line $|x_1 + y_1| \leq \varepsilon$ produces four open line segments l_i and four closed ones l_i', shown in Figure 2.6. The intersection between these segments and $\mathcal{S}^4$ are topologically equivalent to 4-disks (l_i) and annular 4-dimensional surfaces (l_i').

As shown in Figure 2.6, the flow associated to transit orbits defines a mapping between disks, in particular between l_1 and l_2, when heading to m_2, and between l_3 and l_4, when heading to m_1. Differently, the mapping associated to bouncing orbits, which do not cross the equilibrium region, is between the annuli l_2' and l_3' (to m_2) or l_4' and l_1' (to m_1). Asymptotic orbits, corresponding to the axes, represent the boundary between the disks and the annular surfaces.
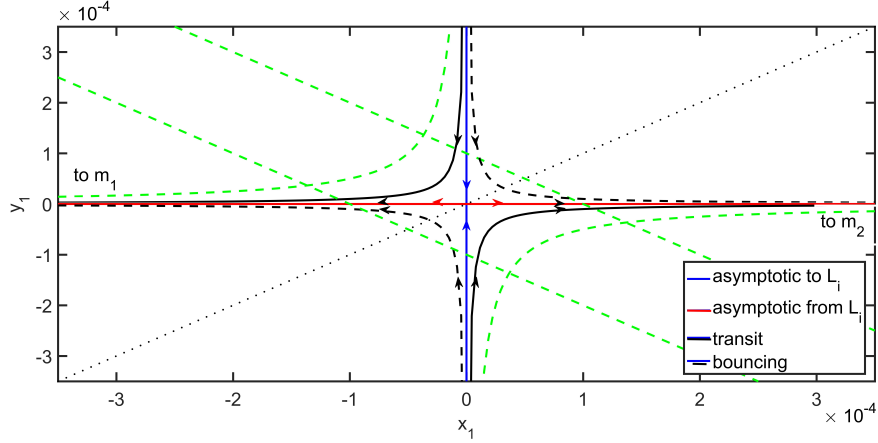
Figure 2.5. Sketch of the flow onto the $[\hat{x}_1, \hat{y}_1]$ plane. The boundaries of the equilibrium region are depicted in green [24].
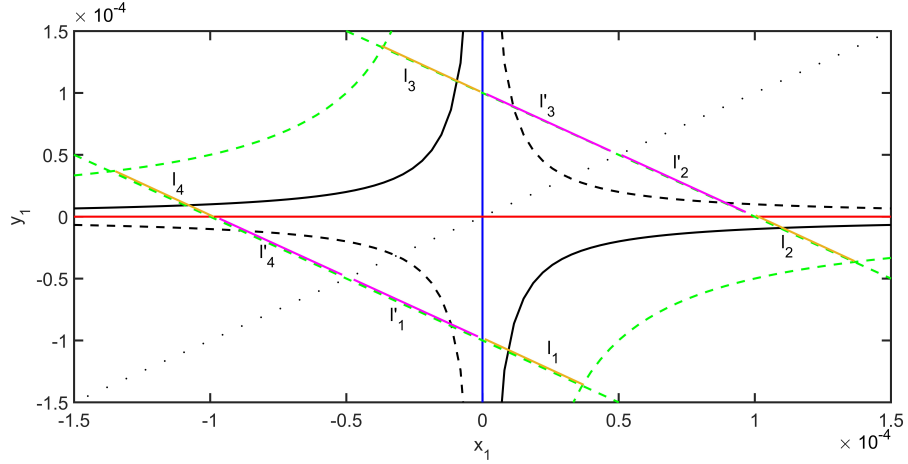
Figure 2.6. Projections of the 4-disks (orange) and annuli (purple) onto the $[\hat{x}_1, \hat{y}_1]$ plane

Recalling system 2.34, the time required a by transit trajectory $\rho x_1 y_1 = -k$ to move from any point $\mathcal{P}_0 = (x_1(t_0), y_1(t_0))$, to $\mathcal{P}^* = (x_1(t^\star) = y_1(t_0), y_1(t^\star) = x_1(t_0))$ can be determined as follows

$$t^\star - t_0 = -\frac{1}{\rho} \log \frac{y_1(t_0)}{x_1(t_0)} \tag{2.39}$$

Assuming for the sake of simplicity $t_0 = 0$, it can be noticed that $t^\star$ tends to infinity as $x_1(t_0)$ or $y_1(t_0)$ approaches zero. Correlations between the time $t^\star$ and the ultimate behavior of orbits outside the equilibrium region will be highlighted in Chapter 3, showing that for initial conditions corresponding to $t^\star \to \infty$ the corresponding trajectories spend a long time orbiting one of the primaries, before to enter again the equilibrium region. Such trajectories are in fact trapped by the gravitational field of the given primary, and are therefore called ballistic captures.

In conclusion to this section, the classification of orbits based on the topological analysis of the linear dynamics onto the $[\hat{x}_1, \hat{y}_1]$ plane is provided

- Lissajous **quasi-periodic orbits**, evolving only inside the equilibrium region, are characterized by $x_1 = x_2 = 0$

- **Bouncing orbits**, which never cross the equilibrium region, correspond to the hyperbolic segments determined by $x_1 y_1 > 0$

- **Transit trajectories**, which cross the equilibrium region, alternately towards m_2 and towards m_1, correspond to the hyperbolic segments determined by $x_1 y_1 < 0$

- **Ballistic capture trajectories**, which cross twice the equilibrium region with relatively long time separating the two crossings

Chapter 3

Long-term capture orbits for low-energy space science missions

In the previous section it was introduced the theoretical background to investigate internal low-energy trajectories in the CR3BP, including an Hamiltonian representation of the linear dynamics in the vicinity of the collinear libration points L_1 and L_2. This allowed characterizing the ultimate behavior of trajectories based on their topological location inside the equilibrium region. Particular interest was devoted to transit trajectories, which allow designing orbital transfers between two celestial bodies, such as the Earth and the Moon, showing that the time $t^\star$, required to cross the equilibrium region, rises rapidly for trajectories which are close to those ones asymptotic to (or from) quasi-periodic orbits.

The characterization of capture orbits was proposed in the form of a theorem by Conley, in the limiting case of the planar CR3BP, stating that: if asymptotic orbits exist then near any such there is a capture orbit [29].

This section is aimed at presenting an extension of Conley's theorem to the spatial CR3BP, leading to a topological location of three-dimensional ballistic captures inside the equilibrium region.

3.1 Conley's theorem for the spatial circular restricted 3-body problem

We consider a 4-sphere $\mathcal{T}$ in $\mathcal{L}$ determined by $x_1 - y_1 = 0$, such that any orbit crosses the sphere if and only if it crosses $\mathcal{L}$, and the following definitions

- a transit trajectory is one which crosses $\mathcal{T}$ arbitrarily early

- an asymptotic trajectory is one converging to, or departing from, a quasi-periodic solution in $\mathcal{L}$. The limit set of asymptotic trajectories is the quasi-periodic libration point orbit

- a capture orbit is one which crosses $\mathcal{T}$ after some relatively long time

The existence of transit orbits for values of the Jacobi constant just below C_i was proved first by Conley, for the planar CR3BP, and further extended to the spatial case by Appleyard in his unpublished PhD thesis [3, 29]. Recently, a method to prove the existence of transit orbits for values of the Jacobi constant relatively smaller than C_i was proposed by Moeckel [115]. Once ascertained the existence of transit trajectories, the topological location of capture orbits inside the equilibrium region can be determined, by investigating possible combination of mappings for the flow outside the equilibrium region.

The two segments of lines $x_1 + y_1 = \pm\varepsilon$ included between the limit hyperbolas $x_1 y_1 = -h/\rho$ correspond to the two 4-spheres bounding the equilibrium region $\mathcal{L}$ which are hereafter referred to as the bounding spheres. As indicated in Figure 2.6, the flow in $\mathcal{L}$ is such that any transit trajectory enters the equilibrium region crossing the disk l_1 or l_3 and leaves the region crossing the disk l_2 or l_4. Therefore, two subsets of the bounding spheres can be determined: $\mathcal{H}_o$, collecting the points leaving $\mathcal{L}$, and $\mathcal{H}_i$, collecting the points entering $\mathcal{L}$, therefore $l_1, l_3 \in \mathcal{H}_i$ and $l_2, l_4 \in \mathcal{H}_o$. Based on this definitions, the above-mentioned mapping between disks can be expressed as follows

$$\mathcal{U}_1 = \{\mathcal{P} \in l_2 | \exists t > 0 \leftrightarrow f(\mathcal{P}, t) \in l_3\} \tag{3.1}$$

$$\mathcal{U}_2 = \{\mathcal{P} \in l_3 \exists t < 0 \leftrightarrow f(\mathcal{P}, t) \in l_2\} \tag{3.2}$$

where $\mathcal{U}_1, \mathcal{U}_2 \in \mathcal{L}$ and the point $\mathcal{P}$ is such that $f(\mathcal{P}, t)$ is a solution of the linear system 2.34 [1].

Recalling that transit and capture trajectories always cross the equilibrium region twice, then for any point on a trajectory leaving the equilibrium region ($\mathcal{P} \in l_2$), the minimum time for the second crossing can be defined as follows

$$t_i = min\{t > 0 | f(\mathcal{P}, t) \in l_3, \mathcal{P} \in l_2\} \tag{3.3}$$

The point on the same trajectory of $\mathcal{P}$ corresponding to t_i is given by the flow mapping

$$\mathcal{P}_i = f(\mathcal{P}, t_i) \tag{3.4}$$

Similar considerations apply for any point on a trajectory entering the equilibrium region ($\mathcal{P} \in l_3$), such that

$$t_o = max\{t < 0 | f(\mathcal{P}, t) \in l_2, \mathcal{P} \in l_3\} \tag{3.5}$$

$$\mathcal{P}_o = f(\mathcal{P}, t_o) \tag{3.6}$$

It is worth to highlight that the two mappings defined above refer to a flow which evolves outside the equilibrium region. In fact, t_i is evaluated from the instant the trajectory leaves the equilibrium region until it enters it again and similar considerations hold for t_o.

From the definitions 3.1 and 3.2, it is possible to say that the domain of $\mathcal{P}_i$ is $\mathcal{U}_1$, while that of $\mathcal{P}_o$ is $\mathcal{U}_2$. The projection of disks l_2 and l_3 onto the $[\hat{x}_1, \hat{y}_1]$ plane, shown in Figure 2.6, provide further information regarding the flow mappings.

---

[1] All the results obtained in this subsection hold if replacing l_3 with l_1 and l_2 with l_4.

The extreme points of these segments belong to the reference axes, therefore they do not represent transit trajectories, but asymptotic ones instead. It follows that the subsets l_2 and l_3 are open in, respectively, $\mathcal{H}_o$ and $\mathcal{H}_i$. According to Lemma 5.1 and Theorem 5.1 in [29], the openness of l_2 and l_3 verifies that the $\mathcal{P}_i$ and $\mathcal{P}_o$ are continuous, inverse each other and define homeomorphisms from domain to range.

Previous result indicates that any orbit crossing l_2 twice must cross l_3 once sometime in between and vice-versa. It is equivalent to say that for a trajectory leaving the equilibrium region towards one of the primaries, i.e. m_2, the previous crossing must have been in the direction from m_1 to m_2, as sketched in Figure 3.1. The same condition does not necessarily hold if considering two disks belonging to the same bounding sphere, such as l_1 and l_2. To examine this case, we have to recall that $\mathcal{T}$ separates $\mathcal{L}$ and is transverse to the bounding spheres. Therefore any trajectory crossing twice the equilibrium region must hit $\mathcal{T}$ in both its hemispheres. It follows that a transit trajectory can not cross twice in a row disks which belong to the same bounding sphere.
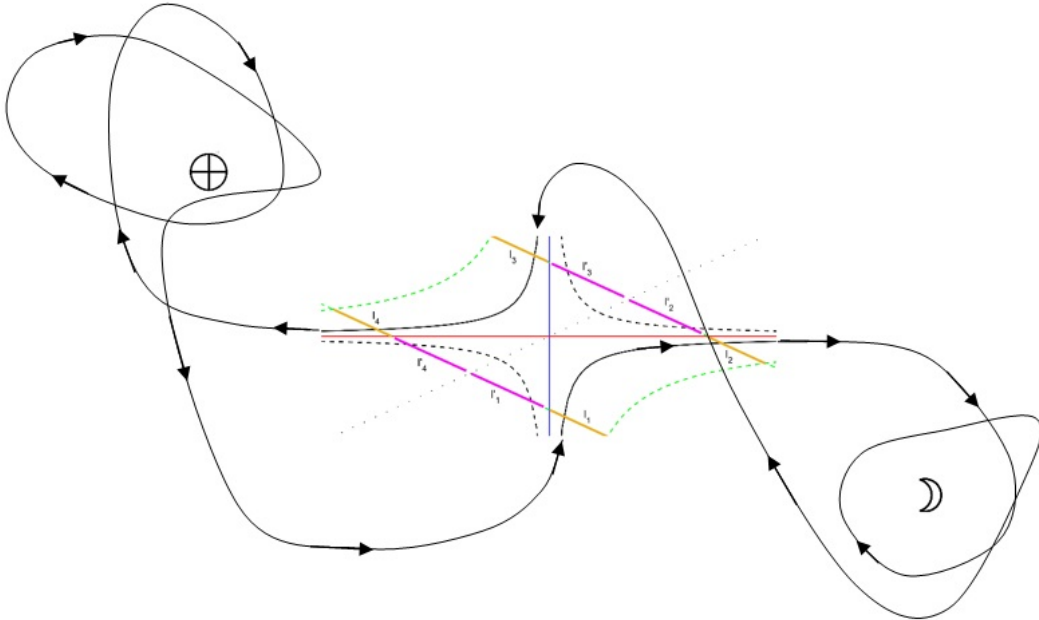
Figure 3.1. Sketch of a transit trajectory onto the $[\hat{x}_1, \hat{y}_1]$ plane

.

The openness of l_2 in $\mathcal{H}_o$ and that of l_3 in $\mathcal{H}_i$ imply that also $\mathcal{U}_1$ and $\mathcal{U}_2$ are open in l_2 and l_3, as can be verified from equations 3.1 and 3.2. Consequently, a point belonging to the boundary of either $\mathcal{U}_1$ or $\mathcal{U}_2$, indicated as $\partial \mathcal{U}_1$ and $\partial \mathcal{U}_2$, is not mapped to l_3 or l_2. According to this, a point $\mathcal{P} \in \partial \mathcal{U}_1 \cap l_2$ belongs to a trajectory which departs asymptotically from the quasi-periodic orbit (it has coordinates $x_1 = 0$), crosses $\mathcal{L}$ ($\mathcal{P} \in l_2$) and, at the same time, can not be mapped to l_3 (equation 3.4 is not verified for $\mathcal{P} \in \partial \mathcal{U}_1$). In conclusion, such a point can only belong to a trajectory which departs asymptotically from the quasi-periodic orbit and takes indefinite time to cross twice the equilibrium region, it is thus a capture orbit. Similar considerations apply for $\mathcal{P} \in \partial \mathcal{U}_2 \cap l_3$, belonging to a capture orbit

which converges asymptotically to the quasi-periodic orbit, as the one sketched in Figure 3.2

Figure 3.2. Sketch of a capture orbit (black solid line) and of the asymptotic trajectory close to it (blue dashed line) onto the $[\hat{x}_1, \hat{y}_1]$ plane

.

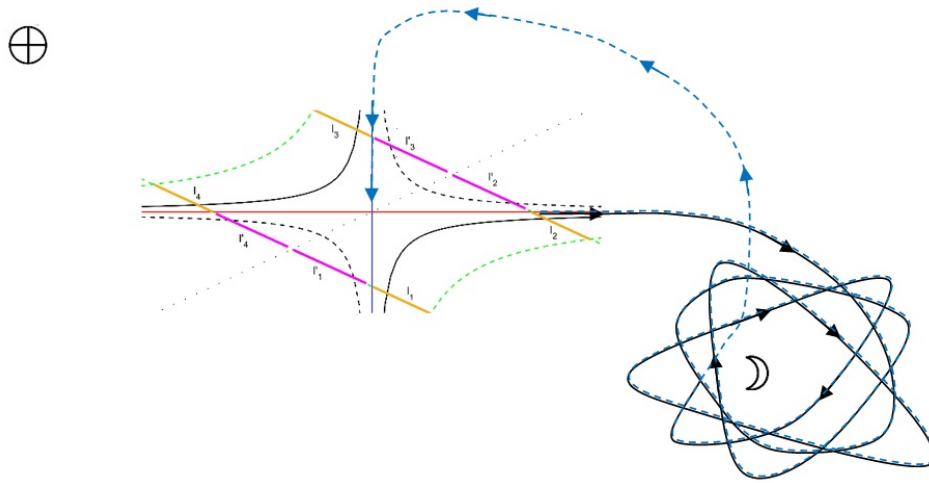The analysis presented in this section is equivalent to that performed by Conley for the planar CR3BP [29] and proves that, also for the spatial case, inside the equilibrium region capture orbits are located in the proximity of asymptotic trajectories. In the following sections, this result is verified by means of numerical analyses.

3.2   Ballistic capture in the Earth-Moon system

Qualitative analysis discussed in sections 3.1 provided the topological characterization of trajectories crossing the equilibrium region, based on only two transformed Hamiltonian coordinates: x_1 and y_1. In particular, capture orbits can be characterized by x_1 or y_1 approaching zero, a condition which, according to equation 2.39, corresponds to $t^\star \to \pm\infty$.

This result is here verified by means of numerical analysis on the Earth-Moon system, according to the parameters reported in Table 3.1.. Low-energy trajectories departing from the equilibrium region surrounding the libration point L_1 and heading to the Moon are calculated by integrating the full nonlinear equations of motion in system 2.22, over a time corresponding to $t_f = 15$ years. The Runge-Kutta family methods implemented in the Matlab function *ode113* are used for this purpose [5], setting a fixed time step of $t_k = 15/100000 \approx 4730sec$, and relative and absolute tolerances equal to, respectively, 1e-18 and 1e-19.

The integration stops when one of the following conditions are matched

- $q_1 < L_{1,x}$, occurring when the trajectory crosses the equilibrium region heading to m_1

- the total time of the simulation is equal to 15 years $(\bar{t} = t_f)$

The dataset produced as output is a 100000×7 matrix, where the elements of the first column are time values corresponding to the Hamiltonian coordinates q_i and p_i on the same row and in columns 2-4 and 5-7. If the integration stops for $\bar{t} < t_f$, then the elements of the dataset corresponding to $t \geq \bar{t}$ are defined as NaN, so that they can be easily filtered during the post-processing of data.

The initial states for the integration are selected among those which should correspond to transit trajectories $(x_1 y_1 < 0)$ and capture orbits $(x_1 \rightarrow 0$ or $y_1 \rightarrow 0)$, through the following systematic procedure

1. A value for the energy level h and the radius of the bounding spheres ε are selected, defining the boundary of the equilibrium region (equation 2.38)

2. A grid onto the $[\hat{x}_1, \hat{y}_1]$ plane is created by means of the following parametric curves, sketched in Figure 3.3

$$x_1 y_1 = -h_k/\rho \quad h_k = 0, \frac{h}{n_h}, 2\frac{h}{n_h}, ..., h$$

$$|x_1 + y_1| = \varepsilon_k \quad \varepsilon_k = 0, \frac{\varepsilon}{n_\varepsilon}, 2\frac{\varepsilon}{n_\varepsilon}, ..., \varepsilon$$

where n_h and n_ε are, respectively, the number of grid elements for the parameters h_k and ε_k

3. The x_1 and y_1 components of the initial states, indicated as α_1 and α_2, are selected corresponding to the intersections of the parametric curves

4. The x_2, y_2, x_3 and y_3 components of the initial states, hereafter indicated as β_1, β_2, γ_1 and γ_2, are selected randomly, within the constraint defined by equation 2.38
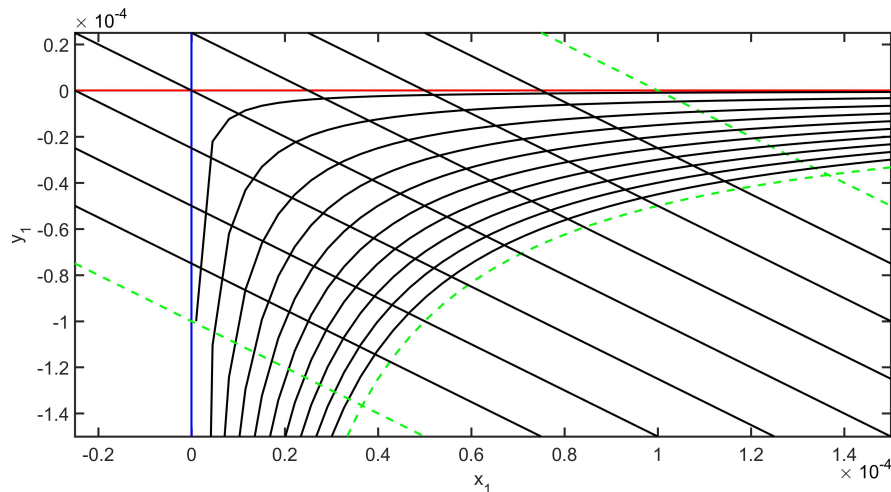

Figure 3.3. Sketch of the grid for the selection of the initial conditions onto the $[\hat{x}_1, \hat{y}_1]$ plane

.

Because the aim is that of verifying that capture trajectories are characterized by either x_1 or y_1 approaching zero, then the values α_1 and α_2 should be selected limiting either one or the other to be adequately far from zero. In particular, capture orbits are here investigated in the vicinity of $\alpha_1 = 0$, thus the following constraint is set $\alpha_2 \leq \alpha_2^{max}$.

The trajectories considered for this analysis cross the equilibrium region once, towards the Moon, or twice, first towards the Moon and then approaching L_1. The former are said long-term capture orbits, while the latter can be either (short-term) capture orbits or transit trajectories and can be distinguished based on the time gap (t_c) between two consecutive crossings of the equilibrium region. The time at each crossing, corresponding to the condition $x_1 + y_1 = \varepsilon$, can be determined from the output data of the integration, then the time gap can be easily computed.

Table 3.1. Earth-Moon simulation parameters

Parameter	Symbol	Value
mass parameter	μ	1.215362e-2
x coordinate of L_1 [DU]	$L_{1,x}$	0.83690020
energy level	h	1e-8
radius of the bounding sphere	ε	7.5e-4
Jacobi constant	C	3.18836
grid elements for hyperbolas	n_h	20
grid elements for straight lines	n_ε	70
maximum value of α_2	α_2^{max}	-6.5e-3
simulation time [years]	t_f	15

As indicated in Table 3.1, the numerical analysis on the Earth-Moon system was performed for a total of 1000 initial conditions, corresponding to C slightly smaller than the critical value for L_1. For each of the trajectories calculated, the values of t_c are compared with α_1 and $t^\star$, as shown in Figure 3.4.

The results in Figure 3.4 confirm the behavior expected for the low-energy trajectories, with captures orbits corresponding to $\alpha_1 \to 0$ and t_c increasing as α_1 approaches zero. Out of the total 1000 trajectories, 120 long-term capture orbits were identified. For these, the number of revolutions about the Moon over the 15 years was calculated, resulting on average equal to 177. A projection of a capture trajectory onto the $[\hat{x}, \hat{y}]$ and the $[\hat{x}_1, \hat{y}_1]$ planes are shown in Figure 3.5.

All of the trajectories calculated almost lay onto the $[\hat{x}, \hat{y}]$ plane. If considering the transformed Hamiltonian coordinates, and in particular equations 2.36 and 2.37, it follows that the out of plane local integral $\mathcal{Z}_2$ is negligible with respect to the in-plane local integral $\mathcal{Z}_1$, as shown in Figure 3.6. It is worth noting that the "flatness" of internal low-energy trajectories is a known issue (see section 1.3.3) and it limits their application to design real missions, which can require higher inclinations. Similarly, examining Figure 3.5, it can be noticed that the order of magnitude for the radius at pericenter is $1e-2$ DU. In fact, the minimum value calculated for the radius at pericenter was $r_p^{min} = 5760$ km which, considering the mean radius of the Moon $R_2 = 1737$ km, corresponds to the minimum altitude at pericenter

$h_p^{min} = 4023$ km. A number of missions could require closer approaches to the celestial body, therefore a solution to control both the inclination and the radius at pericenter for a capture orbit is proposed in Chapter 4.
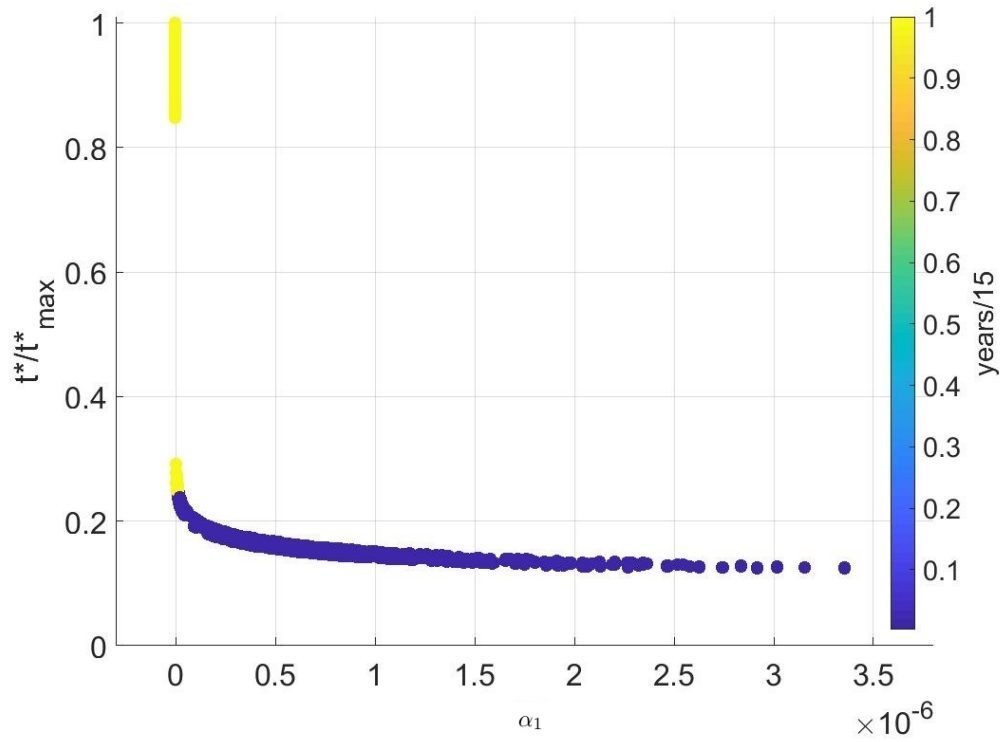

Figure 3.4. Comparison of t_c (colorbar) and $t^\star$ with α_1 for the Earth-Moon system
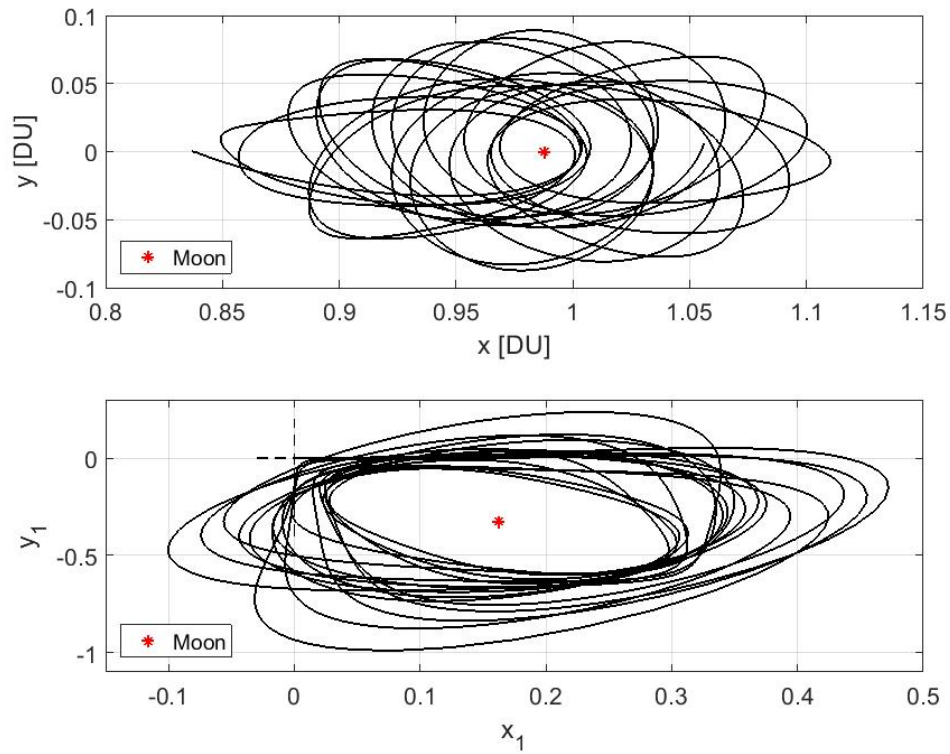
Figure 3.5. A capture orbit around the Moon projected onto the $[\hat{x}, \hat{y}]$ and the $[\hat{x}_1, \hat{y}_1]$ plane
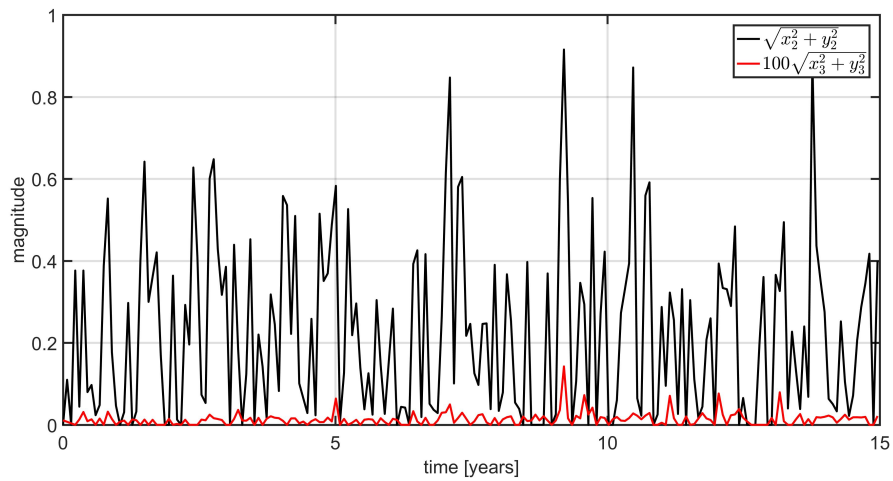

Figure 3.6. Comparison between the magnitude of the in-plane and out of plane oscillatory components for a capture orbit around the Moon

3.3   Effects of the Solar gravitational perturbation on ballistic capture

The theoretical and numerical analyses performed in section 3.1 and 3.2 confirmed the possibility to extend Conley's theorem from the planar to the spatial CR3BP. Because this PhD research project is dedicated to space science missions in the solar system, it could be argued that the Sun gravitational influence, representing a fourth body perturbation, can not be neglected. This is particularly true when investigating trajectories over long time intervals, as did in the previous section [91, 146, 147].

The components of the acceleration associated due to the Sun perturbation are reported below

$$
\begin{cases}
\dot{u}_{p,S} = -G \left[\frac{m_S(x-x_S)}{r_S^3} + \frac{m_S(x_1-x_S)}{r_{1,S}^3} \left(1 - \mu\right) + \frac{m_S(x_2-x_S)}{r_{2,S}^3} \mu \right] \\
\dot{v}_{p,S} = -G \left[\frac{m_S(y-y_S)}{r_S^3} + \frac{m_S(y_1-y_S)}{r_{1,S}^3} \left(1 - \mu\right) + \frac{m_S(y_2-y_S)}{r_{2,S}^3} \mu \right] \\
\dot{w}_{p,S} = -G \left[\frac{m_S(z-z_S)}{r_S^3} + \frac{m_S(z_1-z_S)}{r_{1,S}^3} \left(1 - \mu\right) + \frac{m_S(z_2-z_S)}{r_{2,S}^3} \mu \right]
\end{cases}
\tag{3.7}
$$

where the subscript S refers to the coordinates of the Sun

$$
r_S = \sqrt{(x - x_S)^2 + (y - y_S)^2 + (z - z_S)^2}
$$

and for the i-th primary

$$
r_{i_S} = \sqrt{(x_i - x_S)^2 + (y_i - y_S)^2 + (z_i - z_S)^2}
$$

The acceleration components in system 3.7 can be converted into the dimensionless form, dividing by TU^2/DU^3, and added to the corresponding terms in system 2.3, before to be converted to Hamiltonian variables and integrated numerically. During the integration process, the position of the Sun is updated, assuming a relative motion along a circular orbit, centered in O and with radius equal to $1AU = 1.496e + 8km$.

The effects of the solar gravitational perturbation are hereafter examined for two test cases

- Earth-Moon system, based on the same initial conditions referred in section 3.2, allowing a comparison between the results for the unperturbed and the perturbed case

- Jupiter-Ganymede system, selecting the initial conditions as in section 3.2 and showing that for some scenarios the mentioned perturbation has marginal effects.

For both the systems, each initial condition is propagated considering 8 different initial positions of the Sun. This is defined by the angle θ_S between $\hat{x}$ and the straight line from O to the center of the Sun. The values for θ_S are selected in the range $(0; 360)deg$, with an angular displacement equal to $45deg$, leading to a total of 8000 trajectories computed for each system.

3.3.1   The perturbed Earth-Moon system

The initial conditions selected in section 3.2 and the parameters reported in Table 3.1 are here propagated in a dynamical model which includes the acceleration due to the sun Sun gravitational field, given by equation 3.7. The effects of the solar gravitational perturbation on the long-term behavior of the low-energy trajectories is dramatic. As shown in Figure 3.7 and 3.8, regardless the initial position of the Sun, the behavior of capture time t_c with α_1 is no more predictable. It can be noticed as well that, for $\theta_S \in (-45; 45) deg$ ballistic capture is more favorable with respect to the case $\theta_S \in (45; 315) deg$. In particular, for $\theta_S = 135 deg$ and $\theta_S = 270 deg$ none initial state propagates into along-term ballistic capture. This sets a strict constraint on the launch window, limiting it to those dates corresponding to adequate values of θ_S for the sake of ballistic capture.

The number of revolutions around the moon for long-term capture orbits is affected as well, as reported in Table 3.2. The changing number of revolutions with θ_S leads supposing that also the shape, namely the osculating orbital elements, of capture orbits are affected by the Sun gravity field. This aspect will be investigated in chapter 4.

Table 3.2. Mean number of revolutions around the Moon for long-term capture orbits

$\theta_S[deg]$	No. orbits
0	304
45	182
90	110
135	none
180	96
225	164
270	none
315	195
Unperturbed	177

The numerical analysis on the Earth-Moon system including the solar gravitational perturbation highlights the remarkable impact of such a perturbation on the long-term behavior of low-energy trajectories. A strategy to compensate the effects of the solar gravitational perturbation and producing low-thrust permanent capture is discussed in section 3.4.
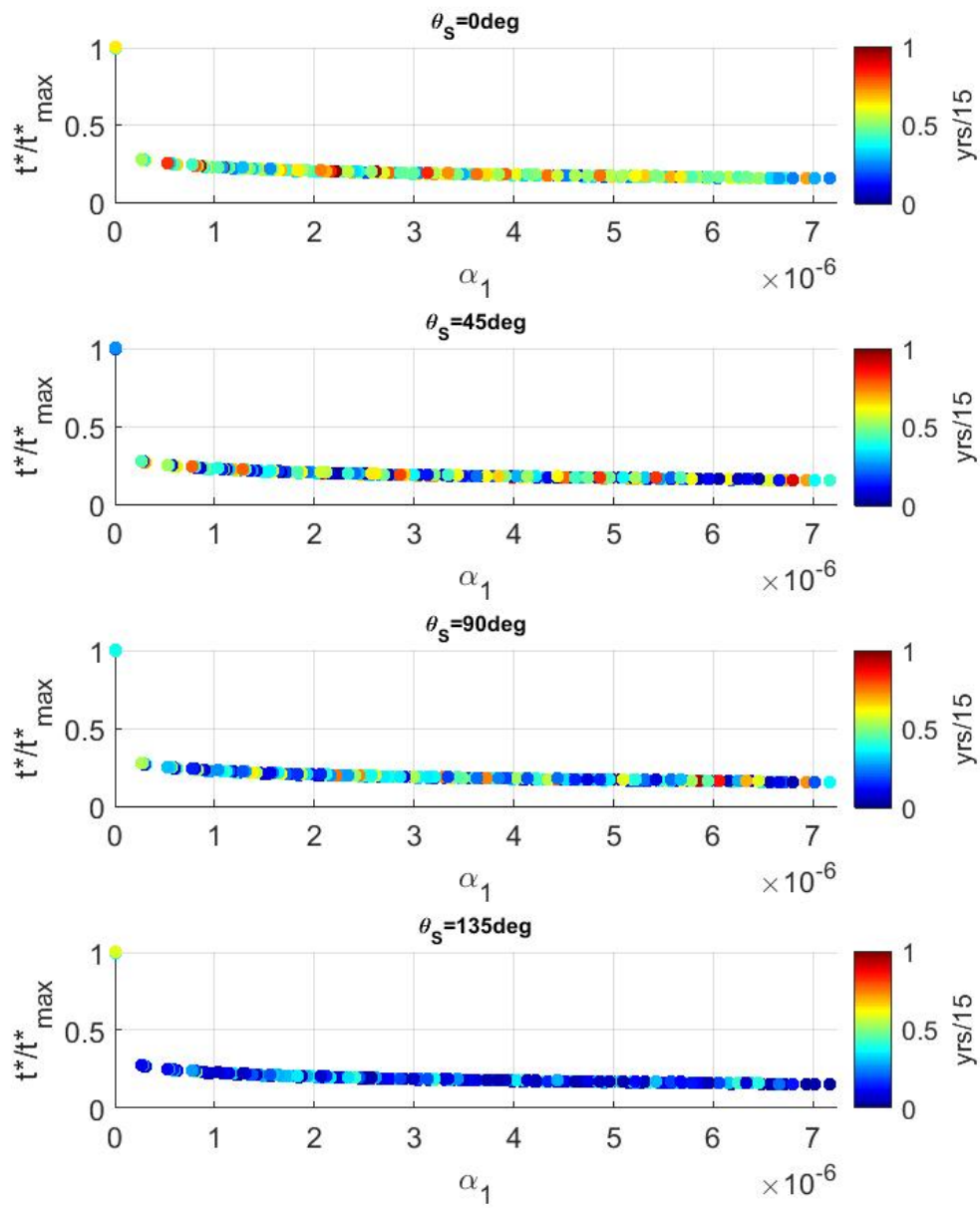
Figure 3.7. Comparison of t_c (colorbar) and $t^\star$ with α_1 for the Sun-perturbed Earth-Moon system with $\theta_S = 0, 45, 90, 135 \ deg$
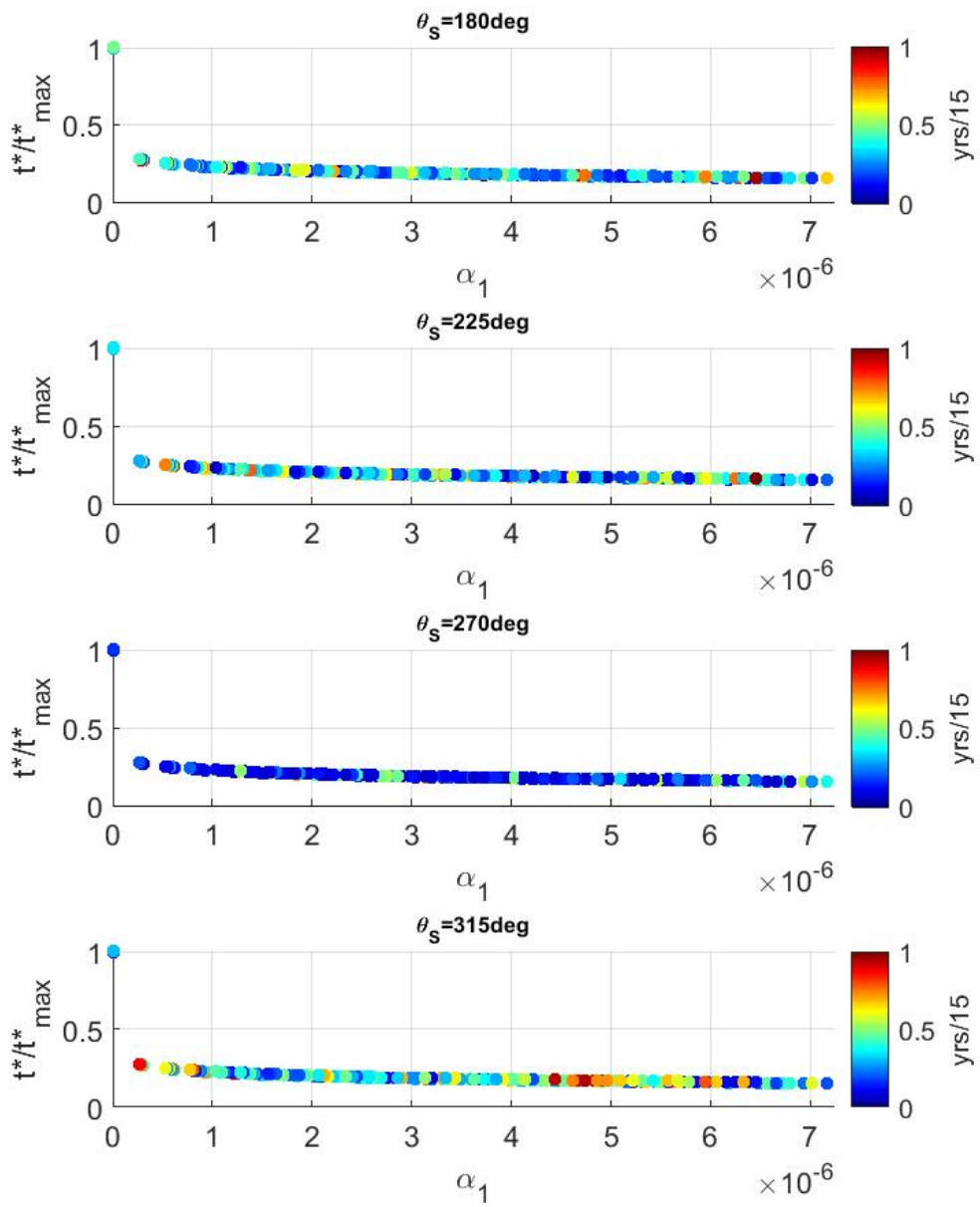
Figure 3.8. Comparison of t_c (colorbar) and $t^\star$ with α_1 for the Sun-perturbed Earth-Moon system with $\theta_S = 180, 225, 270, 315 \ deg$

3.3.2   The perturbed Jupiter-Ganymede system

The existence of long-term capture orbits in the Jupiter-Ganymede system, perturbed by the solar gravitational field is investigated. A total of 1000 initial states is calculated following the procedure proposed in section 3.2 and the parameters in Table 3.3.

Table 3.3. Jupiter-Ganymede simulation parameters

Parameter	Symbol	Value
mass parameter	μ	7.80609493e-05
x coordinate of L_1 [DU]	$L_{1,x}$	0.97058430
energy level	h	1e-8
radius of the bounding sphere	ε	8.5e-3
Jacobi constant	C	3.007643
grid elements for hyperbolas	n_h	40
grid elements for straight lines	n_ε	160
maximum value of α_2	α_2^{max}	-7.5e-3
simulation time [years]	t_f	15

Each initial state is propagated for the 8 values of θ_S considered for the previous case. As shown in Figure 3.9 and 3.10, the behavior of t_c as a function α_1, is consistent with that predicted by the model proposed in section 3.1, despite the presence of the Sun. Long-term capture orbits exist for each value of θ_S and the mean number of revolutions around Ganymede is not significantly affected by the initial position of the Sun, as reported in Table 3.4. In conclusion, the effects of the solar gravitational perturbation are negligible in this scenario. This can be explained noting that the components of the acceleration introduced by the Sun perturbation, reported in equation 3.7, are negligible due to $\mathbf{r}/r_S^3 \approx 0$ and $\mathbf{r_i}/r_S^3 \approx 0$.

Table 3.4. Mean number of revolutions around Ganymede for long-term capture orbits

$\theta_S[deg]$	No. orbits
0	165
45	159
90	161
135	160
180	164
225	164
270	162
315	161
Unperturbed	163
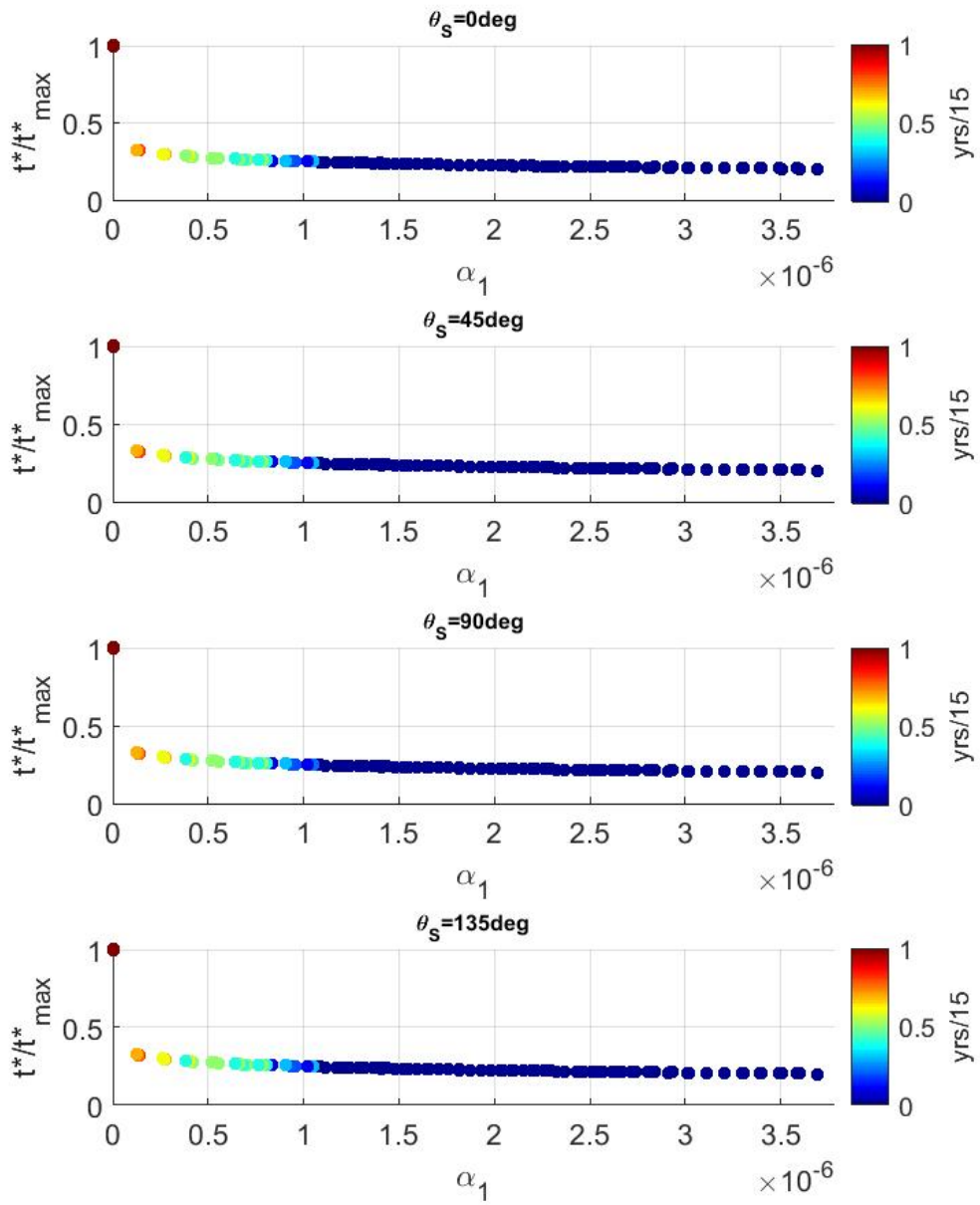
Figure 3.9. Comparison of t_c (colorbar) and $t^\star$ with α_1 for the Sun-perturbed Jupiter-Gabymede system with $\theta_S = 0, 45, 90, 135 deg$
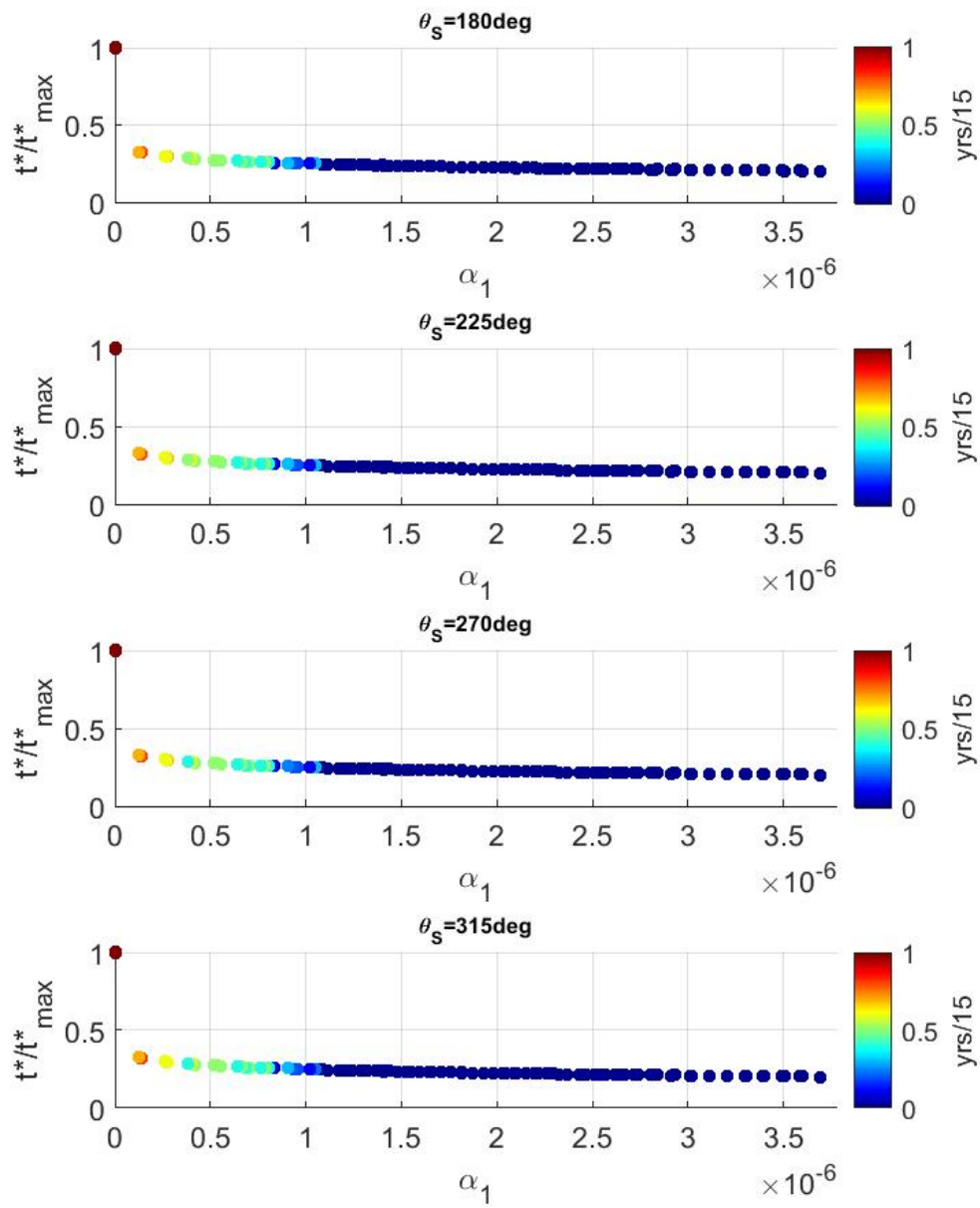
Figure 3.10. Comparison of t_c (colorbar) and $t^\star$ with α_1 for the Sun-perturbed Jupiter-Gabymede system with $\theta_S = 180, 225, 270, 315 \; deg$

The projections of a capture orbit onto the $[\hat{x}, \hat{y}])$ and the $[\hat{x}_1, \hat{y}_1])$ plane are reported in Figure 3.11, showing that the order of magnitude for the radius at pericenter is $1e-3$ DU, with $DU = 6.283e+8$ km. The mean radius of Ganymede is $R_2 = 2634$ km, it follows that, as noticed for the Earth-Moon system, the altitude

at pericenter is considerably high. The magnitude of $\mathcal{Z}_1$ with respect to x_1 and y_1 is shown in Figure 3.12. It can be noticed that the maxima of $\mathcal{Z}_1$ are approximately located at L_1 and L_2.
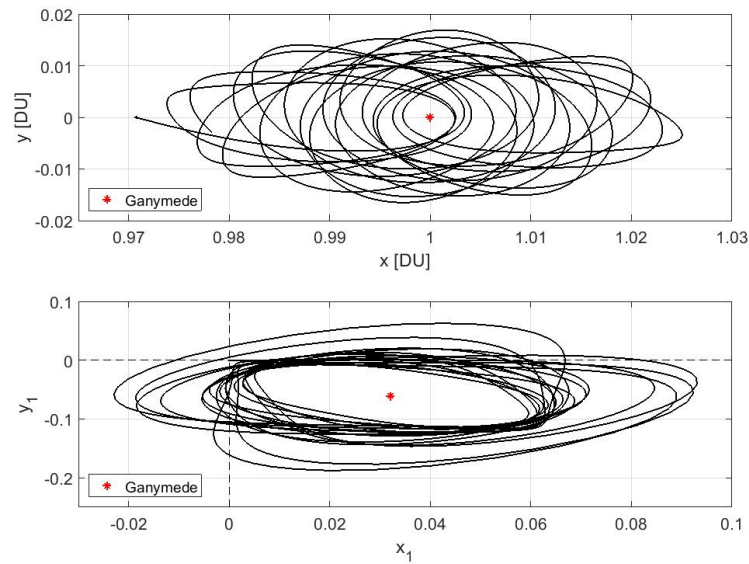
Figure 3.11. A capture orbit around Ganymede projected onto the $[\hat{x}, \hat{y}])$ and the $[\hat{x}_1, \hat{y}_1])$ plane
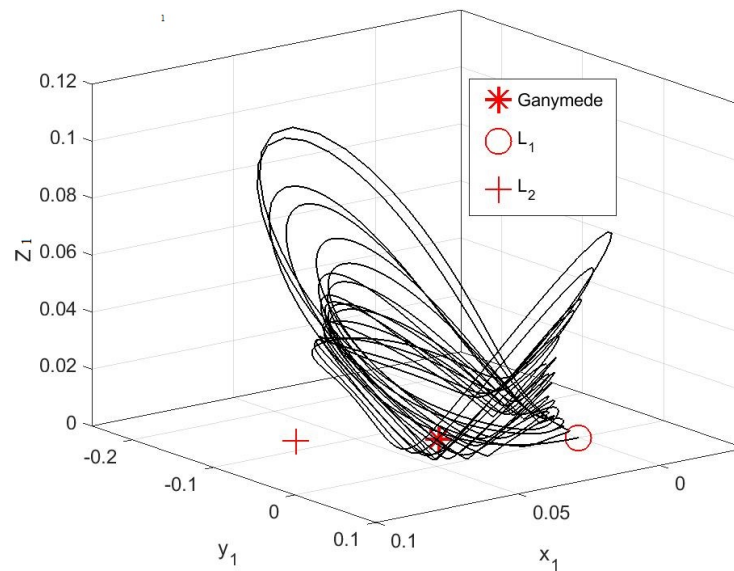
Figure 3.12. Magnitude of the in-plane oscillations as a function of x_1 and y_1 for a capture orbit around Ganymede

3.4   A strategy for powered permanent capture

In this section, a method to produce powered permanent capture from an initial transit trajectory is proposed. The method is based on the topological properties of the flow in the equilibrium region, leading to the definition of a powered capture condition in terms of the transformed Hamiltonian variables x_1 and y_1. When these are converted to the position and velocity space, the total ΔV required by the maneuver can be easily obtained. A preliminary feasibility study is finally performed, aimed at verifying that the ΔV required by the strategy proposed is compatible with current technology available on the market for CubeSats.

The base idea is that of taking advantage of the natural dynamics of the system to reduce the energy required to produce powered permanent capture. As proved in the previous sections, inside the equilibrium region, a transit trajectory is characterized by $x_1 \neq 0$ and $y_1 \neq 0$, and a long-term capture by either $x_1 = 0$ or $y_1 = 0$. Indicating with $\alpha_1(t_0)$ and $\alpha_2(t_0)$ the coordinates of a transit trajectory inside the equilibrium region at time t_0, such a trajectory can be converted into a capture orbit at time $t > t_0$ if one of the following conditions is verified

$$\exists \quad \Delta\alpha_1(t - t_0) : \alpha_1(t) = \alpha_1(t_0) + \Delta\alpha_1(t - t_0) = 0 \tag{3.8}$$

or equivalently

$$\exists \quad \Delta\alpha_2(t - t_0) : \alpha_2(t) = \alpha_2(t_0) + \Delta\alpha_2(t - t_0) = 0 \tag{3.9}$$

It follows that

$$\Delta\alpha_1(t - t_0) = -\alpha_1(t_0) \tag{3.10}$$

and

$$\Delta\alpha_2(t - t_0) = -\alpha_2(t_0) \tag{3.11}$$

In order to develop a guidance strategy, $\Delta\alpha_1$ and $\Delta\alpha_2$ should be converted into a value of ΔV, to be provided by some propulsion system. For the sake of simplicity, lets consider the case represented by equation 3.8, the same considerations will apply for equation 3.9. The transformation from the Hamiltonian variables to the position and velocity coordinates is given by system 2.19 and the α_1 component is reported below, for the sake of clearness [2]

$$\alpha_1(t_0) = \frac{\left(1 + 2\gamma^2\right)\tilde{x}_0 + \left(1 - \gamma^2\right)y_0 + \alpha u_0 - \alpha\sigma v_0}{2\left[\left(1 - \gamma^2\right)\sigma^2 + \alpha^2\right]}$$

Assuming that the position and velocity coordinates are always known and exact, (i.e. the satellite is equipped with an accurate inertial measurement unit), then α_1 can be calculated at any instant of time and the following expression for $\Delta\alpha_1(t - t_0)$ can be set, in which we assume impulsive increments for the velocity components δu and δv

$$\Delta\alpha_1(t - t_0) = \frac{\left(1 + 2\gamma^2\right)\tilde{x}_0 + \left(1 - \gamma^2\right)y_0 + \alpha\left(u_0 + \delta u\right) - \alpha\sigma\left(v_0 + \delta v\right)}{2\left[\left(1 - \gamma^2\right)\sigma^2 + \alpha^2\right]} \tag{3.12}$$

---

[2]It is worth recalling that the symbol ˜ indicates here that the origin of the reference frame is translated to L_i.

Introducing equation 3.12 into 3.10 produces the following result

$$\delta u - \sigma \delta v = -\frac{2}{\alpha} \left[\left(1 + 2\gamma^2 \right) \tilde{x}_0 + \left(1 - \gamma^2 \right) y_0 + \alpha u_0 - \alpha \sigma v_0 \right] \qquad (3.13)$$

The solution of equation 3.13 can be selected for any combination of δu and δv. These are expressed as a fraction of the total $\Delta \alpha_1$ required

$$\begin{cases} \delta u = K_x \left[\left(1 + 2\gamma^2 \right) \tilde{x}_0 + \left(1 - \gamma^2 \right) y_0 + \alpha u_0 - \alpha \sigma v_0 \right] \\ \delta v = K_y \left[\left(1 + 2\gamma^2 \right) \tilde{x}_0 + \left(1 - \gamma^2 \right) y_0 + \alpha u_0 - \alpha \sigma v_0 \right] \end{cases} \qquad (3.14)$$

where the gains K_x and K_y can be conveniently selected depending on the performance of the thruster and are hereafter set equal to $K_x = -\frac{1}{\alpha}$ and $K_y = \frac{1}{\alpha \sigma}$. For a real system, thrust will not be provided instantaneously, but over a time interval δt. It is possible to take advantage of equation 3.14 to evaluate the thrust acceleration to be provided for setting the capture condition 3.9

$$a_x = \frac{\delta u}{\delta t} \qquad (3.15)$$

It is worth noting that, because of some inherent limits of the system, the thruster might not be capable to provide the whole acceleration required in just one burn. Multiple burns ought to be provided to complete the maneuver which, nevertheless, must be accomplished within time $\bar{t}$, when the trajectory departs from the equilibrium region. In fact, once left the equilibrium region, the linear model on which this method is based will not be adequate to describe the dynamics of the system. Including the acceleration term given by equation 3.15 into the dynamic equations of motion, the total velocity variation required by the thruster can be calculated during the integration, according to the following expression

$$\Delta u = \int_{t_0}^{\bar{t}} \frac{\delta u}{\delta t} dt \qquad (3.16)$$

The strategy is verified by applying it to the initial conditions selected for both the perturbed Earth-Moon and the perturbed Jupiter-Ganymede systems, discussed in section 3.3.1 and 3.3.2. The results are shown in Figures 3.13-3.16. It can be noticed that powered permanent capture can be obtained for all the initial conditions and all the scenarios investigated, with the only exception of the Earth-Moon system for $\theta_S = 135$ deg. Under this condition, the solar gravitational perturbation is so strong that it rapidly leads the spacecraft to drift away from the equilibrium region, not allowing the capture strategy to produce its effect. Nevertheless, also in this case the strategy produces a remarked mitigation of the sun gravitational perturbations and long-term captures can be obtained for $\alpha_1 = 0$. The maximum Δu and Δv calculated for each θ_S for the two systems are reported in Tables 3.5 and 3.6

Numerical analyses indicate that, except for extremely adverse scenarios, the strategy proposed leads to the desired capture condition. The suitability of the proposed solution for CubeSat missions is now evaluated, calculating the thrust acceleration required and investigating if thrusters compliant with this performance are nowadays available on the market, or under development.
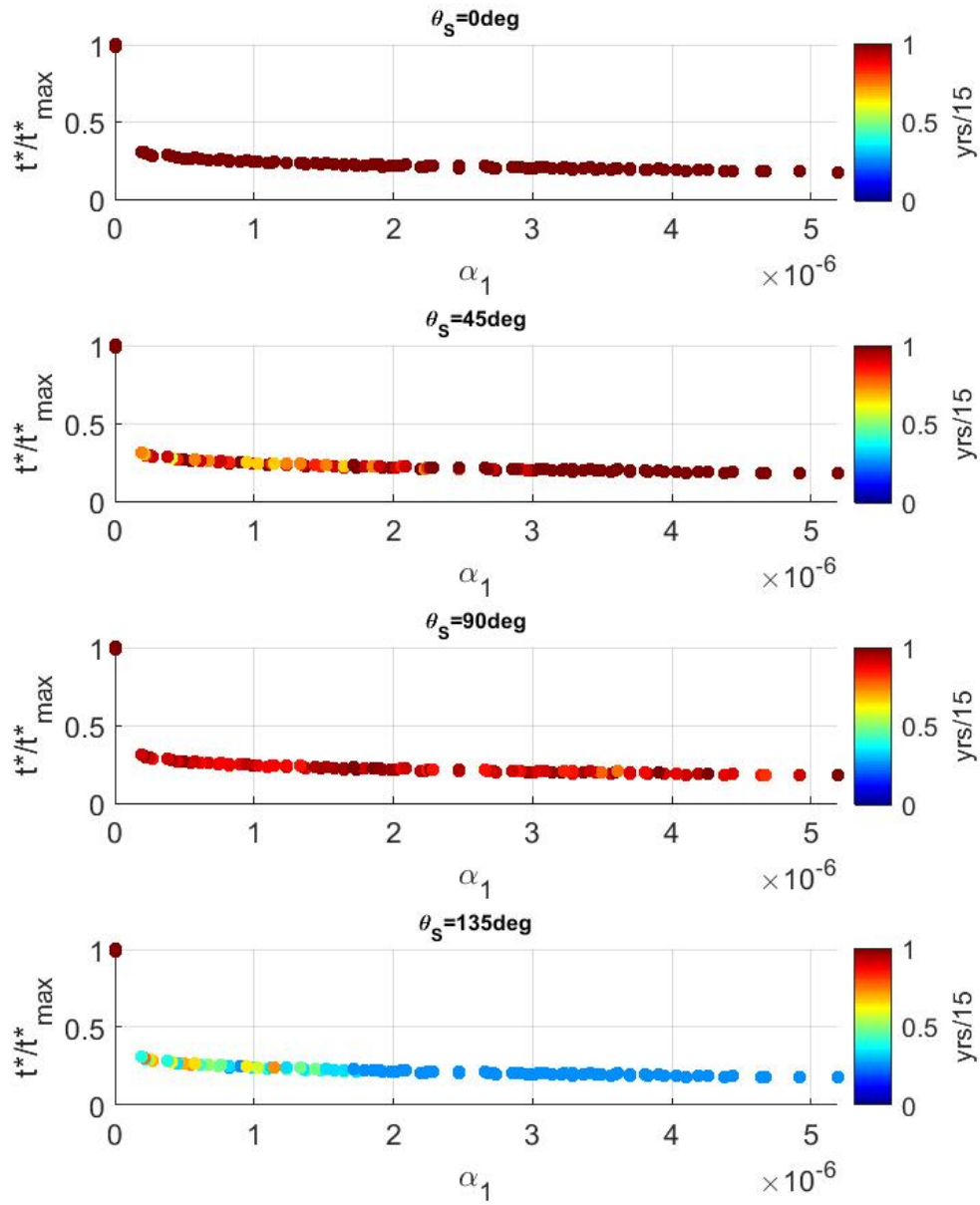
Figure 3.13. Comparison of t_c (colorbar) and $t^\star$ with α_1 for the Sun-perturbed Earth-Moon system with $\theta_S = 0, 45, 90, 135$ deg
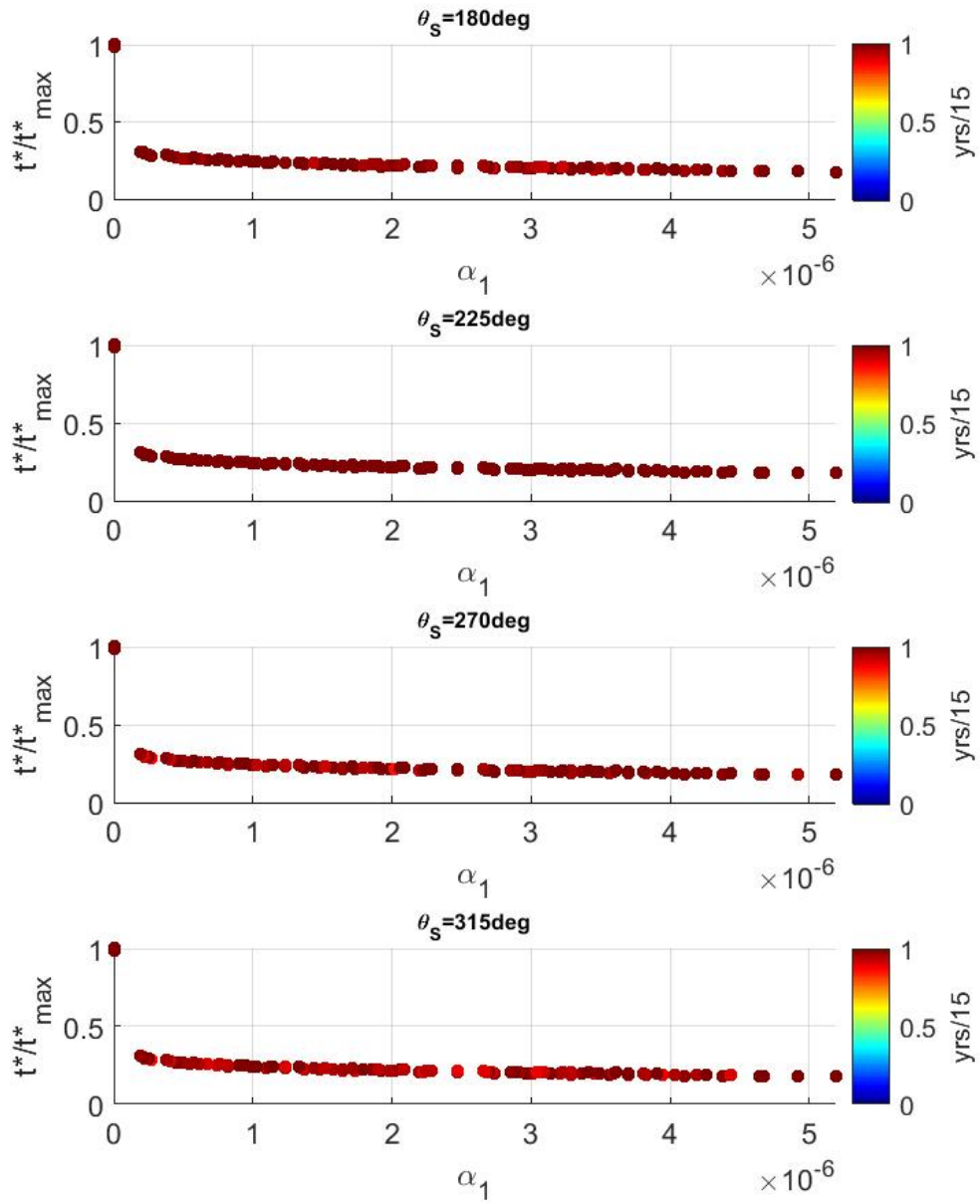
Figure 3.14. Comparison of t_c (colorbar) and $t^\star$ with α_1 for the Sun-perturbed Earth-Moon system with$\theta_S = 180, 225, 270, 315$ deg
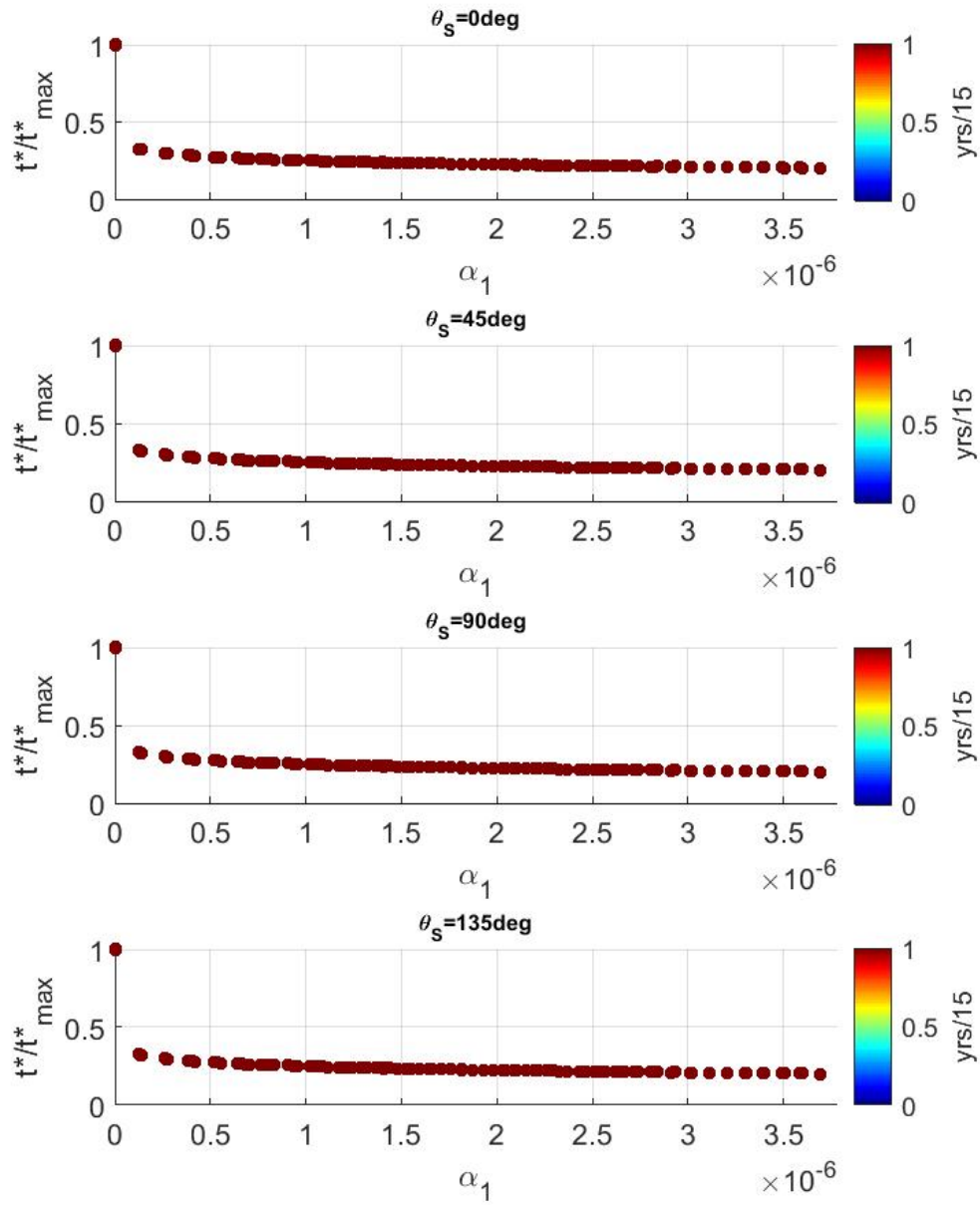
Figure 3.15. Comparison of t_c (colorbar) and $t^\star$ with α_1 for the Sun-perturbed Jupiter-Ganymede system with $\theta_S = 0, 45, 90, 135$ deg
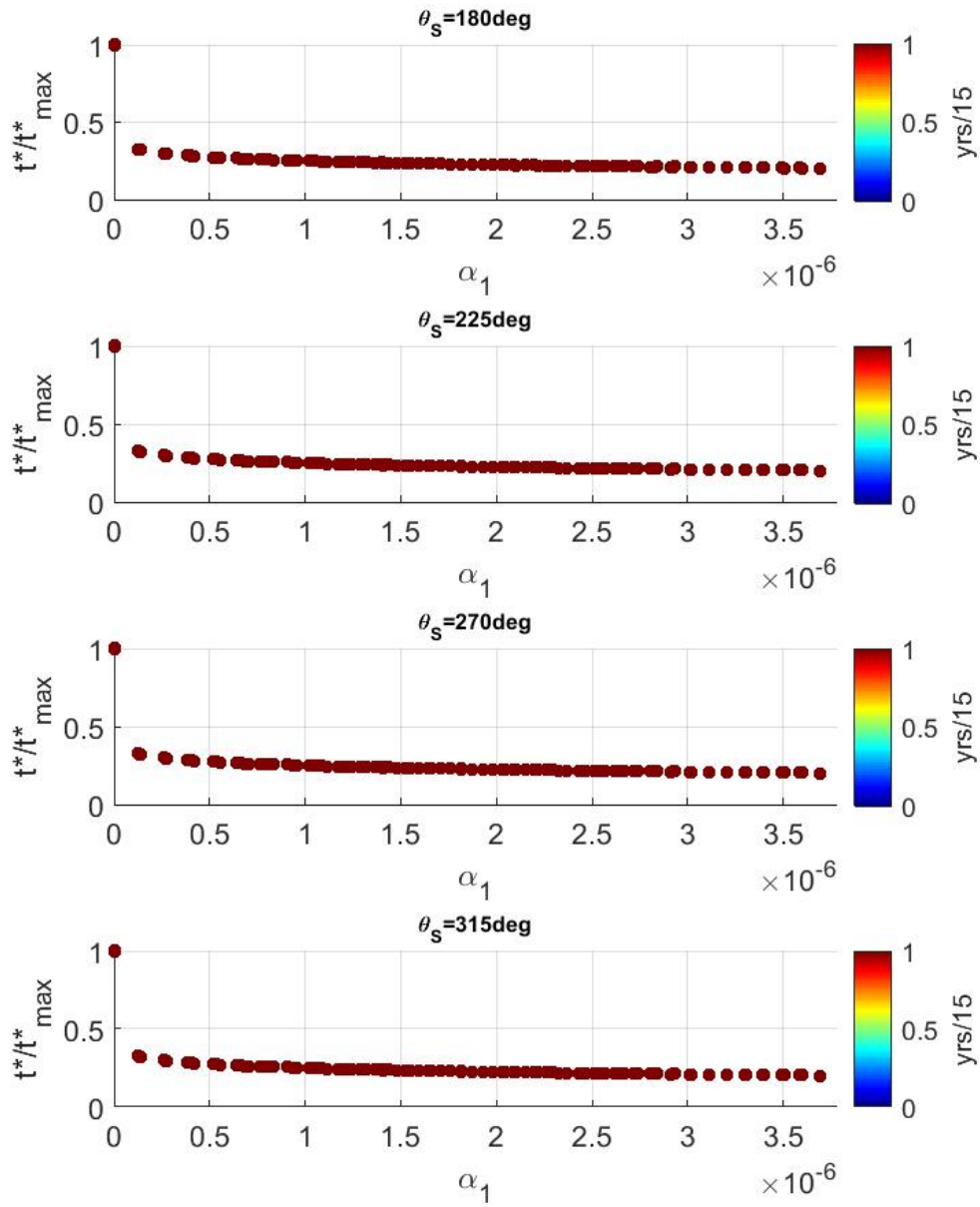
Figure 3.16. Comparison of t_c (colorbar) and $t^\star$ with α_1 for the Sun-perturbed Jupiter-Ganymede system with $\theta_S = 180, 225, 270, 315$ deg

Table 3.5. Maximum ΔV with respect to θ_S and for the Sun-perturbed Earth-Moon system

θ_S [deg]	Δu [m/sec]	Δv [m/sec]
0	3.836e-1	5.160e-2
45	1.158	1.557e-1
90	1.431	1.925e-1
135	-	-
180	2.269e-1	3.052-2
225	1.652e-3	2.222e-4
270	1.095	2.931e-1
315	1.084e-1	1.458e-2
Unperturbed	9.458e-2	1.272e-2

Table 3.6. Maximum ΔV with respect to θ_S and for the Sun-perturbed Jupiter-Ganymede system

θ_S [deg]	Δu [m/sec]	Δv [m/sec]
0	3.512e-2	4.588e-2
45	3.596e-2	4.697e-3
90	3.619e-2	4.729e-3
135	3.533e-2	4.616e-3
180	3.511e-2	4.587e-3
225	9.326e-2	1.218e-2
270	8.708e-2	1.138e-2
315	3.534e-2	4.616e-3
Unperturbed	3.582e-2	4.479e-3

The minimum thrust acceleration needed to perform all the maneuvers is determined as the ratio between maximum velocity variation required $\Delta V^{max} = 1.45$ m/sec (corresponding to $\theta_S = 90$ deg in Table 3.5) and the maximum time to cross the equilibrium region. According to the results of numerical analyses (see Figure 3.17) the equilibrium region is crossed in a time approximately equal to 1 day, therefore, the minimum thrust acceleration required is equal to

$$|\mathbf{a}| = \frac{\Delta V^{max}}{1 day} \approx 1.68e - 5 \quad m/sec^2$$

Such an acceleration is easily produced by the ion-thrusters already developed for CubeSats aimed at solar system exploration [4, 21, 32]. These are typically 6U platforms [126] with mass approximately equal to 15 kg. Referring to such a spacecraft, the minimum thrust required to successfully conclude the capture strategy is equal to 252 μN.

Figure 3.17. Transient for $\Delta u-$ and Δv producing powered permanent capture

Chapter 4

Dynamics of capture orbits from equilibrium region analysis

In chapter 3 the existence of internal ballistic captures for the spatial CR3BP and the topological location of initial co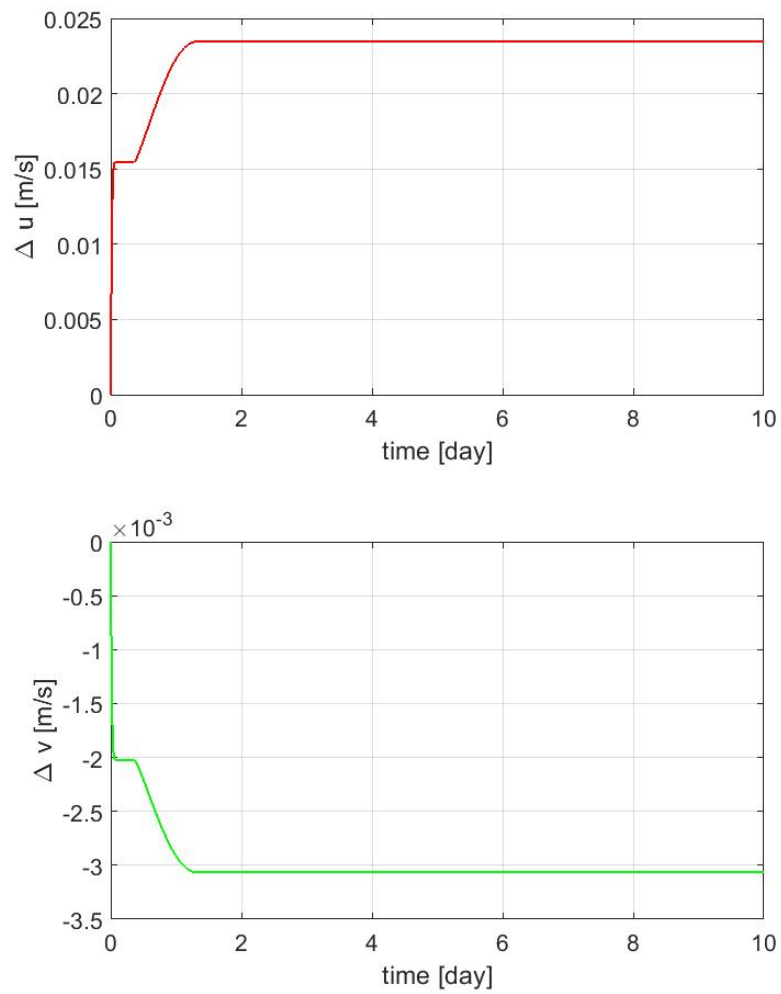nditions corresponding to capture orbits was determined. Such a topological description defaults when the acceleration arising from the solar gravitational perturbation is included in the integration process. This occurs for the Earth-Moon system, on which the effects of the perturbation can be that strong ($\theta_S = 135$ deg and $\theta_S = 270$ deg) to suppress ballistic capture. To overcome this issue, a strategy producing low-thrust permanent capture was developed and verified by numerical analysis, which confirmed its effectiveness and suitability to be implemented on CubeSats.

Capture orbits calculated in chapter 3, both ballistic and powered, are characterized by low inclination and high radius at pericenter. It produces strict limitations when implementing a real mission, whose requirements typically include specific values for the inclination [18, 34], and the peri- and apocenter radius [18, 27, 31, 103]. In the following sections, a method to correlate the osculating orbital elements of a capture orbit and its topological description inside the equilibrium region is provided. The results are verified by means of numerical analysis onto the Earth-Moon system, including an evaluation on the effects of solar gravitational perturbation.

4.1 Influence of the energy level on the orbital elements at capture

In this section, correlations between the osculating orbital elements at capture and the energy fractions h_1 and h_2, corresponding to the magnitude of the in-plane and out of plane periodic oscillators for long-term capture orbits inside the equilibrium region, are deduced.

The motivation in investigating such correlations arises from a result of the numerical analyses in section 3.3, showing that both transit and capture trajectories departing from the equilibrium region are characterized by low values of z, and in particular $z = 0$ along the whole trajectory if the initial conditions verify the equality $(x_3^2 + y_3^2) = 0$. An interpretation of this result can be provided referring to equation 2.38, describing the flow in the equilibrium region as the sum of three local

integrals of motion, each one corresponding to a fraction of the total energy level h of the system

$$\rho x_1 y_1 + \frac{\lambda_1}{2}\left(x_2^2 + y_2^2\right) + \frac{\lambda_2}{2}\left(x_3^2 + y_3^2\right) = h$$

In particular, for a long-term capture orbit $x_1 = 0$ or $y_1 = 0$, then the first local integral is null. The energy fraction of the other integrals can then be indicated as follows

$$\mathcal{Z}_1 : \frac{\lambda_1}{2}\left(x_2^2 + y_2^2\right) = h_1 \tag{4.1}$$

$$\mathcal{Z}_2 : \frac{\lambda_2}{2}\left(x_3^2 + y_3^2\right) = h_2 \tag{4.2}$$

with $h_1 + h_2 = h$. According to equation 4.2 and the above mentioned numerical result, for a long-term capture orbit the condition $z = 0$ corresponds to $h_2 = 0$. Because for $h_2 \neq 0$ also $(x_3^2 + y_3^2) \neq 0$ then $z \neq 0$, it can be guessed that the higher the value of the energy fraction h_2 the higher the maximum magnitude of z and in particular: for a capture orbit, the higher the energy fraction h_2 the higher the inclination of the orbit.

The guessed correlation betweeen h_2 and the inclination at capture can be formulated as follows. First the space and velocity coordinates can be expressed as a function of x_2, x_3, y_2, y_3 from the inverse of transformation 2.31

$$\begin{cases} x = k_1\left(x_2 + jy_2\right) \\ y = k_2\left(x_2 + jy_2\right) \\ z = k_3\left(x_3 + jy_3\right) \\ u = k_4\left(x_2 - jy_2\right) \\ v = k_5\left(x_2 - jy_2\right) \\ w = k_6\left(x_3 - jy_3\right) \end{cases} \tag{4.3}$$

where the coefficients k_i can be determined from transformation 2.31 [165]. The magnitude of the angular momentum can be calculated from the components in system 4.3, producing the following result

$$|\mathbf{Q}|^2 = (xv - yu)^2 + (yw - zv)^2 + (zu - wx)^2 = \left[\left(x_2^2 + y_2^2\right)\left(k_1 k_5 - k_2 k_4\right)\right]^2 +$$

$$+\left(x_3^2 + y_3^2\right)\left\{[k_1 k_6\left(x_2 + jy_2\right) + k_3 k_4\left(x_2 - jy_2\right)]^2 - [k_2 k_3\left(x_2 + jy_2\right) + k_5 k_6\left(x_2 - jy_2\right)]^2\right\} \tag{4.4}$$

Introducing equations 4.1 and 4.2 into equation 4.4 leads to

$$|\mathbf{Q}|^2 = \frac{4h_1^2}{\lambda_1^2}\left(k_1 k_5 - k_2 k_4\right)^2 + \frac{2h_2}{\lambda_2}[k_1^2 k_6^2\left(x_2^2 - y_2^2 + 2jx_2 y_2\right) +$$

$$+k_3^2 k_4^2\left(x_2^2 + y_2^2 - 2jx_2 y_2\right) - k_2^2 k_3^2\left(x_2^2 - y_2^2 + 2jx_2 y_2\right) - k_5^2 k_6^2\left(x_2^2 + y_2^2 - 2jx_2 y_2\right) +$$

$$+\frac{4h_1}{\lambda_1}k_3^2 k_6^2\left(k_1 k_4 - k_2 k_5\right)] \tag{4.5}$$

As can be inferred from transformation 2.38, $k_1^2 k_6^2 = k_2^2 k_3^2$ and $k_3^2 k_4^2 = k_5^2 k_6^2$ then equation 4.5 reduces to

$$|\mathbf{Q}|^2 = \frac{4h_1^2}{\lambda_1^2} (k_1 k_5 - k_2 k_4)^2 + \frac{8h_1 h_2}{\lambda_1 \lambda_2} k_3 k_6 (k_1 k_4 - k_2 k_5) \tag{4.6}$$

Similarly the component of $\mathbf{Q}$ along z is given by

$$Q_z = (xv - yu) = \left(x_2^2 + y_2^2\right)(k_1 k_5 - k_2 k_4) = \frac{2h_1}{\lambda_1} (k_1 k_5 - k_2 k_4) \tag{4.7}$$

The osculating inclination can finally be determined as follows

$$\cos i = \frac{Q_z}{|\mathbf{Q}|} = \frac{\frac{2h_1}{\lambda_1}(k_1 k_5 - k_2 k_4)}{\sqrt{\frac{4h_1^2}{\lambda_1^2}(k_1 k_5 - k_2 k_4)^2 + \frac{8h_1 h_2}{\lambda_1 \lambda_2} k_3 k_6 (k_1 k_4 - k_2 k_5)}} =$$

$$= \frac{1}{\sqrt{\frac{\frac{4h_1^2}{\lambda_1^2}(k_1 k_5 - k_2 k_4)^2 + \frac{8h_1 h_2}{\lambda_1 \lambda_2} k_3 k_6 (k_1 k_4 - k_2 k_5)}{\frac{4h_1^2}{\lambda_1^2}(k_1 k_5 - k_2 k_4)^2}}} =$$

$$= \frac{1}{\sqrt{1 + 2\frac{h_2 \lambda_1 k_3 k_6 (k_1 k_4 - k_2 k_5)}{h_1 \lambda_2 (k_1 k_5 - k_2 k_4)^2}}} = \frac{1}{\sqrt{1 + k_7 \frac{h_2}{h_1}}} \tag{4.8}$$

Then the following equation can be guessed, correlating the inclination with the energy fractions [1]

$$i \approx cos^{-1} \frac{1}{\sqrt{1 + \frac{h_2}{h_1}}} \tag{4.9}$$

Equation 4.9 will be verified by numerical analyses performed in sections 4.2.1 and 4.2.2.

According to equation 4.9, the higher h_2 the higher i, nevertheless the energy level can not grow indefinitely, so neither can h_2. The upper and the lower bound for h are both related to properties of the equilibrium region. A lower bound on h can be defined in terms of the Jacobi constant, recalling that $H = -2C$. In the equilibrium region, where terms of order higher than 2 can be neglected, $H_2 = h$ represents an accurate approximation of the full Hamiltonian function and therefore $h \approx -2C$. We should recall now that the topological description presented in section 3.1, at the basis of all the development discussed here, is verified only if transit trajectories exist, thus if the Jacobi constant is smaller than the critical value C_1 (see section 2.1). Equivalently, the topology of the equilibrium region is not described by equation 2.38 if h exceeds an upper bound at which energy transfers can occur between the in-plane and the out of plane components [82].

Beside the inclination, two other parameters should be defined to characterize capture orbits, the osculating semimejor axis (a) and eccentricity (e). A correlation

---

[1]It is worth noting that the equation was developed based on the dimensionless component instead of dimensional ones. Nevertheless, the proportionality is preserved through the transformation, because it is homothetic.

between the energy fraction h_1 and a is guessed, based on the fact that as h_1 increases the allowed region of motion inside the ZVS broadens [2]. The correlation can be extended to the radius at peri- and apocenter using the Tisserand's relation

$$\frac{1}{2a} + \sqrt{a\left(1 - e^2\right)}\cos i = constant \qquad (4.10)$$

Considering a fixed value of the inclination, equation 4.10 implies that e decreases as a increases. Therefore, increasing h_1 can lead to capture orbits with significantly different pairs of r_p and r_a. This conjecture will be verified by the numerical analyses in section 4.2.1 and 4.2.2.

4.2 Numerical investigation of the osculating orbital elements at capture

The correlations between the osculating orbital elements at capture and the energy fractions, conjectured in the previous section, are verified here by means of numerical analysis on the Earth-Moon system, considering ballistic captures about the Moon. This is achieved by propagating the full nonlinear equations of motion for the CR3BP 2.22 on a set of initial conditions, in the neighborhood of the libration point L_1, systematically selected through the following method

1. long-term capture orbits heading towards the primary m_2 are selected, corresponding to the initial condition $\alpha_2 = 0$ [3]

2. the boundaries of the equilibrium region are set, defining the values of h and ε

3. n_ε elements on the x_1 axis are selected according to the following grid

$$\alpha_1^{(n)} = \frac{n}{n_\varepsilon}\varepsilon \quad n = 0, 1, ..., n_\varepsilon \qquad (4.11)$$

4. the following parametric representations for the energy fractions are defined

$$h_1^{(n)} = \frac{n}{n_h}h \quad n = 0, 1, ..., n_h \qquad (4.12)$$

$$h_2^{(n)} = h - h_1 \quad n = 0, 1, ..., n_h \qquad (4.13)$$

5. introducing equations 4.12 and 4.13 into equations 2.36 and 2.37 produces a parametric representation for the integrals $\mathcal{Z}_1^n$ and $\mathcal{Z}_2^n$, defining

$$\left(x_2^2 + y_2^2\right)^{(n)} \quad n = 0, 1, ..., n_h \qquad (4.14)$$

$$\left(x_3^2 + y_3^2\right)^{(n)} \quad n = 0, 1, ..., n_h \qquad (4.15)$$

---

[2]It is worth recalling that a similar behavior is observed for Keplerian orbits, where a is proportional to the Keplerian energy.

[3]Equivalent results can be achieved selecting long-term captures towards m_1.

6. The phase angles for the complex variables x_2 and x_3 can be defined as follows

$$\chi_1 = 2\tan^{-1}\left(\frac{\Im(x_2)}{1+\Re(x_2)}\right) \tag{4.16}$$

$$\chi_2 = 2\tan^{-1}\left(\frac{\Im(x_3)}{1+\Re(x_3)}\right) \tag{4.17}$$

7. a number m_χ of equivalently spaced phase angles are selected in the range $[0; 2\pi]$, according to the following grid

$$\chi_1^{(m)} = \frac{m}{m_\chi}2\pi \quad m = 0, 1, ..., m_\chi \tag{4.18}$$

$$\chi_2^{(m)} = \frac{m}{m_\chi}2\pi \quad m = 0, 1, ..., m_\chi \tag{4.19}$$

8. Given $\mathcal{Z}_1^n$ and $\mathcal{Z}_2^n$ and equations 4.18 and 4.19, the remaining initial conditions are defined

$$\begin{cases} \beta_1^{(m,n)} = \sqrt{Z_1^n}\cos\chi_1^{(m)} + j\sqrt{Z_1^n}\sin\chi_1^{(m)} \\ \beta_2^{(m,n)} = \sqrt{Z_1^n}\sin\chi_1^{(m)} + j\sqrt{Z_1^n}\cos\chi_1^{(m)} \end{cases} \tag{4.20}$$

$$\begin{cases} \gamma_1^{(m,n)} = \sqrt{Z_1^n}\cos\chi_2^{(m)} + j\sqrt{Z_1^n}\sin\chi_2^{(m)} \\ \gamma_2^{(m,n)} = \sqrt{Z_1^n}\sin\chi_2^{(m)} + j\sqrt{Z_1^n}\cos\chi_2^{(m)} \end{cases} \tag{4.21}$$

A total of 1000 initial conditions are calculated through the procedure indicated for three test cases, corresponding to different energy levels

- $h = 1e-8$, selected as in section 3.3 such that the corresponding C is slightly lower than the critical value C_1

- $h = 8.5e-3$, calculated to have a maximum z of the same order of magnitude as the radius of the sphere of influence of the Moon r_{SOI} [9], according to

$$r_{SOI} = a\left(\frac{m_2}{m_1}\right)^{\frac{2}{5}} \tag{4.22}$$

- $h = 1e-4$, selected between the above mentioned ones.

The values of ε for each h were selected through an iterative process

1. a guessed value for ε is selected

2. the initial conditions corresponding to the guess are determined and used to integrate system 2.22 over a few time steps

3. the Jacobi constant is calculated for the final state of each trajectory

4. the maximum (C^{max}), minimum (C^{min}) and mean (C^{mean}) value of the Jacobi constant are evaluated

5. if $max\{|C^{max} - C^{mean}|, |C^{min} - C^{mean}|\}$ is smaller than the last significant digit of C^{mean} (i.e. $1e-8$), then the value of ε is accepted, otherwise it is recalculated.

The integration process is performed using Matlab *ode113* [5], with relative and absolute tolerances set to 1e-18 and 1e-19. A further stop condition is considered, along with those indicated in section 3.2, occurring when the spacecraft altitude decreases below 50 km. The initial conditions are propagated over a time $t_f = 3$ years, with fixed time step $t_k = 3/100000 \approx 946sec$ and considering the parameters in Table 4.1. In sections 4.2.2 4.3, the acceleration due to the sun Sun gravitational field, expressed by equations 3.7, is considered.

The results from the numerical analysis are then post-processed to investigate the osculating orbital elements at capture. As the trajectory departs from the equilibrium region and is captured by m_2, the Tisserand's relation 4.10 stabilizes to a constant value $\bar{T}_s$. This process is monitored and the time $t_{c,0}$ when the error between the calculated Tisserand's relation and $\bar{T}_s$ enters the band $\pm 5\%$ is considered as the initial capture. The minimum value of the osculating radius at pericenter $(\bar{r}_p)$ is evaluated as the minimum distance between m and m_2, from time $t_{c,0}$ to a desired one $t_{c,f}$

$$\bar{r}_p = min\{r_2(t)\} \quad t_{c,0} \le t \le t_{c,f} \tag{4.23}$$

Indicating with t_p the time at $\bar{r}_p$, then the related radius at apocenter is calculated as follows

$$r_a(t_p) = \bar{r}_a = max\{r_2(t)\} \quad t_p - T \le t \le t_p + T \tag{4.24}$$

where T is the approximated orbital period for the osculating capture orbit, calculated as the time gap between the maximum r_2 before and after $\bar{r}_p$. Similarly, the inclination and the eccentricity are calculated at t_p, according to equation 4.9 and the following expression

$$e = \frac{\bar{r}_a - \bar{r}_p}{\bar{r}_a + \bar{r}_p} \tag{4.25}$$

The mean, maximum and minimum value of for $\bar{r}_p$, $r_a(t_p)$, $i(t_p)$ and $e(t_p)$ are calculated for all the energy levels and their behavior with respect to h_1 and h_2 is investigated, to evaluate the suitability of conjectures in section 4.1.

Table 4.1. Earth-Moon simulation parameters at different energy levels

energy level	h	$1e-8$	$1e-4$	$8.5e-3$
Jacobi constant	C	3.18836	3.18796	3.15222
radius of the bounding sphere ε	1.10158e-2	1.10158e-2	2.873000e-2	

mass parameter	μ	1.215362e-2
x coordinate of L_1 [DU]	$L_{1,x}$	0.83690020
grid elements for hyperbolas	n_h	10
grid elements for straight lines	n_ε	5
grid elements for phase	m_χ	10
simulation time [years]	t_f	3
mission time [days]	$t_{c,f}$	30

4.2.1   The unperturbed Earth-Moon system

The numerical integration of the initial conditions for the unperturbed Earth-Moon system produces capture orbits, regardless the energy level considered. Monitoring the Tisserand's parameter indicates that the time required to cross the equilibrium region and enter the ballistic capture condition is equal to $t_{c,0} = 1$ day. The frequency of impact trajectories increases with h as shown in Table 4.2. This behavior is a direct consequence of the fact that lower radius at pericenter, thus higher probability of impact, can be obtained at higher h, as detailed later in this section.

Table 4.2. Number of lunar impact trajectories with time

t	15 days	30 days	60 days	1 year	3 years
$h = 1e - 8$	0	0	1	256	256
$h = 1e - 4$	0	69	99	246	246
$h = 8.5e - 3$	345	350	360	370	370

The mean, maximum and minimum value for $\bar{r}_p$, $r_a(t_p)$, $i(t_p)$ and $e(t_p)$, were calculated and reported in Figures 4.1-4.9. It can be noticed that, even though the mean value of $\bar{r}_p$ increases with h_1 up to one order of magnitude (Figure 4.1), so does the gap between the maximum and the minimum value (Figure 4.2). A similar behavior, though less marked, is registered for $r_a(t_p)$ (Figures 4.3-4.4). This result, together with that of $\bar{r}_p$, represents a numerical validation of what conjectured in section 4.1, stating that an increase of a with h_1 corresponds to a decrease of e. For the sake of completeness, the behavior of $e(t_p)$ with h_1 and h_1 is shown in Figures 4.5 and 4.6.
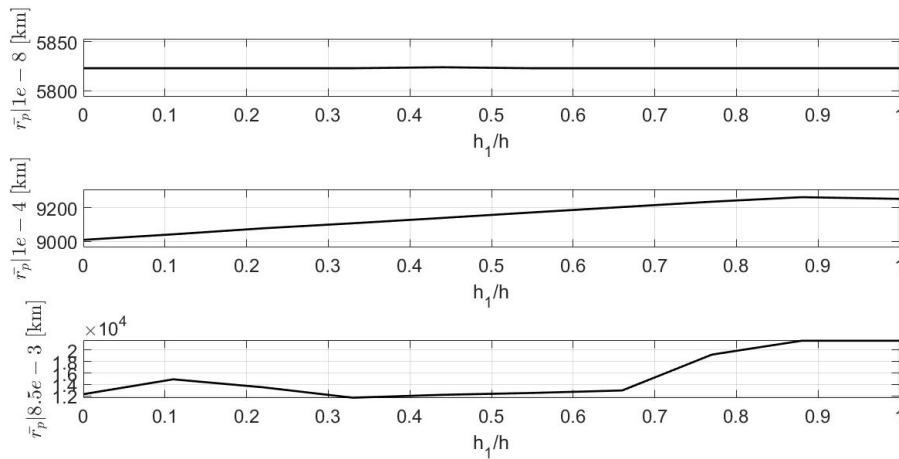
Figure 4.1. Mean values of $\bar{r}_p$ as a function of h_1/h for the three energy levels
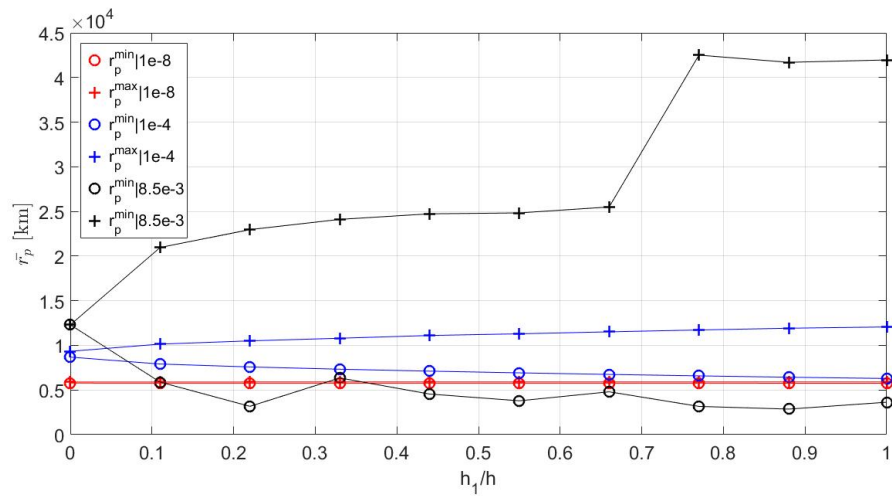
Figure 4.2. Maximum and minimum values of $\bar{r}_p$ as a function of h_1/h for the three energy levels

Figure 4.3. Mean values of $r_a\left(t_p\right)$ as a function of h_1/h for the three energy levels
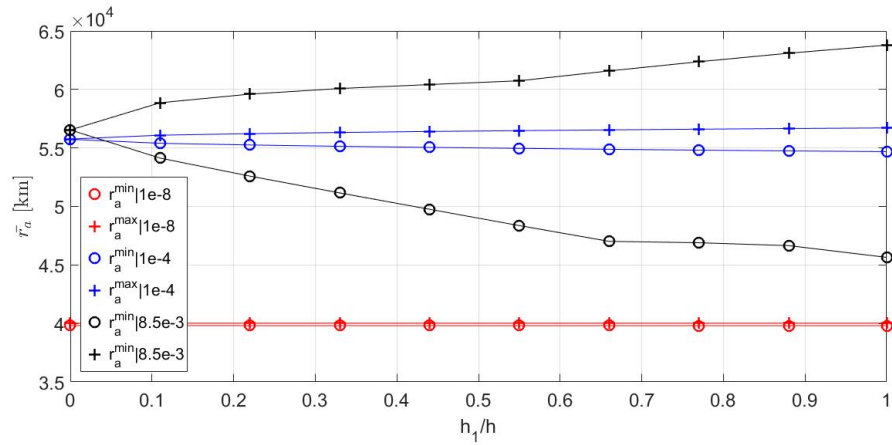
Figure 4.4. Maximum and minimum values of $r_a(t_p)$ as a function of h_1/h for the three energy levels

Figure 4.5. Mean values of $e(t_p)$ as a function of h_1/h for the three energy levels
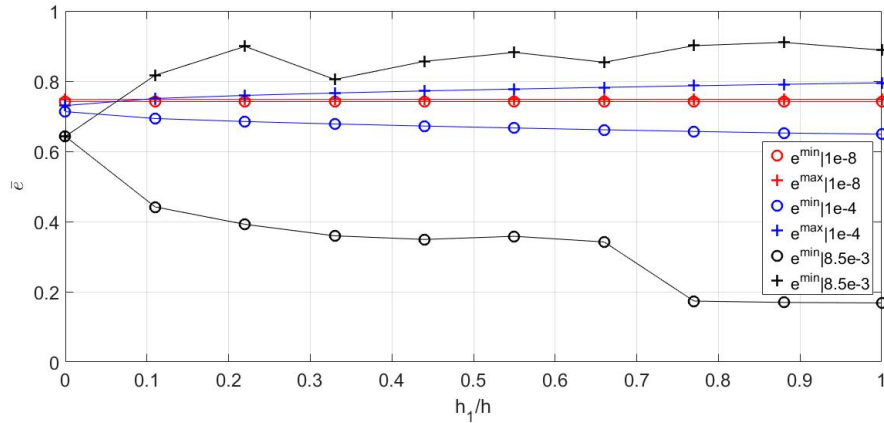
Figure 4.6. Maximum and minimum values of $e(t_p)$ as a function of h_1/h for the three energy levels

Results from the numerical analysis reported in Figure 4.7 and 4.8 show that the inclination increases considerably with h_2, up to a maximum inclination of 87 deg. More in detail, for $h = 1e - 8$ and $h = 1e - 4$ higher inclinations corresponds to higher h_2/h_1, while this condition is not verified for $h = 8.5e - 3$, where the maximum value corresponds to $h_2/h = 0.33$. To explain this fact, it is possible to notice that capture orbits corresponding to high energies are remarkably not planar and thus far from the Keplierian model from which equation 4.9 was obtained. Nevertheless Figure 4.9 shows that z increases monotonically with h_2 confirming also the other conjecture in section 4.1.
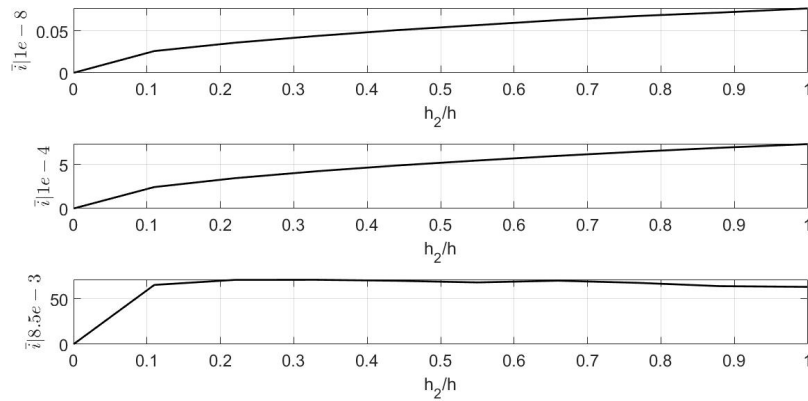
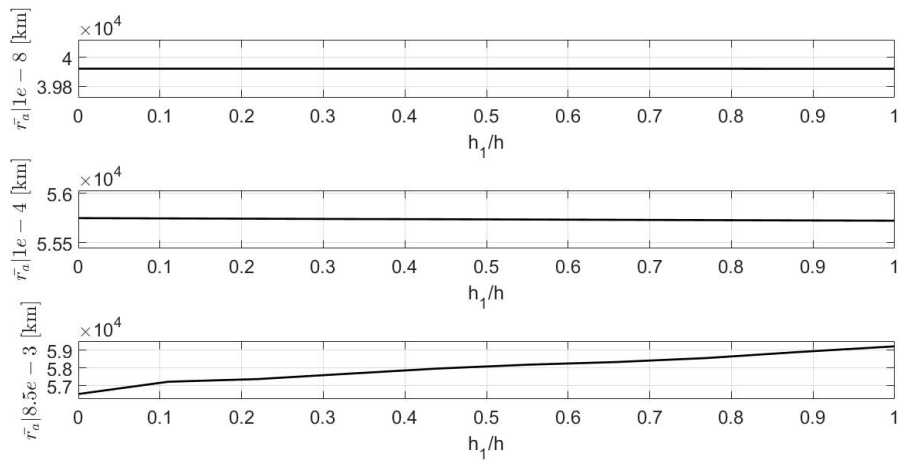**Figure 4.7.** Mean values of $i(t_p)$ as a function of h_2/h for the three energy levels
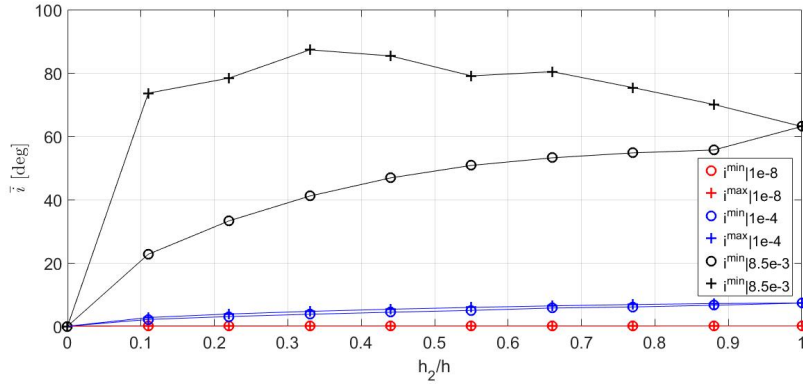
Figure 4.8. Maximum and minimum values of $i\left(t_p\right)$ as a function of h_2/h for the three energy levels
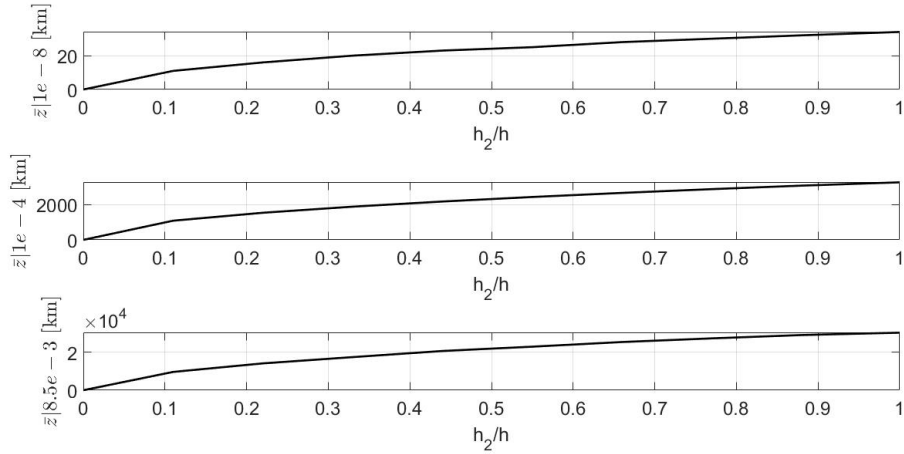
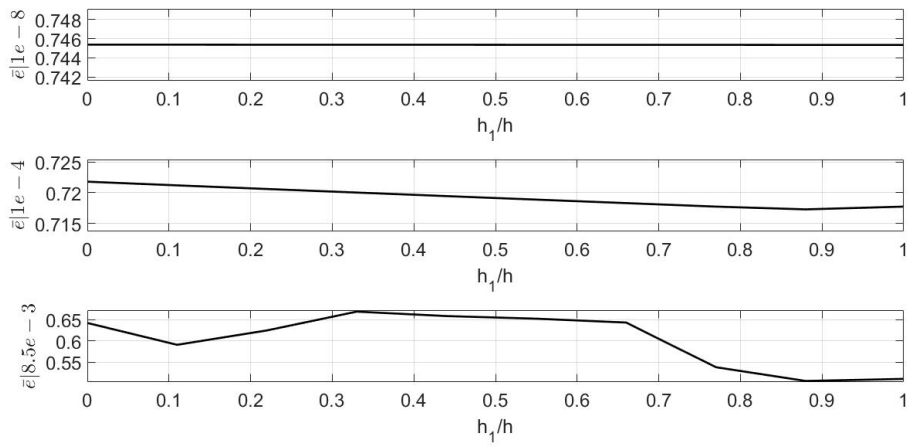**Figure 4.9.** Mean values of $Z\left(t_p\right)$ as a function of h_2/h for the three energy levels

Further correlations can be inferred from the results of the numerical results, which allow correlating the values of the osculating orbital elements to χ_1 and χ_2, indicating the initial conditions corresponding to their extremal values. In particular, it was noticed that the maximum for $\bar{r}_p$ and the minimum $r_a\left(t_p\right)$ correspond to the same condition $\chi_1 = 0$ deg. Another relevant result for the aim of mission design, is related to the inclination, whose maximum and minimum value occur at $\chi_1 = 0$ deg and $\chi_1 = 90$ deg. Converting transformed Hamiltonian coordinates into out of plane position and velocity, the two conditions correspond, respectively, to z^{max} and w^{max}.

In conclusion to this section we can summarize the main results obtained

- β_1 and β_2 are the initial conditions related to the osculating orbital elements a and e, with r_p^{max} and r_p^{min} corresponding to, respectively, $\chi_1 = 45$ deg and $\chi_1 = 0$ deg

- corresponding to high energy levels, β_1 and β_2 have a secondary effect on i, reducing it

- γ_1 and γ_2 are the initial conditions related to the osculating orbital element i, with i^{max} and i^{min} corresponding to, respectively, $\chi_2 = 0$ deg and $\chi_1 = 90$ deg.

These results will be used to develop the guidance strategies aimed at changing the orbital elements at capture, discussed in section 4.3.

4.2.2   The Sun-perturbed Earth-Moon system

The unperturbed model provided some crucial information on the validity of the conjectures proposed in section 4.1. Nevertheless, for an accurate evaluation of the results on the Earth-Moon system, the effects of solar gravitational perturbation should be considered, and these are examined propagating the same initial conditions in section 4.2.1. To be consistent with the results obtained on the capture time in section 3.3.2, the numerical analyses are performed based on the values of the initial angular displacements θ_S. In Table 4.3 the number of impact trajectories for each θ_S and h are reported and it can be noticed that, if compared to the unperturbed results in Table 4.2, the number increases only for the highest energy level. This result can be interpreted after examining Figures 4.10-4.13.

Table 4.3. Number of lunar impact trajectories with time

$h = 1e-8$								
θ_S[deg]	0	45	90	135	180	225	270	315
15 days	0	35	124	87	104	106	124	109
30 days	0	94	124	87	104	106	124	116
60 days	0	123	124	112	104	106	124	124
1 year	124	124	124	124	124	124	124	124
$h = 1e-4$								
θ_S[deg]	0	45	90	135	180	225	270	315
15 days	0	117	71	107	130	121	85	116
30 days	0	117	90	124	130	121	85	122
60 days	0	123	94	127	131	126	108	122
1 year	135	135	135	135	135	135	135	
$h = 8.5e-3$								
θ_S[deg]	0	45	90	135	180	225	270	315
15 days	365	369	355	378	381	375	359	372
30 days	379	390	382	390	387	387	387	390
60 days	386	390	390	390	389	389	390	390
1 year	390	390	390	390	390	390	390	

The results of the perturbation on the variation of the mean values of $\bar{r}_p$ and $i(t_p)$ are shown in Figures 4.10-4.13. It can be noticed that the Sun gravitational pull produces a similar effect on both $\bar{r}_p$ and $i(t_p)$ for $h = 1e-8$, the former is increased up to a factor two and the latter up to one order of magnitude. The behavior is rather more complex for $h = 8.5e-3$, the effect is almost independent from θ_S and, in particular, increases i for $h_2/h < 0.6$ and decreases it for $h_2/h > 0.6$.

The complexity in predicting the effects of the solar gravitational perturbation indicates the need for a more accurate model, capable of including the presence of the Sun in a preliminary phase though providing an equivalently simple representation of the ultimate behavior of orbits, based on their topological location in the equilibrium region. Such a model is presented in chapter 5.
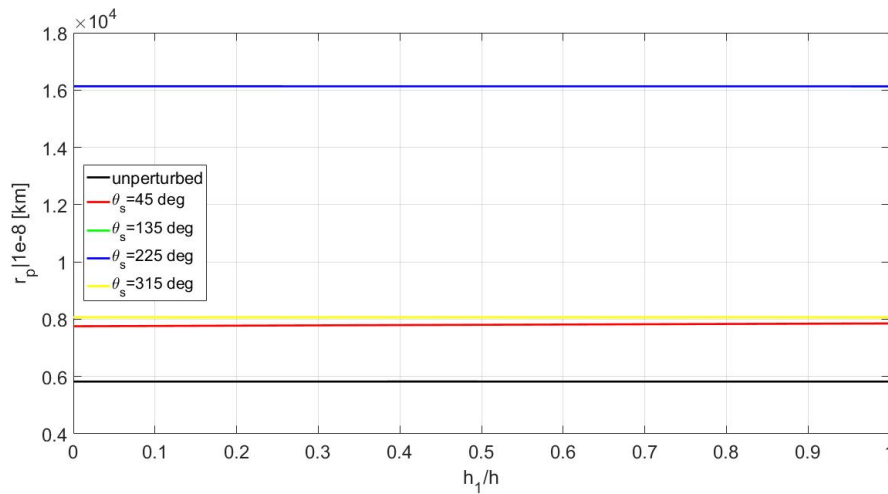

Figure 4.10. Comparison of the mean values of $\bar{r}_p$ as a function of h_1/h and θ_S with $h = 1e-8$
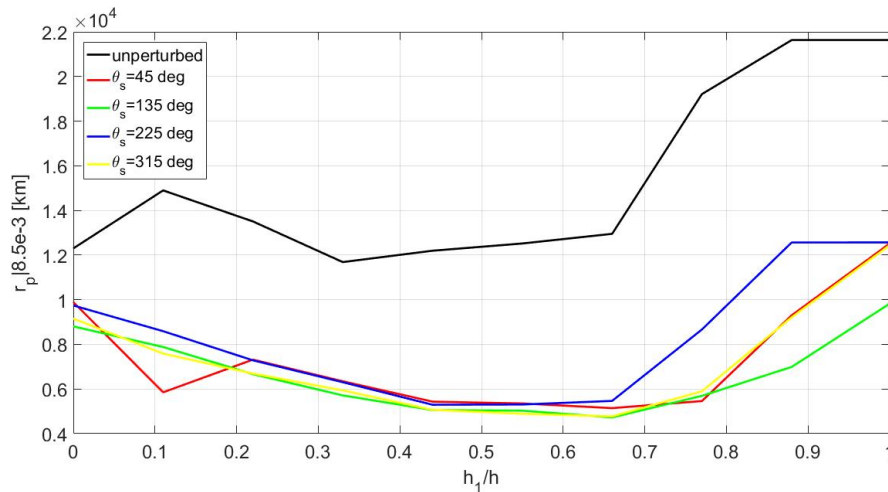

Figure 4.11. Comparison of the mean values of $r_a(t_p)$ as a function of h_1/h and θ_S with $h = 8.5e-3$
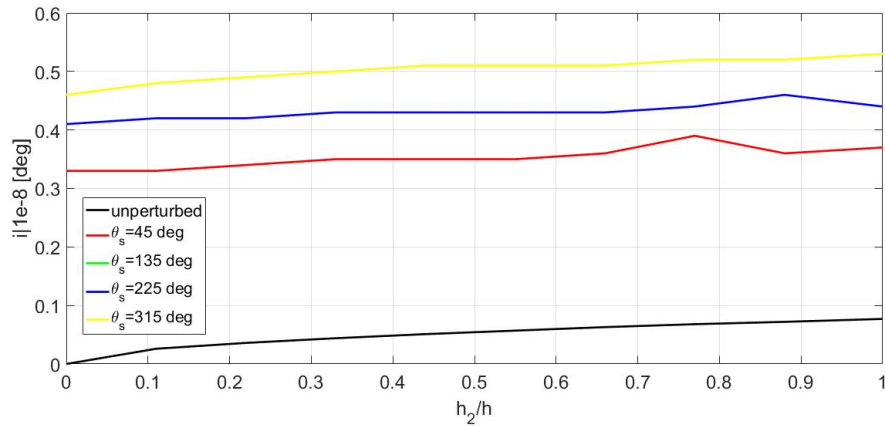
Figure 4.12. Comparison of the mean values of $i(t_p)$ as a function of h_1/h and θ_S with $h = 1e - 8$
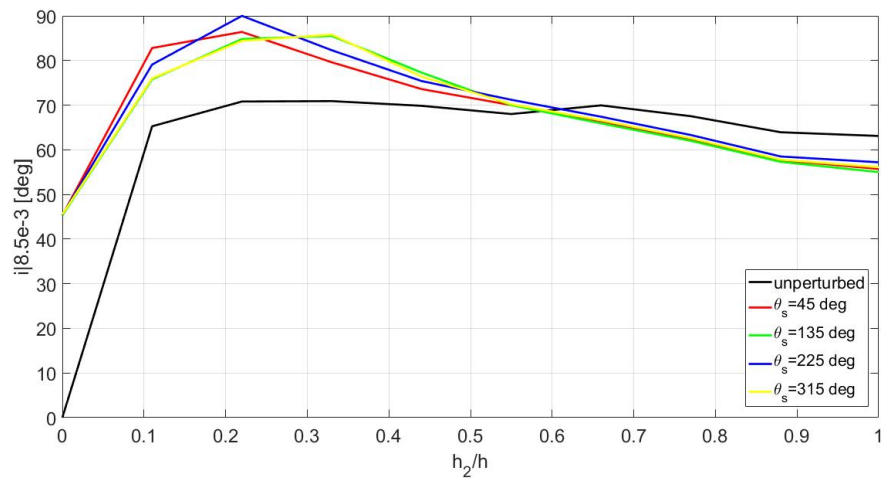

Figure 4.13. Comparison of the mean values of $i(t_p)$ as a function of h_1/h and θ_S with $h = 8.5e - 3$

4.3 A guidance strategy to change the orbital elements at capture

In the previous sections, correlations between the osculating orbital elements at capture and the initial conditions of orbits in the equilibrium region were conjectured and verified by means of numerical analyses. Operating as in section 3.4, the value of the initial conditions β_1, β_2, γ_1 and γ_2 can be modified by thrust acceleration producing adequate changes in the velocity of the spacecraft. A method to adjust the mentioned parameters, is proposed here, aimed at modifying the osculating orbital elements of a capture orbit, with focus on the orbital inclination and the radius at pericenter. The model is verified including also the effects of solar gravitational perturbation.

As indicated by equation 4.9, the inclination at capture depends on the energy level and in particular on the fraction h_2, which can be modified by thrusting along $\hat{z}$ producing a change in the velocity Δw. The value of Δw can be calculated based on equations 2.17 for the out of plane oscillatory motion, rearranged as follows

$$w(t) = \gamma\sqrt{(\gamma_1^2 + \gamma_2^2)}\cos{(\gamma t + \phi)} \tag{4.26}$$

Including equation 4.2 into the previous one leads to

$$w(t) = \gamma\sqrt{\frac{2h_2}{\lambda_2}}\cos{(\gamma t + \phi)} \tag{4.27}$$

Recalling that the inclination can be related to h_2 by equation 4.9, then the Δh_2 necessary to produce the desired change of inclination Δi can be expressed as follows

$$\Delta h_2 = f(i)h_1\cos{\Delta i} \tag{4.28}$$

where the function $f(i)$ can be obtained numerically, from the linear regression of numerical data in sections 4.2.2 and reported below

$$f(i) = (5.48921 \cdot i - 8.44624) \cdot 10^{-6} \tag{4.29}$$

Based on this, the impulsive change of velocity necessary to produce the desired Δi can be determined from equation 4.27

$$\delta w = \gamma\sqrt{\frac{2f(i)h_1\cos{\Delta i}}{\lambda_2}} \tag{4.30}$$

Finally the corresponding mean thrust acceleration can be calculated from the finite increment $a_z = \Delta w/\Delta t$

$$a_z = \frac{\gamma}{\Delta t}\sqrt{\frac{2f(i)h_1\cos{\Delta i}}{\lambda_2}}cos(\phi) = K_z\sqrt{f(i)\cos{\Delta i}} \tag{4.31}$$

where the constant K_z includes the gain of the thruster.

Similarly the value of r_p can be minimized (or maximized) recalling that, according to the results in section 4.2.1, the corresponding initial condition is characterized

by $\chi_1 = 45$ deg ($\chi_1 = 0$ deg). Given a trajectory crossing the equilibrium region, it is possible to provide a Δv (or Δu) producing a variation of β_1 verifying $\chi_1 = 45$ (see equation 4.20). If the use of continuous thrusters is considered again, the acceleration to be provided to obtain the required Δv, can be calculated applying the mentioned conditions to equation 2.18

$$a_y = \frac{k_y}{\Delta t} \left(-\frac{\left(1 + 2\lambda_2^2\right)\left(\lambda_2^2 - 1 - L_{1,x}\right)}{\lambda_1 \tau} + \frac{\left(\lambda_2^2 - 1\right) y}{\lambda_1} + \frac{u}{\tau} - -v \right) \qquad (4.32)$$

The suitability of equations 4.31 and 4.32 is verified by applying them [4] to increase the inclination and reducing the radius at pericenter of a capture orbit characterized by $h = 1e-3$ corresponding to $C = 1.18273$) and $h_2 = 0$. The trajectory, sketched in Figure 4.9 for the $\theta_S = 0$, enters the equilibrium region from m_1 and crosses it heading to m_2, with $\alpha_2 = 0$. Except for the mentioned ones, all the initial conditions were selected randomly, according to the methods and constraints discussed in section 4.2. The inclination and radius at pericenter of the capture orbit for different θ_S are reported in table 4.4
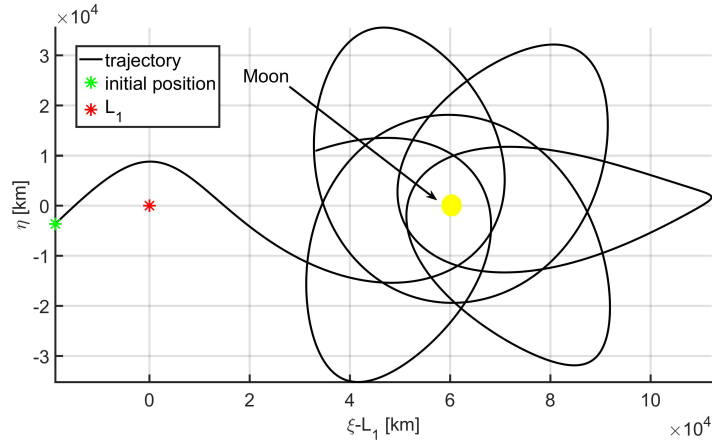

Figure 4.14. Projection onto the $\left[\hat{\xi}, \hat{\eta}\right]$ plane of the initial capture trajectory for $h = 1e-3$ and $\theta_S = 0$ deg.

---

[4] As in section 3.4, the accelerations are converted to the Hamiltonian components and integrated with system 2.22.

Table 4.4. Values of $i(t_p)$ and $\bar{r}_p$ for the ballistic capture orbit

θ_S [deg]	i [deg]	r_p [km]
0	0.21	7565
45	0.18	10013
90	0.19	8143
135	0.25	6107
180	0.34	7077
225	0.30	9653
270	0.28	9166
315	0.30	6495

The resulting changes on i and r_p for three different test cases, characterized by the energy provded, are reported in Tables 4.5 and 4.6. The results indicate that the Δw required by the out of plane maneuver for a marked Δi can be considerably larger than the corresponding Δv required to minimize $\bar{r}_p$.

Table 4.5. Δi and corresponding Δw with θ_S

$\Delta h_2 \rightarrow$ $\downarrow \theta_S$ [deg]	3.11e-5 Δi [deg] $\mid \Delta w$ $\left[\frac{m}{sec}\right]$	1.32e-4 Δi [deg] $\mid \Delta w$ $\left[\frac{m}{sec}\right]$	3.9e-4 Δi [deg] $\mid \Delta w$ $\left[\frac{m}{sec}\right]$
0	6.31 | 18.45	25.42 | 78.79	71.61 | 236.46
45	5.96 | 20.00	25.42 | 78.79	71.65 | 260.31
90	6.40 | 20.89	25.12 | 89.41	67.90 | 265.69
135	7.08 | 19.32	27.41 | 89.55	72.60 | 249.17
180	6.81 | 18.32	26.51 | 78.22	70.90 | 234.52
225	6.13 | 19.33	24.22 | 82.64	75.36 | 249.90
270	6.09 | 20.91	24.34 | 89.52	72.80 | 266.04
315	6.54 | 19.96	26.52 | 85.33	75.61 | 259.13

Table 4.6. r_p and corresponding Δv with θ_S

$K_y \rightarrow$ $\downarrow \theta_S$ [deg]	1e-3 r_p [km] $\mid \Delta v$ $\left[\frac{m}{sec}\right]$	2e-3 r_p [km] $\mid \Delta v$ $\left[\frac{m}{sec}\right]$	2.5e-3 r_p [km] $\mid \Delta v$ $\left[\frac{m}{sec}\right]$
0	4763 | 31.19	3295 | 55.24	2804 | 62.01
45	5083 | 33.83	3252 | 57.17	2696 | 66.36
90	3897 | 34.66	2342 | 58.34	1872 | 67.62
135	6441 | 31.92	2226 | 57.28	1833 | 63.14
180	4342 | 30.75	3011 | 52.56	2561 | 61.25
225	5207 | 32.85	3448 | 55.72	2891 | 64.77
270	4347 | 34.90	2635 | 57.70	2131 | 68.02
315	3431 | 32.96	2142 | 55.83	1790 | 64.85

It is worth noting that the values of ΔV in Tables 4.5 and 4.6 are remarkably higher than those reported in Table 3.5 to produce permanent capture. In particular, the maximum value $\Delta w^{max} = 266.04$ m/sec is associated to a $\Delta i = 72.8$ deg for $\theta_S = 270$ deg. Considering that $t_{c,0} = 1$ day is the time required to cross the equilibrium region, then the mean acceleration required is equal to

$$a_z^{max} = \frac{\Delta w^{max}}{1 day} \approx 3.08e-3 \quad m/sec^2$$

As discussed in section 3.4, the corresponding value of the thrust required for the maneuver can be calculated considering a typical 6U CubeSat aimed at solar system exploration, with mass $m_{CS} = 15$ kg.

$$F_z^{max} = m_{CS} a_z^{max} \approx 4.62e-2 \quad N$$

Similarly, the maximum acceleration and thrust required to minimize $\bar{r}_p$, for the ($\Delta v^{max} = 68.02$ m/sec and $\theta_S = 270$ deg, corresponding to an altitude of about 340 km from the lunar surface, are calculated and reported below

$$a_y^{max} = \frac{\Delta v^{max}}{1 day} \approx 7.87e-4 \quad m/sec^2$$

$$F_z^{max} = m_{CS} a_z^{max} \approx 1.18e-2 \quad N$$

The maximum values for the thrust, required by the guidance strategies proposed (capture, minimization of r_p and change of inclination) are reported in Table 4.7.

Table 4.7. Maximum thrust [N] required by a 15 kg CubeSat for the guidance strategies

capture	minimum r_p	Δi
$F_x = 2.48e-4 \mid F_y = 3.35e-5$	$F_y = 1.18e-2$	$F_z = 4.62e-2$

The maximum thrust and corresponding ΔV provided by some commercial thrusters [4, 21, 22, 32] are reported in Table 4.8. All the devices are compatible with the requirements of the capture strategy, but only one of is suitable to perform the other strategies in the worst case examined, and it is the BGT-X1 green monopropellant thruster [22]. A point should be stressed here, the worst case referred to in this analysis is definitely extreme, in fact corrections such as $\Delta i = 72.8$ deg and $\Delta r_p = 7035$ km are not typically required by ordinary mission corrections. In this perspective, the use of ion thrusters, and in particular RIT 10 EVO [4], is suitable for ordinary mission profiles, in which Δi of few degrees and Δr_p of a few kilometers are required.

Table 4.8. Properties of some commercial thrusters compatible with a 6U and 15 kg CubeSat

|	RIT 10 EVO [4]	BIT-1 [21]	BIT-3[21]	BGT-X1 [22]	IFM Nano [32]
Max thrust [N]	5e-3	1.85e-4	1.15e-3	0.1	5e-4
Power [W]	50	8	75	4.5	40
Total mass [kg]	1.8	0.75	1.5	1.5	0.87
Volume [U][5]	2	1	2	1	1
Max ΔV [m/sec]	28.8	1.07	6.62	576	2.88

For the sake of completeness, the Δv and Δw required for the worst cases in Tables 4.5 and 4.6 are compared with those required to perform the same maneuver using a "traditional" single impulse approach. The minimum impulse $\Delta w|_{imp}^{min}$ required for a change of inclination $\Delta i = 72.80$ deg can be calculated as follows

$$\Delta w|_{imp}^{min} = \sqrt{\frac{2Gm_2}{R_2^{max}} \left(1 - \cos \Delta i\right)} \approx 324 \quad m/sec \tag{4.33}$$

The minimum impulse $\Delta v|_{imp}^{min}$ required to reduce the radius at pericenter from $r_{p,0} = 9166$ km to $r_{p,f} = 2131$ km is given by the following equation

$$\Delta v|_{imp}^{min} = \sqrt{Gm_2 \left[\left(\frac{2}{r_{p,f}} - \frac{1}{r_{p,f} + r_{a,f}}\right) - \left(\frac{2}{r_{p,0}} - \frac{1}{r_{p,0} + r_{a,0}}\right)\right]} \approx 198 \quad m/sec \tag{4.34}$$

Both the impulsive changes of velocity are sensibly higher than those obtained from continuous thrust, with difference in Δw and Δv equal to, respectively, 58 m/sec and 130 m/sec. The result confirms the validity of the guidance strategies as suitable alternative solutions. The orbit produced by applying both Δw^{max} and Δv^{max} is represented in Figure 4.15, showing notable differences with with respect to initial one, in Figure 4.14.
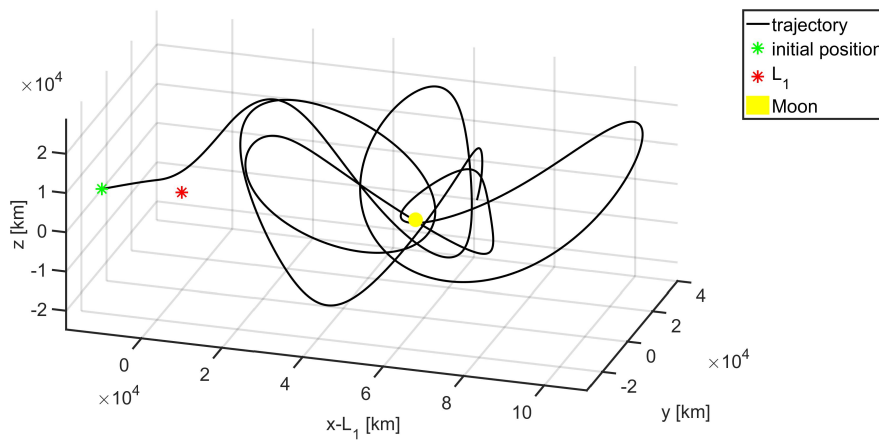
Figure 4.15. A sketch of the resulting capture orbit with $i = 72$ deg and $h_p = 340$ km

In this chapter, as in Section 3.4, guidance strategies were proposed to drive the satellite into the desired capture orbit. To perform such maneuvers, knowledge regarding the state of the spacecraft, namely its position and velocity, is necessary. This task is achieved by means of a navigation system which operates in synergy with the guidance actuators. An analysis of navigation strategies is beyond the scope of this work, which assumes the state to be known, nevertheless some indications are worth to be outlined. Studies in the field indicate that navigation accuracy below 100 meters in position and 0.1 cm/sec in velocity might be required, and this could be achieved by using radio telescopes on-ground and X-band antenna on-board [158]. To guarantee communication between the satellite and the ground station, regardless of its attitude, omnidirectional coverage is needed, thus a minimum of two patched antennas. Due to power limitations, the satellite might not be able to communicate during some phases, such as maneuvering. Therefore an inertial measurement unit capable to update the state of the spacecraft based on the last data received and the measurements from the on-board devices (three-axis accelerometers and gyroscopes) would be required.

Chapter 5

Design of low-energy trajectories in the Elliptic Restricted 4-Body Problem

Internal low-energy trajectories have been investigated extensively in the previous chapters, developing a method for the systematic selection of the initial conditions corresponding to transit trajectories and capture orbits. These methods led the design of guidance strategies aimed at producing powered permanent capture and modifying the orbital elements at capture, in particular allowing adjustment on the inclination and radius at peri- or apocenter.

As emerged in sections 3.3 and 4.2.2, the effects of the solar gravitational perturbation can be as relevant to alter the behavior of the flow in the equilibrium region and, consequently, the ultimate behavior of orbits. This result is substantiated by several mission-oriented works, indicating that real missions may require more accurate models, not only because of the gravitational perturbations but also because the orbits of the primaries are not circular [1, 64, 65, 68, 91]. In fact, final trajectories are typically calculated after a long iterative process, which consists in the numerical integration of the nonlinear equations of motion using refined models and the results from the CR3BP as initial guess.

A significant improvement in mission design should be driven by the development of tools which include the effects of the mentioned perturbations though providing a compact description similar to that obtained for the CR3BP. This result is achieved here in the dynamical framework of the spatial Elliptic Restricted 4-Body Problem (ER4BP). In particular, the model is developed based on a theorem by Conley and Easton [30], stating that the basic topological properties of the phase space flow of the CR3BP are persistent in the presence of perturbations. It follows that a representation of the ER4BP dynamics equivalent to the phase space description of the CR3BP can be developed when the effects of the eccentricity and the gravitational pull of the fourth body are not prominent.

A topological characterization of internal low-energy trajectories in the ER4BP, equivalent to that discussed for the CR3BP, is achieved using the Hamiltonian formalism and applying canonical transformations to reduce the Hamiltonian function for the ER4BP to a form equivalent to that of the CR3BP. In this way, the accuracy

of the ER4BP is preserved, while its complexity is addressed to the coordinate transformation only. In this new model, the guidance strategies discussed in chapters 3.4 and 4.3 can be still applied, and powered permanent capture and adjustment of the orbital elements at capture can be performed [24, 25, 26]. The model is verified by means of numerical analyses on the Sun-Earth-Moon system, proving that a systematic selection of initial conditions can still lead to the design of capture orbits, and on the Jupiter-Europa-Io system, in which the initial conditions can be selected to take advantage of the effects of orbital resonance on quasi-periodic orbits.

5.1   A dynamical model for the Sun-Earth-Moon system

Low-energy trajectories are here investigated in the dynamical framework of the ER4BP, consisting of three primaries of masses $m_1 > m_2 > m_3$ and the spacecraft, whose mass m is negligible if compared to the others. The 4-body system is studied under the hypotheses that the spheres of influence of the primares are "nested" and in particular

- m_2 and m_3 form a binary system, with center of mass O_b under the gravitational pull of the primary m_1

- m_3 orbits m_2 along a Keplerian orbit with semimajor axis a_b and eccentricity e_b

- the relative motion of O_b and m_1 with respect to the center of mass O of the whole system represents a Keplerian orbit with semimajor axis a and eccentricity e

- the orbital plane of the binary system and that of m_1 and O_b are tilted of an angle ϵ.

Such a model is suitable to describe the Sun-Earth-Moon system.
A sketch of the system is shown in Figure 5.1, where the distances $m_1 - O$, $O_b - O$, $m_2 - O_b$ and $m_3 - O_b$ are indicated as A_1, A_2, a_1 and a_2 and can be calculated based on the definition of center of mass and noting that $A_1 + A_2 = a$ and $a_1 + a_2 = a_b$, producing the following result

$$\begin{cases} A_1(t) = \frac{(m_2+m_3)R(t)}{M} \\ A_2(t) = \frac{m_1 R(t)}{M} \end{cases} \tag{5.1}$$

$$\begin{cases} a_1(t) = \frac{m_3 R_b(t)}{M-m_1} \\ a_2(t) = \frac{m_2 R_b(t)}{M-m_1 M} \end{cases} \tag{5.2}$$

with $M = \sum_{i=1}^{3} m_i$, $R = \frac{a\left(1-e^2\right)}{(1+e\cos\theta)}$, $R_b = \frac{a_b\left(1-e_b^2\right)}{(1+e_b\cos\theta_b)}$ where θ and θ_b indicate the true anomaly of m_1 and that of m_2.
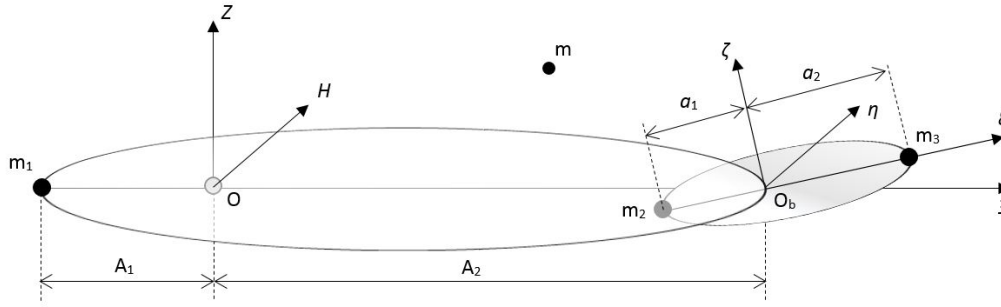
Figure 5.1. Sketch of the 4-body system

The dynamic equations of motion for m can be written in an inertial reference frame $\left[\hat{\Xi}, \hat{H}, \hat{Z}\right]$, centered in O with $\hat{\Xi}$ pointing from m_1 to O_b at the initial time t_0, $\hat{Z}$ parallel to the angular momentum vector of the (m_1, O_b) system and $\hat{H}$ completing the rectangular reference frame

$$\begin{cases} \ddot{\Xi} = -G\{\frac{m_1[\Xi-Xi_1(\theta)]}{R_1^3} + \frac{m_2[\Xi-Xi_2(\theta,\theta_b)]}{R_2^3} + \frac{m_3[\Xi-Xi_3(\theta,\theta_b)]}{R_3^3}\} \\ \ddot{H} = -G\{\frac{m_1[H-H_1(\theta)]}{R_1^3} + \frac{m_2[H-H_2(\theta,\theta_b)]}{R_2^3} + \frac{m_3[H-H_3(\theta,\theta_b)]}{R_3^3}\} \\ \ddot{Z} = -G\{\frac{m_1[Z-Z_1(\theta)]}{R_1^3} + \frac{m_2[Z-Z_2(\theta,\theta_b)]}{R_2^3} + \frac{m_3[Z-Z_3(\theta,\theta_b)]}{R_3^3}\} \end{cases} \tag{5.3}$$

where (Ξ_i, H_i, Z_i) indicate the coordinates of the i-th primary, and R_i indicates the distance between m and the i-th primary. System 5.3 can be rearranged in a reference frame $\left[\hat{\xi}, \hat{\eta}, \hat{\zeta}\right]$, centered in O_b with $\hat{\xi}$ pointing from m_2 to m_3, $\hat{\zeta}$ parallel to the angular momentum vector of the binary system and $\hat{\eta}$ orthogonal to the others. It is worth noting that such a reference frame rotates rigidly with the primaries in the binary system at the angular velocity $\dot{\theta}_b$. The system is studied considering an initial position of the primaries such that $\hat{\xi}$ and $\hat{\eta}$ are parallel to, respectively $\hat{\Xi}$ and $\hat{H}$[1]. The rotating frame can be transformed into the inertial one by the following sequence of transformations

1. a rotation $\mathcal{R}_2\left(\epsilon\right)$ about $\hat{\eta}$, rotating $\hat{\zeta}$ parallel to $\hat{Z}$ and producing the frame $\left[\hat{\xi}', \hat{\eta}', \hat{Z}\right]$

2. a rotation $\mathcal{R}_3\left(\theta - \theta_b\right)$ about $\hat{Z}$, rotating $\hat{\xi}$ parallel to $R(t)$ and producing the frame $\left[\hat{\xi}'', \hat{\eta}'', \hat{Z}\right]$

3. a translation along $\hat{\xi}''$ from O_b to O and producing the frame $\left[\hat{X}, \hat{Y}, \hat{Z}\right]$

4. a rotation $\mathcal{R}_3\left(\theta\right)$ about $\hat{Z}$, producing $\left[\hat{\Xi}, \hat{H}, \hat{Z}\right]$ by rotating $\hat{\xi}'''$ and $\hat{\eta}'''$ parallel to, respectively, $\hat{\Xi}$ and $\hat{H}$.

---

[1]It is worth noting that this hypothesis does not cause any loss of generality and is selected only to provide a simpler representation.

The equations for the transformation are given below

$$\begin{cases} \Xi = X \cos\theta - Y \sin\theta \\ H = X \sin\theta + Y \cos\theta \\ Z = \xi \cos\epsilon + \zeta \cos\epsilon \end{cases} \tag{5.4}$$

with

$$\begin{cases} X = A_2(t) + \xi \cos\beta \cos\epsilon + eta \sin\beta - \zeta \cos\beta \sin\epsilon \\ Y = -\xi \sin\beta \cos\epsilon + eta \cos\beta + \zeta \sin\beta \sin\epsilon \end{cases}$$

where $\beta = \theta_b - \theta$.

The coordinates of the primaries in the binary system can be easily determined from Figure 5.1 and correspond to $\mathbf{P}_2 = (-a_1, 0, 0)$ and $\mathbf{P}_3 = (a_2, 0, 0)$. Transformation 5.4 can be applied to express $\mathbf{P}_2$ and $\mathbf{P}_3$ in the inertial coordinates, obtaining

$$\begin{cases} \Xi_2 = \cos\theta \left(A_1 - a_1 \cos\beta \cos\epsilon \right) + a_1 \sin\beta \sin\theta \cos\epsilon \\ H_2 = \sin\theta \left(A_2 - a_1 \cos\beta \cos\epsilon \right) + a_1 \sin\beta \cos\theta \cos\epsilon \\ Z_2 = -a_1 \sin\epsilon \end{cases} \tag{5.5}$$

$$\begin{cases} \Xi_3 = \cos\theta \left(A_2 + a_2 \cos\beta \cos\epsilon \right) + a_2 \sin\beta \sin\theta \cos\epsilon \\ H_3 = \cos\theta \left(A_2 + a_2 \cos\beta \cos\epsilon \right) + a_2 \sin\beta \sin\theta \cos\epsilon \\ Z_3 = a_2 \sin\epsilon \end{cases} \tag{5.6}$$

Similarly, the coordinates of m_1 in the inertial frame are simply given by $\mathbf{P}_1 = (-A_1 \cos\theta, -A_1 \sin\theta, 0)$, and can be converted to rotating ones from equation 5.4, obtaining

$$\begin{cases} \xi_1 = -A \cos\beta \cos\epsilon \\ \eta_1 = -A \sin\beta \\ \zeta_1 = A \cos\beta \sin\epsilon \end{cases} \tag{5.7}$$

Introducing equations 5.5-5.6 into system 5.3 allows representing the dynamics in the rotating frame coordinates

$$\begin{cases} \ddot{X} = \ddot{\theta}Y + 2\dot{\theta}\dot{Y} + \dot{\theta}^2 X + \frac{\partial \mathcal{V}}{\partial X} \\ \ddot{Y} = -\ddot{\theta}X + -\dot{\theta}\dot{X} + \dot{\theta}^2 Y + \frac{\partial \mathcal{V}}{\partial Y} \\ \ddot{Z} = \frac{\partial \mathcal{V}}{\partial Z} \end{cases} \tag{5.8}$$

with $\mathcal{V} = G \sum_{i=1}^{3} m_i / R_i$. Introducing the units of distance, mass and time reported below

$$\begin{cases} DU = R(t) \\ MU = M \\ TU = \sqrt{\frac{R(t)^3}{GM}} \end{cases} \tag{5.9}$$

The position of the primaries can be expressed in dimensionless coordinates

$$\begin{cases} x_1 = \mu_1 - 1 \\ y_1 = 0 \\ z_1 = 0 \end{cases} \tag{5.10}$$

$$\begin{cases} x_2 = \mu_1 - \frac{\mu_3 \cos\beta \cos\epsilon R_b(t)}{(1-\mu_1)R(t)} \\ y_2 = \frac{\mu_3 \sin\beta \cos\epsilon R_b(t)}{(1-\mu_1)R(t)} \\ z_2 = -\frac{\mu_3 \sin\epsilon R_b(t)}{(1-\mu_1)R(t)} \end{cases} \tag{5.11}$$

$$\begin{cases} x_3 = \mu_1 + \frac{\mu_2 \cos\beta \cos\epsilon R_b(t)}{(1-\mu_1)R(t)} \\ y_3 = -\frac{\mu_2 \sin\beta \cos\epsilon R_b(t)}{(1-\mu_1)R(t)} \\ z_3 = \frac{\mu_2 \sin\epsilon R_b(t)}{(1-\mu_1)R(t)} \end{cases} \tag{5.12}$$

with $\mu_i = \frac{m_i}{M}$. Equivalently, system 5.8 can be rearranged in the dimensionless form given below

$$\begin{cases} x' = u \\ y' = v \\ z' = w' \\ u' = 2v + K(\theta)\left(\frac{\partial \mathcal{V}}{\partial x} + x\right) \\ v' = -2u + K(\theta)\left(\frac{\partial \mathcal{V}}{\partial y} + y\right) \\ w' = K(\theta)\left(\frac{\partial \mathcal{V}}{\partial z} + z\right) - z \end{cases} \tag{5.13}$$

where the time derivative is replaced by the derivative in θ, indicated by the apostrophe $'$, $K(\theta) = \frac{1}{1+e\cos\theta}$ and $\upsilon = \sum_{i=1}^{3} \frac{\mu_i}{r_i}$.

The dependence of the ER4BP on θ (or equivalently on time) does not allow defining any equilibrium point. In fact, trying to calculate an integral of motion analogous to the Jacobi constant (see equations 2.6-2.8) produces the following equation

$$x''x' + y''y' + z''z' = K(\theta)\left[\frac{\partial \upsilon}{\partial x}x' + \frac{\partial \upsilon}{\partial y}y' + \frac{\partial \upsilon}{\partial z}z' + x'x + y'y + z'z\right] =$$

$$= x''x' + y''y' + z''z' = K(\theta)\left[\frac{\partial \upsilon}{\partial \theta} + x'x + y'y + z'z\right] \tag{5.14}$$

It can be noticed that the right hand side of equation 5.14 can not be integrated, as clarified by the extended expression below

$$\int_{\theta_0=0}^{\theta} (x''x' + y''y' + z''z')\, d\theta = \int_{\theta_0=0}^{\theta} K(\theta)\left[\frac{\partial \upsilon}{\partial \theta} + x'x + y'y + z'z\right] d\theta =$$

$$= K(\theta)\left[\upsilon + \frac{1}{2}\left(x^2 + y^2 + z^2\right)\right] - \int_{\theta_0=0}^{\theta} K(\theta)'\left[\upsilon + \frac{1}{2}\left(x^2 + y^2 + z^2\right)\right] d\theta \rightarrow$$

$$\rightarrow \frac{1}{2}\left(x'^2 + y'^2 + z'^2\right) + \frac{z^2}{2} =$$

$$= K(\theta)\left[\upsilon + \frac{1}{2}\left(x^2 + y^2 + z^2\right)\right] - \int_{\theta_0=0}^{\theta} K(\theta)'\left[\upsilon + \frac{1}{2}\left(x^2 + y^2 + z^2\right)\right] d\theta \tag{5.15}$$

In particular, the last term on the right hand side of equation 5.15 depends on the system dynamics 5.13, whose analytic solution is not known, therefore it can not be evaluated analytically. Because neither an integral of motion nor the equilibrium points exist for the ER4BP, further processing is required to define a flow equivalent to that for the linear CR3BP dynamics in the equilibrium region. This process is described in detail in section 5.2.

5.2   Hamiltonian formalism and normal forms

System 5.13 can be expressed using the Hamiltonian formalism

$$
\begin{cases} \mathbf{q}' = \frac{\partial H}{\partial \mathbf{p}'} \\ \mathbf{p}' = -\frac{\partial H}{\partial \mathbf{q}'} \end{cases} \tag{5.16}
$$

where the Hamiltonian function can be determined including the conjugate positions $[q_1, q_2, q_3] = [x, y, z]$ and momenta $[p_1, p_2, p_3] = [u - y, v + x, w]$ into equation 5.13

$$
H = \frac{1}{2}\left(q_1^2 + q_2^2 + p_1^2 + p_2^2 + p_3^2 + 2p_1 q_2 - 2p_2 q_1\right) + \frac{q_3^2}{2} - K(\theta)\left[\sum_{i=1}^{3}\frac{\mu_i}{r_i} + \frac{1}{2}\left(q_1^2 + q_2^2 + q_3^2\right)\right] \tag{5.17}
$$

where $r_i = \sqrt{\sum_{i,j=1}^{3}\left(q_j - q_{j,i}\right)^2} = \rho^{\frac{1}{2}}$ represents the distance between the spacecraft and the i-th primary of coordinates $(q_{1,i}, q_{2,i}, q_{3,i})$.

A form of equation 5.17 equivalent to the linear Hamiltonian for the CR3BP 2.33 can be developed, allowing extending the results of the topological analysis based on the Siegel-Moser representation, discussed in sections 2.4 and 3.1. A first step consists in isolating the terms associated to the perturbations (the eccentricities and the gravitational energy of the fourth body), expanding in power series the non-polynomial terms of equation 5.17. It is worth highlighting that for μ_1/r_1 to be considered as a perturbation its value must be small, therefore the motion of m must be investigated far from m_1 [2]. An example of such a scenario is represented by Earth-Moon internal low-energy trajectories in the Sun-Earth-Moon system.

Indicating with $F(e, e_b, \mu_1/a)$ the non-polynomial terms in equation 5.17, the expansion produces the following expression

$$
F\left(e, e_b, \mu_1/a\right) = K\left(\theta\right)\left[\sum_{i=1}^{3}\frac{\mu_i}{r_i} + \frac{1}{2}\left(q_1^2 + q_2^2 + q_3^2\right)\right] =
$$

$$
= F^{\star} + \left[e\frac{\partial F}{\partial e} + e_b\frac{\partial F}{\partial e_b} + \frac{\mu_1}{a}\frac{\partial F}{\partial\left(\mu_1/a\right)} + o(e, e_b, \mu_1/a)\right] \tag{5.18}
$$

where the symbol $\star$ identifies the function evaluated at the point of linearization ($e = e_b = \mu_1/a = 0$) and, for the sake of simplicity, the term μ_1/r_1 was replaced by the parameter , based on the fact that $r_1 \approx a$ for the scenario examined here.

For the sake of compactness, the expanded expression of the terms in equation 5.18 is reported in the appendix, except for the first one whose formulation is straightforward

$$
F^{\star} = \frac{\mu_2}{r_2^{\star}} + \frac{\mu_3}{r_3^{\star}} + \frac{1}{2}\left(q_1^2 + q_2^2 + q_3^2\right) \tag{5.19}
$$

with

$$
\frac{\mu_2}{r_2^{\star}} = \frac{\mu_2}{\sqrt{\left(q_1 + \mu\right)^2 + q_2^2 + q_3^2}}
$$

---

[2]Similar results can be obtained for any other primary, following the same procedure described below.

$$\frac{\mu_3}{r_3^\star} = \frac{\mu_2}{\sqrt{(q_1 - 1 + \mu)^2 + q_2^2 + q_3^2}}$$

$$\mu = \frac{m_3}{m_2 + m_3}$$

Including equations 5.18 and 5.19 into equation 5.17 results in the expression below

$$H = \frac{1}{2}\left(p_1^2 + p_2^2 + p_3^2 + 2p_1q_2 - 2p_2q_1\right) - \frac{\mu_2}{r_2^\star} - \frac{\mu_3}{r_3^\star} +$$

$$- \left[e\frac{\partial F}{\partial e} + e_b\frac{\partial F}{\partial e_b} + \frac{\mu_1}{a}\frac{\partial F}{\partial (\mu_1/a)} + o(e, e_b, \mu_1/a)\right] \tag{5.20}$$

Comparing equation 5.20 to 2.21, it can be noticed that the terms in the square brackets of equation 5.20 represent a perturbation. Therefore, based on a theorem by Conley and Easton which proves the robustness of the linear CR3BP topological properties with respect to small perturbations [30], equation 5.20 can be linearized with respect to the collinear libration point L_1 or L_2. The selection of the rotating frames for the 3-body and the 4-body system is such that, in the dimensional form, the coordinates of the mentioned points are the same for both the models. The linear Hamiltonian for the ER4BP is reported below (see appendixes B and C)

$$H_2 = \frac{1}{2}\left(p_1^2 + p_2^2 + p_3^2 + 2p_1q_2 - 2p_2\tilde{q}_1\right) - K\left(\tilde{q}_1^2 - \frac{q_2^2}{2} - \frac{q_3^2}{2}\right)$$

$$-e\cos\theta\left[D_1\left(\tilde{q}_1^2 - \frac{q_2^2}{2} - \frac{q_3^2}{2}\right) + \frac{1}{2}\left(\tilde{q}_1^2 + q_2^2 + q_3^2\right) + D_2\left(\tilde{q}_1\cos\beta\cos\epsilon - q_2\sin\beta\cos\epsilon + q_3\sin\epsilon\right)\right] +$$

$$-e\cos\theta\left[D_3\left(\tilde{q}_1^2 - \frac{5q_2^2}{2} - \frac{5q_3^2}{2}\right)\right] - e_b\left[D_4\left(\tilde{q}_1\cos\beta\cos\epsilon - q_2\sin\beta\cos\epsilon + q_3\sin\epsilon\right) + D_5\right] +$$

$$-\frac{\mu_1}{a}\left[D_6\left(\tilde{q}_1\cos\beta\cos\epsilon - q_2\sin\beta\cos\epsilon + q_3\sin\epsilon\right) + D_7 + D_8\left(\tilde{q}_1^2 - \frac{5q_2^2}{2} - \frac{5q_3^2}{2}\right)\right] = h \tag{5.21}$$

where $K = \left(\frac{1-\mu}{|L_{i,x}+\mu|^3} + \frac{\mu}{|L_{i,x}-1+\mu|^3}\right)$ and the value of the coefficients D_i is reported in Appendix C.

The perturbation terms can be absorbed by a canonical transformation $(\mathbf{q}, \mathbf{p}, \theta_b, \theta) \rightarrow (\mathbf{Q}, \mathbf{P})$, producing the transformed linear Hamiltonian function having the same form as equation 2.23.

$$H_2(\mathbf{Q}, \mathbf{P}) = H(\mathbf{q}, \mathbf{p}, \theta_b, \theta) + \frac{\partial S}{\partial(\theta_b - \theta)}\frac{\partial(\theta_b - \theta)}{\partial\theta} + \frac{\partial S}{\partial\theta} + o(e, e_b, \mu_1/a) \tag{5.22}$$

The form in equation 5.22 is achieved by introducing a generating function $S(\mathbf{q}, \mathbf{p}, \theta_b, \theta)$ such that

$$\begin{cases} \mathbf{p} = \frac{\partial S}{\partial \mathbf{q}} \\ \mathbf{Q} = \frac{\partial S}{\partial \mathbf{P}} \end{cases} \tag{5.23}$$

For the sake of compactness, the transformation is detailed in Appendix D, considering here only the result, given below

$$H_2 = \frac{1}{2}\left(P_1^2 + P_2^2 + P_3^2\right) + P_1Q_2 - P_2Q_1 - K\left(Q_1^2 - \frac{1}{2}Q_2^2 - \frac{1}{2}Q_3^2\right) = h \tag{5.24}$$

The Hamiltonian function expressed by equation 5.24, provides a description of the ER4BP dynamics equivalent to that of the linear CR3BP dynamics. It follows that transformation 2.31 can be applied, producing a description in the Siegel-Moser variables, reported below

$$H_2 = \rho x_1 y_1 + \frac{\lambda_1}{2} \left(x_2^2 + y_2^2 \right) + \frac{\lambda_2}{2} \left(x_3^2 + y_3^2 \right) = h$$

The result obtained in this section, substantiating Conely and Easton theorem [30], can be interpreted referring to lunar capture orbits. In particular, initial conditions corresponding to capture orbits for the (unperturbed) Earth-Moon system, selected as discussed in section 3.2, can be converted into initial conditions corresponding to capture orbits for the ER4BP, by applying the canonical transformation defined by the generating function 5.23. This result is confirmed in the next section by means of numerical analysis.

5.3   Ballistic capture in the Sun-Earth-Moon system

In chapter 3, a model aimed at predicting the ultimate behavior of internal low-energy trajectories, based on their topological properties when crossing the equilibrium region, was developed. The model was verified by means of numerical analyses, proving its suitability for the unperturbed CR3BP and lacking of accuracy when relevant fourth body perturbation is considered. According to the result in section 5.2, a canonical transformation can be defined such that the initial conditions determined for the CR3BP can be converted into initial conditions for the ER4BP preserving the topological properties characterizing them. It follows that, propagating these initial conditions in the ER4BP produces trajectories whose ultimate behavior is equivalent to that of the corresponding trajectory calculated for the CR3BP. Such a result is here verified by means of numerical analysis on the Sun-Earth-Moon system.

The initial conditions selected in section 3.2 are transformed according to equation 5.23 and propagated using the full nonlinear equations of motion for the ER4BP 5.13. The process is performed using Matlab *ode113* function, setting a fixed time step of $t_k = 15/100000 \approx 4730 sec$ and relative and absolute tolerances equal to, respectively, 1e-18 and 1e-19. Both the stop conditions and the simulation parameters (see Table 3.1) are the same as in section 3.2, to allow a comparison of the results. The mass of the Sun is set to $m_1 = 1.9885e + 30 kg$.

Figure 5.2 shows the behavior of t_c according to α_1 and $t^\star$. It can be noticed that the systematic behavior shown in Figure 3.4 is recovered, with capture trajectories corresponding to $\alpha_1 \to 0$. Nevertheless, it emerged that $t^\star$ is not an indicator as good as it is for the CR3BP. A total of 108 long-term capture orbits were identified with a mean number of revolutions around the Moon equal to 180.

Even though an equilibrium region does not exist for the ER4BP, because of the time dependence of the problem, due to the eccentric motion of the primaries and the fourth body, the solution proposed in the previous section allows defining a subset of the phase space in which a compact representation of transit trajectories and capture orbits is similar to that in the equilibrium region for the CR3BP.
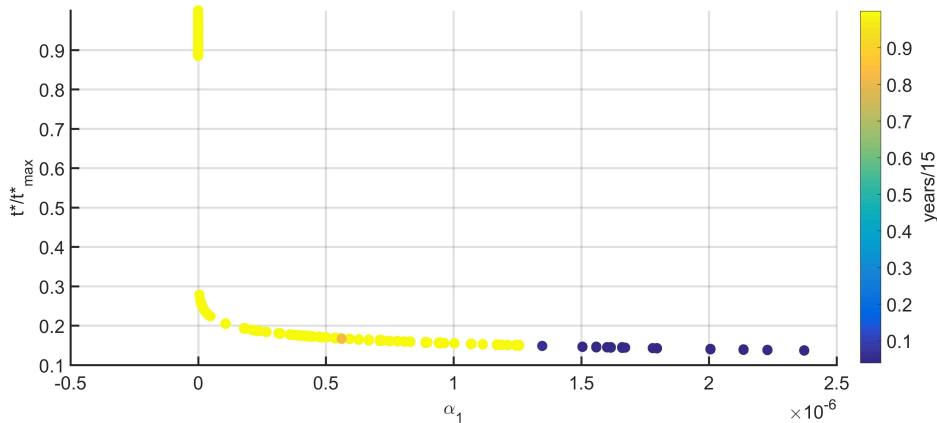
Figure 5.2. Comparison of t_c (colorbar) and $t^\star$ with α_1 for the Sun-Earth-Moon system modeled in the ER4BP

5.4 A dynamical model for the Jupiter-Europa-Io system

The method proposed in sections 5.1 and 5.2 can also provide useful information regarding the effect of orbital resonance in restricted 4-body system. A model is developed here for applications on the Jupiter-Europa-Io system, whose masses are, respectively, $m_1 >> m_2 > m_3$ and the mass of the spacecraft is negligible. The system is modeled as indicated below [3]

- the center of mass of the system is indicated as O

- the relative motion of m_2 and m_1 with respect to O describes a Keplerian orbit with semimajor axis a and eccentricity e

- the relative motion of m_3 and m_1 with respect to O describes a Keplerian orbit with semimajor axis a_p and eccentricity e_p

- the orbital plane of the two system are tilted of an angle ϵ.

The subscript p is selected to indicate the system whose smaller primary (m_3) produces the fourth body perturbation. A sketch of the system is shown in Figure 5.3, where the distances between the primaries and the center of mass can be calculated by equations 5.1 and 5.2, replacing R_b with $R_p = \frac{a_p\left(1-e_p^2\right)}{(1+e_p\cos\theta_p)}$, where θ_p indicates the true anomaly of m_1 in the (m_1, m_3) system[4].

Considering the inertial reference frame $\left[\hat{\Xi}, \hat{H}, \hat{Z}\right]$, centered in O with $\hat{\Xi}$ pointing from m_1 to m_2 at the initial time t_0, $\hat{Z}$ parallel to the angular momentum vector of the (m_1, m_2) system and $\hat{H}$ completing the rectangular reference frame, the dynamic equations of motion of m can be expressed using system 5.3.

---

[3]It can be noted that both m_2 and m_3 orbit m_1, differently than the Sun-Earth-Moon system, discussed in section 5.1, where m_3 orbits m_2 and they together revolve around m_1.

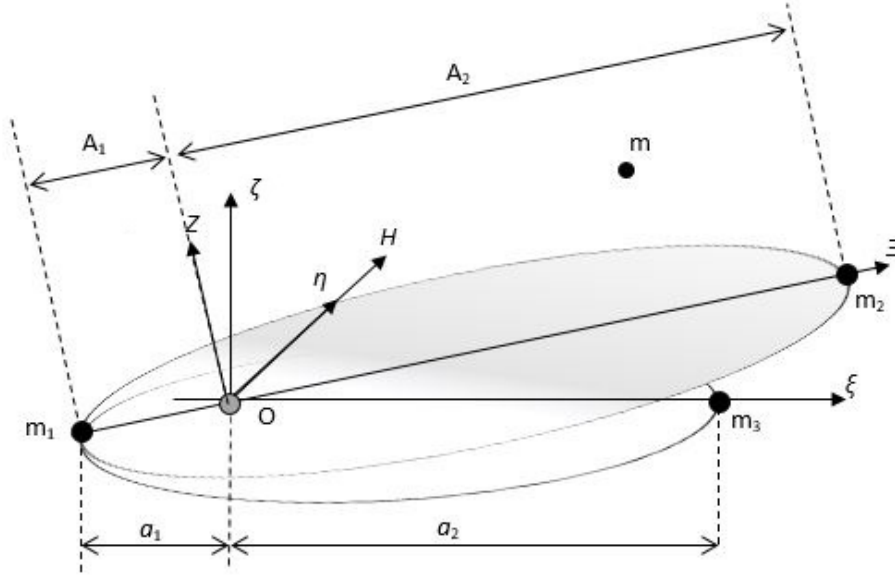[4]In not indicated, the symbols have the same meaning as in section 5.1.

Figure 5.3. Sketch of the Jupiter-Europa-Io system

These can be rearranged in the reference frame $\left[\hat{\xi}, \hat{\eta}, \hat{\zeta}\right]$, centered in O and rotating at the same angular velocity $\dot{\theta}_p$ of the (m_1, m_2) system. Axis $\hat{\xi}$ lays in the orbital plane of the (m_1, m_3) system, $\hat{\zeta}$ is parallel to the angular momentum vector of (m_1, m_3) and $\hat{\eta}$ is orthogonal to the others. For the sake of simplicity, it is possible to assume that at t_0 $\hat{\xi}$ points from m_1 to m_3, therefore $\hat{\eta}$ is parallel to $\hat{H}$. Coordinates in such a non-uniformly rotating frame can be calculated from the inertial ones by applying the following transformations

1. a rotation $\mathcal{R}_2(-\varepsilon)$ about $\hat{H}$ producing the intermediate frame $[\hat{\Xi}', \hat{H}', \hat{Z}]$

2. a rotation $\mathcal{R}_3(-\theta)$ about $\hat{Z}$ producing the final frame $[\hat{\xi}, \hat{\eta}, \hat{\zeta}]$ frame

which produce the following expression

$$
\begin{cases}
\xi = \cos\epsilon \, (\Xi \cos\theta + H \sin\theta) + Z \sin\epsilon \\
\eta = -\Xi \sin\theta_p + H \cos\theta \\
\zeta = -\sin\epsilon \, (\Xi \cos\theta + H \sin\theta) + Z \cos\epsilon
\end{cases} \tag{5.25}
$$

The same process indicated in section 5.1 can be repeated (from equation 5.4 to 5.9) considering the transformation 5.25 and the following set of auxiliary variables[5] for system 5.4

$$
\begin{cases}
X = \xi \cos\epsilon - \zeta \sin\epsilon \\
Y = \eta \\
Z = \xi \sin\epsilon + \zeta \cos\epsilon
\end{cases} \tag{5.26}
$$

---

[5]A new expression is required because they depend on the transformation between the inertial and the rotating reference frame, which is different for the two models considered.

The result is that equations of motion in the dimensionless form, equal to system 5.13 are obtained for the new model and are reported below for the sake of clearness

$$\begin{cases} x' = u \\ y' = v \\ z' = w' \\ u' = 2v + K\left(\theta\right)\left(\frac{\partial \mathcal{V}}{\partial x} + x\right) \\ v' = -2u + K\left(\theta\right)\left(\frac{\partial \mathcal{V}}{\partial y} + y\right) \\ w' = K\left(\theta\right)\left(\frac{\partial \mathcal{V}}{\partial z} + z\right) - z \end{cases}$$

The coordinates of the i-th primary in the inertial frame are (Ξ_i, H_i, Z_i); it can be noticed that $\Xi_2 = A_2 \cos\theta$, $H_2 = A_2 \sin\theta$ and $Z_2 = 0$. These can be converted into the corresponding coordinates in the rotating frame by applying the transformation 5.25. The coordinates of the remaining primaries can be easily determined in the rotating frame, corresponding to $\xi_1 = -a_1 \cos\left(\theta_p - \theta\right)$, $\eta_1 = -a_1 \sin\left(\theta_p - \theta\right)$, $\xi_3 = a_2 \cos\left(\theta_p - \theta\right)$, $\eta_3 = a_2 \sin\left(\theta_p - \theta\right)$ and $\zeta_1 = \zeta_3 = 0$. Considering the unit of distance in equation 5.9, the position of the primaries in dimensionless coordinates can be expressed as follows

$$\begin{cases} x_1 = -\frac{R_p(\theta_p)}{R(\theta)}\frac{\mu_3}{1-\mu_2}\cos\left(\theta_p - \theta\right)\cos\epsilon \\ y_1 = -\frac{R_p(\theta_p)}{R(\theta)}\frac{\mu_3}{1-\mu_2}\sin\left(\theta_p - \theta\right) \\ z_1 = -\frac{R_p(\theta_p)}{R(\theta)}\frac{\mu_3}{1-\mu_2}\cos\left(\theta_p - \theta\right)\sin\epsilon \end{cases}$$

$$\begin{cases} x_2 = \mu_2 - 1 \\ y_2 = 0 \\ z_2 = 0 \end{cases} \tag{5.27}$$

$$\begin{cases} x_3 = \frac{R_p(\theta_p)}{R(\theta)}\frac{\mu_1}{1-\mu_2}\cos\left(\theta_p - \theta\right)\cos\epsilon \\ y_3 = \frac{R_p(\theta_p)}{R(\theta)}\frac{\mu_1}{1-\mu_2}\sin\left(\theta_p - \theta\right) \\ z_3 = \frac{R_p(\theta_b)}{R(\theta)}\frac{\mu_1}{1-\mu_2}\cos\left(\theta_p - \theta\right)\sin\epsilon \end{cases}$$

A peculiarity of the Jupiter-Europa-Io system is that it shows orbital resonance, in fact the orbital period of Europa and that of Io are related by a ratio which is (almost) an integer number, and in particular $n = 2.01$, therefore $\theta_p = n\theta$. The effects of resonance on the quasi-periodic libration point orbits and some particular solutions are investigated in the following section.

5.5 Resonance analysis and quasi-periodic solutions

Operating as in section 5.2, the system dynamics 5.13 can be expressed using the Hamiltonian formalism. Based on this representation, the Hamiltonian function can be expanded in power series to highlight the dependence on the perturbation terms, which for the Jupiter-Europa-Io system are the eccentricity e and the mass of the fourth body causing the perturbation μ_i, which can be arbitrarily selected between

the two smaller primaries. If selecting Io (μ_3) as the casue of the perturbation the following form of the Hamiltonian function is obtained (see the appendix)

$$H = \frac{1}{2}\left(p_1^2 + p_2^2 + p_3^2\right) + p_1 q_2 - p_2 \tilde{q}_1 - \frac{\mu_1}{r_1^\star} - \frac{\mu_2}{r_2^\star} +$$

$$\mu_3 \{ 2\frac{\mu_1{}^3}{r_1^\star}\frac{a_p}{a}\left[\tilde{q}_1 \cos\left(\theta_p - \theta\right)\cos\epsilon + q_2 \sin\left(\theta_p - \theta\right) + q_3 \cos\left(\theta_p - \theta\right)\sin\epsilon\right]\} +$$

$$+ e\left[\frac{\mu_2}{r_2^\star} + \frac{1}{2}\left(\tilde{q}_1^2 + q_2^2 + q_3^2\right)\right]cos\theta + o(e, \mu_3) \tag{5.28}$$

where the symbol $\star$ indicates the function evaluated at the point of linearization $(e = 0, \mu_3 = 0)$.

Introducing an adequate generating function (see equation 5.22) and the canonical transformation 2.31, the Hamiltonian function above can be expressed as the sum of three local integrals of motion 2.33, representing the linear dynamics, and higher order terms. The derivation of the function is reported in Appendix E and F and leads to the following expression

$$H_2 = \rho x_1 y_1 + \frac{\lambda_1}{2}\left(x_2^2 + y_2^2\right) + \frac{\lambda_2}{2}\left(x_3^2 + y_3^2\right) + \hat{H}_3\left(\mathbf{x}, \mathbf{y}, \theta_p, \theta\right) \tag{5.29}$$

The order three terms of equation 5.29 can be absorbed by means of a further canonical transformation $(\mathbf{x}, \mathbf{y}, \theta_p, \theta) \rightarrow (\mathbf{R}, \mathbf{S})$, producing

$$H_2\left(\mathbf{x}, \mathbf{y}\right) + H_3\left(\mathbf{x}, \mathbf{y}\right) + \frac{\partial S}{\partial\left(\theta_p - \theta\right)}\frac{\partial\left(\theta_p - \theta\right)}{\partial\theta} + \frac{\partial S}{\partial\theta} =$$

$$= \rho R_1 S_1 + \frac{\lambda_1}{2}\left(R_2^2 + S_2^2\right) + \frac{\lambda_2}{2}\left(R_3^2 + S_3^2\right) + H_3^{res}\left(\mathbf{R}, \mathbf{S}, \theta_p, \theta\right) \tag{5.30}$$

As opposite to the Sun-Earth-Moon case, discussed in Section 5.1, the canonical transformation is unable to absorb the term $\hat{H}_3$ completely. Namely, it is known as the problem of small denominators, because the canonical transformation defaults when some coefficients at its denominator approach zero (see the coefficients $b_{i,j,k,l}^{(n)}$ or $b_{i,j}^{(n)}$ in Appendix G).

For the Jupiter-Europa-Io system this occurs because of $n = 2.01$, therefore, some order three terms of the Hamiltonian function can not be absorbed and these are given by

$$H_3^{res} = 2\left(R_3 + S_3\right)\left(b_{10}^{(1)}\cos^2\theta + b_{10}^{(2)}\cos\theta\sin\theta + b_{10}^{(6)}\sin^2\theta\right) \tag{5.31}$$

Stationary points for the residual term $\hat{H}_3{}^{res}$ can be calculated, as indicated in Appendix H, producing the following result

$$\begin{cases} \tilde{\phi}_{3,s} = k\pi, \quad k \in \mathbf{Z} \\ \tilde{\rho}_{3,s} = -\frac{H_3^{res}}{b_{10}^{(1)} + b_{10}^{(2)} + b_{10}^{(6)}} \end{cases} \tag{5.32}$$

The existence of stationary points, setting to zero the residual terms of the Hamiltonian function, implies the existence of orbits which show quasi-periodic behavior also in presence of the orbital resonance. This result is verified by means of numerical analysis, propagating different initial conditions selected in the neighborhood of Jupiter-Europa libration point L_1 and evaluating the effects of the gravitational perturbation of Io on the resulting trajectories. The the vertical oscillator is selected for this study, characterized by initial conditions null onto the $[\hat{x}_1, \hat{y}_1]$ and $[\hat{x}_2, \hat{y}_2]$ planes, corresponding to $\alpha_1 = \alpha_2 = \beta_1 = \beta_2 = 0$, and selecting randomly the initial conditions onto the $[\hat{x}_3, \hat{y}_3]$ plane. The full nonlinear equations of motion 5.13 are integrated using Matlab *ode113* solver, setting relative and absolute tolerance equal to 1e-18 and 1e-19. The simulation parameters are reported Table 5.1 and a sketch of the orbits of the primaries in the rotating reference frame is shown in Figure 5.4

Table 5.1. Parameters of the Jupiter-Europa-Io system

Parameter	Symbol	Value
Mass of Jupiter	m_1	1.899e+27 kg
Mass of Europa	m_2	4.799e+24 kg
Mass of Io	m_3	8.932e+22 kg
Jupieter-Europa semimajor axis	a	6.711e+5 km
Jupieter-Io semimajor axis	a_p	4.218+5 km
Jupieter-Europa eccentricity	e	0.0094
Jupieter-Io eccentricity	e_p	0.0041
Inclination between the orbital planes	ϵ	0.430 deg

The initial conditions are propagated for a total time corresponding to 200 times the orbital period of Europa $T_2 = 2\pi\sqrt{\frac{a^3}{Gm_2}}$. The effect of the orbital resonance on a vertical oscillator is reported in Figure 5.5.
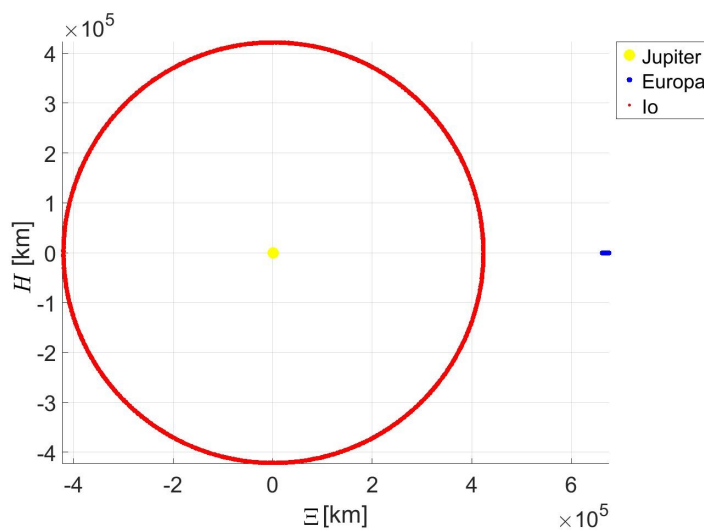

Figure 5.4. The orbits of Jupiter, Europa and Io in the rotating reference frame

Figure 5.5 shows a marked increase in the amplitude of the oscillations, from approximately $5.1e-08$ to $2.9e-04$ DU. To prove that this result is addressed to the orbital resonance introduced by Io, the same initial conditions are propagated setting $m_3 = e_p = 0$. The result is shown in Figure 5.6 and indicate that the amplitude of the oscillations is constant if the fourth body is discarded, thus it confirms that the result shown in Figure 5.5 is due to the gravitational perturbation of Io.
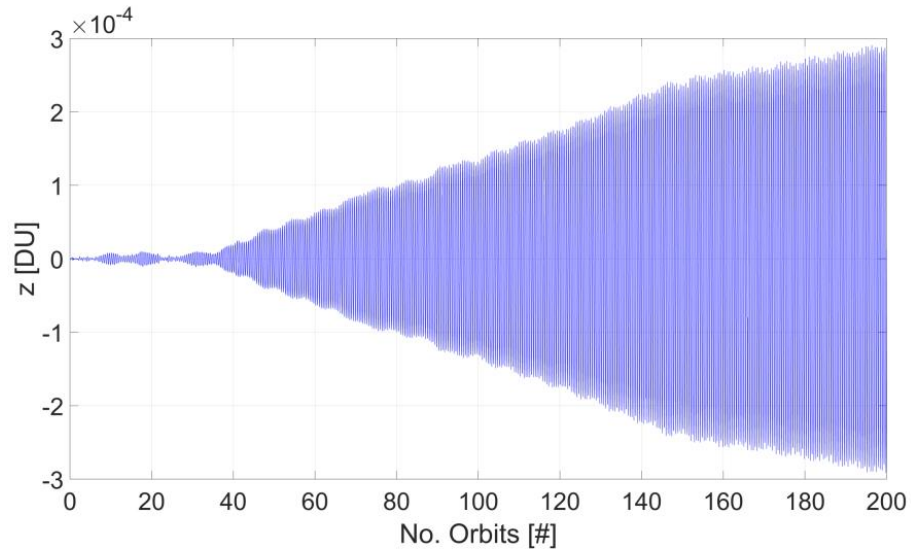

Figure 5.5. Effect of resonance on the amplitude of the vertical oscillations
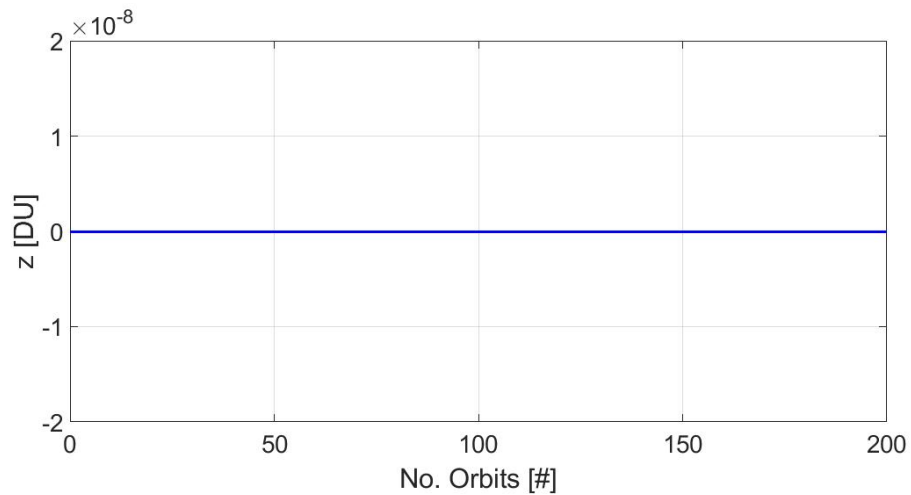
Figure 5.6. Non-resonant behavior of the vertical oscillator in the CR3BP

Finally, the trajectory associated to one of the stationary points determined in section 5.4 is computed, to verify its quasi-periodic behavior. In particular, the trajectory is calculated setting $\tilde{\phi}_{3,s} = 0$ and $\hat{H}_3^{res} = 1e-15$. The resulting path, reported in Figure 5.7, shows that quasi-periodic oscillations have (almost) constant amplitude, which never exceeds the limit value $1.0e-05$ DU. The quasi-periodic

trajectory in the inertial reference frame (Ξ, H, Z) is reported in Figure 5.8. Because the magnitude of the out of plane oscillations is small, this component is plotted after multiplying it by a factor 1e+03, to provide a clearer representation.
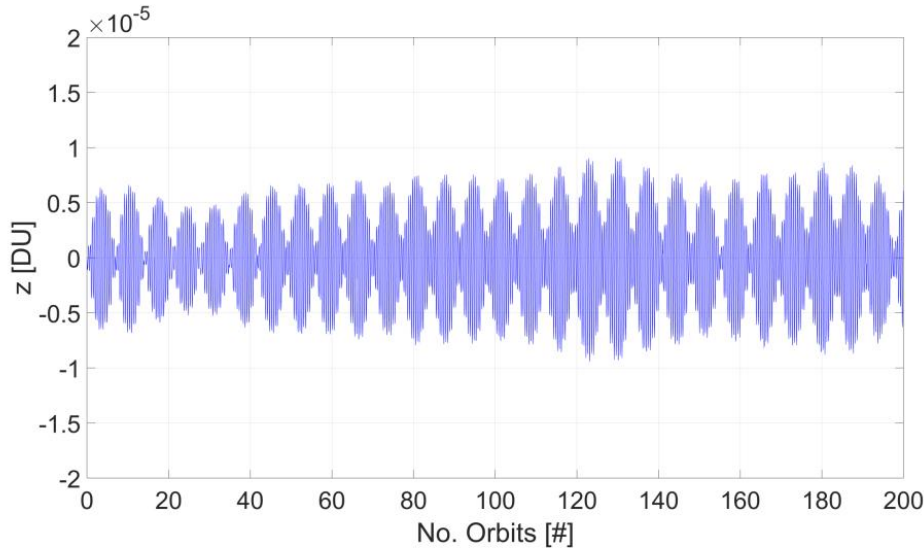

Figure 5.7. Quasi-periodic behavior of the vertical oscillator associated to a stationary point in the ER4BP
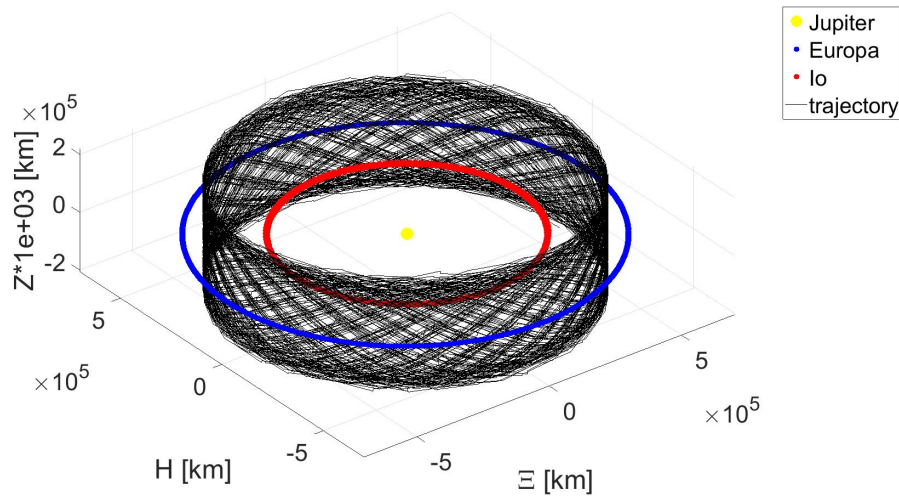

Figure 5.8. Orbit of the primaries and quasi-periodic orbit in the inertial reference frame

The model presented in this chapter allows an in-depth investigation on the behavior of transit, capture and quasi-periodic trajectories in the dynamical framework of the spatial ER4BP. The model takes advantage of the robustness of the CR3BP flow in the neighborhood of the collinear libration points L_1 and L_2, which allows setting the Hamiltonian function for the ER4BP to a normal form equivalent to that of the CR3BP. Based on this, the tools developed for the topological characterization

of orbits in the CR3BP can be applied also to investigate low-energy trajectories in the ER4BP. Furthermore, when orbital resonance occurs, small denominators theory allows isolating the higher order terms of the Hamiltonian function associated to the resonance. Selecting an adequate canonical transformations allows defining initial conditions for trajectories which are quasi-periodic in presence of the resonance.

Chapter 6

Purely magnetic attitude determination and control systems for space science missions in LEO

Mission operations often require the capability to orient the spacecraft towards a specific direction. To achieve this goal both an adequately accurate knowledge of the spacecraft orientation in space, namely its attitude, and autonomous feedback control on the attitude, by means of some actuators, are required. The on-board system producing these operations is named the attitude determination and control system (ADCS) and represents a fundamental element in spacecraft design.

The success of a space science mission based on CubeSat platforms operating in LEO strongly depends on the performance and robustness of the ADCS, given the fact that most of the payload used for space science applications can operate only at some prescribed attitude [172]. The design of ADCS for CubeSats is a rather challenging task, because the limited power and computational resources available on board, together with the low development budget, set strict constraints on the complexity of the algorithms and on the selection of actuators and sensors. It is worth to highlight that the latter are typically components-off-the-shelf (COTS) which are not specifically developed for space (or high-performance) applications.

High-precision ADCS designed for CubeSats are nowadays available on the market, though not common, and include star trackers, sensors which can produce attitude determination with accuracy higher than 0.01 deg, and compact reaction wheels, which can provide a control torque of the order of some mN [93, 182]. These systems are rather expansive, if compared to other CubeSat on-board systems, and can require a significant volume or power to operate adequately. Commonly, attitude determination sensors, such as magnetometers and gyroscopes, are micro electro-mechanical systems (MEMS) and electric coils, named magnetorquers, are used as actuators. MEMS gyroscopes are accurate angular rate sensors, nevertheless, because of technological limitations, they usually have structure defects which produce high drift and require compensation, thus opening to alternative methods of angular rate determination [38]. As a consequence of it, magnetometer-only solutions started

being developed and are gathering growing attention [8, 63, 70, 72, 79, 109, 110, 131, 132, 145, 157, 161, 168]

In this chapter, the design of a purely magnetic ADCS is proposed, including the design of algorithms for the attitude control and determination. The aim of the system is representing an effective backup solution in case of failure of the primary ADCS, increasing the overall reliability of the platform. Such a solution is specifically developed for CubeSats and takes into account the constraints set by the use of COTS devices, the power budget and the computational resources available. In particular, the software part is designed to be implemented on the FPGA core of a standard on-board computer (OBC) and therefore further constraints are set in order to maximize area usage efficiency.

Two attitude control algorithms are developed, to produce both stabilization after deployment (detumbling) and coarse pointing using the only input form a three-axis mangetometer and the torque produced by three magnetorquers, mutually orthogonal. A magnetometer-only attitude estimation algorithm is finally implemented, providing an input to increase the pointing accuracy of the system.

6.1 Attitude dynamics and magnetic control

Attitude dynamics is modeled considering the spacecraft as a rigid body, free to rotate about its center of mass under the only effect of the control torque. The principal axes of inertia are used to define a body-fixed reference frame which rotates rigidly with the spacecraft $\mathcal{F}_b = [\hat{x}_b, \hat{y}_b, \hat{z}_b]$. Spacecraft attitude can be defined by means of the Euler angles $(\varphi, \vartheta, \psi)$ correlating $\mathcal{F}_b$ with an inertial reference frame, selected here as the geocentric inertial (GCI) frame, indicated as $\mathcal{F}_i = [\hat{x}_i, \hat{y}_i, \hat{z}_i]$ [181], by means of the attitude matrix [181]

$$\mathcal{F}_b = A\mathcal{F}_i$$

The angular velocity at which $\mathcal{F}_b$ rotates with respect to $\mathcal{F}_i$ represents the angular velocity of the spacecraft, whose components are the angular rates $\omega = [\omega_x, \omega_y, \omega_z]$. Based on this representation, attitude dynamics can be defined by the following set of kinematic and Euler equations

$$\begin{cases} \dot{\varphi} = \omega_x + \sin\varphi \tan\vartheta\omega_y + \cos\varphi \tan\vartheta\omega_z \\ \dot{\vartheta} = \omega_x \cos\varphi - \sin\varphi\omega_z \\ \dot{\psi} = \frac{\sin\varphi\omega_y - \cos\varphi\omega_z}{\cos\theta} \\ \dot{\omega}_x = \left(\frac{J_y - J_z}{J_x}\omega_y\omega_z + \tau_x \right) \\ \dot{\omega}_y = \left(\frac{J_z - J_x}{J_y}\omega_x\omega_z + \tau_y \right) \\ \dot{\omega}_z = \left(\frac{J_x - J_yz}{J_z}\omega_x\omega_y + \tau_z \right) \end{cases} \tag{6.1}$$

where J_i and τ_i indicate, respectively, the principal moment of inertia and the external torque along the direcion $i = x, y, z$.

It is worth noting that system 6.1 is singular for $\theta = k\frac{\pi}{2} \quad k \in \mathbb{Z}$. This can be avoided using the quaternion representation instead of Euler angles [36]. The former will be used for the numerical integrations discussed in the following sections, but the

Euler angles are preferred for the representation of the results. Attitude dynamics equations based on quaternions are reported below

$$
\begin{cases}
\dot{\epsilon}_1 = \frac{1}{2}\epsilon_0\omega_x + \epsilon_2\omega_z - \epsilon_3\omega_y \\
\dot{\epsilon}_2 = \frac{1}{2}\epsilon_0\omega_y - \epsilon_1\omega_z + \epsilon_3\omega_x \\
\dot{\epsilon}_3 = \frac{1}{2}\epsilon_0\omega_z + \epsilon_1\omega_y - \epsilon_2\omega_x \\
\dot{\epsilon}_0 = -\frac{1}{2}\epsilon_1\omega_x + \epsilon_2\omega_y + \epsilon_3\omega_z \\
\dot{\psi} = \frac{\sin\varphi\omega_y - \cos\varphi\omega_z}{\cos\theta} \\
\dot{\omega}_x = \left(\frac{J_y - J_z}{J_x}\omega_y\omega_z + \tau_x\right) \\
\dot{\omega}_y = \left(\frac{J_z - J_x}{J_y}\omega_x\omega_z + \tau_y\right) \\
\dot{\omega}_z = \left(\frac{J_x - J_yz}{J_z}\omega_x\omega_y + \tau_z\right)
\end{cases}
\tag{6.2}
$$

where ϵ_0 represents the scalar part of the quaternion.

The control torque τ is provided by external devices, and depends on the control law defined during the design phase and the characteristic of the actuator. In particular, considering a magnetorquer, consisting of an electromagnetic coil, the torque produced is given by the interaction between the magnetic dipole moment produced by the device $\mathbf{m}$ and the geomagnetic field crossing the coil surface $\mathbf{B_b}$, according to the following equation [181]

$$
\tau = \mathbf{m} \times \mathbf{B_b}
\tag{6.3}
$$

where the subscript b indicates the value measured in the body frame. The magnetic dipole moment of a coil is given by the simple expression $\mathbf{m} = NAI\hat{n}$, where N and A are, respectively, the number of turns of and the area enveloped by the coil, I is the electric current in the conductor and $\hat{n}$ represents the direction orthogonal to the coil. If three mutually orthogonal coils are installed on the CubeSat, then the resulting torque has a component along each direction of $\mathcal{F}_b$ and three-axis control can be achieved.

Given a fixed design for the magnetorquer, and assuming that each one of them is orthogonal to one axis of $\mathcal{F}_b$, the only control parameter which allows modulating the torque is the electric current. In fact, control laws are designed to correlate the value of the current provided to each coil to the desired attitude motion. In particular, this is achieved by developing adequate closed-loop control laws which process the feedback provided by on-board sensors, to calculate the values of I. This task is performed in the next two sections.

6.2 Detumbling and magnetomter-only angular rates determination

When a spacecraft is deployed to its final orbit it can happen that the angular rates are much higher than those desired for attitude maneuvering. The high rotational kinetic energy is provided partly by the deployment system and mostly by the launcher upper stage, whose angular rates change during the flight and the deployment. This happens because as the mass of the rocket changes (propellant

ejection, staging, satellite deployment,etc) so do the moments of inertia. Predicting the magnitude and direction of the spacecraft angular velocity is complex and, in the general case, the satellite will be tumbling. Therefore, a specific detumbling control must be designed to stabilize the spacecraft within the minimum time compatible with the mission requirements. After the spin motion of the spacecraft has been damped to the desired level, the control policy can be switched to pointing or attitude maneuvering and mission operations can start.

A detumbling control is proposed in this section, aimed at producing the desired stabilization based on the only input of a three-axis magnetometer and the control torque produced by magnetorquers. This can be a suitable backup solution to recover missions in which the ADCS sensor addressed to angular rate measurement (i.e., a gyroscope) is not capable of providing any information, because of a failure or saturation. The algorithm does not require any a-priori information about the satellite RAAN (Ω), true anomaly (θ), inclination(i), attitude and angular rates.

The proposed detumbling control represents a variation of the classical B-dot in which [181]

$$\mathbf{m} = -K_d \dot{\mathbf{B}}_{\mathbf{b}} \tag{6.4}$$

where K_d is the control gain. The B-dot can be easily implemented approximating the time derivative with the finite difference between two consecutive samplings $\mathbf{B}_{\mathbf{b}}^{(\mathbf{k})}$ of the magnetometer

$$\dot{\mathbf{B}}_{\mathbf{b}} = f_k \left(\mathbf{B}_{\mathbf{b}}^{(\mathbf{k})} - \mathbf{B}_{\mathbf{b}}^{(\mathbf{k})} \right)$$

where f_i is the sampling frequency of the magnetometer.

It can be noticed that the torque can be maximized by setting $\mathbf{m}$ orthogonal to $\mathbf{B}_{\mathbf{b}}$. According to equation 6.4, this is not guaranteed by the classical B-dot, therefore it is reformulated in the following way. The time derivative of the geomagnetic field vector can be expressed as follows [181]

$$\dot{\mathbf{B}}_{\mathbf{b}} = \dot{\mathbf{B}}_{\mathbf{i}} - \omega \times \mathbf{B}_{\mathbf{b}} \tag{6.5}$$

The term $\dot{\mathbf{B}}_{\mathbf{i}}$ in equation 6.5 represents the rate of change of the magnetic field due to the orbital motion of the spacecraft and is negligible when the rates are higher than 0.13 deg/sec for a LEO satellite [36], which is the case examined here. Consequently, during the detumbling, equation 6.5 can be approximated as follows

$$\dot{\mathbf{B}}_{\mathbf{b}} = \mathbf{B}_{\mathbf{b}} \times \omega = \mathbf{B}_{\mathbf{b}} \times \omega_\perp \tag{6.6}$$

where $\omega_\perp$ is the projection of the ω orthogonal to $\mathbf{B}_{\mathbf{b}}$. The following expression for $\mathbf{m}$ is then set, verifying the orthogonality

$$\mathbf{m} = K_d \left(\omega_\perp \times \mathbf{B}_{\mathbf{b}} \right) \tag{6.7}$$

It is now necessary to determine the expression of $\omega_\perp$. Because the cross product does not allow inverting equation 6.6, then the following guessed expression is considered

$$\omega_\perp = \frac{\dot{\mathbf{B}}_{\mathbf{b}} \times \mathbf{B}_{\mathbf{b}}}{|\mathbf{B}_{\mathbf{b}}|^2} \tag{6.8}$$

The suitability of equation 6.8 can be verified by introducing equation 6.8 into 6.6, as follows

$$\dot{\mathbf{B}}_{\mathbf{b}} = \mathbf{B}_{\mathbf{b}} \times \omega_\perp = \mathbf{B}_{\mathbf{b}} \times \frac{\dot{\mathbf{B}}_{\mathbf{b}} \times \mathbf{B}_{\mathbf{b}}}{|\mathbf{B}_{\mathbf{b}}|^2} = \dot{\mathbf{B}}_{\mathbf{b}} + \mathbf{B}_{\mathbf{b}} \left(\frac{\dot{\mathbf{B}}_{\mathbf{b}} \cdot \mathbf{B}_{\mathbf{b}}}{|\mathbf{B}_{\mathbf{b}}|^2} \right) \approx \dot{\mathbf{B}}_{\mathbf{b}} \qquad (6.9)$$

It is known that the B-dot control is Lyapunov stable and this property is extended to the proposed modification [36]. It follows that the magnitude of ω decreases monotonically approaching zero. Nevertheless, for a variety of missions, maintaining a residual angular rate along one axis is desirable, therefore the capability to estimate the angular rates and modulate the detumbling control according to them represents an interesting challenge.

Angular rates determination is performed here based on three consecutive samplings from the three-axis magnetometer. According to equations 6.7 and 6.8, the vectors $\mathbf{B}_{\mathbf{b}}$, $\omega_\perp$ and $\mathbf{m}$ are mutually orthogonal and the following auxiliary rectangular reference frame $\mathcal{F}_a$ can be defined

$$\begin{cases} \xi_1 = \frac{\mathbf{B}_{\mathbf{b}}}{|\mathbf{B}_{\mathbf{b}}|} \\ \xi_2 = \frac{\omega_\perp}{|\omega_\perp|} \\ \xi_3 = -\frac{\mathbf{m}}{|\mathbf{m}|} \end{cases} \qquad (6.10)$$

The simple case of a spacecraft with spherical mass distribution is considered first, before to extend the result to the general case. Under this hypothesis, the last three equations of system 6.2 can be expressed by the following vector equation as follows

$$\dot{\omega} = \frac{\mathbf{m} \times \mathbf{B}_{\mathbf{b}}}{J} = \frac{\tau}{J} \qquad (6.11)$$

where J is the moment of inertia of the spacecraft. Equation 6.11 indicates that the control torque can only produce a change in the angular rate along the direction ξ_2, thus the attitude motion produces a rotation of $\mathcal{F}_a$ around ξ_2. Considering short intervals of time, such that the change $\dot{\mathbf{B}}_{\mathbf{i}}$ is negligible and compatible with the sampling frequency of common MEMS magnetometers $f_k = (1; 100)$ Hz, then the only change in $\mathbf{B}_{\mathbf{b}}$ is produced by the attitude motion of the spacecraft. In fact, $\mathbf{B}_{\mathbf{b}}$ is measured by a magnetometer fixed to the spacecraft and therefore rotates with it. Consequently, the vector $\dot{\mathbf{B}}_{\mathbf{b}}$ is always orthogonal to ξ_2, as shown in Figure 6.1. Furthermore, any rotation of $\dot{\mathbf{B}}_{\mathbf{b}}$ around ξ_2 can only be caused by a rotation of the spacecraft about the same axis. The rotation between two consecutive values of $\dot{\mathbf{B}}_{\mathbf{b}}$ can be calculated by the cross product and leads to the following expression for the angular velocity

$$\omega^{\mathbf{k}} = f_k \frac{\dot{\mathbf{B}}_{\mathbf{b}}^{\mathbf{k}} \times \dot{\mathbf{B}}_{\mathbf{b}}^{k-1}}{|\dot{\mathbf{B}}_{\mathbf{b}}|^2} \qquad (6.12)$$
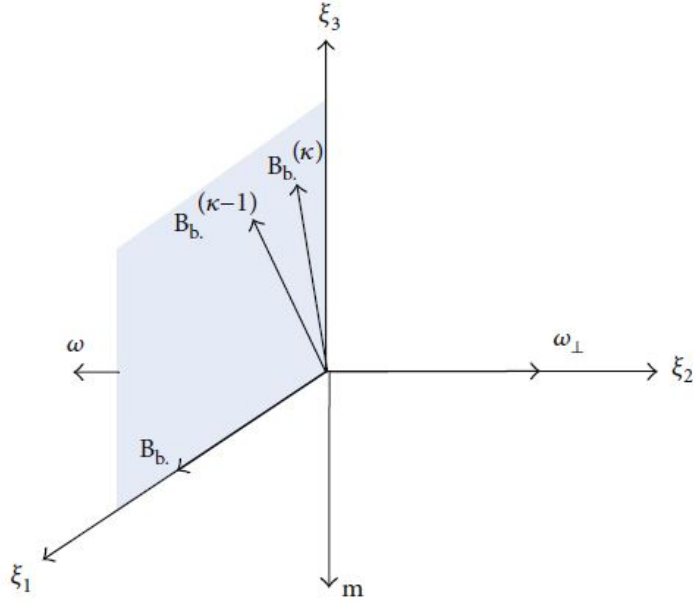
Figure 6.1. Rotation of $\dot{\mathbf{B}}_\mathbf{b}$ with respect to the auxiliary frame

Equation 6.12 allows estimating the unknown angular rates of a spherical space-craft based on three consecutive measurements of $\mathbf{B_b}$. When extending the results to a spacecraft with a generic mass distribution, the full tensor of inertia $\mathbf{J}$ should be considered instead of J into equation 6.11

$$\dot{\omega} = \mathbf{J}^{-1} \left(-\omega \times \mathbf{J}\omega + \mathbf{m} \times \mathbf{B_b} \right) \tag{6.13}$$

Therefore changes in the angular rates along the ξ_1 and ξ_3 direction are not null and depend on the shape of the tensor. Nevertheless, the general behavior described before is preserved and the main drawback in using equation 6.12 for a generic mass distribution is related to the high frequency disturbance caused by the non-linear terms in equation 6.13.

The effect of the non-linear term introduces high errors in the determination. These can be compensated by adding the following term to equation 6.12

$$\Delta\omega^k = -f_j \mathbf{J}^{-1} \left(-\omega^{k-1} \times \mathbf{J}\omega^{k-1} \right) \tag{6.14}$$

which attempts to discard the non-linear term based on the previous estimation of the angular rates. The sum of equtions 6.12 and 6.14 can finally be processed by a second-order Bessel low-pass filter, characterized by the following transfer function

$$H(s) = \frac{3}{\left(s/f_{co} \right)^2 + 3 \left(s/f_{co} \right) + 3} \tag{6.15}$$

where f_{co} is the filter cutoff frequency.

The proposed algorithms for detumbling control and angular rate determination are validated by means of numerical analysis, in section 6.4, and tested by hardware-in-the-loop simulations, discussed in chapter 7.

6.3 B-pointing and magnetometer-only attitude determination

Attitude control requires, in the vast majority of cases, attitude determination. CubeSats are not typically equipped with attitude sensors, such as star trackers, therefore attitude is estimated from the inputs of a three-axis gyroscope, measuring the angular rates, together with a three-axis magnetometer and/or a Sun sensor, which can define the attitude of the spacecraft with respect to a reference vector, represented by the geomagnetic field for the first device and the Sun direction for the second one. The implementation of a backup solution, allowing attitude control though coarse or with degraded performance allows increasing the reliability of the system, therefore the chances of success for the mission. Such a solution might be necessary in the unlucky event of an attitude device failure or of anomalies in flight operations.

The attitude control and determination strategy proposed in this section represents a backup solution suitable for implementation on CubeSats. The strategy consists of three phases

1. detumbling and angular rate determination, based on the algorithms discussed in section 6.2, producing the stabilization after the deployment at a desired spin of rotation

2. B-pointing, leading the spacecraft to some desired attitude with respect to the geomagnetic field, producing a predictable attitude motion

3. magnetometer-only attitude estimation, which provides the attitude matrix relating $\mathcal{F}_b$ to $\mathcal{F}_i$, allowing higher accuracy pointing.

The first phase was discussed in the previous section and allows stabilizing the spacecraft with desired angular rates.It is wort to focus now on the following phases, which provide increasing control on the spacecraft.
B-pointing control is aimed at producing a desired attitude for the spacecraft with respect to the geomagnetic field $\mathbf{B_b}$. The magnetic dipole moment for B-pointing is reported below

$$\mathbf{m_p} = K_p \mathbf{B_b} \times (\hat{r} \times \xi_1) \tag{6.16}$$

where K_p is the control gain and $\hat{r}$ represents the unit vector in the body frame that will be aligned with $\mathbf{B_b}$. For the sake of clearness, setting $\hat{r} = \hat{x}_b$, the control defined by equation 6.16 leads $\hat{x}_b$ to be parallel to $\mathbf{B_b}$. In fact, it can be noticed that vector $\mathbf{m_p}$ produces a torque orthogonal to the plane defined by $\hat{r}$ and $\mathbf{B_b}$, whose magnitude increases with the angular displacement between the two mentioned vector, as a consequence of the product $\hat{r} \times \xi_1$.

The B-pointing control does not allow setting a fixed attitude with respect to a direction $\mathcal{F}_i$ because the only reference vector is the magnetic field measured by the three-axis magnetometer. Nevertheless it produces a predictable attitude for the spacecraft which is suitable for operations in backup mode, as shown by the numerical analysis in section 6.4 and the hardware-in-the-loop (HiL) simulations discussed in chapter 7. During the B-pointing control, attitude estimation is performed, based on

the only measurements of a three-axis magnetometer and a model of the geomagnetic field, stored on the on-board computer.

Magnetometer-only attitude determination is a challenging task, mainly because the measurements from a three-axis magnetometer can provide information on only two axes of the spacecraft attitude. To resolve all three axes either some constraints on the attitude motion or a filtering process are required. Typically this second solution is implemented, using some form of the Kalman filter leading to models which can reach an accuracy below 5 deg on attitude and 0.01 deg/sec [72, 109, 145, 161, 168]. It is worth noting that, such a Kalman filter processes all the 6 (or 7) attitude dynamics variables defined in equation 6.1 (6.2), therefore an implementation on FPGA would be rather complex and, furthermre, would require considerable area and power usage. These might might exceed the limit of the device that, it should be recalled, is shared with the other on-board systems.

The solution proposed in this section does not depend on the use of a Kalman filter and it only relies on the measurements of a three-axis magnetometer and the geomagnetic field data stored on the OBC memory, providing the values of $\mathbf{B}_i$. Indicating with $\mathbf{A}^k$ the attitude matrix from $\mathcal{F}_b$ to $\mathcal{F}_i$ at time t_k, the following equality can be expressed

$$\mathbf{B}_i^k = \mathbf{A}^k \mathbf{B}_b^k \tag{6.17}$$

Then calculating the time derivative at both sides

$$\dot{\mathbf{B}}_i^k = \mathbf{A}^k \left(\dot{\mathbf{B}}_b^k + \omega_\perp^{\mathbf{k}} \times \mathbf{B}_b^k \right) \tag{6.18}$$

Except for the attitude matrix, all the quantities in equations 6.17 and 6.18 can be determined or measured. In particular, $\omega_\perp^{\mathbf{k}}$ can be calculated from equation 6.8 and equation 6.18 can rearranged as follows

$$\dot{\mathbf{B}}_i^k = \mathbf{A}^k \left(\dot{\mathbf{B}}_b^k + \omega_\perp^{\mathbf{k}} \times \mathbf{B}_b^k \right) = \mathbf{A}^k \left(\dot{\mathbf{B}}_b^k + \frac{\dot{\mathbf{B}}_b^k \times \mathbf{B}_b^k}{|\mathbf{B}_b^k|^2} \times \mathbf{B}_b^k \right) =$$

$$= \mathbf{A}^k \left(\dot{\mathbf{B}}_b^k + \frac{\left[-\left(\mathbf{B^T}_b^k \mathbf{B}_b^k \right) \dot{\mathbf{B}}_b^k + \left(\mathbf{B^T}_b^k \dot{\mathbf{B}}_b^k \right) \mathbf{B}_b^k \right]}{|\mathbf{B}_b^k|^2} \right) = \mathbf{A}^k \left(\xi_1^k \cdot \dot{\mathbf{B}}_b^k \xi_1^k \right) \tag{6.19}$$

Based on equations 6.17 and 6.19, two vectors ($\mathbf{B}$ and $\dot{\mathbf{B}}$) can be defined in the two reference frames $\mathcal{F}_b$ and $\mathcal{F}_i$, allowing the implementation of the unsymmetrical TRIAD for estimating matirx $\mathbf{A}$ [7, 177]

$$\mathbf{A}^k = \left[\hat{b}_1 \vdots \hat{b}_3 \vdots \hat{b}_4 \right] \left[\hat{r}_1 \vdots \hat{r}_3 \vdots \hat{r}_4 \right] \tag{6.20}$$

where the unit vectors are defined as follows[1]

$$\begin{cases} \hat{b}_1 = \xi_1^k \\ \hat{b}_2 = \frac{\xi_1^k \cdot \dot{\mathbf{B}}_b^k \xi_1^k}{|\dot{\mathbf{B}}_b^k|} \\ \hat{b}_3 = \hat{b}_1 \times \hat{b}_2 \\ \hat{b}_4 = \hat{b}_1 \times \hat{b}_3 \end{cases} \tag{6.21}$$

---

[1]It is worth noting that even though $\dot{\mathbf{B}}_i$ is neglected in the derivation of equation 6.8, its direction $\hat{b}_1$ can provide useful information and is in fact used to estimate the attitude matrix

$$\begin{cases} \hat{b}_1 = \frac{\mathbf{B_i}^k}{|\mathbf{B_i}^k|} \\ \hat{b}_2 = \frac{\dot{\mathbf{B}}_{\mathbf{i}}^k}{|\dot{\mathbf{B}}_{\mathbf{i}}^k|} \\ \hat{r}_3 = \hat{r}_1 \times \hat{r}_2 \\ \hat{r}_4 = \hat{r}_1 \times \hat{r}_3 \end{cases} \tag{6.22}$$

Equation 6.20 produces the attitude matrix which can be used to convert any vector in the inertial frame to the corresponding one in the body frame and vice-versa. Considering the given direction $\hat{\bar{r}}_i$, the corresponding valuein the body frame can be calculated by $\mathbf{A}^k$ and it can be introduced in equation 6.16, replacing ξ_1, producing magnetic pointing towards $\hat{\bar{r}}_b$

$$\mathbf{m_p} = K_p \mathbf{B_b} \times \left(\hat{r} \times \hat{\bar{r}}_b \right) \tag{6.23}$$

For instance, if $\hat{\bar{r}}_i$ represents the radial position of the satellite in GCI and $\hat{r} = \hat{x}_b$ $\mathbf{m_p}$ will produce nadir-pointing.

The use of the same equation for more processes (i.e. B-pointing, nadir-pointing,etc) is particularly convenient when using FPGA, because the same structure implementing one equation can be use multiple times, reducing area usage, a detailed in chapter 7.

6.4 Numerical validation of the algorithms

The algorithms in sections 6.2 and 6.3 are validated by means of numerical analysis, using Matlab Simulink *ode8* fixed step solver to integrate system 6.2 setting a time step of 0.1 sec. The attitude dynamics of a 3U CubeSat is simulated, considering the inertial properties and magnetorquer design reported in Table 6.1[2]. The CubeSat has volume $340 \times 10 \times 10 \ mm^3$ and a total mass of 4 kg.

Table 6.1. Simulation parameters

Moments of inertia	
$J_x \ [kgm^2]$	6.5e-3
$J_y \ [kgm^2]$	4.09e-2
$J_z \ [kgm^2]$	4.09e-2
Coils	
N_x	320
N_y	220
N_z	220
$A_x \ [m^2];$	3.2e-3
$N_y \ [m^2]$	1.49e-2
$N_z \ [m^2]$	1.49e-2

To represent effective backup solutions and increase the chances of success for the mission, the algorithms proposed should be effective under unknown or uncertain

---

[2]The parameters are those of Tigrisat, the 3U CubeSat designed and launched by the School of Aerospace Engineering of Sapienza University of Rome in 2014

deployment conditions, within the limits of LEO CubeSat missions. Therefore, montecarlo numerical simulations are performed, for a total of 100 different initial conditions selected considering an error up to 10% on the estimation of the moments of inertia and random initial: RAAN, true anomaly, inclination, altitude, attitude and angular rates. The range for the initial conditions were selected considering that the vast majority of CubeSat LEO missions are performed in sun-synchronous orbits which are almost circular ($e \leq 0.03$) and polar. In Table 6.2, the range for each initial condition is reported

Table 6.2. Initial conditions

Orbital elements
$\Omega, \theta \in [-180; 180] \; deg$
$i \in [80; 100] \; deg$
$h \in [400; 700] \; km$
Attitude
$\varphi, \vartheta, \psi \in [-180; 180] \; deg$
$\omega_x, \omega_y, \omega_z \in [-10; 10] \; deg/sec$

The detumbling and the angular rates estimation algorithms were tested first. The results of the integration (calculated for $K_d = 3e + 4$) are reported in Figure 6.2, showing the behavior of angular rates in time, and Figure 6.3, showing the error between the angular rates calculated by the ode solver and the ones estimated by the algorithm. A time equal to 3 orbital periods (T_o) is considered for the purpose of the analysis and it can be noticed that both the algorithms produce the expected result, with both the angular rates and the estimation errors approaching zero. The effectiveness of the detumbling can be evaluated in terms of the rotational kinetic energy, reported below

$$T_r = \frac{1}{2}\omega^T \mathbf{I} \omega \tag{6.24}$$

For all the initial conditions the rotational kinetic energy decreases by a factor 1000 and the error on the estimation of the angular rates enters the error band ± 0.2 deg/sec. In Table 6.3, the results for the worst case $\omega = [10, 10, 10] \; \text{deg}/sec$ are reported in detail. In here, detumbling and settling time indicate, respectively, the time required for $T_r(t)/T_r(t_0) = 1/1000$ and $max\{\omega_i\} \leq \pm 0.2$ deg/sec.

Table 6.3. Selected results for $\omega = [10, 10, 10] \; \text{deg}/sec$ and $i = 97.79$ deg

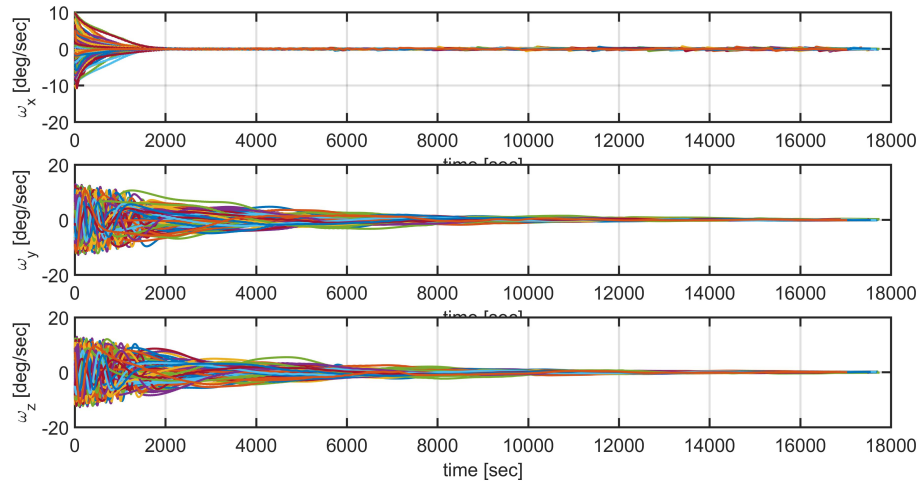| Altitude [km]	700	600	500	400
Detumbling time [sec]	7961	6228	5170	4374
Settling time [sec]	1454	1541	1102	1022

Figure 6.2. Behavior of angular rates during the deumbling for 100 initial conditions selected as in Table 6.2
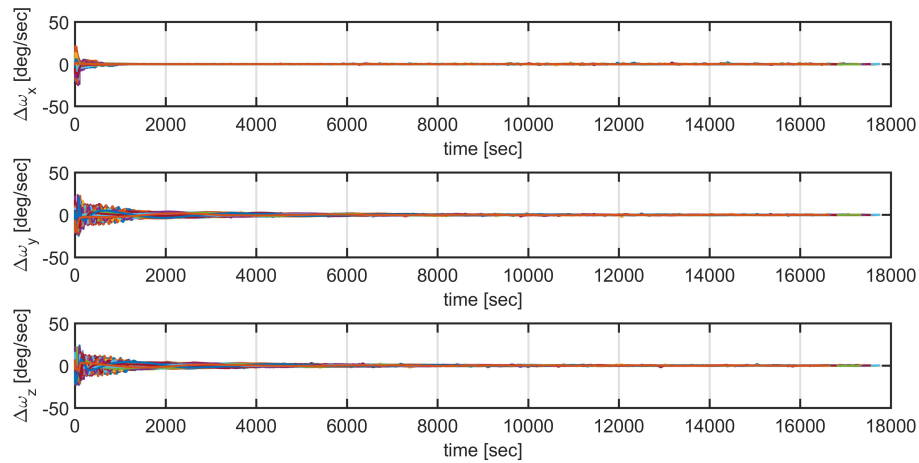

Figure 6.3. Error on the estimation of angular rates during the deumbling for 100 initial conditions selected as in Table 6.2

It is worth noting that the settling time is almost independent from the initial conditions. This aspect is further emphasized in Figures 6.4-6.6, showing the behavior of the estimation error with time for different values of f_k and considering an error of the 10% on J_x and J_y.
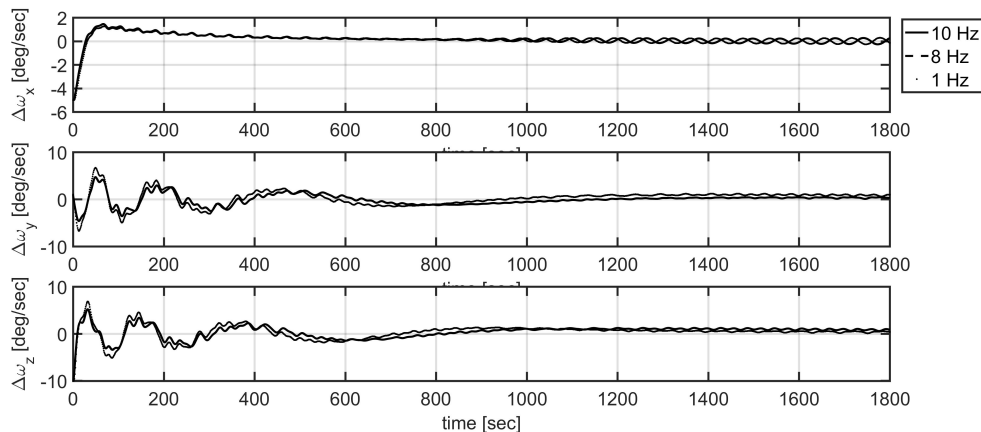
Figure 6.4. Estimation errors on angular rates for 1Hz (solid line), 8 Hz(dashed line) and 10 Hz (dotted line) sampling frequency
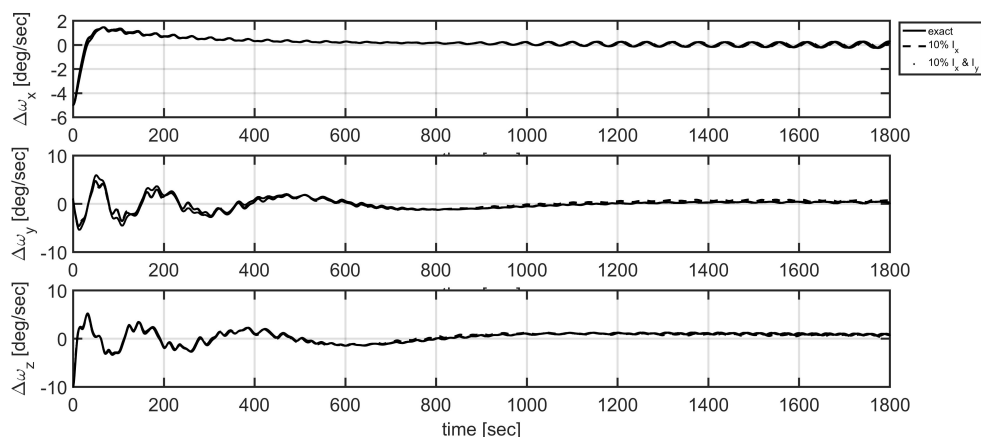
Figure 6.5. Estimation errors on angular rates for exact J_i (solid line), 10% error on J_x (dashed line) and 10% error on both J_x and J_y (dotted line)
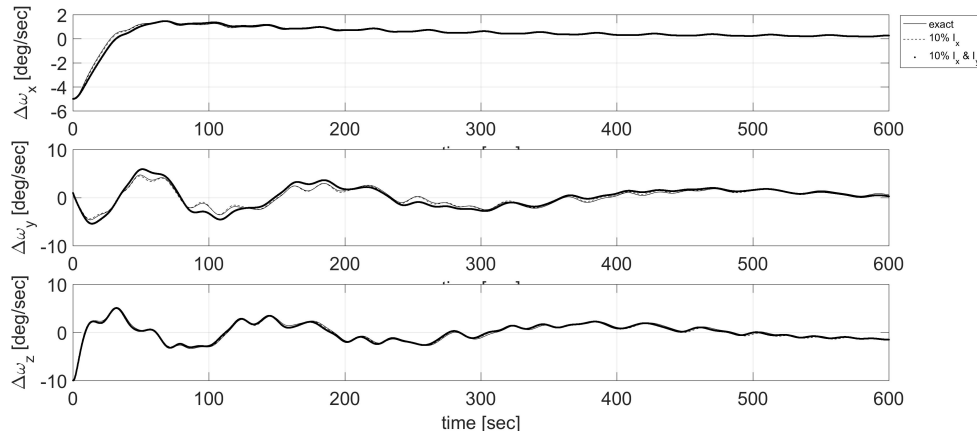
Figure 6.6. Detail of Figure 6.5 in the time interval 0-600 sec

The B-pointing and attitude estimation algorithms can then be verified using the same parameters in Table 6.1. It is worth recalling that the attitude estimation algorithm produces the attitude matrix $\mathbf{A}$. Estimating the error on the matrix produces results which are difficult to interpret, therefore a comparison in terms of the Euler angles is discussed first, for the above mentioned worst case $\omega = [10, 10, 10]$ deg $/sec$, $h = 700km$ and $i = 97.79$ deg. The effectiveness of B-pointing in producing the target attitude $\hat{r} = [1, 0, 0]$ can be examined from Figure 6.7.

The comparison between the Euler angles calculated by the ode solver and by the estimation algorithm, along with the corresponding errors, are shown in Figures 6.8 and 6.9. The final value of the errors can be evaluated from Figure 6.10 and are equal to $\Delta\varphi = 3.67$ deg, $\Delta\vartheta = 4.99$ deg and $\Delta\psi = 15.60$ deg.
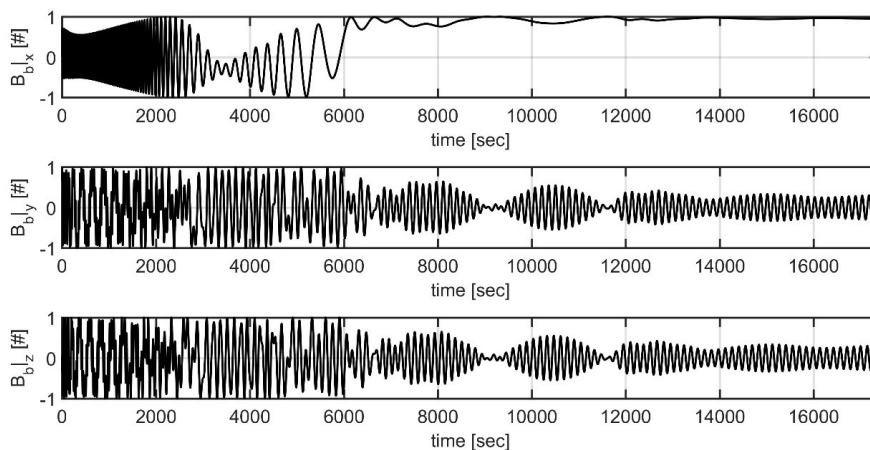

Figure 6.7. Attitude behavior with respect to geomagnetic field for $\omega = [10, 10, 10]$ deg $/sec$, $h = 700km$ and $i = 97.79$ deg
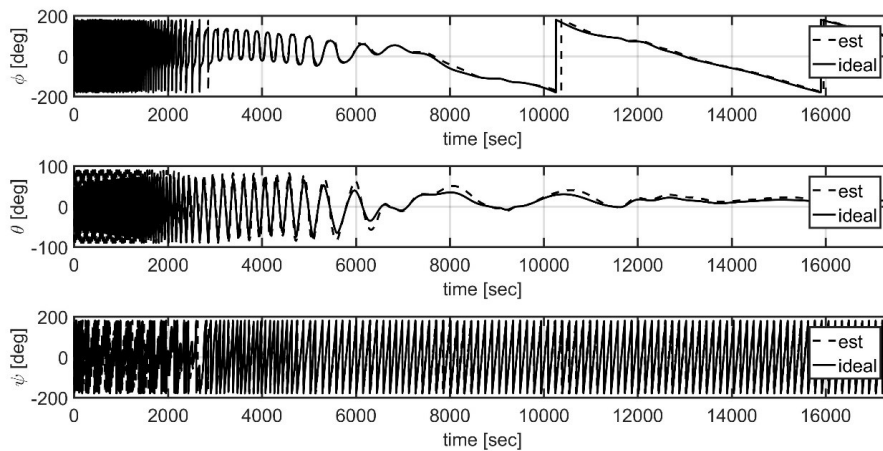
Figure 6.8. Behavior of Euler angles during the detumbling and B-pointing for $\omega = [10, 10, 10]$ deg$/sec$, $h = 700km$ and $i = 97.79$ deg
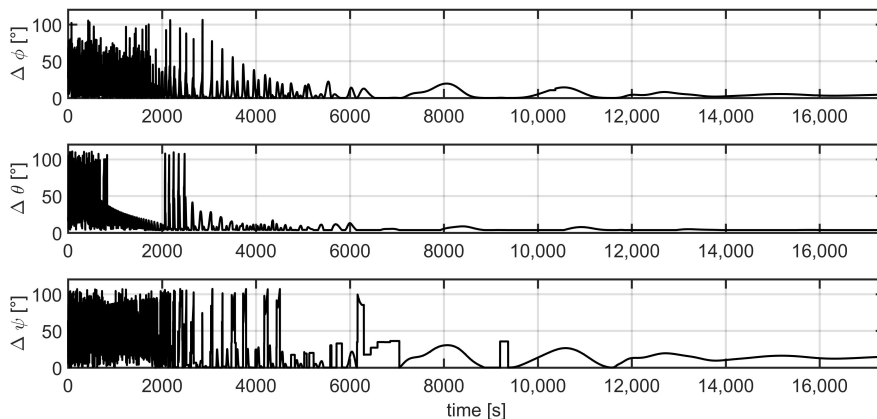

Figure 6.9. Error on the estimation of Euler angles during the detumbling and B-pointing for $\omega = [10, 10, 10]$ deg$/sec$, $h = 700km$ and $i = 97.79$ deg
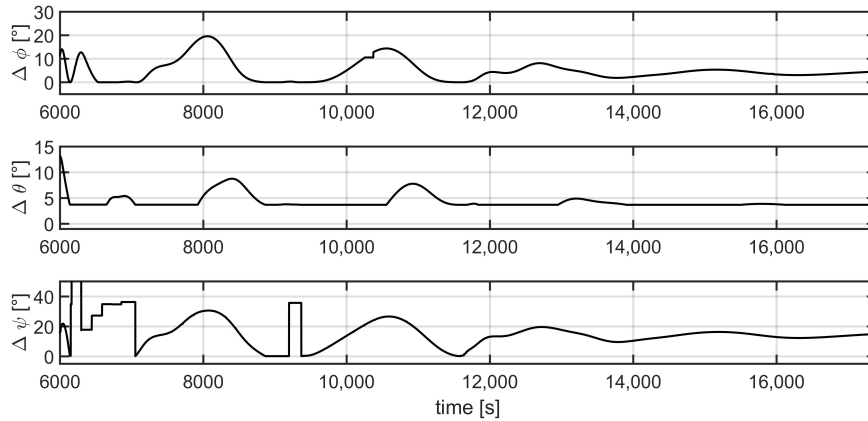
Figure 6.10. Detail of Figure 6.9 for angles in the range ± 30 deg

The Mean Squared Error (MSE) between the attitude matrix calculated from the results of the ode solver and from the attitude estimation algorithm is calculated for the mentioned case and represented in Figure 6.10. The final value of MSE for the test case considered assumes a final value of 1.172e-2, entering the $\pm 10\%$ error band (with respect to the final value) in 16680 sec. This tool can be used for montecarlo analysis over the 100 initial conditions previously introduced, aimed at evaluating the robustness of the algorithm. The values for the MSE of the simulations are shown in Figure 6.12
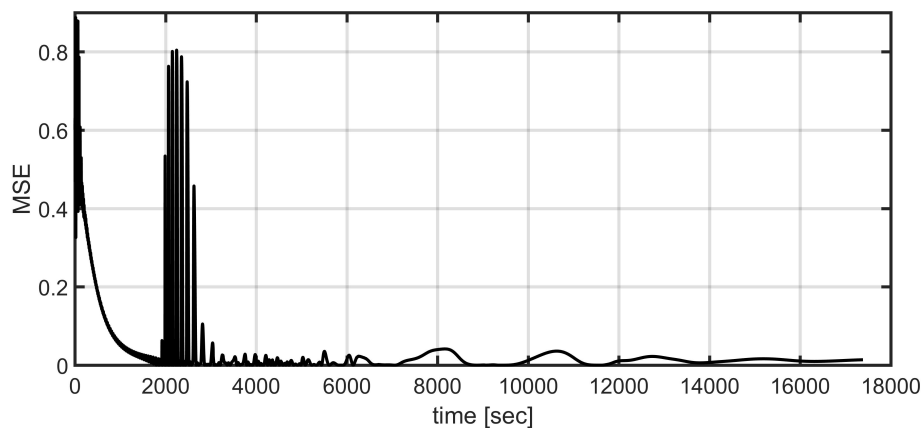

Figure 6.11. Meas Squared Error calculated for $\omega = [10, 10, 10]$ deg $/sec$, $h = 700km$ and $i = 97.79$ deg
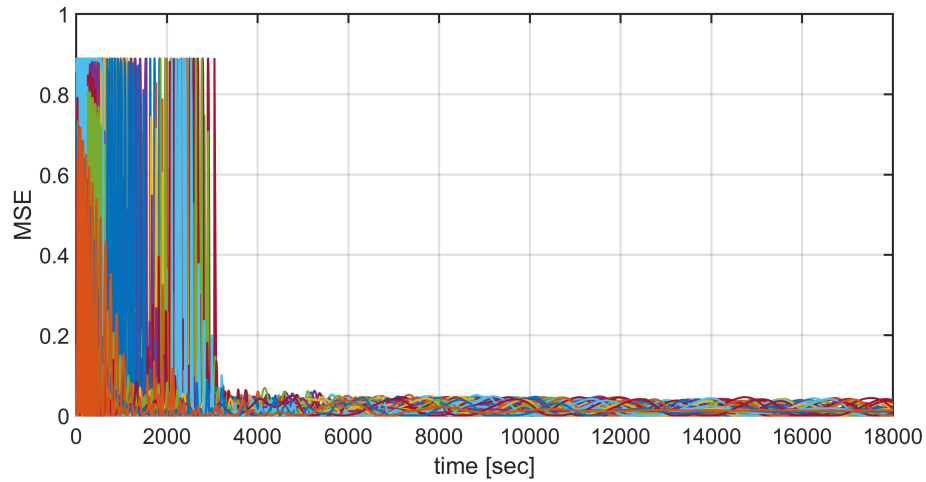
Figure 6.12. Behavior of the mean squared error with time during the detumbling and
B-pointing for 100 initial conditions selected as in Table 6.2

Figure 6.12 indicates that the maximum value for MSE can be as high as 0.04. This relatively high error is related to the low sampling frequency which can be simulated in Simulink, in order to limit the time of the simulations. In the next chapter, HiL simulations are performed on a real CubeSat OBC using a real magnetometer.

Chapter 7

Hardware implementation and experimental testing

The successful development of an ADCS starts from concept design and should include numerical and experimental validation of the algorithms and hardware, to confirm its performance and robustness in different operative scenarios. CubeSat ADCS are typically based on COTS sensors that are not specifically developed for space applications, and are often developed based on novel system architecture, such as the algorithms presented in chapter 6. For this reason, experimental testing should represent an essential part of the development process. Nevertheless, because of the limited budget and development time available for CubeSat missions, the effort dedicated to tests is limited and typically focused on numerical simulations, which do not provide any feedback regarding real hardware [169, 180].

It is known from statistical analysis that the majority of CubeSat mission end in failure right after the deployment. Even though, according to statistical analysis [101], the impact of ADCS failure on the number of "dead on arrival" CubeSats seems to be marginal, a system-oriented interpretation of the results provides a clearer view on the issue. In fact, if ADCS failures may not affect the functionality of the other on-board systems, they do not allow those systems to operate in the design conditions, jeopardizing the mission, eventually causing its failure. Some strategies for low-cost software-in-the-loop or even hardware-in-the-loop (HiL) testing of ADCS have been proposed in the recent past [37, 62, 162, 179], outlining suitable low-cost solutions to improve the reliability of CubeSat missions.

In this final chapter, the implementation of a Hardware-in-the-Loop (HiL) setup is discussed. The setup is used to test the ADCS algorithms presented in Chapter 6, evaluating their performance.

7.1 Hardware-in-the-loop setup

Numerical analysis in section 6.4 provided an overview of the performance of the ADCS algorithms previously introduced. Nevertheless, the characteristics of real hardware on which the mentioned algorithm should work were not taken into account. These are finally considered in HiL simulations discussed here. A sketch of the HiL setup is shown in Figure 7.1.

It consists of

- a $3 \times 3 \times 3 \ m^3$ Helmholtz cage [86], used to reproduce the Earth magnetic field $\mathbf{B}_i$ at any orbital position of the satellite, estimated by the orbital propagator running on the facility control computer (see below)

- FPGA-based OBC, on which the control algorithm are implemented and providing as output the electric current for the magnetorquers

- 12-bit MEMS three-axis magnetometer, measuring the magnetic field generated by the Helmholtz cage

- facility control computer, propagating the orbital motion to calculate $\mathbf{B}_i$ and integrating the attitude dynamics equations determining the Euler angles and angular rates.

In the HiL simulations presented, attitude dynamics is simulated using Matlab Simulink fixed step *ode8* integrator. The integration time for the software is synchronized with the time of the HiL simulations, which can be selected to be up to 10 times faster than real time.
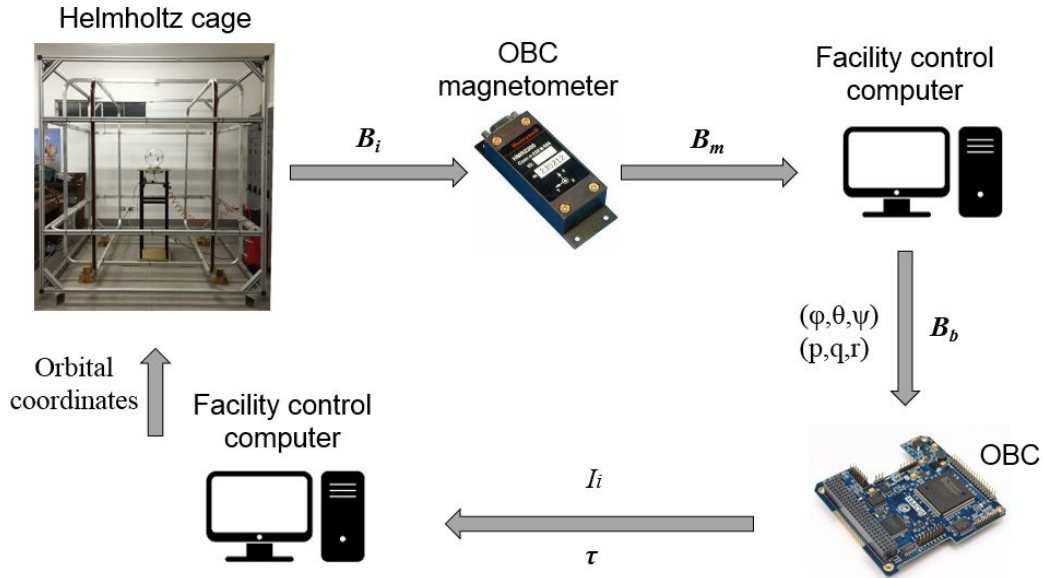

Figure 7.1. Sketch of the HiL setup

It is worth noting that, since the spacecraft attitude dynamics is simulated, the magnetometer will not read values of the magnetic field in $\mathcal{F}_b$ ($\mathbf{B}_b$), but in $\mathcal{F}_i$ instead ($\mathbf{B}_i$). Therefore, the coordinate transformation from ($\mathbf{B}_i$) to ($\mathbf{B}_b$) is performed at each iteration by Simulink, based on the values of ($\mathbf{B}_i$) measured by the magnetometer and the Euler angles calculated integrating system 6.2. The calculated value of ($\mathbf{B}_b$) is then processed by the OBC, to determine the magnetic dipole moment required to perform the detumbling and B-pointing control, according to equations 6.7 and 6.23. Once determined $\mathbf{m}$, the value of the current on the i-th

coil is calculated as $I_i = \frac{m_i}{N_i A_i}$ $(i = x, y, z)$ and sent to the power board, which feeds the magnetorquers.

The Helmholtz cage used is that of the Flight Mechanics Laboratory "Michele D. Sirinian", part of the School of Aerospace Engineering at Sapienza University of Rome [164]. The magnetic field generated by each pair of coils of the Helmholtz cage can be estimated by the following approximated relation

$$B = \frac{2\mu_0 N I_c}{\pi l} \frac{2}{\left(1 + \kappa^2\right)\sqrt{2 + \kappa^2}} \tag{7.1}$$

where μ_0 is the permeability of free space, $N = 54$ is the number of turns of each coil, $l = 1.24$ m is the half length of the side of the coils, $\kappa = 0.5445$ is the ratio of the distance between two coils and I_c is the electric current in the coils, whose determination is explained in the next paragraph. The facility was designed to operate in the range +/- 2 Gauss along each direction. The Helmholtz cage are activated and controlled by a system including

- 3 power supplies, each one feeding one pair of coils, allowing the generation of a magnetic field vector with desired intensity and direction

- a facility control computer, on which the orbital motion of the satellite is simulated, based on the input orbital parameters, and the corresponding value of $\mathbf{B}_i$ for each position of the satellite is calculated in real-time, using either the dipole or the IGRF model [36]

- a calibrated three-axis magnetometer, measuring the magnetic field in the central and constant region of the Helmholtz cage.

All the mentioned elements form a closed-loop system which operates according to a control code implemented in Matlab and operating as follows

1. the orbital propagator is updated and the target value of $\mathbf{B}_i$ is calculated

2. the facility control computer receives the measurement from the magnetometer $\mathbf{B}_m$

3. based on the error between the nominal and the measured value, $\mathbf{B}_i - \mathbf{B}_m$, a PID controller estimates the currents $I_{c,i}$ to be provided by the i-th power supply to recreate the desired $\mathbf{B}_i$

4. the i-th power supply is set to the corresponding $I_{c,i}$ and the magnetic field vector inside the cage is modified

5. the loop repeats until stop command is sent.

The duration of each cycle can be selected in the range $[0.1; 1]$ sec, therefore allowing accelerated simulations up to a factor 10.

The ADCS algorithms were implemented on the FPGA core of the CubeSat OBC ABACUS [130]. Because attitude and angular rates are determined in two different steps, the size of the vectors and matrices computed through the process are limited to 3×1 and 3×3. All the vector and matrix operations are rearranged

into the following matrix equation of size 3, which can be implemented on FPGA by means of the Faddeev algorithm [51], using a single systolic array architecture [14, 133, 176].

$$\mathbf{U} = \mathbf{W}\mathbf{X}^{-1}\mathbf{Y} + \mathbf{Z} \tag{7.2}$$

The angular rates estimation in equation 6.12 can be rearranged in a form suitable for systolic array implementation, by setting the following values for the matrices in equation 7.2

$$\begin{cases} \mathbf{W} = \left(\dot{\mathbf{B}}_b^{\mathbf{k}} \times \dot{\mathbf{B}}_b^{k} - 1\right)[1,1,1] \\ \mathbf{X} = \dot{\mathbf{B}}_b^{\mathbf{k}^T}\dot{\mathbf{B}}?\mathbf{k}_b\mathbf{1} \\ \mathbf{Y} = \mathbf{1} \\ \mathbf{Z} = \mathbf{0} \end{cases} \tag{7.3}$$

where $\mathbf{1}$ and $\mathbf{0}$ indicate the 3×3 identity and zero matrices.
Similarly, the attitude determination algorithm in equation 6.20 can be rearranged as follows

$$\begin{cases} \mathbf{W} = \left[\hat{b}_1\dot{:}\hat{b}_3\dot{:}\hat{b}_4\right] \\ \mathbf{X} = \left[\hat{r}_1\dot{:}\hat{r}_3\dot{:}\hat{r}_4\right] \\ \mathbf{Y} = \mathbf{1} \\ \mathbf{Z} = \mathbf{0} \end{cases} \tag{7.4}$$

7.2   Hardware-in-the-loop simulations

The HiL system discussed in section 7.1 allowed experimental verification of the algorithms presented in Chapter 6. Some relevant results are collected and commented hereafter, to provide a highlight on the performance and limits of the ADCS system.

The HiL simulations of the detumbling and B-pointing algorithms are discussed first, for the test cases reported in Table 7.1. The two algorithms are not applied at the same time, as for numerical simulations, because of the constraints on the power usage, fixed to 250 mW for each coil. The coils used in the setup have $N = 400$, $A = 9.03e - 3\ m^2$ and work at a supply voltage of $V_{drive} = 3$ V, consequently the current is limited to $I_{drive} = 83$ mA, corresponding to a maximum $|\mathbf{m}| = 0.3\ Am^2$ for each coil. The detumbling algorithm is applied first using a high value for K_d, then when the angular rates decrease to 0.01 deg/sec, the B-pointing is activated at $K_p = 30$ and lower $K_d = 500$.

Table 7.1. HiL parameters for three test cases (TC) at th deployment

Parameter	Symbol	Value
Altitude	h [km]	600
Inclination	i [deg]	97.79
Eccentricity	e	0
Euler angles	$[\varphi, \vartheta, \psi]$	$[0, 0, 0]$
Angular rates	$[\omega_x, \omega_y, \omega_z]$	$[5, 3, -3]$

Parameter	TC1	TC2	TC3
Only detumbling			
K_d	1000	1000	1000
K_p	0	0	0
Detumbling and B-pointing			
$\hat{r}$	$[1, 0, 0]$	$\left[0, 0.5\sqrt{2}, 0.5\sqrt{2}\right]$	$\left[0, 0.5\sqrt{2}, 0.5\sqrt{2}\right]$
K_d	500	500	500
K_p	30	30	30
Model	Dipole	Dipole	IGRF

The Euler angles with respect to the target attitude for the three test cases are reported in Figures 7.2-7.4, showing that the detumbling is successfully completed within 1.5 orbital periods and the B-pointing produces the desired attitude. The minimum[1], maximum and mean error on the Euler angles are estimated for all the test cases after a time corresponding to 5 orbital periods, and reported in Table 7.2

Table 7.2. Error on the Euler angles for the B-pointing algorithm without attitude determination

Error	TC1	TC2	TC3
$\Delta\varphi_{min}$	0.09	-8.38	-9.59
$\Delta\varphi_{max}$	18.78	9.24	7.38
$\Delta\varphi_{mean}$	4.98	0.01	-0.07
$\Delta\vartheta_{min}$	0.03	-9.41	-5.58
$\Delta\vartheta_{max}$	12.71	10.42	6.63
$\Delta\vartheta_{mean}$	0.03	-0.03	0.06
$\Delta\vartheta_{min}$	0.07	-9.73	-6.58
$\Delta\vartheta_{max}$	13.44	10.14	5.99
$\Delta\vartheta_{mean}$	0.06	-1.71	-0.04

It can be noticed that the error on the Euler angles for TC1 (< 19 deg/sec) is sensibly higher than that for TC2 and TC3 (< 11 deg/sec). Analysis of results from the HiL simulations, indicate that this is due to the selection of the target attitude. In fact, for $\hat{r} = [1, 0, 0]$ the ADCS will drive the satellite as long as the magnetic field measured $\hat{x}_b$ is equal to the magnitude of the magnetic field $|\mathbf{B}_b|$. Obviously,

---

[1]The minimum here indicates the maximum error with negative sign.

the measured value at time t can never exceed $|\mathbf{B}_b|$ then the control shows aperiodic behavior, limiting its accuracy. Differently, when the control is shared by two or more components, such as for $\hat{r} = \left[0, 0.5\sqrt{2}, 0.5\sqrt{2}\right]$, then the measurements in $\hat{y}_b$ and $\hat{z}_b$ can, at different times, exceed the target value $0.5\sqrt{2}|\mathbf{B}_b|$ and the behavior of the control is therefore oscillatory, about the target value. This can be proved by observing that the maximum and minimum error for for TC2 and TC3, reported in Table 2, are (almost) equally distributed about the mean value. This is not the case for TC1, in which the maximum value is much larger in magnitude than the minimum one.
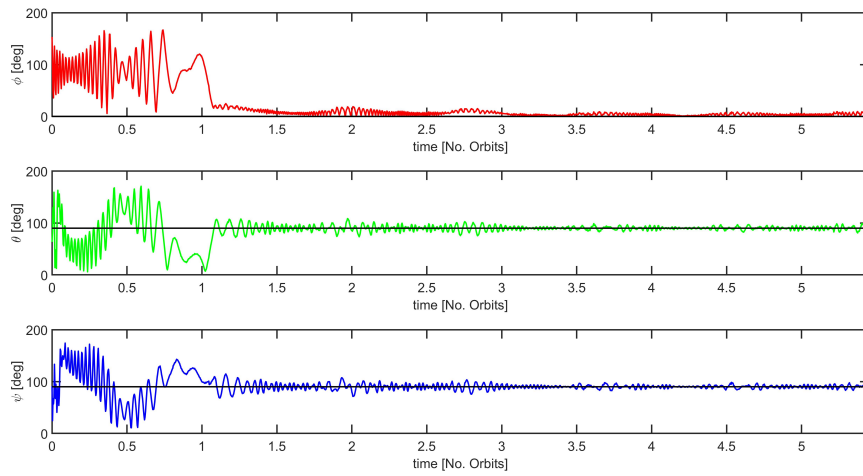

Figure 7.2. Euler angles for the Test Case 1, $\hat{r} = [1, 0, 0]$ and dipole model
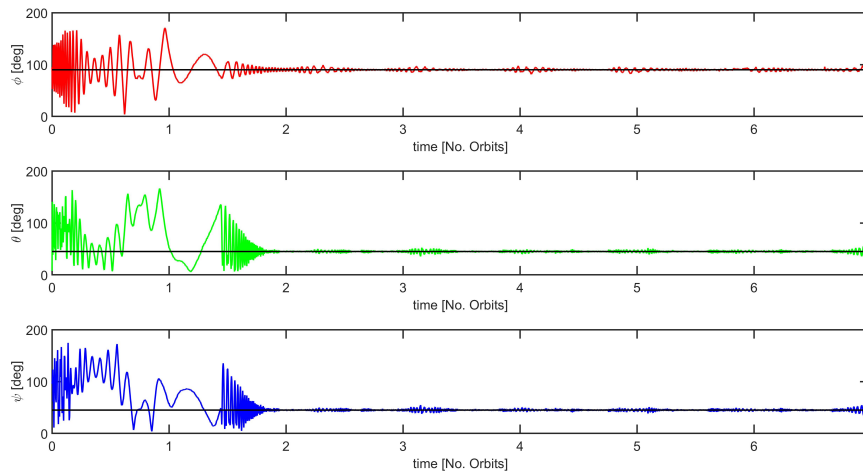

Figure 7.3. Euler angles for the Test Case 2, $\hat{r} = \left[0, 0.5\sqrt{2}, 0.5\sqrt{2}\right]$ and dipole model
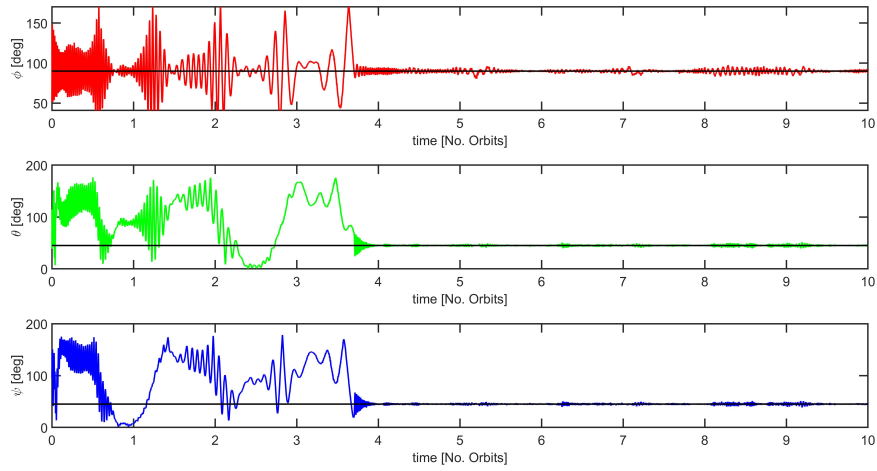
Figure 7.4. Euler angles for the Test Case 3, $\hat{r} = \left[0, 0.5\sqrt{2}, 0.5\sqrt{2}\right]$ and IGRF model

The behavior in time of the angular rates for the three test cases is plotted in Figures 7.5-7.7, showing that the dumbling phase is successfully concluded in 1.5 orbital periods at most, reaching the final value in the range ± 0.2 deg/sec.
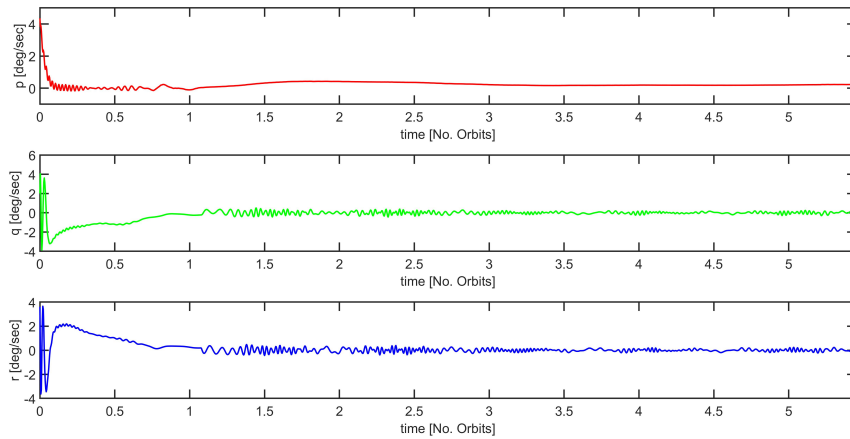

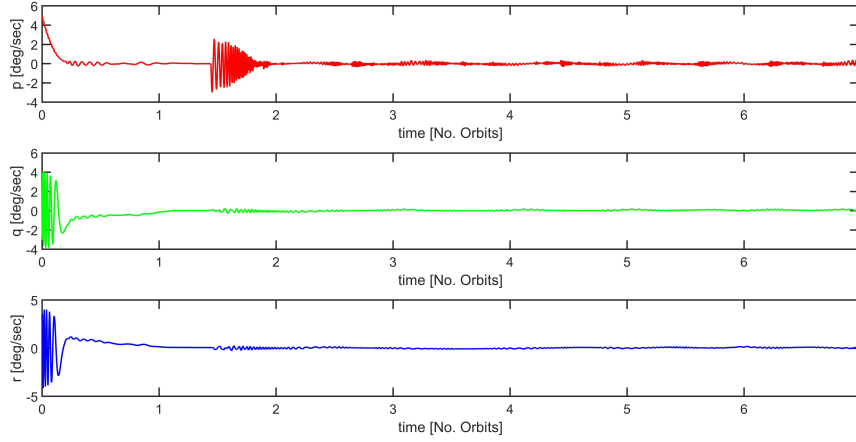**Figure 7.5.** Euler angles for the Test Case 1, $\hat{r} = [1, 0, 0]$ and dipole model

Figure 7.6. Euler angles for the Test Case 2, $\hat{r} = \left[0, 0.5\sqrt{2}, 0.5\sqrt{2}\right]$ and dipole model
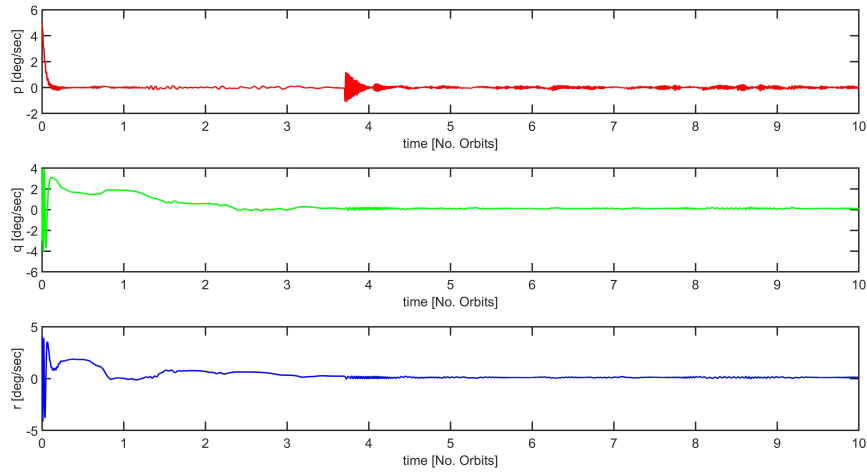

Figure 7.7. Euler angles for the Test Case 3, $\hat{r} = \left[0, 0.5\sqrt{2}, 0.5\sqrt{2}\right]$ and IGRF model

After validating the control section of the algorithm, the performance of the estimation algorithms are evaluated. These are implemented using systolic array architecture, based on the arrangement in equations 7.3 and 7.4, corresponding to the resources indicated in Table 7.3. As in section 6.4, the Euler angles inferred from the attitude estimation are compared to those calculated by the ode solver. The comparison and the error are reported in Figures 7.8 and 7.9 for the worst case $\omega = [10, 10, 10] \deg/sec$, $h = 700km$ and $i = 97.79$ deg. The maximum errors from HiL simulations are lower than those calculated from numerical analysis, and correspond to $\Delta\varphi = 3.96$ deg, $\Delta\vartheta = 2.69$ deg and $\Delta\psi = 1.41$ deg. The higher accuracy of the real system is related to the higher sampling frequency of the real hardware, corresponding to 100 Hz for the MEMS three-axis magnetometer and set to 1000 Hz for the OBC. In fact, these values can not be set for the numerical integrations, which are performed at a time step of 0.1 sec, to limit the computational

time. Also the value of the MSE on the estimated **A** converges to a considerably lower value, equal to 1.247e-8.
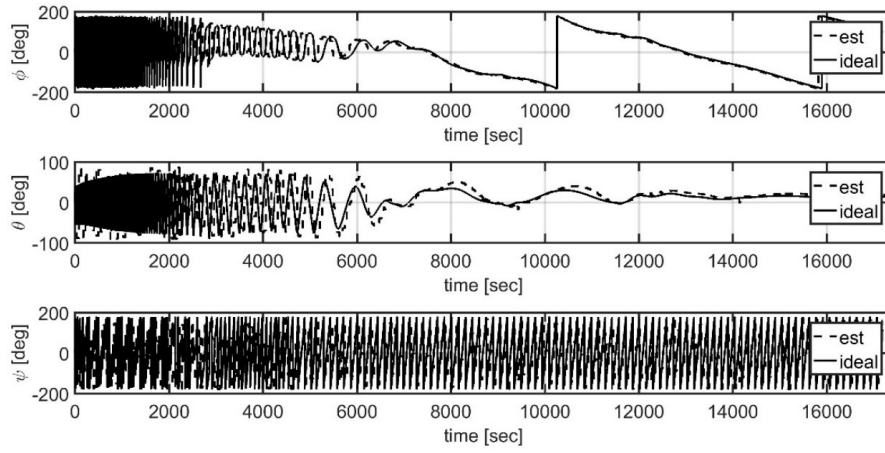

Figure 7.8. Behavior of Euler angles during the detumbling and B-pointing in HiL simulations for $\omega = [10, 10, 10]$ deg $/sec$, $h = 700km$ and $i = 97.79$ deg
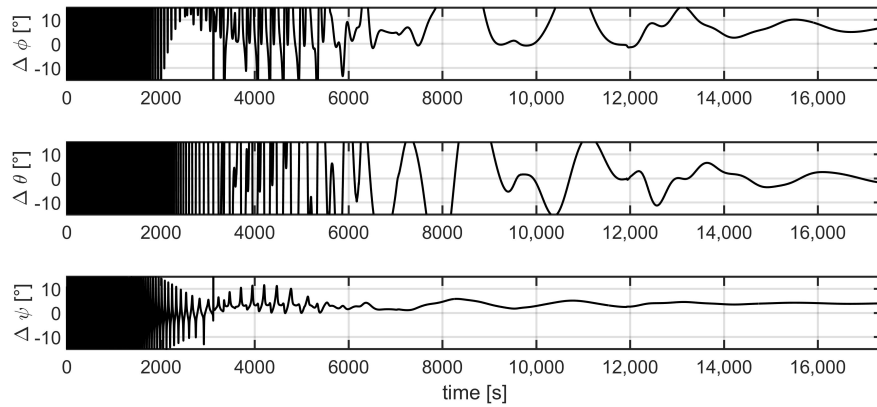

Figure 7.9. Error on the estimation of Euler angles during the detumbling and B-pointing in HiL simulations for $\omega = [10, 10, 10]$ deg $/sec$, $h = 700km$ and $i = 97.79$ deg
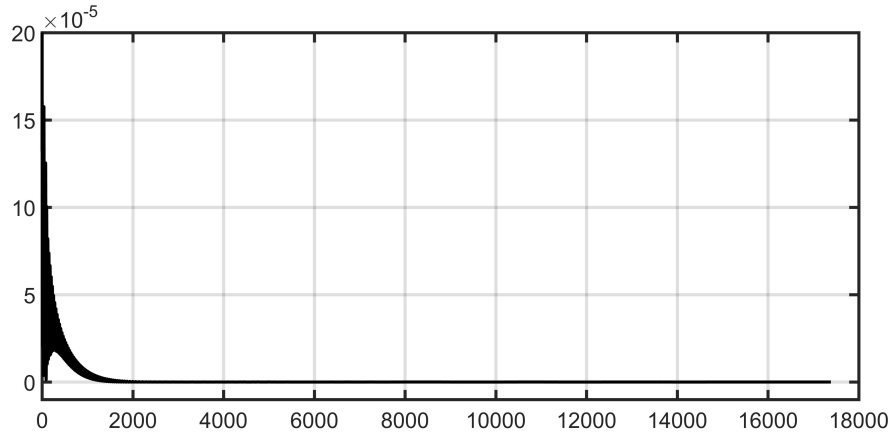
Figure 7.10. Mean Squared Error calculated in HiL simulations for $\omega = [10, 10, 10]$ deg $/sec$, $h = 700km$ and $i = 97.79$ deg

Table 7.3. Resources utilization and power required for the attitude and angular rates estimation algorithms

Resource	Utilization
Look Up Table	4738
Flip Flop	2576
DSP	30
Power [W]	0.277

Finally, the angular rates are examined, by comparison with the corresponding values from the ode solver, producing the estimation errors shown in Figure 7.11. The steady state error of ± 0.2 deg/sec is reached in the settling time of 11771 sec, approximately equal to 2 orbital periods.
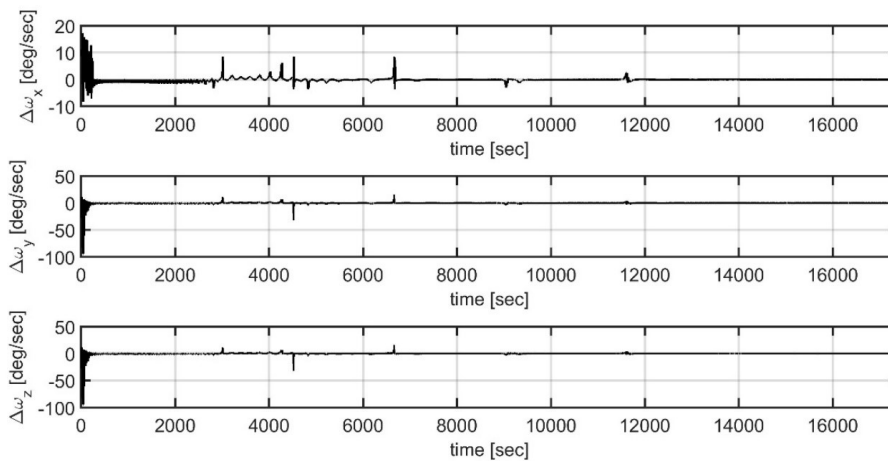
Figure 7.11. Error on the estimation of angular rates during the detumbling and B-pointing in HiL simulations for $\omega = [10, 10, 10]$ deg $/sec$, $h = 700km$ and $i = 97.79$ deg

In conclusion, the HiL simulations showed that the ADCS algorithms introduced in Chapter 6 and previously verified numerically, are suitable for being implemented with hardware commonly used on CubeSats. The performance of the implemented algorithms confirm those from numerical simulations, indicating the benefit of higher sampling frequency in producing a more accurate estimation on attitude. Constraints related to the power usage, the properties of the power board and of the actuators, limit the maximum magnetic dipole moment, thus the maximum control action. This must be split into two segments, producing first the detumbling and then the B-pointing. The change between the two phases is produced by a modification of the control gains for the two algorithms. Taking advantage of the determination algorithms, the switching condition can be defined in terms of the angular rates, activating it when their value is smaller than some selected threshold.

Chapter 8

Conclusions

This manuscript collects three years of research that focuses on space science missions and aims at providing new techniques which can enhance solar system exploration and low Earth orbit missions using CubeSats.

Low-energy trajectories are needed to achieve orbital transfers between the celestial bodies in the solar system by means of small satellites. In particular, limiting the transfer time is a strict constraint when using CubeSats, because their on-board systems are based on COTS devices, which are not designed to operate in the hostile space environment beyond Earth. Internal transfers, existing in the dynamical framework of the CR3BP were selected based on this consideration. A Hamiltonian description of the phase space surrounding the collinear equilibrium points L_1 or L_2, named the equilibrium region, was produced and the flow mappings in this region were investigated. The analysis allowed characterizing three-dimensional transit and capture orbits, based on their topological location in the equilibrium region. Furthermore, correlations between the capture time and the behavior of the osculating orbital elements at capture were identified for long-term ballistic captures.

The effects of the gravitational perturbation by a fourth body, such as the Sun, were evaluated, proving they can have dramatic impact on the topological description provided for the CR3BP. To mitigate or compensate these effects, low-thrust guidance strategies were developed, allowing powered permanent capture and adjusting the osculating orbital elements at capture. A comparative analysis was set, verifying that the continuous thrust required is lower than that for traditional impulsive maneuvers. Furthermore, the availability of thrusters compatible with the thrust requirements for different scenarios was investigated. The analysis indicates that recent ion-thrusters are suitable devices to produce permanent capture and make small corrections to the orbital elements. When significant changes are required, the use of monoprop thrusters seems to be the only solution compatible with CubeSat mass, volume and power constraints.

The model proposed for the CR3BP was finally extended to the ER4BP, which allows taking into account the presence of a fourth body, such as the Sun, and the eccentric motion of the primaries from the early analysis (or design) phase. The use of canonical transformations allowed defining a new set of coordinates that sets the Hamiltonian function for the ER4BP in a form equivalent to that of the CR3BP in the neighborhood of L_1 and L_2. Therefore, the systematic topological description of

transit trajectories and capture orbits, obtained for the CR3BP, was extended to the ER4BP. The advantage introduced using this model can be expressed in terms of: (1) extended launch window, capture conditions were in fact verified regardless the position of the primary causing the perturbation, and (2) savings in ΔV required, because the higher accuracy of the model produces a more accurate injection into the target orbit, therefore reducing the use of thrusters for orbital corrections.

For CubeSats operating in LEO, new techniques aimed at improving the reliability of the ADCS were investigated, and discussed in the two final chapters of the manuscript. A purely magnetic ADCS was developed, including two control algorithms, producing the detumbling and pointing of the spacecraft, and two estimation algorithms, to determine the angular rates and the attitude matrix, based only on the input of a three-axis magnetometer. The algorithms were verified by means of numerical analysis, proving their suitability in producing the desired tasks. In particular, the detumbling algorithm is an implementation of the classical B-dot algorithm, which ensures the orthogonality condition between the control vector, the magnetic dipole moment produced by the magnetorquers, and the geomagnetic field vector, increasing the efficiency. Magnetic pointing is performed without any attitude information, with accuracy down to 10 deg, suitable for the ADCS proposed, which is meant to be a backup solution to be activated if some complex scenarios do not allow the correct use of the primary system or strategy. Attitude and angular rate determination algorithm were verified as well, proving their robustness under unknown or uncertain conditions at the deployment, by means of montecarlo simulations.

A final verification on the performance and robustness of the ADCS was performed by means of HiL simulations, using a Helmholtz cage facility to recreate the magnetic environment along the orbit and a real device, a 12-bit MEMS three-axis magnetometer. The algorithms were implemented on the FPGA core of a CubeSat OBC, after arranging them in the form of the Faddeev algorithm. This allows taking advantage of systolic array architecture to increase the usage efficiency of the OBC. HiL simulations verified the suitability of the control algorithms, proving the results obtained from the numerical analysis, and allowed defining the accuracy of the angular rate and attitude estimation algorithms, lower than, respectively, 0.2 deg/sec and 5/deg.

Even though the characterizing features of solar system and LEO mission show different criticality and readiness level, the research performed for this thesis indicates that, regardless of the aim of the mission, the development of space science using CubeSats is now mature enough to lead the development of, and take advantage from, new dedicated techniques for mission analysis, supporting the project from the early design phase to experimental test.

Appendix

Appendix A - Power series expansion of the non polynomial terms of the Hamiltonian function for the CR3BP

The Hamiltonian function for the CR3BP is expressed by equation 2.21 which, for the sake of clarity, is reported below

$$H = \frac{1}{2}(p_1^2 + p_2^2 + p_3^2) + (p_1 q_2 - p_2 q_1) - \left(\frac{1-\mu}{r_1} + \frac{\mu}{r_2}\right)$$

Translating the origin of the system at L_i

$$\begin{cases} \tilde{q}_1 = q_1 - L_{i,x} \\ \tilde{p}_2 = p_2 - L_{i,x} \end{cases}$$

The Hamiltonian function, up to an inessential constant, can be written as follows

$$H = \frac{1}{2}\left(p_1^2 + \tilde{p}_2{}^2 + p_3^2\right) + (p_1 q_2 - \tilde{p}_2 \tilde{q}_1) - \tilde{q}_1 L_{i,x} - \left(\frac{1-\mu}{r_1} + \frac{\mu}{r_2}\right) \tag{8.1}$$

The previous equation can be rearranged in a linear form after expanding in power series the non polynomial terms, given below

$$\frac{1-\mu}{r_1} = \frac{1-\mu}{\left[(\tilde{q}_1 + \mu + L_{i,x})^2 + q_2^2 + q_3^2\right]^{\frac{1}{2}}}$$

$$\frac{\mu}{r_2} = \frac{\mu}{\left[(\tilde{q}_1 - 1 + \mu + L_{i,x})^2 + q_2^2 + q_3^2\right]^{\frac{1}{2}}}$$

Introducing the auxiliary variables

$$\xi = \frac{2\tilde{q}_1 (L_{i,x} + \mu) + \tilde{q}_1{}^2 + q_2^2 + q_3^2}{(L_{i,x} + \mu)^2}$$

$$\eta = \frac{2\tilde{q}_1 (L_{i,x} + \mu - 1) + \tilde{q}_1{}^2 + q_2^2 + q_3^2}{(L_{i,x} + \mu - 1)^2}$$

Then the non polynomial terms can be rearranged as follows

$$\frac{1-\mu}{r_1} = \frac{1-\mu}{|L_{i,x} + \mu| (1 + \xi)^{\frac{1}{2}}}$$

$$\frac{\mu}{r_2} = \frac{\mu}{|L_{i,x} + \mu - 1| (1 + \eta)^{\frac{1}{2}}}$$

Therefore, the non polynomial terms can be set in a linear form from selecting the second order terms of the expansions in ξ and η

$$\frac{1 - \mu}{r_1} = \frac{1 - \mu}{|L_{i,x} + \mu|} \left(1 - \frac{1}{2}\xi + \frac{1 \cdot 3}{2 \cdot 4}\xi^2 + \frac{1 \cdot 3 \cdot 5}{2 \cdot 4 \cdot 6}\xi^3 + o(\xi^4)\right) \approx \frac{1 - \mu}{|L_{i,x} + \mu|} \left(1 - \frac{1}{2}\xi\right)$$

$$\frac{\mu}{r_2} = \frac{1 - \mu}{|L_{i,x} + \mu - 1|} \left(1 - \frac{1}{2}\eta + \frac{1 \cdot 3}{2 \cdot 4}\eta^2 + \frac{1 \cdot 3 \cdot 5}{2 \cdot 4 \cdot 6}\eta^3 + o(\eta^4)\right) \approx \frac{1 - \mu}{|L_{i,x} + \mu - 1|} \left(1 - \frac{1}{2}\eta\right)$$

Producing the second order Hamiltonian function

$$H_2 = \frac{1}{2} \left(p_1^2 + \tilde{p_2}^2 + p_3^2\right) + (p_1 q_2 - \tilde{p_2}\tilde{q_1}) - \tilde{q_1}\left[L_{i,x} - \left(\frac{1 - \mu}{(L_{i,x} + \mu)^2} - \frac{\mu}{(L_{i,x} + \mu - 1)^2}\right)\right] +$$

$$- \frac{1 - \mu}{|L_{i,x} + \mu|^3}\left(\tilde{q_1}^2 - \frac{1}{2}q_2^2 - \frac{1}{2}q_3^2\right) - \frac{\mu}{|L_{i,x} + \mu - 1|^3}\left(\tilde{q_1}^2 - \frac{1}{2}q_2^2 - \frac{1}{2}q_3^2\right) \qquad (8.2)$$

According to the definition of $L_{i,x}$, the term in square brackets is zero, then equation 8.2 reduces to equation 2.23

$$H_2 = \frac{1}{2} \left(p_1^2 + \tilde{p_2}^2 + p_3^2\right) + (p_1 q_2 - \tilde{p_2}\tilde{q_1}) - K\left(\tilde{q_1}^2 - \frac{1}{2}q_2^2 - \frac{1}{2}q_3\right)$$

with $K = \frac{1 - \mu}{|L_{i,x} + \mu|^3} + \frac{\mu}{|L_{i,x} - 1 + \mu|^3}$.

Appendix B - Power series expansion of the non polynomial terms of the Hamiltonian function for the Sun-Earth-Moon ER4BP

In this appendix, the series expansions in equation 5.20 are developed in detail. We consider first the expansion in e, reported below

$$\frac{\partial F}{\partial e}\Big|^\star = \frac{\partial K(\theta)}{\partial e}\Big|^\star \left[\frac{\mu_2}{r_2^\star} + \frac{\mu_3}{r_3^\star} + \frac{1}{2}\left(q_1^2 + q_2^2 + q_3^2\right)\right] + K^\star \left[\sum_{i=1}^{3} \frac{\mu_i}{r_i} \frac{\partial 1/r_i}{\partial e}\right]^\star$$

where the superscript $\star$ indicates the function evaluated at point $(e = 0, e_b = 0, \mu_1/a = 0)$. Noting that $\frac{\partial K}{\partial e} = -\cos\theta$, $K^\star = 1$, $\frac{\partial 1/r_i}{\partial e}\Big|^\star = -\frac{1}{2r_i^3}\frac{\partial \rho_i}{\partial e}$ and

$$\begin{cases} \frac{\partial \rho_1}{\partial e}\Big|^\star = 0 \\ \frac{\partial \rho_2}{\partial e}\Big|^\star = [2a_b\mu_3 \cos\theta \left(a_b\mu_3 + aq_1 \cos\beta \cos\epsilon - aq_2 \sin\beta \cos\epsilon + aq_3 \sin\epsilon\right)] / a^2 \\ \frac{\partial \rho_3}{\partial e}\Big|^\star = -[2a_b\mu_2 \cos\theta \left(-a_b\mu_2 + aq_1 \cos\beta \cos\epsilon + aq_2 \sin\beta \cos\epsilon + aq_3 \sin\epsilon\right)] / a^2 \end{cases}$$

then $\frac{\partial F}{\partial e}\Big|^\star$ can be rearranged as follows

$$\frac{\partial F}{\partial e}\Big|^\star = -\cos\theta \left[\frac{\mu_2}{r_2^\star} + \frac{\mu_3}{r_3^\star} + \frac{1}{2}\left(q_1^2 + q_2^2 + q_3^2\right)\right] +$$

$$-\frac{\mu_2\mu_3 a_b\cos\theta}{a}\left(q_1\cos\beta\cos\epsilon - q_2\sin\beta\cos\epsilon + q_3\sin\epsilon\right)\left(\frac{1}{r_3^3|^\star} - \frac{1}{r_2^3|^\star}\right) - \frac{\mu_2\mu_3 a_b^2\cos\theta}{a^2}\left(\frac{\mu_3}{r_3^3|^\star} - \frac{\mu_2}{r_2^3|^\star}\right)$$

Similarly for the expansion in e_b

$$\frac{\partial F}{\partial e_b}|^\star = K^\star\left[\sum_{i=1}^3 \frac{\mu_i}{r_i}\frac{\partial 1/r_i}{\partial e_b}\right]^\star$$

Including the values

$$\begin{cases} \frac{\partial \rho_1}{\partial e_b}|^\star = 0 \\ \frac{\partial \rho_2}{\partial e_b}|^\star = \left[2a_b\mu_3\cos\theta_b\left(a_b\mu_3 + aq_1\cos\beta\cos\epsilon - aq_2\sin\beta\cos\epsilon + aq_3\sin\epsilon\right)\right]/a^2 \\ \frac{\partial \rho_3}{\partial e}|^\star = -\left[2a_b\mu_2\cos\theta_b\left(-a_b\mu_2 + aq_1\cos\beta\cos\epsilon + aq_2\sin\beta\cos\epsilon + aq_3\sin\epsilon\right)\right]/a^2 \end{cases}$$

Produces

$$\frac{\mu_2\mu_3 a_b\cos\theta_b}{a}\left(q_1\cos\beta\cos\epsilon - q_2\sin\beta\cos\epsilon + q_3\sin\epsilon\right)\left(\frac{1}{r_3^3|^\star} - \frac{1}{r_2^3|^\star}\right) - \frac{\mu_2\mu_3 a_b^2\cos\theta_b}{a^2}\left(\frac{\mu_3}{r_3^3|^\star} - \frac{\mu_2}{r_2^3|^\star}\right)$$

Finally the expansion in μ_1/a must be evaluated to complete the process

$$\frac{\partial F}{\partial \mu_1/a}|^\star = K^\star\left[\frac{1}{r_1^3|^\star} + \mu_2\frac{\partial 1/r_2}{\partial \mu_1/a}|^\star + \mu_3\frac{\partial 1/r_3}{\partial \mu_1/a}|^\star\right] = \frac{1}{r_1^3|^\star} - \frac{\mu_2}{r_2^3|^\star}\frac{\partial \rho_2}{\partial \mu_1/a} - \frac{\mu_3}{r_3^3|^\star}\frac{\partial \rho_3}{\partial \mu_1/a}$$

The first term can be neglected, because the system is studied in the proximity of the binary system. The remaining terms can be calculated introducing the following values for the partial derivatives

$$\begin{cases} \frac{\partial \rho_1}{\partial \mu_1/a} = -2\left(q_1 + 1\right) \\ \frac{\partial \rho_2}{\partial \mu_1/a} = \frac{2a_b\mu_3\sin\epsilon(aq_3 + a_b\mu_3\sin\epsilon)}{a} - \frac{2(aq_1 + a_b\mu_3\cos\beta\cos\epsilon)(a - a_b\mu_3\cos\beta\cos\epsilon)}{a} + \\ -\frac{2a_b\mu_3\cos\epsilon\sin\beta(aq_2 - a_b\mu_3\sin\beta\cos\epsilon)}{a} \\ \frac{\partial \rho_3}{\partial \mu_1/a} = -\frac{2a_b\mu_2\sin\epsilon(aq_3 - a_b\mu_3\sin\epsilon)}{a} - \frac{2(aq_1 + a_b\mu_3\cos\beta\cos\epsilon)(a + a_b\mu_2\cos\beta\cos\epsilon)}{a} + \\ -\frac{2a_b\mu_2\cos\epsilon\sin\beta(aq_2 + a_b\mu_2\sin\beta\cos\epsilon)}{a} \end{cases}$$

Appendix C - Linear form for the Hamiltonian function for the Sun-Earth-Moon ER4BP

System 5.16 is linearized about the collinear libration point L_1 or L_2 of the CR3BP, with coordinates $L_i = [L_{i,x}, 0, 0, 0, L_{i,x}, 0]$. The goal is achieved by series expansion of equation 5.18 up to second order terms in q_i and p_i. The result is equivalent to the linear Hamiltonian function for the CR3BP and a perturbation term which can be absorbed, as shown in Appendix D by a canonical transformation. As a first step, the origin of the coordinate system is translated to L_i, by applying $\tilde{q}_1 = q_1 - L_x$ and $\tilde{p}_2 = p_2 - L_x$. Then introducing the mass parameter $\mu = \mu_3/(\mu_2 + \mu_3)$, the non-polynomial terms of equation 5.18 can be rearranged as in Appendix A

$$\frac{\mu_2}{r_2^\star} = \frac{1 - \mu}{|L_{i,x} + \mu|\left(1 + \xi\right)^{1/2}}$$

$$\frac{\mu_2}{r_2^{\star}} = \frac{1 - \mu}{|L_{i,x} + \mu| \, (1 + \eta)^{1/2}}$$

producing

$$\begin{cases} \frac{\mu_2}{r_2^{\star}} = \frac{1-\mu}{|L_{i,x}+\mu|^3} \frac{1-\mu}{|L_{i,x}+\mu|^3} \left(\tilde{q}_1^2 - \frac{1}{2}q_2^2 - \frac{1}{2}q_3^2 \right) \\ \frac{\mu_3}{r_3^{\star}} = \frac{\mu}{|L_{i,x}+\mu-1|^3} \frac{\mu}{|L_{i,x}+\mu-1|^3} \left(\tilde{q}_1^2 - \frac{1}{2}q_2^2 - \frac{1}{2}q_3^2 \right) \end{cases}$$

$$\begin{cases} \frac{1-\mu}{r_2^3|^{\star}} = \frac{1-\mu}{|L_{i,x}+\mu|^5} \frac{1-\mu}{|L_{i,x}+\mu|^5} \left(\tilde{q}_1^2 - \frac{5}{2}q_2^2 - \frac{5}{2}q_3^2 \right) \\ \frac{\mu}{r_3^3|^{\star}} = \frac{\mu}{|L_{i,x}+\mu-1|^5} \frac{\mu}{|L_{i,x}+\mu-1|^5} \left(\tilde{q}_1^2 - \frac{5}{2}q_2^2 - \frac{5}{2}q_3^2 \right) \end{cases}$$

Introducing the previous values into equation 5.18 results into equation 5.21.

Appendix D - Canonical transformation absorbing perturbation terms for the Sun-Earth-Moon ER4BP

The second order terms in e, e_b and μ_1 of equation 5.21 can be absorbed by a canonical transformation $(\mathbf{q}, \mathbf{p}, \theta_b, \theta) \to (\mathbf{Q}, \mathbf{P})$ defined from the generating function S verifying equation 5.23. If the transformed coordinates 5.23 are introduced into equation 5.21, the perturbation terms can be expressed as follows

$$F_2 = E_1 \left(\theta_b, \theta \right) Q_1 + E2 \left(\theta_b, \theta \right) Q_2 + E_3 \left(\theta_b, \theta \right) Q_3 + E_4 \left(\theta_b, \theta \right)$$

The generating function can be determined starting from the general form of order two reported below

$$S = q_1 P_1 + q_2 P_2 + q_3 P_3 + f_1 \left(\theta_b, \theta \right) q_1 + f_2 \left(\theta_b, \theta \right) P_2 + f_3 \left(\theta_b, \theta \right) q_2 + f_4 \left(\theta_b, \theta \right) P_1 + f_5 \left(\theta_b, \theta \right) q_3 + f_6 \left(\theta_b, \theta \right) P_3$$

where the functions fi are selected according to the form of E_i, such as

$$f_i \left(\theta_b, \theta \right) = b_1^i \cos \theta + b_2^i \sin \theta + b_3^i \cos \beta + b_4^i \sin \beta$$

The change of coordinates associated to transformation is reported below

$$\begin{cases} q_1 = Q_1 - f_4 \\ q_2 = Q_2 - f_2 \\ q_3 = Q_3 - f_6 \end{cases} \qquad \begin{cases} p_1 = P_1 + f_1 \\ p_2 = P_2 + f_3 \\ p_3 = P_3 + f_5 \end{cases}$$

Introducing the above listed coordinates leads to the following expression (where the superscript $'$ indicates the derivative with respect to θ).

Then the value of the coefficients b_j^i must be selected to produce equation 5.24, corresponding to the following conditions

$$\begin{cases} -f_3 + 2 \left(\frac{\mu}{|L_{i,x}+\mu|^3} + frac1 - \mu |L_{i,x} + \mu - 1|^3 \right) f_4 + f_1' + E_1 = 0 \\ -f_1 - \left(\frac{\mu}{|L_{i,x}+\mu|^3} + frac1 - \mu |L_{i,x} + \mu - 1|^3 \right) f_2 + f_3' + E_2 = 0 \\ - \left(\frac{\mu}{|L_{i,x}+\mu|^3} + frac1 - \mu |L_{i,x} + \mu - 1|^3 \right) f_6 + f_5' + E_3 = 0 \\ f_1 - f_2 + f_4' = 0 \\ f_3 + f_4 + f_2' = 0 \\ f_5 + f_6' = 0 \end{cases}$$

The solutions, determined using symbolic algebra and the software Matlab, are reported below

$$b_1^1 = -E_2 \cos\theta + \frac{\mu}{|L_{i,x} + \mu|^3} \cos\theta + \frac{1-\mu}{|L_{i,x} + \mu - 1|^3} \cos\theta + E_1 \sin\theta$$

$$b_2^1 = \frac{\frac{\mu}{|L_{i,x} + \mu|^3} \cos\theta + \frac{1-\mu}{|L_{i,x} + \mu - 1|^3} \cos\theta + E_1 \sin\theta - E_2 \cos\theta}{\tan\theta}$$

$$b_1^2 = -\cos\theta \left(\frac{\mu}{|L_{i,x} + \mu|^3} + \frac{1-\mu}{|L_{i,x} + \mu - 1|^3} - E_2 \right)$$

$$b_1^2 = -\frac{\cos^2\theta}{\sin\theta} \left(\frac{\mu}{|L_{i,x} + \mu|^3} + \frac{1-\mu}{|L_{i,x} + \mu - 1|^3} - E_2 \right)$$

$$b_1^3 = -\frac{\frac{\mu}{|L_{i,x} + \mu|^3} + \frac{1-\mu}{|L_{i,x} + \mu - 1|^3} - E_2}{\sin\theta}$$

$$b_1^5 = E_3 \sin\theta$$

$$b_2^5 = -E_3 \cos\theta$$

All the b_j^i not indicated are equal to zero.

Appendix E - Power series expansion of the non polynomial terms of the Hamiltonian function for the Jupiter-Europa-Io ER4BP

The Hamiltonian function for the Jupiter-Europa-Io system modeled in the ER4BP is introduced in equation 5.28. The perturbations related to e and μ_3 can be isolated by expanding the non-polynomial terms as reported below

$$F(e, \mu_3) = \tau \left[\sum_{i=1}^{3} \frac{\mu_i}{r_i} + \frac{1}{2} \left(q_1^2 + q_2^2 + q_3^2 \right) \right] = F^* + e \frac{\partial F}{\partial e}|^* + \mu_3 \frac{\partial F}{\partial \mu_3}|^* + o(e, \mu_3)$$

where the superscript * indicates the function evaluated at point $(e = 0, \mu_3 = 0)$. It can be noticed that $K(\theta)^\star = 1$ and $R(t)^\star = a$, therefore the term $F^\star$ can be expressed as follows

$$F^\star = \left[\frac{\mu_1}{r_1^*} + \frac{\mu_2}{r_2^*} + \frac{1}{2} \left(q_1^2 + q_2^2 + q_3^2 \right) \right] \tag{8.3}$$

Similarly, the dimensionless distances $r_i^\star$ are determined based on the results $a_1^\star = 0$ and $a_2^\star = \frac{a_p\left(1 - e_p^2\right)}{1 + e_p \cos\left(\theta_p - \theta\right)}$, as reported below

$$\begin{cases} r_1^\star = \left[(q_1 - \mu_2)^2 + q_2^2 + q_3^2 \right]^{\frac{1}{2}} \\ r_2^\star = \left[(q_1 - \mu_2 + 1)^2 + q_2^2 + q_3^2 \right]^{\frac{1}{2}} \\ r_3^\star = \left[\left(q_1 - \mu_2 - \frac{a_2^\star}{a} \cos\left(\theta_p - \theta\right) \cos\epsilon \right)^2 + \left(q_2 - \frac{a_2^\star}{a} \sin\left(\theta_p - \theta\right) \right)^2 + \left(q_3 - \frac{a_2^\star}{a} \sin\left(\theta_p - \theta\right) \sin\varepsilon \right)^2 \right]^{\frac{1}{2}} \end{cases}$$

The expression for the expansion in e is given below

$$\frac{\partial F}{\partial e}|^\star = \frac{\partial K(\theta)}{\partial e}^\star \left[\sum_{i=1}^3 \frac{\mu_i}{r_i} + \frac{1}{2}\left(q_1^2 + q_2^2 + q_3^2\right)\right]^\star + \left[\sum_{i=1}^3 \mu_i \frac{\partial 1/r_i}{\partial e}\right]^\star$$

and introducing $\frac{\partial 1/r_i}{\partial e}|^\star = -\frac{1}{2r_i^3}\frac{\partial \rho_i}{\partial e}$ leads to the following result

$$\frac{\partial F}{\partial e}|^\star = -cos\theta \left[\frac{\mu_2}{r_2^\star} + \frac{1}{2}\left(q_1^2 + q_2^2 + q_3^2\right)\right]$$

Similarly, the derivative in μ_3 can be expanded as follows

$$\frac{\partial F}{\partial \mu_3}|^\star = \frac{\partial}{\partial \mu_3}\left(\frac{\mu_1}{r_1} + \frac{\mu_3}{r_3}\right)|^\star = \mu_1 \frac{\partial 1/r_1}{\partial \mu_3}|^\star + \mu_3 \frac{\partial 1/r_3}{\partial \mu_3}|^\star = -\frac{\mu_1}{r_1^3|^\star}\frac{\partial \rho_1}{\partial \mu_3}|^\star + \frac{1}{r_3^3|^\star}$$

where

$$\frac{\partial \rho_1}{\partial \mu_3}|^* = M\frac{\partial \rho_1}{\partial m_3} = 2\frac{a_2^*}{a}\left[(q_1 - \mu_2)\cos(\theta_p - \theta)\cos \epsilon + q_2 \sin(\theta_p - \theta) + q_3 \cos(\theta_p - \theta)\sin \epsilon\right]$$

Merging the two equations above results into the expression for the partial derivative in μ_3

$$\frac{\partial F}{\partial \mu_3}|^\star = -2\frac{\mu_1}{r_1^3|^\star}\frac{a_2^\star}{a}\left[(q_1 - \mu_2)\cos(\theta_p - \theta)\cos \epsilon + q_2 \sin(\theta_p - \theta) + q_3 \cos(\theta_p \theta)\sin \epsilon\right] + \frac{1}{r_3^3|^\star}$$

Introducing the equations above results into equation (5.28), whose order three terms are reported below

$$H = \frac{1}{2}\left(p_1^2 + p_2^2 + p_3^2\right) + p_1 q_2 - p_2 \tilde{q}_1 - \frac{\mu_1}{r_1^\star} - \frac{\mu_2}{r_2^\star} +$$

$$\mu_3\{2\frac{\mu_1}{r_1^\star}^3\frac{a_p}{a}\left[\tilde{q}_1 \cos(\theta_p - \theta)\cos \epsilon + q_2 \sin(\theta_p - \theta) + q_3 \cos(\theta_p - \theta)\sin \epsilon\right]\} +$$

$$+e\left[\frac{\mu_2}{r_2^\star} + \frac{1}{2}\left(\tilde{q}_1^2 + q_2^2 + q_3^2\right)\right]cos\theta + o(e, \mu_3)$$

Appendix F - Linear form and canonical transformation for the Hamiltonian function of the Jupiter-Europa-Io ER4BP

In order to set the Hamiltonian function for the ER4BP in its normal form, equation 5.28 should first be expanded in power series about the collinear equilibrium point L_1 or L_2, with coordinates $L_i = [L_{i,x}, 0, 0, 0, L_{i,x}, 0]$. It is worth noting that the term $\frac{\mu_3}{r_3^3|^\star}$ in the equation can be neglected, because the motio is investigated far from m_3, obtaining the following expression for the Hamiltonian

$$H = H_2 + H_3 = \frac{1}{2}\left(p_1^2 + p_2^2 + p_3^2\right) + p_1 q_2 - p_2 q_1 - c_0\left(q_1^2 - \frac{q_2^2}{2} - \frac{q_3^2}{2}\right) +$$

$$+e\cos\theta\frac{\mu_2}{1-\mu_2}+c_1(\theta_p,\theta)q_1+c_2(\theta_p,\theta)q_2+c_3(\theta_p,\theta)q_3+$$

$$+e\cos\theta\left\{\left[\frac{3-\mu_2}{|1-\mu_2|^3}+1\right]\frac{q_1^2}{2}+\left[1-\frac{\mu_2}{|1-\mu_2|^3}\right]\frac{q_2^2}{2}+\left[1-\frac{\mu_2}{|1-\mu_2|^3}\right]\frac{q_3^2}{2}\right\}+$$

$$+\frac{3k_2}{\cos\epsilon}\left\{\left[2\cos^2(\theta_p-\theta)\cos^2\epsilon-\frac{6}{|\mu_2|}+\frac{\sin(\theta_p-\theta)}{|\mu_2|}+\frac{\cos(\theta_p-\theta)\sin\epsilon}{|\mu_2|}\right]q_1^2\right\}+$$

$$+\frac{3k_2}{\cos\epsilon}\left\{\frac{\sin(\theta_p-\theta)+1}{|\mu_2|}q_2^2+\frac{\cos(\theta_p-\theta)\sin\epsilon+1}{|\mu_2|}q_3^2\right\}+o(e,\mu_3)$$

where $c_0=\frac{\mu_2}{|q_1^\star+\mu_1|^3}+\frac{\mu_1}{|q_1^\star+\mu_1-1|^3}$, $c_1=k_1\cos\theta+k_2\cos(\theta_p-\theta)$, $c_2=\frac{-k_2}{2\cos\epsilon}\sin(\theta_p-\theta)$, $c_3=\frac{-k_2\tan\epsilon}{2}\cos(\theta_p-\theta)$, $k_1=e\frac{\mu_2}{\mu_2-1}$ and $k_2=\frac{4\mu_2\mu_3 a_2^\star}{\mu_1^3 a}\cos\epsilon$.

The order three terms of equation 5.28 can be absorbed by a canonical transformation $(\mathbf{q},\mathbf{p},\theta_p,\theta)\to(\mathbf{Q},\mathbf{P})$, producing $H=H_2(\mathbf{Q},\mathbf{P})+H_4(\mathbf{Q},\mathbf{P},\theta_p,\theta)$. The transformation is achived by introducing a generating function S such that

$$\begin{cases}\mathbf{p}=\frac{\partial S}{\partial\mathbf{q}}\\\mathbf{Q}=\frac{\partial S}{\partial\mathbf{P}}\end{cases}$$

The Hamiltonian function after the transformation is reported below

$$H(\mathbf{Q},\mathbf{P})=H(\mathbf{q},\mathbf{p}),\theta_p,\theta)+\frac{\partial S}{\partial(\theta_p-\theta)}\frac{\partial(\theta_p-\theta)}{\partial\theta}+\frac{\partial S}{\partial\theta}$$

The generating function can be defined starting from the general form reported below

$$S=q_1P_1+q_2P_2+f_1(\theta_p,\theta)q_1+f_2(\theta_p,\theta)P_2+f_3(\theta_p,\theta)q_2+f_4(\theta_p,\theta)P_1+$$

$$+q_3P_3+f_5(\theta_p,\theta)q_3+f_6(\theta_p,\theta)P_3$$

where the functions $f_i(\theta_p,\theta)$ have to be accurately selected to absorb order three terms. The change of coordinates associated to transformation is reported below

$$\begin{cases}q_1=Q_1-f_4\\q_2=Q_2-f_2\\q_3=Q_3-f_6\end{cases}\quad\begin{cases}p_1=P_1+f_1\\p_2=P_2+f_3\\p_3=P_3+f_5\end{cases}$$

Introducing the above listed coordinates leads to the following expression (where the superscript $'$ indicates the derivative with respect to θ)

$$\frac{1}{2}(P_1^2+P_2^2+P_3^2)+P_1Q_2-P_2Q_1-c_0\left(Q_1^2-\frac{Q_2^2}{2}-\frac{Q_3^2}{2}\right)+$$

$$+P_1f_1+P_2f_3-P_1f_2+P_2f_4+P_2f_2'+P_1f_4'+P_3f_5+P_6f_6'+$$

$$+Q_2f_1-Q_1f_3+2c_0Q_1f_4-c_0Q_2f_2+Q_1f_1'+Q_2f_3'-c_0Q_3f_6+Q_3f_5'+$$

$$+c_1Q_1+c_2Q_2+c_3Q_3$$

The next step is setting to zero the terms in f_i and c_i in the previous equation. According to the expressions of c_i the following form for $f_i(\theta_p, \theta)$ can be selected

$$f_i(\theta_p, \theta) = b_1^{(i)} \cos\theta + b_2^{(i)} \sin\theta + b_3^{(i)} \cos(\theta_p - \theta) + b_4^{(i)} \sin(\theta_p - \theta) \qquad (8.4)$$

where the coefficients b_j^i can be determined introducing the new coordinates into the transformed Hamiltonian, producing the following expression

$$P_1 f_1 + P_2 f_3 - P_1 f_2 + P_2 f_4 + P_2 f_2' + P_1 f_4' + P_3 f_5 + P_6 f_6' +$$

$$+ Q_2 f_1 - Q_1 f_3 + 2b Q_1 f_4 - c_0 Q_2 f_2 + Q_1 f_1' + Q_2 f_3' - b Q_3 f_6 + Q_3 f_5' +$$

$$+ c_1 Q_1 + c_2 Q_2 + c_3 Q_3 = 0$$

The calculated values for the coefficients are reported below, where $n = \frac{\partial \theta_p}{\partial \theta}$.

$$\begin{cases} b_1^{(3)} = \frac{k_1}{2(c_0 - 1)} \\ b_1^{(4)} = -\frac{k_1(c_0 - 2)}{2c_0(c_0 - 1)} \\ b_2^{(1)} = -\frac{k_1}{2(c_0 - 1)} \\ b_2^{(2)} = -\frac{k_1}{c_0(c_0 - 1)} \\ b_3^{(3)} = -\frac{k_2\left(n^2 - 2n + c_0 - \frac{n^3 - 3n^2 + 2n - 2c_0}{2\cos\varepsilon}\right)}{n^4 + 4n^3 + n^2 + (4 + c_0) - 2c_0 n - 2c_0^2 + 2c_0} \\ b_3^{(4)} = -\frac{k_2\left(n^2 - 2n - c_0 + 2 - \frac{n-1}{\cos\varepsilon}\right)}{n^4 + 4n^3 + n^2 + (4 + c_0) - 2c_0 n - 2c_0^2 + 2c_0} \\ b_4^{(1)} = -\frac{k_2\left(n^3 - 3n^2 + 2n - c_0 n + c_0 - \frac{n^2 - 2n - 2c_0}{2\cos\varepsilon}\right)}{n^4 + 4n^3 + n^2 + (4 + c_0) - 2c_0 n - 2c_0^2 + 2c_0} \\ b_4^{(2)} = -\frac{k_2\left(2n - 2 - \frac{n^2 - 2n + 2c_0 + 2}{2\cos\varepsilon}\right)}{n^4 + 4n^3 + n^2 + (4 + c_0) - 2c_0 n - 2c_0^2 + 2c_0} \\ b_3^{(6)} = -\frac{k_2 \tan\varepsilon}{2(n^2 - 2n - c_0 + 1)} \\ b_4^{(5)} = b_3^{(6)}(n - 1) \end{cases}$$

All the b_j^i not indicated are equal to zero. Based on the results in the system above, the Hamiltonian can be obtained from the following change of coordinates

$$\begin{cases} q_1 = Q_1 - b_1^4 \cos\theta - b_3^4 \cos(\theta_p - \theta) \\ q_2 = Q_2 - b_2^2 \sin\theta - b_4^2 \sin(\theta_p - \theta) \\ q_3 = Q_3 - b_3^6 \cos(\theta_b - \theta) \\ p_1 = P_1 + b_2^1 \sin\theta + b_4^1 \sin(\theta_p - \theta) \\ p_2 = P_2 + b_1^3 \cos\theta + b_3^3 \cos(\theta_p - \theta) \\ p_3 = P_3 + b_4^5 \sin(\theta_p - \theta) \end{cases}$$

Appendix G - Canonical transformation absorbing order three terms for the Jupiter-Europa-Io ER4BP

The form of the order-three terms in equation 5.30 is reported below, collecting terms in **Q** and **P**

$$H_3 = a_{2000} Q_1^2 + a_{1100} Q_1 Q_2 + a_{1010} Q_1 P_1 + a_{1001} Q_1 P_2 + a_{0200} Q_2^2 + a_{0110} Q_2 P_1 +$$

$$+a_{0101}Q_2 P_2 + a_{0020}P_1^2 + a_{0011}P_1 P_2 + a_{0002}P_2^2 + b_{20}Q_3^2 + b_{11}Q_3 P_3 + b_{02}P_3^2 +$$

$$+b_{10}Q_3 + b_{01}P_3$$

These order three terms can be absorbed by means of a canonical transformation producing the change of coordinates $(\mathbf{Q}, \mathbf{P}, \theta_p, \theta) \to (\mathbf{R}, \mathbf{S})$, defined by the following generating function

$$S = Q_1 S_1 + Q_2 S_2 + Q_3 S_3 + Q_1 Q_2 + Q_1^2 + Q_2^2 + Q_3^2 + f_{2000}Q_1^2 + f_{0200}Q_2^2 +$$

$$+ f_{0020}S_1^2 + f_{0002}S_2^2 + f_{xx2x}S_1^2 + f_{xxx2}S_2^2 + f_{1001}Q_1 S_2 + f_{0011}S_1 S_2$$

$$+ f_{1000}Q_1 + f_{0100}Q_2 + f_{0010}S_1 + f_{0001}S_2 + g_{20}Q_3^2 + g_{02}S_3^2 + g_{x2}S_3^2 +$$

$$+ g_{10}Q_3 + g_{01}S_3$$

The functions $f_{i,j,k,l}(\theta_p, \theta)$ and $g_{i,j}(\theta_p, \theta)$ depend on some coefficients $b^{(n)}_{i,j,k,l}$ and $b^{(n)}_{i,j}$ which should be selected to verify the following equality

$$H_2(\mathbf{R}, \mathbf{S}) + H_3(\mathbf{R}, \mathbf{S}) + \frac{\partial S}{\partial(\theta_p - \theta)}\frac{\partial(\theta_p - \theta)}{\partial \theta} + \frac{\partial S}{\partial \theta} =$$

$$= \rho R_1 S_1 + \frac{\lambda_1}{2}\left(R_2^2 + S_2^2\right) + \frac{\lambda_2}{2}\left(R_3^2 + S_3^2\right)$$

Aiming at investigating the effects of resonance on quasi-periodic orbits ($Q_1 = 0$, $P_1 = 0$), then the generating function reduces to

$$S = Q_1 S_1 + Q_2 S_2 + Q_3 S_3 + Q_2^2 + Q_3^2 + f_{0200}Q_2^2 + f_{0002}S_2^2 + f_{xxx2}S_2^2 +$$

$$+ f_{0100}Q_2 + f_{0001}S_2 + g_{20}Q_3^2 + g_{02}S_3^2 + g_{x2}S_3^2 + g_{10}Q_3 + g_{01}S_3$$

Corresponding to the following change of coordinates

$$\begin{cases} Q_1 = R_1 \\ Q_2 = R_2 - 2S_2(f_{0002} + f_{xxx2}) - f_{0001} \\ Q_3 = R_3 - S_3(g_{02} + g_{11}) - g_{01} \\ P_1 = S_1 \\ P_2 = 2R_2(1 + f_{0200}) + S_2(1 - 4f_{0002} - 4f_{xxx2}) - 2f_{0001} + f_{0100} \\ P_3 = 2R_3(1 + g_{20}) + S_3(1 - 4g_{02} - 4g_{11}) - 2g_{01} + g_{10} \end{cases}$$

Appendix H - Determination of stationary points for the Jupiter-Europa-Io ER4BP

It is known from the problem of small denominators that the canonical transformation discussed in Appendix H defaults in the case of resonance, that is when the denominator of some coefficients, $b^{(n)}_{i,j,k,l}$ or $b^{(n)}_{i,j}$, is close to zero.

In fact, the denominator of $b^{(1)}_{10} = b^{(1)}_{01}$, $b^{(2)}_{10} = b^{(2)}_{01}$ and $b^{(6)}_{10} = b^{(6)}_{01}$ is equal to zero for $n = i\lambda_2 + \epsilon$. Considering the Jupiter-Europa-Io system, $n = 2.01$ and $\lambda_2 = 2.15$, therefore, the residual order-three term of $\hat{H}$ is given by

$$H_3^{res} = 2\left(R_3 + S_3\right)\left(b^{(1)}_{10}\cos^2\theta + b^{(2)}_{10}\cos\theta\sin\theta + b^{(6)}_{10}\sin^2\theta\right)$$

A periodic solution for the residual term H_3^{res} can be calculated based on the following property of transformation 2.31 [165]

$$\begin{cases} R_3 = \rho_3 e^{j\phi_3} \\ S_3 = j\rho_3 e^{-j\phi_3} \end{cases}$$

Applying the property above to the equation 5.30 produces the following form for the residual terms of the Hamiltonian function

$$H_3^{res} = \frac{\rho_3}{2} \left(je^{-j\phi_3} - e^{j\phi_3} \right) \left[\left(b_{10}^{(1)} - b_{10}^{(6)} \right) \left(e^{2j\theta} + e^{-2j\theta} \right) + b_{10}^{(2)} \left(e^{2j\theta} - e^{-2j\theta} \right) + 2b_{10}^{(1)} - 2b_{10}^{(6)} \right]$$

The previous equation can be rearranged using Euler's formula on the exponential terms

$$H_3^{res} = -\frac{\rho_3}{2} \left(b_{10}^{(1)} + b_{10}^{(2)} + b_{10}^{(6)} \right) \cos \left(\phi_3 - 2\theta \right)$$

The dependence on the true anomaly θ can be absorbed by introducing the canonical transformation $(\rho_3, \phi_3, \theta) \rightarrow (\tilde{\rho}_3, \tilde{\phi}_3)$ defined by the following generating function

$$S = \rho_3 \tilde{\phi}_3 - 2\epsilon \rho_3 \theta$$

The corresponding change of coordinate is reported below (the variables not reported are not transformed)

$$\begin{cases} \rho_3 = \tilde{\rho}_3 \\ \phi_3 = \tilde{\phi}_3 + 2\epsilon\theta \end{cases}$$

which produces in the end

$$H_3^{res} = -\frac{\tilde{\rho}_3}{2} \left(b_{10}^{(1)} + b_{10}^{(2)} + b_{10}^{(6)} \right) \cos \tilde{\phi}_3 - 2\epsilon\tilde{\rho}_3$$

Stationary points exist for the equation above, corresponding to

$$\begin{cases} \tilde{\phi}_{3,s} = k\pi, \quad k \in \mathbb{Z} \\ \tilde{\rho}_{3,s} = -\frac{\hat{H}_3^{res}}{b_{10}^{(1)} + b_{10}^{(2)} + b_{10}^{(6)}} \end{cases}$$

Bibliography

[1] Anderson, R.L.; Lo, M.W. Spatial approaches to moons from resonance relative to invariant manifolds. *Acta Astronautica*, **2014**, 105, 335-372

[2] Angelopoulos, V. The ARTEMIS Mission. *Space Science Reviews*, **2011**, 164 (1-4), 3-25

[3] Appleyard, D.F. Invariant Sets near the collinear Lagrangian Points of the Nonlinear Restricted Three-Body Problem, PhD thesis, University of Wisconsin, **1970**

[4] http://www.space-propulsion.com/spacecraft-propulsion/propulsion-systems/electric-propulsion/index.html

[5] Ashino, R.; Nagese, M.; Vaillancourt, R. Behind and beyond the MATLAB ODE suite. *Computers & Mathematics with Applications*, **2000**, 40 (4-5), 491-512

[6] Bannoura, W.; Parisot, F.; Vaze, P.; Zaouche, G. Jason-3 Project Status. OSTST (Ocean Surface Topography Science Team), Boulder (CO), USA, 9-11 October 2013

[7] Bar-Itzhack, T.Y.; Harman, R.R. Optimized TRIAD Algorithm for Attitude Determination. *J. Guid. Control Dynam.* **1997**, 20 (1), 208-211

[8] Bar-Itzhack, I.Y.; Oshman, Y. Attitude Determination from Vector Observations, *IEEE Transactions on Aerospace and Electronic Systems*, **1985**, AES-21 (1), 128-136

[9] Bate, R.R.; Mueller, D.D.; White, J.E. Fundamentals of Astrodynamics, 1st ed.; Dover Pubns: New Yorkm USA, 1971

[10] Beckman, M.; Janes, L. Finding Acceptable James Webb Space Telescope Mission Orbits from a Fixed Ariane Flight Profile. Proceedings AIAA/AAS Astrodynamics Conference, San Diego (CA), USA, 2005

[11] Belbruno, E. Celestial Mechanics Theory Meets the Nitty-Gritty of Trajectory Design. *SIAM News*, **2004**, 37 (6)

[12] Belbruno, E.A.; Miller, J.K. Sun-pertrubed Earth-to-Moon Transfers with Ballistic Capture. *J. Guid. Control Dynam.*, **1993**, 16 (4), 770-775

[13] Benz, W.; Broeg, C.; Barczy, T.; Baumjohann, W.; Deleuil, M.; Ehrenreich, D.; Fortier, A.; Gillon, M.; Gutierrez, A.; Kiss, L.; d'Etangs, A. L.; Liseau, R.; Olofsson, G.; Piotto, G.; Pollacco, D.; Queloz, D.; Ragazzoni, R.; Renotte, E.; Santos, N.; Spohn, T.; Steller, M.; Thomas, N.; Udry, S.; the CHEOPS Team CHEOPS: ESA First Small Science Mission - Scientific Objectives, Mission Concept, and Challenges for the Scientific Community. Proceedings of the 4S (Small Satellites Systems and Services) Symposium, Port Petro (Majorca Island), Spain, 26-30 May 2014

[14] Bigdeli, A.; Biglari-Abhari, M.; Salcic, Z.; Lai, Y.T. A New Pipelined Systolic Array-Based Architecture for Matrix Inversion in FPGAs with Kalman Filter Case Study. EURASIP Journal of Applied Signal Processing, 2006, 1-12

[15] Birkhoff, G.D. The restricted problem of three bodies. *Rendiconti del Circolo Matematico di Palermo*, **1915**, XXXIX, 265-334

[16] Bokelmann, K.A.; Russell, R.P. Halo orbit to science orbit captures at planetary moons. *Acta Astronaut.*, **2017**, 134, 141-151

[17] Bosanac, N. Trajectory Design for a Cislunar Cubesat Leveraging Dynamical Systems Techniques: The Lunar Ice Cube Mission. Proceedings of the 27th AAS/AIAA Space Flight Meeting, San Antonio (TX), USA, 5-9 February 2017

[18] Bosanac, N., Cox, A.D., Howell, K.C., Folta, D.C.: Trajectory design for a cislunar CubeSat leveraging dynamical systems techniques: The Lunar IceCube mission, *Acta Astronauti.*, **2018**, 14, 283-296

[19] Buffington, B. Trajectory Design Concept for the Proposed Europa Clipper Mission. AIAA/AAS Astrodynamics Specialist Conference, San Diego (CA), USA, 4-7 August 2014

[20] Burke, L.M.; Falck, D.; McGuire, M.L. Interplanetary Mission Design Handbook: Earth-to-Mars Mission Opportunities 2026 to 2045. NSA/TM-2010-216764, October 2010

[21] http://busek.com/technologies___ion.htm

[22] http://busek.com/technologies___greenmonoprop.htm

[23] Campagnola, S,M Ozaki, N.; Verspieren, Q.; Oguri, K.; Kakihara, K.; Funase, R.; Yam, C.H.; Ferella, L.; Yamaguchi, T.; Kawatsu, Y.; Yarnoz, D.G.; Mission Analysis for JAXA's Earth-Moon Libration-Orbit Cubesat. Proc. of the 67th International Astronautical Congress, Guadalajara, Mexico, 26-30 September 2016

[24] Carletta, S.; Pontani, M.; Teofilatto, P. Long-term capture orbits for low-energy space missions.*Celest. Mech. Dyn. Astron.*, **2018**, 130 (46)

[25] Carletta, S.; Pontani, M.; Teofilatto, P. Dynamics of three-dimensional capture orbits from libration region analysis.*Acta Astronautica*, **2019**, 165, 331-343

[26] Carletta, S.; Pontani, M.; Teofilatto, P. Design of low-energy capture trajectories in the elliptic restricted four-body problem. Proceedings of the 70th International Astronautical Congress, Washington (USA), 21-25 October 2019

[27] Circi, C.; Teofilatto, P. On the dynamics of weak stability boundary lunar transfers. *Celest. Mech. Dyn. Astron.*, **2001**, 79, 41-72

[28] Conley, C.C. Low Energy Transit Orbits in the Restricted Three-Body Problem. *SIAP*, **1968**, 16 (4), 732-746

[29] Conley, C.C. On the Ultimate Behavior of Orbits with Respect to an Unstable Critical Point l. Oscillating, Asymptotic, and Capture Orbits. *Journal of Differential Equations*, **1969**, 5, 136-158

[30] Conley, C.C.; Easton, R. Isolated invariant sets and isolating blocks. *Transactions of the Americal Mathematical Society*, **1971**, 158 (1), 35-61

[31] Conte, D.; Di Carlo, M.; Ho, K.; Spencer, D.B.; Vasile, M. Earth-Mars transfers through Moon distant retrograde orbits*Acta Astronautica*, **2018**, 143, 372-379

[32] https://www.cubesatshop.com/wp-content/uploads/2017/04/ENP-IFM-Nano-Thruster-Product-Overview.pdf

[33] Davis, K.; Anderson, R.L.; Scheeres, D.J.; Born, G.H. Locally Optimal Transfers Between Libration Point Orbirs Using Invariant Manifolds. *Celest. Mech. Dyn. Astron.*, **2010**, 107, 471-485

[34] Davis, D.C.; Philips, S.M.; McCarthy, B.P. Trajectory design for Saturnian Ocean Worlds orbiters using multidimensional Poincaré maps. *Acta Astronautica*, **2018**, 143, 16-28

[35] de Sousa-Silva, P.P.; Terra, M.O. A survey of different classes of Earth-to-Moon trajectories in the patched three-body approach. *Acta Astronaut.*, **2016**, 123, 340-349

[36] de Ruiter, A.H.; Damaren, C.; Forbes, J.R. Spacecraft Dynamics and Control: An Introduction, 1st ed.; John Wiley & Sons. Ltd.: Chichester (West Sussex) UK, 2013.

[37] Delabie, T.; Vandoren, B.; De Munter, W.; Raskin, G.; Vandenbussche, B.; Vandepitte, D. Testing and calibrating an advanced cubesat attitude determination and control system, Proceedings Volume 10698, Space Telescopes and Instrumentation 2018: Optical, Infrared, and Millimeter Wave, SPIE Astronomical Telescopes and Instrumentation, Austin (TX), USA, 10-15 June 2018

[38] Diao, Z.; Quan, H.; Lan, L.; Han, Y. Analysis and compensation of MEMS gyroscope drift. 2013 Seventh International Conference on Sensing Technology (ICST), Wellington, New Zeland, 3-5 December 2013

[39] Domenech, C.; Wehr, T.; Fischer, J. Toward an Earth Clouds, Aerosols and Radiation Explore (EarthCARE) thermal flux determination: Evaluation using

Clouds and the Earth's Radiant Energy System (CERES) true along-track data. *JGR Atmospheres*, **2011**, 116(D6)

[40] Doré, O.; Werner, M.W.; Ashby, M.; Banerjee, P.; Battaglia, N.; Bauer, J.; Benjamin, R.A.; Bleem, L.E.; Bock, J.; Boogert, A.; Bull, P.; Capak, P.; Chang, T.-J.; Chiar, J.; Cohen, S.H.; Cooray, A.; Crill, B.; Cushing, M.; de Putter, R.; Driver, S.P.; Eifler, T.; Feng, C.; Ferraro, S.; Finkbeiner, D.; Gaudi, B.S.; Greene, T.; Hillenbrand, L.; Höflich, P.A.; Hsiao, E.; Huffenberger, K.; Jansen, R.A.; Jeong, W.-S.; Joshi, B.; Kim, D.; Kim, M.; Kirkpatrick, J.D.; Korngut, P.; Krause, E.; Kriek, M.; Leistedt, B.; Li, A.; Lisse, C.M.; Mauskopf, P.; Mechtley, M.; Melnick, G.; Mohr, J.; Murphy, J.; Neben, A.; Neufeld, D.; Nguyen, H.; Pierpaoli, E.; Pyo, J.; Rhodes, J.; Sandstrom, K.; Schaan, E.; Schlaufman, K.C.; Silverman, J.; Su, K.; Stassun, K.; Stevens, D.; Strauss, M.A.; Tielens, X.; Tsai, C.-W.; Tolls, V.; Unwin, S.; Viero, M.; Windhorst, R.A.; Zemcov, M. Science Impacts of the SPHEREx All-Sky Optical to Near-Infrared Spectral Survey: Report of a Community Workshop Examining Extragalactic, Galactic, Stellar and Planetary Science. Report of the First SPHEREx Community Workshop, https://arxiv.org/abs/1606.07039

[41] Entekhabi, D.; Njoku, E.; O'Neill, P.; Kellogg, K.; Entin, D. The NASA Soil MOISTURE Active Passive (SMAP) Mission Formulation. 2011 IEEE International Geoscience and Remote Sensing Symposium, Vancouver (BC), Canada, 24-29 July 2011

[42] ESA, EarthCARE-Earth Clouds, Aerosols and Radiation Explorer. SO-1257(1), September 2001

[43] ESA, Cosmic Vision: Space Science for Europe 2015-2025, October 2005

[44] ESA, Euclid Mapping the geometry of the dark Universe, ESA/SRE(2011)12, July 2011

[45] ESA, JUICE Jupiter Icy Moons Explorer Science Management Plan, ESA/SPC(2012)20, 20 June 2012

[46] ESA, CHEOPS Definition Study Report, ESA/SRE(2013)7, November 2013

[47] ESA, PLATO Revealing habitable worlds around solar-like stars. 24th International Symposium on Space Flight Dynamics, April 2014

[48] ESA Industrial Policy Committee, Science Programme Technology Development Plan: Programme of Work for 2017 and Related Procurement Plan, December 2016.

[49] Euler, L. Theoria Motuum Lunae. Typis Academiae Imperialis Scientiarium Petropoli, 1722

[50] Fabacher, E.; Kemble, S.; Trenkel, C.; Dunbar, N. Multiple Sun-Earth Saddle Point flybys for Lisa Pathfinder. *Adv Space Res*, **2013**, 52 (1), 105-116

[51] Faddeev, D.K.; Sominsky, I. Problems in Higher Algebra, Translated by G. Yankovsky; from the 1968 Russian edition; Mir Publishers: Moscow, USSR, 1968

[52] Fantino, E.; Castelli, R. Efficient design of direct low-energy transfers in multi-moon systems. *Celest. Mech. Dyn. Astron.*, **2017**, 127 (4), 429-450

[53] Fantino, E.; Gómez, G.; Masdemont, J.J.; Ren, Y. Efficient design of direct low-energy transits in multi-moon systems. *Acta Astronaut.*, **2010**, 67, 1038-1052

[54] Farquhar, R.W. The Flight of ISEE-3/ICE: Origins, Mission History and a Legacy. *J. Astronaut. Sci.*, **2001**, 49 (1), 23-73

[55] Farquhar, R.W.; Dunham, D.W.; Hsu, S.C. Orbital Acrobatics in the Sun-Earth-Moon System. Proc. of the Second International Symposium on Spacecraft Flight Dynamics, 191-198, Darmstadt, BRD, 20-23 October 1986

[56] Foing, B.H.; Racca, G.D.; Marini, A.; Heather, D.J.; Koschny, D.; Grande, M.; Huovelin, J.; Keller, H.U.; Nathues, A.; Josset, J.L.; Malkki, A.; Schmidt, W.; Noci, G.; Birk, R.; Iess, L.; Sodnik Z.; McManamon, *P. SMART-1 Mission to the Moon: Technology and Science Goals*, March 2003

[57] Folta, D.; Beckman, B. Orbit Mission Design: Applications Of Numerical And Dynamical Methods, Proceedings of the Conference Libration Point Orbits and Applications, pp. 85-113, Girone (Spain), 10-14 June 2002

[58] Folta, D.C.; Webster, C. Transfer Trajectory Options for Servicing Sun-Earth-Moon Libration Point Missions. 29th AAS/AIAA Space Flight Mechanics Meeting, Ka"anapali (HI), USA, 13-17 January 2019

[59] Folta, D.C.; Pavlak, T.A.; Haapala, A.F.; Woodard, L.M. Earth-Moon libration point orbit stationkeeping: Theory, modeling and operations. *Acta Astronautica*, **2013**, 94, 1-13

[60] Folta, D.C.; Pavlak, T.A.; Haapala, A.F.; Howell, K. Preliminary design considerations for access and operations in Earth-Moon L1/L2 orbits. AAS/AIAA Spaceflight Mechanics Meeting, Kauai (HI), USA, 10-14 February 2013

[61] Folta, D.C.; Bosanac, N.; Cox, A.; Howell, K.C. The Lunar IceCube Mission Design: Construction of Feasible Transfer Trajectories with a Constrained Departure. 26th AAS/AIAA Spaceflight Mechanics Meeting, Napa (CA), USA, 14-18 February 2016

[62] Gavrilovich, I.; Krut, S.; Gouttefarde, M.; Pierrot, F.; Dusseau, L. Test Bench For Nanosatellite Attitude Determination And Control System Ground Tests, The 4S Symposium, Small Satellites Systems and Services 2014, 04-08 June 2014

[63] Gebre-Egziabher, D.; Elkaim, G.G.; Powell, J.D.; Parkinson, B.W. A gyro-free quaternion-based attitude determination system suitable for implementation using low cost sensors. Proceedings of the IEEE Position Location and Navigation Symposium, San Diego (CA), USA, 13-16 March 2000

[64] Giancotti, M.; Pontani, M.; Teofilatto, P. Lunar capture trajectories and homoclinic connections through isomorphic mapping. *Celest. Mech. Dyn. Astron.*, **2012**, 114, 55-76

[65] Giancotti, M.; Pontani, M.; Teofilatto, P. Cylindrical isomorphic mapping applied to invariant manifold dynamics for Earth-Moon Missions. *Celest. Mech. Dyn. Astron.*, **2014**, 120, 249-268

[66] Goel, A.; Krishnamoorthy, S.; Swenson, T.; West, S.; Li, A.; Crew, A.; Philips, D.J.; Screve, A.; Close, S. Design for CubeSat-based dust and radiation studies at Europa. *Acta Astronaut.*, **2017**, 136, 204-218

[67] Gòmez, G.; Masdemont, J.; Mondelo, J.M. Libration Point Orbits: A Survey from the Dynamical Point of View. AAS/AIAA Astrodynamics Specialist Conference, Denver (CO), USA, 14-17 August 2000

[68] Gómez, G.; Koon, W.S.; Lo, M.W.; Marsden, J.E.; Ross, S.D.; Masdemont, J.J. Invariant Manifolds, the Spatial Three-Body Problem and Petit Grand Tour of Jovian Moons. *Libration point orbits and applications*, World Scientific Publishing Company, River Edge (NJ), USA, pp. 587-601, 2003

[69] Grebow, D.J.; Ozimek, M.T.; Howell, K.C.; Folta, D.C. Multi-Body Orbit Architecture for Lunar South Pole Coverage. *J. Spacecraft Rockets*, **2008**, 45 (2), 344-358

[70] Hajiyev, C.; Demet, C.G. Review of gyroless attitude determination methods for small satellites. *Progress in Aerospace Science*, **2017**, 90, 54-66

[71] Hardgrove, C.; Bell, J.; Thangavelautham, J.; Klesh, A.; Starr, R.; Colaprete, T.; Robinson, M.; Drake, D.; Johnson, E.; Christian, J.; Genova, A.; Dunham, D.; Williams, B.; Nelson, D.; Babuscia, A.; Scowen, P.; Cheung, K. M.; McKinney, T.; Taits, A.; Hernandez, V.; Wren, P.; Thoesen, A.; Godber, A.; Beasley, M. The Lunar Polar Hydrogen Mapper (LunaH-Map) Mission: Mapping Hydrogen Distributions in Permanently Shadowed Regions of the Moon's South Pole. Annual Meeting of the Lunar Exploration Analysis Group, Columbia (MA), USA, No. 1863, 20-22 October 2015

[72] Hart, C. Satellite Attitude Determination Using Magnetometer Data Only. AIAA Aerospace Science Meeting Including The New Horizons Forum and Aerospace Exposition, Orlando (FL), USA, 5-9 January 2009

[73] Hill, G.W. Researches in the lunar theory. *Amer. J. Math.*, **1878**, 1

[74] Hill, G.W. Illustrations of Periodic Solutions in the Problem of Three Bodies. *Astronomical Journal*, **1902**, 22, 93-97, 117-121

[75] Hovland, S. ESA Human Lunar Architecture Activities. International Lunar Conference, Toronto, Canada, 18-23 September 2005

[76] Huang, J.; Rao, W.; Meng, L.; Huang, H. Research and Development of Chang'e-2 Satellite. Proc. of the 63rd IAC, Naples, Italy, 1-5 October 2012

[77] Hurwitz, A. Ueber die Bedingungen, unter welchen eine Gleichung nur Wurzeln mit negativen reellen Theilen besitzt. *Math.Ann.*, **1895**, 46 (2), 273-284

[78] Hyeraci, N.; Topputo, F. Method to Design Ballistic Capture in the Elliptic Restricted Three-Body Problem. *J. Guid. Control. Dynam*, **2010**, 33 (6), 1814-1823

[79] Hyo-Sung, A. Gyroless Attitude Estimation of Sun-Pointing Satellites Using Magnetometers. *IEEE Geoscience and Remote Sensing Letters*, **2005**, 2 (1), 8-12

[80] ISRO, Annual Report 2016-2017, 2017

[81] Jacobi, C.G.J. Compte Rendus de l'Acad. des Sciences, Paris, 3 (59), 1836

[82] Kaloshin, V.; Zhang, K. Arnold diffusion for smooth convex systems of two and a half degrees of freedom. *Nonlinearity*, **2015**, 28, 2699-2720

[83] Katagiri, S.; Oki, R.; Shimizu, S.; Kimura, T.; Nakajima, T.; Okamoto, H.; Sugimoto, N.; Nakajima, T.Y.; Sato, M.; Takayabu, Y.; Sato, K.; Nishizawa, T.; Matsui, T.; Hagihara Y. EarthCARE science mission objectives. International Archives of the Photogrammetry, Remote Sensing and Spatial Information Sciences XXXVIII, Kyoto, Japan, 9-12 August 2010

[84] Keck Institute for Space Studies, Small Satellites: a Revolution in Space Science. Final Report of Workshops on Small Satellite Systems, Pasadena (CA), USA, 16-20 July 2012 and 29-31 October 2012

[85] Robinson, K.F.; Spearing, S.F.; Hitt, D. NASA's Space Launch System: Opportunities for Small Satellites to Deep Space Destinations. Proc. of the 32nd Annual AIAA/USU Conference on Small Satellites, Logan (UT), USA, 4-9 August 2018

[86] Klesh, A.; Seagraves, S.; Bennet, M.; Boone, D.; Cutler, J.; Bahcivan, H. Dynamically driven Helmholtz cage for experimental magnetic attitude determination, *Advances in the Astronautical Sciences*, **2010**, 135, 147-160

[87] Klesh, A.; Baker, J.; Castillo-Rogez, J.; Halatek, L.; Murphy, N.; Raymond, C.; Sherwood, B.; Bellardo, J.; Cutler, J.; Lightsey, G. INSPIRE: Interplanetary NanoSpacecraft Pathfinder In Relevant Environment. Proc. of the 27th AIAA/USU Conference, Logan (UT), USA, SSC13-XI-8, 10-15 August 2013

[88] Klesh, A.T.; Baker, J.; Krajewski, J. MarCO: Flight Review and Lessons Learned. Proc. of the 33rd Annual AIAA/USU Conference on Small Satellites, Logan (UT), USA, 3-8 August 3-8 2019

[89] Kolemen, E.; Kasdin, N.J.;Gurfil, P.Quasi-Periodic Orbits of the Restricted Three-Body Problem Made Easy. Proc. of the 3rd International Conference on New Trends in Astrodynamics and Applications, Princeton (NJ), USA, 68-77, 16-18 August 2006

[90] Koon, W.S.; Lo, M.W.; Marsden, J.E.; Ross, S.D. Constructing a Low Energy Transfer Between Jovian Moons. *Contemp. Math.*, **2000**, 292, 129-146

[91] Koon, W.S.; Lo, M.W.; Marsden, J.E.; Ross, S.D. Low Energy transit to the Moon, *Celestial Mechanics and Dynamical Astronomy*. **2001**, 81, 63-73

[92] Kraft, S.; Del Bello, U.; Harnisch, B.; Bouvet, M.;Drusch, M.;Bézy, J.-L. Fluorescence imaging spectrometer concepts for the Earth explorer mission candidate flex. Proc. Volume 10564, International Conference on Space Optics 2012, Ajaccio, France, 9-12 October 2012

[93] http://www.cubesatpointing.com/DownloadFiles/Datasheets/KULADCSDatasheet.pdf

[94] Lagrange, J. Mécanique Analytique. Veuve Desaint, Paris, France, 1788

[95] Laguardia, G. Analysis of Weak Stability Boundary transfers for an Earth-Moon system for the European Student Moon Orbiter. 49th AIAA Aerospace Sciences Meeting, Orlando (FL), USA, 4-7 January 2011

[96] Lam, T.; Arrieta-Camacho, J.; Buffington, B. The Europa ission: Multiple Europa Flyby Trajectory Design Trafes and Challenges. AAS/AIAA Astrodynamics Specialist Conference, Vail (CO), USA, 9-13 Augusti 2015

[97] Lam, T.; Buffington, B.; Campagnola, S. A Robust Mission Tour for NASA's Planned Europa Clipper Mission. 2018 Space Flight Mechanics Meeting, Session: Asteroid and Non-Earth Orbiting Missions I, Kissimmee (FL), USA, 8-12 January 2018

[98] Landau, D.F.; Longuski, J.M. Trajectories for Human Missions to Mars, Part 1: Impulsive Transfers. *J Spacecraft Rockets*, **2006**, 43 (5), 1035-1042

[99] Landau, D.F.; Longuski, J.M. Trajectories for Human Missions to Mars, Part 2: Low-Thrust Transfers. *J Spacecraft Rockets*, **2006**, 43 (5), 1035-1042

[100] Landgraf, M.; Hechler, M.;Kemble, S. Mission design for Lisa Pathfinder. *Class.Quant.Grav.*, **2005**, 22, 487-492

[101] Langer, M.; Bouwmeester, J. Reliability of CubeSats–Statistical Data, Developers' Beliefs and the Way Forward, Proceedings of the AIAA/USU Conference on Small Satellites, SSC16-X-2, 6-11 August 2016

[102] Li, M.; Zheng, J. Indirect transfer to the Earth-Moon L1 libration point. *Celest. Mech. Dyn. Astron.*, **2010**, 108, 108-203, 2010

[103] Liang, Y; Xu, M.; Xu, S. The cislunar polygonal-like periodic orbit: Construction, transition and its application. *Acta Astronautica*, **2017**, 133, 282-301

[104] Libre, J., Martínez, R., Simó, C. Tranversality of the invariant manifolds associated to the Lyapunov family of periodic orbits near L2 in the restricted three-body problem. *J. Differ. Equations*, **1985**, 58 (1), 104-156

[105] https://www.elisascience.org/articles/elisa-mission/lisa-mission-gravitational-universe

[106] Liu, L.; Liu, Y.; Cao, J.; Hu, S.; Tang, G.; Xie, J. CHANG'E-2 lunar escape maneuvers to the Sun–Earth L2 libration point mission. *Acta Astronautica*, **2014**, 93, 390-399

[107] Lu, J.; Zhang, M.; Lu, Q. Transfer Trajectory Design for Mars Exploration. *International Journal of Astronomy and Astrophysics*, **2013**, 3, 5-16

[108] Luo, Z.F., Topputo, F., Bernelli-Zazzera, F., Tang, G.J.: Constructing ballistic capture orbits in the real Solar System model. *Celest. Mech. Dyn. Astron.*, **2014**, 120 (4), 433-450

[109] Ma, G.F.; Jiang, X.Y. Unscented Kalman filter for spacecraft attitude estimation and calibration using magnetometer measurements. 2005 International Conference on Machine Learning and Cybernetics, Guangzhou, China, August 2005

[110] Ma, H.; Xu, S. Magnetomter-only attitude and angular velocity filtering estimation for attitude changing spacecraft. *Acta Astronautica*, **2014**, 102, 89-102

[111] Matt, G. The advanced telescope for high energy astrophysics. *Astronomische Nachrichten*, **2019**, 340 (1-3), 35-39

[112] McNamara, P., Racca, G. Overview of Lisa Pathfinder. LISA-LPF-RP-0002, March 2009

[113] McNutt, L.; Johnson, L.; Kahn, P.; Castillo-Rogez, J.; Frick, A. Near-Earth Asteroid (NEA) Scout. AIAA SPACE 2014 Conference and Exposition, San Diego (CA), USA, AIAA 2014-4435, 4-7 August 2014

[114] Mingotti, G.; Topputo, F.; Bernelli-Zazzera, F. Earth-Mars transits with ballistic escape and low-thrust capture. *Celest. Mech. Dyn. Astron.*, **2011**, 110 (2), 169-188

[115] Moeckel, R. A variational proof of existence of transit orbits in the restricted three-body problem. *Dyn. Syst. Int. J.*, **2005**, 20, 45-58.

[116] Moore, C.; Joshi, J.; Herrmann, N. Deep-Space CubeSats on Exploration Mission-1. Proc. of the 68th IAC (International Astronautical Congress), Adelaide, Australia, 25-29 September 2017

[117] Moser, J. On the generalization of a theorem of A.Liapounoff. *Comm. Pur. Appl. Math.*, **1958**, XI, 257-271

[118] Nakamiya, M.; Yamakawa, H.; Scheers, D.J.; Yoshikawa, M. Interplanetary Transfers Between Halo Orbits: Connectivity Between Escape and Capture Trajectories. *J. Guid. Control. Dynam*, **2010**, 33 (3), 803-813

[119] https://www.nanosats.eu/#database

[120] NASA, Apollo 11 Flight Plan, AS-506/CSM-107LM-5, July 1969

[121] NASA, FY 2016 Agency Financial Report, November 2016

[122] NASA Jet Propulsion Laboratory, 2016 Annual Report, March 2017

[123] NASA, GRACE-FO Tracking Earth's Mass in Motion, NP-2017-4-002-GSFC

[124] https://solarsystem.nasa.gov/missions/artemis/indepth

[125] NASA, Wide-Field InfaRed Survey Telescope WFIRST Final Report, arXiv:1208.401

[126] https://www.nasa.gov/content/nextstep-overview

[127] https://www.nasa.gov/feature/nasa-selects-lockheed-martin-s-skyfire-cubesat-for-em-1-secondary-payload

[128] https://www.nasa.gov/topics/universe/features/webb-l2.html

[129] https://history.nasa.gov/SP-350/ch-9-5.html

[130] Nascetti, A.; Pancorbo-D'Ammando, D.; Truglio, M. Abacus advanced board for active control of university satellites, Proceedings of the 2nd IAA Conference on University Satellite Missions and Cubesat Workshop, International Academy of Astronautics, Roma, Italy, 3-9 February 2013

[131] Natanson, G.A.; McLaughlin, S.F.; Nicklas, R.C. A method of determining attitude from magnetometer data only. NASA Goddard Space Flight Center, Flight Mechanics/Estimation Theory Symposium, Silver Spring (MD), USA, 01 December 1990, 359-380

[132] Natanson, G.A.; Challa, J.; Deutschmann, J.; Baker, D.F. Magnetometer only attitude and rate determination for a gyro-less spacecraft. Third International Symposium on Space Mission Operations and Ground Data Systems, Greenbelt (MD), USA, November 1994. 791-798

[133] Nurdin, D.S.; Md.Isa, M.N.; Ismail, R.C.; Ahmad, M.I. High Performance Systolic Array Core Architecture Design for DNA Sequence. MATEC Web of Conferences, 2018, 150

[134] Oschima, K.; Campagnola, S.; Yam, C.H.; Kayama, Y.; Kawatsu, Y.; Ozaki, N.; Verspieren, Q.; Kakihara, K.; Oguri, K.; Funase, R. EQUULEUS Mission Analysis: Design of the Transfer Phase. Proc. of the 31st International Symposium on Space Technology and Science (ISTS), Matsuyama-Ehime, Japan, 3-9 June 2017

[135] Paolozzi, A.; Ciufolini, A.; Paris, C.; Sindoni, G. LARES: A New Satellite Specifically Designed for Testing General Relativity. *Int. J. Aerospace Eng*, **2015**

[136] Parker, J.S. Targeting Low-Energy ballistic lunar transits. *The J. Astronaut. Sci.*, **2011**, 58 (3), 331-334

[137] Parker, J.S.; Anderson, R.L. Low-Energy Lunar Trajectory Design, Deep Space Communications and Navigation Series. JPL Deep Space Communications and Navigation Systems, 3-5, July 2013

[138] Pérez-Palau, D.; Epenoy, R. Fuel optimization for low-thrust Earth-Moon transfer via indirect optimal control. *Celest. Mech. Dyn. Astron.*, **2018**, 130 (21)

[139] Poincaré, H. *Les méthodes nouvelles de la mécanique céleste*, Tome 1-3; Gauthier-Villars et fils, Paris, 1892

[140] Pontani, M.; Teofilatto, P. Low Energy Earth-Moon transits involving manifolds through isomorphic mapping. *Acta Astronaut.*, **2013**, 91, 96-106

[141] Pontani, M.; Teofilatto, P. Polyhedral representation of invariant manifolds applied to orbit transits in the Earth-Moon system. *Acta Astronaut.*, **2016**, 119, 218-232

[142] Pontani, M.; Teofilatto, P. Invariant manifold connections via polyhedral representation. *Acta Astronaut.*, **2017**, 137, 512-521

[143] Pontani, M.; Giancotti, M.; Teofilatto, P. Manifold dynamics in the Earth–Moon system via isomorphic mapping with application to spacecraft end-of-life strategies. *Acta Astronaut.*, **2014**, 105, 218-229

[144] Post, K.E.; Belbruno, E.; Topputo, F. Efficient Cis-Lunar Trajectories. GLEX 2012, Washington DC, USA, 22-24 May 2012

[145] Psiaki, M.L. Global Magnetomter-Based Spacecraft Attitude and Rate Estimation. *J. Guid. Control Dynam.* 2004, 27 (2), 240-250

[146] Qi, Y.; Xu, S. Earth–Moon transfer with near-optimal lunar capture in the restricted four-body problem. *Aerospace Science and Technology*, **2016**, 55, 282-291

[147] Qu, Q.; Xu, M., Peng, K. The cislunar low-thrust trajectories via the libration point, *Astrophysics and Space Science.* **2017**, 361(96)

[148] Racca, G.D.; Whitcomb, G.P.; Foing, B.H.; The SMART-1 Mission. *ESA Bulletin*, **1998**, 95

[149] Racca, G.D.; Laureijs, R.; Stagnaro, L.; Salvignol, J.C.; Lorenzo Alvarez, J.; Saavedra Criado, G.; Gaspar Venancio, L.; Short A.; Strada, P.; Bönke, T.; Colombo, C.; Calvi, A.; Maiorano, E.; Piersanti, O.; Prezelus, S.; Rosato, P.; Pinel, J.; Rozemeijer, H.; Lesna, V.; Musi, P.; Sias, M.; Anselmi, A.; Cazaubiel, V.; Vaillon, L.; Mellier, Y.; Amiaux, J.; Berthé, M.; Sauvage, M.; Azzollini, R.; Cropper, M.; Pottinger, S.; Jahnke, K.; Ealet, A.; Maciaszek, T.; Pasian, F.; Zacchei, A.; Scaramella, R.; Hoar, J.; Kohley, R.; Vavrek, R.; Rudolph, A.; Schmidt, M. The Euclid mission design. Proc SPIE 9904 Space Telescopes and Instrumentation 2016: Optical, Infrared and Millimeter Wave, 19 July 2016

[150] Rando, N.; Marti, D.; Lumb, D.; Verhoeve, P.; Oosterbroek, T.; Bavddaz, M.; Fransen, S.; Linder, M.E.; Peyrou-Lauga, R.; Voirin, T.; Braghin, M.; Mangunsong, S.; Van Pelt, M.; Wille, E. Status of the ESA L1 mission candidate ATHENA. Proc. SPIE 8443, Space Telescopes and Instrumentation 2012: Ultraviolet to Gamma Ray, 25 September 2012

[151] Rast, M.; Schwehm, G.; Attema, E. Payload-Mass Trends for Earth Observation and Space-Exploration Satellites. ESA Bulletin, 97, March 1999

[152] https://www.roscosmos.ru/22347/

[153] https://www.roscosmos.ru/23316/

[154] https://www.roscosmos.ru/media/files/srg_2019_eng.pdf

[155] Routh, E.J. A Treatise on the Stability of a Given State of Motion: Particularly Steady Motion; Macmillan and Co: London, UK, 1877

[156] Rybus, T.; Seweryn, K. Planar air-bearing microcravity simulators: Review of applications, existing solutions and design parameters. *Acta Astronaut.*, **2016**, 120, 239-259

[157] Santoni, F.; Bolotti, F. Attitude determination of small spinning spacecraft using three axis magnetometer and solar panels data. *Proc. IEEE Aerospace Conf.*, **2000**, 127-133

[158] Schaire, S.; Wong, Y.F.; Altunc, S.; Bussey, G.; Shelton, M.; Folta, D.; Gramling C.; Celeste, P.; Anderson, M.; Perrotto, T. Lunar and Lagrangian Point L1/L2 CubeSat Communication and Navigation Considerations. 31st Annual AIAA/USU Conference on Small Satellites, Logan (UT), USA, 5-10 August 2017

[159] Schoenmaekers, J. Post-launch Optimisation of the SMART-1 Low-thrust Trajectory to the Moon. Proceedings of the 18th International Symposium on Space Flight Dynamics, pp. 505-510, Munich, Germany, 11-15 October 2004

[160] Schwartz, J.L.; Peck, M.A.; Hall, C.H. Historical Review of Air-Bearing Spacecraft Simulator. *J. Guid. Control Dynam.*, **2003**, 26 (4), 513-522

[161] Searcy, J.D.; Pernicka, H.J. Magnetometer-Only Attitude Determination Using Novel Two-Step Kalman Filter Approach. *J. Guid. Control Dynam.* 2012, 35 (6), 1639-1701

[162] Sherwood, B,; Spangelo, S.; Frick, A.; Castillo-Rogez, J.; Klesh, A.; Wyatt, E.J.; Reh, K.; Baker, J. Planetary CubeSats come of age. Proc. of the 66th International Astronautical Congress (IAC 2015), Jerusalem, Israel, IAC-15-A3.5.8, 12-16 October 2015

[163] Shou, H.-N. Microsatellite Attitude Determination and Control Subsystem Design and Implementation: Software-in-the-Loop Approach, *Mathematical Problems in Engineering*, **2014**

[164] https://web.uniroma1.it/scuolaingegneriaaerospaziale/flight-mechanics-lab

[165] Siegel, C.L.; Moser, J.K. Lectures on Celestial Mechanics, Reprint of the 1971 Edition; Springer-Verlag Berlin Heidelberg New York, 1995

[166] Solanki, S.K.; Teriaca, L.; Barthol, P.; Curdt, W.; Inhester B. European Solar Physics: moving from SOHO to Solar Orbiter and beyond. *Mem. S.A.It.*, **2013**, 84, 286-314

[167] Stanley, P.; Seaton, B.; Mather, J. James Webb Telescope Project: JWST Mission Operations Concept Document. JWST-OPS-002018, January 2006

[168] Sugimura, N., Kuwahara, T.; Yoshida, K. Attitude Determination and Control System for Nadir Pointing Using Magnetorquer and Magnetometer. 2016 IEEE Aerospace Conference, Big Sky (MT), USA, 5-12 March 2016

[169] Swantwout, M. The First One Hundred CubeSats: A Statistical Look, *Journal of Small Satelites*, **2013,** 2 (2), 213-233

[170] Sweetser, T.H.; Broschart, S.B.; Angelopoulos, V.; Whiffen, G.J.; Folta, D.C.; Chung, M.K.; Hatch, S.J.; Woodard, M.A. ARTEMIS Mission Design. *Space Science Reviews*, **2011**, 165 (1-4), 27-57

[171] Szebehely, V. *Theory of orbits, the restricted problem of three bodies*; Academic Press, New York, 1967

[172] Testani, P.; Teofilatto, P.; Nascetti, A.; Truglio, M. A Nadir-Pointing Magnetic Attitude Control System for Tigrisat Nanosatellite. Proc. of the 64th International Astronautical Congress, Beijing, China, 22-27 September 2013

[173] Thébault, E.; Finlay, C.C.; Beggan, C.D.; et al. International Geomagnetic Reference Field: the 12th generation. *Earth Planet Sp* , **2015**, 67 (79)

[174] Topputo, F.; Belbruno, E. Earth-Mars transits with ballistic capture*Celest. Mech. Dyn. Astron.*, **2015**, 121, 329-346

[175] Topputo, F.; Biggs, J.; Di Lizia, P.; Massari, M.; Mani, K.;Dei Tos, D.; Cervone, A.; Sundaramoorthy, P.; Noomen, R.; Mestry, S.; Speretta, S.; Ivanov, A.; Richard, M.; Labate, D.; Jochemsen, A.; Gailis, J.; Furfaro, R.; Reddy, V.; Walker, R. Lunar Meteroid Impact Observer (LUMIO): A CubeSat at Earth-Moon L2. 8th Interplanetary CubeSat Workshop, Milan, Italy, 28-29 May 2019

[176] Vucha, M.; Rajawat, A. Design and FPGA Implementation of Systolic Array Architecture for Matrix Multiplication. *International Journal of Computer Applications*, **2011**, 26 (3), 18-22

[177] Wahba, G. A Least Squares Estimate of Spacecraft Attitude. *SIAM Review*, **1965**, 7 (3), 409

[178] Walker, R.; Koschny, D.; Carnelli, I.; ESA CDF Study Team. Miniaturised Asteroid Remote Geophysical Observer (M-ARGO): a stand-alone deep space CubeSat system for low-cost science and exploration missions. 8th Interplanetary CubeSat Workshop, Milan, Italy, 2017.A.3.1, 28-29 May 2019

[179] Wegner, S.; Majd, E.; Taylor, L.; Thomas, R.; Egziabher, D.G. Methodology for Software-in-the-Loop Testing of Low-Cost Attitude Determination Systems, SSC17-WK-09

[180] Wenschel, L.; Brown, J.; Toorian, A.; Coelbo, R.; Puig-Suari, J.; Twiggs, R. CubeSat Development in Education and into Industry, Proceedings of the AIAA Space 2006 Conference, San Jose (CA), USA, 19 September 2006

[181] Wertz, J.R. (ed.) Spacecraft Attitude Determination and Control, 3rd ed.; Kluwer Academic Publisher: Dordrecht, The Netherlands, 1978; 343–429.

[182] https://storage.googleapis.com/blue-canyon-tech-news/1/2019/10/BCT_DataSheet_Components_ACS_F2.pdf In these final chapters the concept design

[183] Yu, W.; Richon, K. James Webb Space Telescope Launch Window Trade Analysis. 24th International Symposium on Space Flight Dynamics, Laurel (MD), USA, 2014

[184] Zanzottera, A.; Mingotti, G.; Castelli, R.; Dellnitz, M. Low-Energy Earth-to-Halo Transfers in the Earth–Moon Scenario with Sun-Perturbation. *Nonlinear and Complex Dynamics*, **2011**, 31-51

[185] Zhang, H.; Li, S. A general method for the generation and extension of collinear libration point orbits. *Celest. Mech. Dyn. Astron.*, **2016**, 126 (4)